Structural diversity and optical properties of ternary and quaternary chalcogenides

by

Abishek Kannan Iyer

A thesis submitted in partial fulfillment of the requirements for the degree of

Doctor of Philosophy

Department of Chemistry
University of Alberta

Abstract

New ternary and quaternary chalcogenides were synthesized by reactions of elements or binary starting materials at high temperatures, with an emphasis on identifying structures that are noncentrosymmetric which may lead to useful properties such as nonlinear optical behaviour, magnetic ordering, or ionic conductivity. Within the quaternary $RE–M–M'–Ch$ systems (RE = rare-earth elements; M, M' = d-block metals and p-block metalloids; Ch = S, Se), about 30 new compounds were discovered. Most of them belong to a versatile family of noncentrosymmetric hexagonal chalcogenides $RE_3M_{1-x}M'Ch_7$, for which the limits of formation were tested. They include $RE_3CuGaCh_7$ and $La_3Ag_{0.6}GaCh_7$, which violate the condition of charge balance normally seen in this family; La_3MGaSe_7 (M = Zn, Cd), which illustrate that M atoms can occupy more than one site; $RE_3M_{0.5}GeS_7$ (M = Co, Ni, Pd), which extend the number of examples of nonstoichiometric derivatives of this family; and $La_3Sn_{0.5}InCh_7$, which present an exception to the rule that higher-valent substituents prefer the tetrahedral site. Attempts were made to understand the site preferences of different M and M' atoms through bond valence sum and band structure calculations. Other quaternary phases identified in this system are $RE_4InSbSe_9$, which is isostructural to a previously known sulfide NLO material, and RE_7MInS_{13} (M = Co, Fe), which adopts a new structure type. Ternary and quaternary Ba-containing chalcogenides were also investigated. They include $Ba_4Ga_2Se_8$ and $Ba_{12}In_4Se_{20}$ exhibiting diselenide units Se_2^{2-}, which are less commonly found than disulfide units S_2^{2-}. The quaternary chalcogenide $BaRE_2In_2Ch_7$ exhibits five-coordinate In in trigonal bipyramidal geometry. Several quaternary chalcogenides in the Ba–M–M'–Ch system were found that

exhibit noncentrosymmetric structures built up of M- and M'-centred tetrahedra: $Ba_4Ga_4GeSe_{12}$, $BaZnM'Se_4$ (M' = Si, Ge), and $Ba_5CdGa_6Se_{15}$. Measurement of optical properties showed that $BaZnM'Se_4$ and $Ba_5CdGa_6Se_{15}$ are promising candidates for NLO materials with second harmonic generation responses comparable to those of benchmark materials.

Preface

This thesis summarizes the work performed by me and my co-workers in the Mar research group in the Department of Chemistry, University of Alberta from September 2013 to December 2017. My contribution in the work presented is briefly summarized below. A. Mar, the corresponding author, was involved in the manuscript preparation and submission.

Chapter 2 was authored by Iyer, A. K; Rudyk, B. W.; Lin, X.; Singh, H.; Sharma, A. Z.; Wiebe, C. R.; Mar, A. titled "Noncentrosymmetric rare-earth copper gallium chalcogenides $RE_3CuGaCh_7$ (RE = La-Nd; Ch = S, Se). An unexpected combination" was published in *J. Solid State Chem.* **2015**, *229*, 150–159.My contribution to this study includes the synthesis, data collection, analysis, characterization, and preparing the manuscript. B. W. Rudyk assisted in the data collection and analysis of the XPS data and X. Lin helped in the collection of single crystal data. H. Singh assisted with the synthesis and A. Z. Sharma working with C. R. Wiebe collected the magnetic data of the sample La_3CuGaS_7.

Chapter 3 was authored by Iyer, A. K; Yin, W.; Rudyk, B. W.; Lin, X.; Nilges, T.; Mar, A, titled "Metal ion displacements in noncentrosymmetric chalcogenides $La_3Ga_{1.67}S_7$, $La_3Ag_{0.6}GaCh_7$ (Ch = S, Se), and La_3MGaSe_7 (M = Zn, Cd)" and published in *J. Solid State Chem.* **2016**, *243*, 221-231. My contribution to this study includes the synthesis, data collection, analysis, characterization, and preparing the manuscript. B. W. Rudyk assisted in the data collection and analysis of the XPS data and X. Lin helped in the collection of

single crystal data. T. Nilges helped in performing anharmonic refinements for the compounds La$_3$Ag$_{0.6}$GaCh$_7$ (Ch = S, Se).

Chapter 4 was authored by Iyer, A. K; Yin, W.; Lee, E.; Lin, X.; Mar, A., titled "Quaternary rare-earth sulfides RE$_3$M$_{0.5}$GeS$_7$ (RE = La–Nd, Sm; M = Co, Ni) and Y$_3$Pd$_{0.5}$SiS$_7$" and published in *J. Solid State Chem.* **2017**, *250*, 14–20. My contribution to this study includes the synthesis, data collection, analysis, characterization, and preparing the manuscript. W. Yin assisted in single data collection and manuscript preparation. E. Lee assisted with synthesis and X. Lin synthesized the compound Sm$_3$Co$_{0.5}$GeS$_7$ and collected the XRD data collection.

Chapter 5 was authored by Iyer, A. K; Yin, W.; Lee, E. J.; Bernard, G. M.; Michaelis, V. K.; Mar, A., titled "Quaternary Chalcogenides La$_3$Sn$_{0.5}$InS$_7$ and La$_3$Sn$_{0.5}$InSe$_7$" and published in *Z. Anorg. Allg. Chem.* **2017**, *643*, 1867–1873. My contribution to this study includes the synthesis, data collection, analysis, characterization, and preparing the manuscript. W. Yin assisted in diffuse reflectance data collection and manuscript preparation. E. Lee assisted with synthesis. G. M. Bernard and V. K. Michaelis collected and analyzed the ^{119}Sn NMR data.

Chapter 6 was authored by Yin, W.; Iyer, A. K; Li, C.; Yao, J.; Mar, A titled "Noncentrosymmetric rare-earth selenides RE$_4$InSbSe$_9$ (RE = La–Nd)" and published in *J. Alloys Compd.* **2017**, *710*, 424–430. My contribution to this study includes the data collection, analysis, magnetic measurements, and preparing the manuscript. W. Yin proposed the project, synthesis, and manuscript preparation. C. Li working in J. Yao's research group collected diffuse reflectance and SHG measurements.

Chapter 7 was authored by Iyer, A. K; Yin, W.; Stoyko, S. S.; Rudyk, B. W.; Mar, A. titled *"Quaternary rare-earth sulfides Nd_7FeInS_{13} and Pr_7CoInS_{13}"* published in *J. Solid State Chem.* **2017**, *251*, 50-54. My contribution to this study includes the synthesis, data collection, analysis, characterization, and preparing the manuscript. B. W. Rudyk and S. S. Stoyko observed the formation of the compounds as part of their previous research. W. Yin assisted with the synthesis of the compounds.

Chapter 8 was authored by Yin, W.; Iyer, A. K; Li, C.; Yao, J.; Mar, A. titled "Quaternary chalcogenides $BaRE_2In_2Ch_7$ (RE = La-Nd; Ch = S, Se) containing $InCh_5$ trigonal bipyramids" and published in *Dalton Trans*. **2017**, *45*, 12329–12337. My contribution to this project was synthesis, data collection, and LMTO calculations. W. Yin proposed the project and prepared the manuscript. C. Li working in J. Yao's research group collected diffuse reflectance and SHG measurements.

Chapter 9 was authored by Yin, W.; Iyer, A. K; Li, C.; Yao, J.; Mar, A., titled "$Ba_4Ga_2Se_8$: A ternary selenide containing chains and discrete Se_2^{2-} units" and published in *J. Solid State Chem.* **2016**, *237*, 144–149. My contribution to this project was synthesis, data collection, and LMTO calculations. W. Yin proposed the project and prepared the manuscript. C. Li working in J. Yao's research group collected diffuse reflectance and SHG measurements.

Chapter 10 was authored by Yin, W.; Iyer, A. K; Li, C.; Yao, J.; Mar, A., titled "When two becomes one: $Ba_{12}In_4Se_{20}$, not quite isostructural to $Ba_{12}In_4Se_{19}$" and published in *J. Alloys Compd.* **2017**, *710*, 424–430. My contribution to this project was synthesis, data collection and structure refinement. W. Yin proposed the project and prepared the

manuscript. C. Li working in J. Yao's research group collected diffuse reflectance and SHG measurements. A. Mar, the corresponding author, was involved in the manuscript preparation and submission.

Chapter 11, 12 and 13 were all authored by Yin, W.; Iyer, A. K; Li, C.; Lin, X.; Yao, J.; Mar, A.

Chapter 11 titled "Noncentrosymmetric selenide $Ba_4Ga_4GeSe_{12}$" and was published in *J. Solid State Chem.* **2016**, *241*, 131-136; Chapter 12 titled "$Ba_5CdGa_6Se_{15}$, a congruently-melting infrared nonlinear optical material with strong SHG response" was published in *J. Mater. Chem. C* **2017**, *5*, 1057-1063 and Chapter 13 titled "Noncentrosymmetric chalcogenides $BaZnSiSe_4$ and $BaZnGeSe_4$ featuring one-dimensional structures" *J. Alloys Compd.* **2017**, *708*, 414-421. My contribution to this project was synthesis, data collection and structure refinement. W. Yin proposed the project and prepared the manuscript. X. Lin assisted with the structure refinement. C. Li working in J. Yao's research group collected diffuse reflectance and SHG measurements. A. Mar, the corresponding author, was involved in the manuscript preparation and submission.

Acknowledgement

Throughout the course of my Ph.D. I have had the opportunity to work under and with a lot of amazing people. Their help and support has been crucial towards the contents of this thesis.

First and foremost, I would like to express my deepest gratitude to Dr. Arthur Mar, my supervisor, teacher, and mentor. At first, I would like to thank for accepting me as a graduate student in his group. Dr. Mar's transparent personality and sense of humor made him more of a friend than a supervisor to me. During the course of my graduate studies he taught me to embrace both success and failure equally, something which made me enjoy doing research and want to continue with it in my future as well. He has always been available to offer help with research by providing ideas and with the writing of journal articles.

I would like to thank Dr. Wenlong Yin, post-doctoral student who was a co-author in most of the papers I published during the course of my graduate studies for his useful discussions and assistance with synthesis and crystallography. Without him a lot of the work in this thesis may not have been completed. His motto of "work and workout" not just helped me with my research but also made me go to the gym! I would like to thank all past and present group members Brent, Xinsong, Anton, Krishna, Mansura, Danisa, Yuqiao, Dundappa, Vidyanshu, Dong and Alex for their constant support and good times in the lab. I would like to thank University of Alberta for providing me with all the facilities to conduct my research. I would like to thank Dr. Norman Gee, my teaching assistant coordinator for his support to help me become a better teacher. The skill I learned during

Table of Contents

List of Tables

List of Figures

xxiii

List of symbols and abbreviations

θ	Angle of reflection
k	Wavevector
λ	Wavelength
ρ	Density
μ	Absorption coefficient
ω	frequency
1D, 2D, 3D	One-, two-, three-dimensional
$a, b, c, \alpha, \beta, \gamma$	Unit cell parameters
A	Alkali metal or Alkaline-earth metals
ASA	Atomic sphere approximation
Ch	Chalcogenides
COHP	Crystal orbital Hamilton population
COOP	Crystal orbital overlap population
DOS	Density of states
DSC	Differential scanning calorimetry
d_{hkl}	d-spacing
EDX	Energy Dispersive X–ray spectroscopy
e^-	Electron
$\boldsymbol{E}$	Electric Field
E_f	Fermi level
E_g	Band gap
F_{hkl}	Structure factor
f_j	Scattering factor of atom j

hkl	Miller indices
IR	Infra-red
j	Angular momentum
LDA	Local density approximation
LMTO	Linear muffin-tin orbital
M	*d*-block elements
NLO	Nonlinear optics
NMR	Nuclear magnetic resonance
PPMS	Physical property measurement
P	Polarizability
RE	Rare-earth
S	Goodness-of-fit
SEM	Scanning electron microscope
SHG	Second harmonic generation
TB	Tight-binding
Tr	Triels (Group 13 elements)
Tt	Tetrels (Group 14 elements)
UV	Ultra-violet
V	Cell volume
XRD	X-ray diffraction
XPS	X-ray photoelectron spectroscopy
YAG	Yttrium aluminium garnet
Z	Atomic number

Chapter 1

Introduction

The many different ways that elements can combine can result in diverse structures and physical properties of solid state compounds. This thesis describes the synthesis of new chalcogenides with the aim of exploring their structural diversity and optical properties.

1.1 Chalcogenides

Chalcogenides are compounds of the group-16 elements or chalcogens (Ch), consisting of O, S, Se, and Te. Because O differs significantly in electronegativity (3.5 for O compared to 2.5 for S, 2.4 for Se, and 2.1 for Te),[1] oxides are typically distinguished from the rest of the chalcogenides, which exhibit strongly covalent character. For example, TiO_2 (rutile, space group $P4_2/mmm$) exhibits a three-dimensional framework whereas TiS_2 (CdI_2-type, space group $P\bar{3}m$) has a layered structure, with Ti atoms occupying octahedral sites in both cases. Layered structures are more common for the heavier chalcogenides because the presence of a van der Waals gap implies lower charges consistent with the lesser electronegativity of S (**Figure 1–1**).[2,3,4]
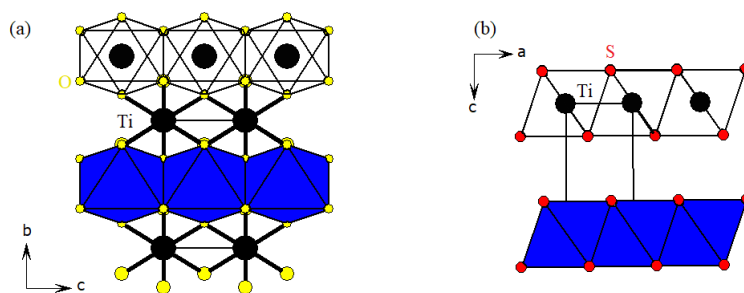
Figure 1-1. Structural bonding difference between TiO_2 and TiS_2.

Revived interest in layered metal dichalcogenides MCh_2 is motivated by the search for materials for energy applications, such as solar cells (MoS_2), Li-ion batteries (WS_2), and water

splitting catalysts (MoS_2 and $MoSe_2$).[5] Another consequence of the lower electronegativities is the propensity to form homoatomic *Ch–Ch* bonds in the heavier chalcogenides, as seen in FeS, which is superconducting at 4 K, and FeSe, whose superconducting critical temperature increases from 8 K to 44 K when intercalated with LiOH resulting in $[(Li_{0.8}Fe_{0.2})OH]Fe(S_{1-x}Se_x)$ ($0 < x <$ 1).[6] In general, chalcogenides tend to have smaller band gaps than oxides and are attractive as semiconducting materials.

This thesis explores two broad series of quaternary chalcogenides: *RE-M-M'-Ch* (*RE* = rare-earth elements; *M*, *M'* = d-block metals and p-block metalloids; *Ch* = S, Se) and Ba-*M-M'-Ch* (*M*, *M'* = usually late d-block metals and p-block metalloids; *Ch* = S, Se, Te). A particular focus is on chalcogenides that have small band gaps and are simultaneously noncentrosymmetric (lacking a centre of inversion), which make them suitable as nonlinear optical (NLO) materials operating in the infrared region, in contrast to oxides which operate in the UV-visible region.

1.2   Nonlinear optical materials

NLO materials are used to convert the specific coherent wavelengths produced by lasers into wavelengths in other spectral regions such as UV-visible (0.2–2 μm) and infrared (3–20 μm), where lasers have poor efficiency. The technology for UV-visible lasers, which are based on metal oxide NLO materials, is well developed and finds applications in high-capacity communication networks (fiber optics) and precision scientific instruments (beam splitters and mirrors).[7] In contrast, metal chalcogenides with their smaller band gaps are appropriate for infrared lasers, which are useful for visualization of tissue, environmental monitoring, and security applications.[8–11] Benchmark materials are plentiful for UV-visible NLO materials, and their key properties are unlikely to be improved any further; however, there are relatively few candidates for IR NLO materials and research is ongoing to improve their properties (**Table 1–1**).

2

Table 1-1. Commercially used NLO materials.[12]

Compound	Space group	Band Gap (eV)	SHG intensities (pm/V)	Transparency (μm)
Oxides				
β- BaB_2O_4 (BBO)	$R3c$	6.2	2.2 (at 1.064 μm)	0.18–3.5
LiB_3O_5 (LBO)	$Pm2_1$	7.78	0.67	0.15–3.2
$KBe_2BO_3F_2$ (KBBF)	$R32$	8.00	0.49	0.15–3.7
Chalcogenides				
$AgGaS_2$ (AGS)	$I\bar{4}2d$	2.73	23 (at 1.05 μm)	0.47–11.4
$AgGaSe_2$ (AGSe)	$I\bar{4}2d$	1.83	41.4 (at 9.27 μm)	0.76–17
$ZnGeP_2$ (ZGP)	$I\bar{4}2d$	2.0	70 (at 5.29 μm)	0.75–12

The origin of NLO behaviour is well understood. When a medium is subjected to an external electric field E, the charge distribution in the solid is distorted and a polarization (electric dipole moment per unit volume) P develops. In most substances, the relationship is linear:

$P = \varepsilon_o \chi(1)E$ where ε_o = permittivity in vacuum and $\chi(1)$ = linear electric susceptibility coefficient.

However, in a few special substances, the relationship is nonlinear and can be expanded as a power series:

$$P = \varepsilon_o [\chi(1)E + \chi(2)EE + \chi(3)EEE + \cdots]$$

where $\chi(2)$ and $\chi(3)$ = second and third order nonlinear electric susceptibility coefficients [13]

Second harmonic generation (SHG) refers to the doubling of light frequency ($\omega, \omega \rightarrow 2\omega$) which is observed when the second-order nonlinear susceptibility is high. This effect was first discovered by Franken in 1961 when he passed light from a ruby laser (λ= 6.94 μm, fundamental radiation) through large single crystals of quartz (λ= 3.47 μm, second-harmonic radiation).

3

Although it is most desirable to measure SHG activity on large single crystals, Kurtz proposed in 1968 that it could also be measured on polycrystalline samples, with the understanding that SHG efficiencies depend strongly on particle sizes. For NLO materials to be practical, they should exhibit Type-I phase matchability. [14] Type-I phase matching occurs when n (ω) = n (2ω) where n (ω) refractive index of the fundamental wave and n (2ω) is the refractive index of the second harmonic wave. The diagnostic feature of a type-I phase matchable material is that the SHG intensity increases with particle sizes (**Figure 1–2**).[15]
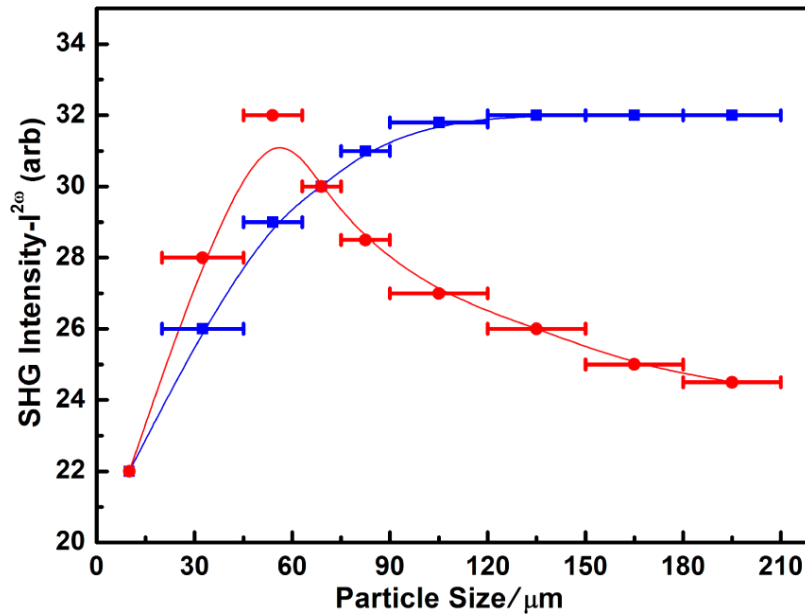
Figure 1-2. Phase matching (LiNbO$_3$, blue) and non-phase matching (SiO$_2$, red) curves for a powder measurement[16]

A good candidate for an NLO material should possess several properties.[15]

1. Wide transparency range, either in the far infrared region for chalcogenides or deep UV region for oxides and halides

2. Type-I phase matchability

3. Good chemical and thermal stability; ease of processability (e.g., crystal cutting and polishing)

4. Relatively large NLO coefficients in the expected spectroscopic region.

Currently, the commercially available IR NLO materials suffer from certain limitations which restrict their wider use. $AgGaS_2$ and $AgGaSe_2$ suffer from poor thermal conductivity and negative anisotropic thermal expansion, causing thermal stress during crystal growth. A serious problem is multiphoton absorption, which results in laser-induced damage of the NLO material.[8]

The requirement of noncentrosymmetry in NLO materials limits the possible space groups and thus their parent crystal classes that they can adopt. Other kinds of physical properties, such as optical activity, piezoelectricity, and pyroelectricity, also depend on this absence of an inversion centre, but there are subtle differences in the crystallographic requirements. Out of the 32 crystal classes, which represent the point symmetry of a crystal structure, 21 are acentric, but out of these, all but one (432) are compatible with the occurrence of SHG signals in NLO materials, as summarized by Halasyamani based on an earlier description by Glazer (**Figure 1–3**). In fact, piezoelectricity (generation of an electrical potential upon application of mechanical stress) and SHG share the same symmetry requirements. Further, all pyroelectric materials (generation of temporary voltage across a crystal due to change in temperature) exhibit SHG behaviour, but the reverse is not true.[17]
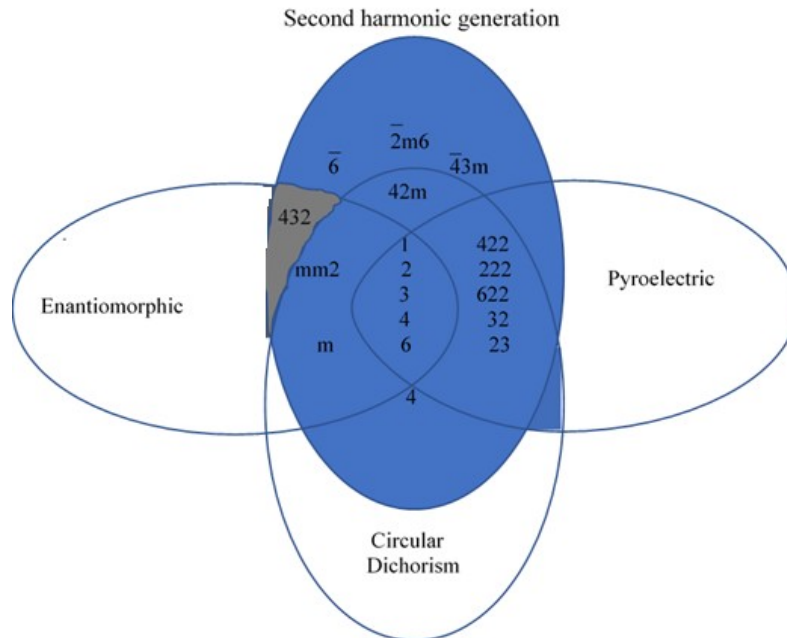
Figure 1-3. Noncentrosymmetric crystal classes and their properties.

To date, there is no obvious way to guarantee that a given compound will crystallize in a noncentrosymmetric structure, although many strategies have been developed to maximize the chances that it will do so.[18] The most frequent strategy is to incorporate anionic building blocks that are noncentrosymmetric, most commonly tetrahedra [MCh_4] where M is metal ions of different charges (2+, 3+, 4+, 5+), although trigonal planes such as [BS_3]$^{3-}$, [$HgSe_3$]$^{3-}$ have also been used, with the hope that they attain arrangements in the crystal structure without an inversion centre. Electronic factors are also important. Other kinds of polyhedra can become asymmetric if they undergo second-order Jahn-Teller distortions (e.g. octahedra) in d^0 (e.g., Ta^{5+}, Zr^{4+}, Nb^{5+}, Ti^{4+}, Mo^{6+}) or d^{10} (Zn^{2+}, Cd^{2+}) systems. Metal ions that contain stereochemically active lone pairs such as Sn^{2+} or Sb^{3+} can also form distorted polyhedra. Finally, if a series of noncentrosymmetric structures already exists, it is sensible to prepare new or missing members of these series. In

6

general, more complex compositions allow greater flexibility and control to tune desired properties; thus it is worthwhile investigating not only new binary and ternary chalcogenides, but also quaternary chalcogenides. Lastly, for practical applications, it is important to be able to grow large crystals easily.

Characterization of the SHG behaviour was performed in collaboration with Prof. Jiyong Yao at the Centre for Crystal Research and Development, Technical Institute of Physics and Chemistry, Chinese Academy of Science. The sample is placed in a fused-silica tube under vacuum. A Q-switched Ho:Tm:Cr:YAG laser was used as the radiation source (λ = 2.05 μm). The light with primary wavelength is passed through the sample and the intensity of any converted light of doubled frequency is measured. This SHG intensity is then compared with that of a benchmark material (e.g. $AgGaS_2$ or $AgGaSe_2$). The measurement is repeated for polycrystalline samples which were ground and sieved according to different particle size ranges (25–45, 45–58, 58–75, 75–106, 106–150, and 150–212 μm).

1.3 *RE-M-M'-Ch*

About 50 years ago, a series of quaternary rare-earth chalcogenides $RE_3MM'Ch_7$ (RE = rare-earth metals; M = transition metals; M' = tetrels and triels; Ch = S, Se) with noncentrosymmetric hexagonal structures (space group $P6_3$) was first identified by Flahaut and co-workers. They suggested that this series should be highly versatile because of the wide variety of elements that can be substituted for the M and M' components. If formal charges of 3+ for RE atoms and 2– for Ch atoms are assigned, the requirement of charge balance restricts the combinations of M and M' components such that the sum of their charges is 5+. Even with this restriction, many compounds are possible, but only a few were fully characterized at the time

(**Table 1–2**). In fact, the structural characterization was lacking for most compounds, and at best, only unit cell constants were available, extracted through powder XRD analyses.[19, 20] The first full single crystal structure determination was for La_3CuSiS_7, and this became established as the name of the structure type. It was not until several decades later that subtle differences in the crystal structures of different members of this series became appreciated; in particular, complications can arise because of partial site occupancies or varying coordination preferences. For example, it was initially assumed that Ag-containing members of this series were stoichiometric compounds, but later this was shown not to be the case.[21] The incomplete structural characterization of these compounds suggested that further investigation was worthwhile.

Table 1-2. Various combinations possible in for $RE_3MM'Ch_7$.[19, 20]

Rare-Earth	M	M occupancy	M'	Formula
	I	100 %	IV	$RE_3MM'Ch_7$
	Cu, Ag		Tt = Si, Ge, Sn	e.g. La_3CuSiS_7
	II	100 %	III	$RE_3MM'Ch_7$
RE^{3+}	transition metals (Mn-Zn, Cd)		Tr = Al, Ga	e.g. La_3MnGaS_7
	III	100 %	II	$RE_3MM'Ch_7$
	Sc-Cr, Sb, Bi, In, Yb, Lu		Be	e.g. La_3CrBeS_7
	II	50 %	IV	$RE_3M_{0.50}M'Ch_7$
	transition metals Mn-Ni		Tt = Si, Ge, Sn	e.g. $La_3Mn_{0.5}SiS_7$

Revived interest in these compounds came when investigators began searching for new magnetic and optical materials. In 1983, Gopalakrishnan and co-workers showed that La_3MAlS_7 and La_3MFeS_7 (M = Mg, Mn, Fe, Ni, Zn) exhibited low-dimensional antiferromagnetism consistent with the presence of chains of M-centred octahedra in these structures.[22] Later, the possibility that these compounds may be candidates for NLO materials was evaluated. However, early investigations were not encouraging, when DiSalvo and co-workers observed that $La_3Mg_{0.5}SiS_7$ and La_3CuGeS_7 exhibited poor SHG response.[23] Ferroelectric behaviour has been predicted for La_3MnGaS_7 (with Curie temperatures as high as 1000 K), but this has never been

confirmed.[24]   The attractive feature of these series of compounds is that it appears to be highly versatile to substitution and thus their properties are amenable to tuning.   Although the M' component always occupies a tetrahedral site, the M component can occupy either octahedral or trigonal planar sites, with variable occupancies (33–100%). Over the past 10 years, the freedom to tune the M component has led to new compounds $Y_3Zn_{0.5}SiS_7$, $La_3In_{0.5}(Ge_{0.5}In_{0.5})S_7$, $La_3Ga_{0.5}(Ga_{0.5}Ge_{0.5})S_7$ which show promising SHG behaviour.[25,26]   An important point is that because SHG effects can vary depending on the fundamental wavelength, so one cannot easily dismiss a compound as a poor NLO material quickly. Finally, nonstoichiometric members, mainly the Ag-containing representatives, were found to exhibit occupational disorder over several sites with unusually large anisotropic displacement parameters similar in magnitude to the ionic conductor Cu_6PS_5I.[27]

Table 1-3. Reported compounds for different combinations of $RE_3MM'Ch_7$.

I + IV	II + III	II + IV	III + IV	IV + IV
$RE_3CuSiCh_7$ [28, 29] $RE_3CuGeCh_7$ [30, 31] $RE_3CuSnCh_7$ [32] (RE = Y-Nd, Sm- Er; Ch = S, Se) $RE_3Ag_{1-x}SiCh_7$ [33, 34] $RE_3Ag_{1-x}GeCh_7$ [35,36] (RE = La-Nd, Sm, Gd,Er; Ch = S, Se; x = 0 – 0.5) $RE_3Ag_{0.8}SnS_7$ [37] (RE = La, Ce) $La_3AgSnSe_7$ [37] Sm_3NaSiS_7 [27] RE_3NaGeS_7 [38] (RE = Ce, Nd, Sm, Gd, Yb)	$La_3MnGaSe_7$ [39] RE_3FeGaS_7 [40, 41] (RE = La, Pr, Nd, Sm, Gd, Dy, Tb) $RE_3FeGaSe_7$ [40,41] (RE = Nd, Gd, Dy) RE_3CoGaS_7 [40] (RE = La, Nd, Sm, Dy, Er, Tb) $RE_3CoGaSe_7$ [40] (RE = Nd, Sm, Gd) RE_3NiGaS_7 [40] (RE = Nd, Sm, Dy, Er) $RE_3NiGaSe_7$ [40] (RE = Nd, Gd) RE_3FeInS_7 [42] (RE = La, Ce, Pr) La_3CoInS_7 [42] La_3NiInS_7 [42]	$La_3Mg_{0.5}SiS_7$ [23] $La_3Mg_{0.5}GeS_7$ [23] $RE_3Mg_{0.5}GeS_7$ (RE = Y, Ce-Nd, Sm, Gd-Er) [43] $RE_3Mg_{0.5}MSe_7$ (RE = Ce, Pr, M = Si, Ge) [44] $RE_3Mn_{0.5}SiSe_7$ (RE = La, Ce, Sm) [39] $RE_3Mn_{0.5}GeS_7$ (RE = Y, Ce-Nd, Sm, Gd-Er) [39, 45] $RE_3Fe_{0.5}GeS_7$ [46] (RE = Y, La-Pr, Sm, Gd-Tm) $RE_3Fe_{0.5}SiSe_7$ [39] (RE = La, Ce, Sm) $RE_3Fe_{0.5}GeSe_7$ [39] (RE = La, Ce, Sm) $Y_3Zn_{0.5}SiS_7$ [25] $La_3Fe_{0.61}SnSe_7$ [47]	$Sm_3Al_{0.33}SiS_7$ [25] $Sm_3In_{0.33}SiS_7$ [47] $Y_3Si_{0.5}AlS_7$ [47] $Dy_3Al_x(Si_yAl_{1-y})S_7$ [25] $RE_3Sb_{0.33}SiS_7$ [48] (RE = La, Pr) $RE_3Sb_{0.33}SiSe_7$ [49] $La_3Sb_{0.31}GeSe_7$ [47]	$RE_3Ge_{1-x}Ch_7$ [50] $RE_3Sn_{1-x}Ch_7$ [50]

To date, over 300 compounds have now been discovered that have the composition $RE_3MM'Ch_7$, according to Pearson's Crystal Data (**Table 1-3**).[51] There are many combinations of M and M' that are possible to satisfy the condition of charge balance. The M' atoms are always in tetrahedral sites, but the M atoms vary in their coordination preference, leading to several branches of this family of chalcogenides (**Figure 1–4**). Within the first category, there are 155 compounds belonging to the I-IV combinations, such as La_3CuSiS_7, in which the monovalent M atoms occupy a trigonal planar site. Within the second category, there are 242 compounds belong to II-IV or II-III combinations, in which the divalent M atoms occupy an octahedral site. In the case of II-IV combinations, the M sites must be half-occupied, as in $La_3Mn_{0.5}SiS_7$. Other combinations are possible but much rarer. When M and M' are the same elements, ternary compounds such as $Ce_3Al_{1.67}S_7$ (or $Ce_3(Al)_{0.67}AlS_7$) are formed. There are about 142 reports of such ternary chalcogenides. It is of interest to determine if all possibilities for M and M' combinations have been exhausted, or if the condition of charge balance must always be obeyed.
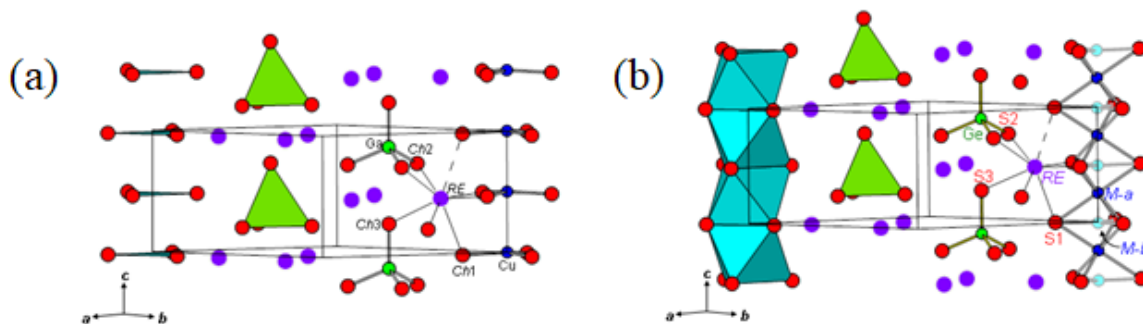
Figure 1-4. Crystal structure of $RE_3M_{1-x}M'Ch_7$ where (a) M is trigonal planar; and (b) where M is octahedra.

In contrast to ternary $RE–M–Ch$ systems, which have now been well investigated, with well over 1500 compounds now having been identified, quaternary $RE–M–M'–Ch$ systems could

potentially reveal many more compounds, given the large number of combinations possible. To date, only 600 quaternary chalcogenides $RE–M–M'–Ch$ (excluding alkali, alkaline-earth metals, and halides) have been discovered. Of these, most belong to the $RE_3M_{1-x}M'Ch_7$ family. Other quaternary chalcogenides include: RE_4GaSbS_9 (RE = Pr, Nd, Sm, Gd–Ho), RE_4InSbS_9 (RE = La, Pr, Nd), $RE_2CuInCh_5$ (RE = La–Pr),[54, 55] $RECuPbCh_3$ (RE = Tb–Lu), $RE_5CuPb_3S_{11}$ (RE = Y, La–Nd, Sm; Gd–Tm), $RE_2Mn_3Sb_4Se_{12}$ (RE = Pr, Nd, Sm, Gd), $La_4FeSb_2Ch_{10}$, $RE_2PbSi_2S_8$ (RE = Y, La–Nd, Sm–Ho), $RE_2PbSi_2Se_8$ (RE = Y, La–Nd, Sm, Gd) and $RE_3PbGe_2S_8$ (RE = La, Ce).[52–62] The compounds Sm_4GaSbS_9 and La_4InSbS_9 have been found to show large SHG intensity.

1.4 Ba-*M-M'-Ch*

Closely related to the rare-earth-containing chalcogenides discussed above are those in which the RE component is replaced by an alkaline-earth element. In particular, many Ba-containing chalcogenides have been discovered in recent years. There are now many examples in the Ba–M–M'–Ch system where M and M' are late transition metals (Cu, Ag, Cd, Zn) or triels (Al, Ga, In). In the 1980s and 1990s, one of the main challenges in preparing chalcogenides containing more electropositive elements such as alkali and alkaline-earth metals was handling these reactive starting materials. In the 2000s, application of flux methods (through the addition of polychalcogenides such as K_xS_y) led to the discovery of many new ternary chalcogenides, especially those containing alkali metals.[63] The air stability of BaS and BaSe made them attractive as starting materials. Within the Ba–M–Ch systems, $BaAl_2S_4$ doped with Eu^{2+} was found to be a promising luminescent material, and $BaGa_4S_7$ was found to be a good IR NLO material exhibiting high SHG intensity and high laser-induced damage thresholds.[64, 65] Ba–M–Ch compounds (for M = triels, tetrels, and pnicogens) are now numerous (**Table 1–4**). Among these, a few are noncentrosymmetric (as highlighted in the Table), including BaM_4Ch_7. When the investigation is

extended to quaternary Ba–M–M'–Ch systems (dominated mainly by M, M' = triels, tetrels), relatively a larger proportion of the compounds are found to be noncentrosymmetric.

Table 1-4. Reported ternary compounds in the Ba/M/Ch system.

Ba/M/Ch (M = Al, Ga, In)	Ba/M/Ch (M = Si, Ge, Sn)	Ba/M/Ch (M = P, As, Sb)
BaM_4Ch$_7$[65–68] (M = Al, Ga; Ch = S, Se)	Ba$_2$$MCh_4$ [77-81] (M = Si, Ge, Sn; Ch = S, Se, Te)	Ba$_3$P$_2$$Ch_8$[92] ($Ch$ = S, Se)
Ba$_5$$M_2Ch_8$[69,70] ($M$ = Al, Ga; Ch = S, Se)	**BaGe$_2$$Ch_5$**[82, 83] ($Ch$ = S, Se)	BaPCh_3[93] (Ch = S, Se)
Ba$_4$Ga$_2$S$_7$[71]	**Ba$_8$Sn$_4$S$_{15}$**[84]	Ba$_3$Sb$_2$$Ch_7$[96] ($Ch$ = S, Se)
Ba$_3$Ga$_2$S$_6$[71]	**Ba$_7$Sn$_5$S$_{15}$**[82]	BaM_2Se$_4$[95, 96] (M = Bi, Sb)
Ba$_2$$M_2Ch_5$[72] ($M$ = Al, Ga; Ch = S, Se)	Ba$_6$Sn$_7$S$_{20}$[82]	Ba$_2$$M_2Ch_5$ [97-99] (M = As, Sb; Ch = S, Se)
BaM_2Ch$_4$[73, 74] (M = Al, Ga, In; Ch = S, Se)	Ba$_2$Ge$_2$S$_6$[79]	Ba$_3$Bi$_{6.67}$Se$_{13}$[100]
Ba$_4$$M_2S_8$[75] ($M$ = Ga, In)	Ba$_7$Sn$_3$Se$_{13}$[83]	BaBiTe$_3$[101]
Ba$_{12}$In$_4$S$_{19}$[75]	**Ba$_6$Sn$_6$Se$_{13}$**[86]	BaP$_4$Te$_2$[102]
Ba$_5$Ga$_4$Se$_{10}$[76]	**Ba$_2$SnCh_5**[87, 88] (Ch = Se, Te)	Ba$_8$Sb$_6$S$_{17}$[103]
	Ba$_2$Ge$_2$Ch$_5$[89, 90] (Ch = Se, Te)	
	Ba$_3$GeS$_5$[91]	

*Compounds in bold are noncentrosymmetric

Within the ternary Ba/M/Ch there are not many compounds which crystallize in noncentrosymmetric space groups, so the search was expanded to quaternary compounds. The quaternary system Ba-M-M'-Ch is mainly dominated by compounds where M and M' are triels and tetrels. It is interesting to note that a much larger number of the reported compounds were found to crystallize in a noncentrosymmetric space group (**Table 1–5**).

Table 1-5. Reported quaternary compounds in the Ba/M/M'/Ch system

Chalcogen	M = late transition metals			$M = Tr$	$M = Tt$
	Cu, Ag		Zn, Cd	Al, Ga, In	Si, Ge, Sn
	$M' = Tr$	$M' = Tt$			
S	Ba_2AgInS_4[104] $Ba_2Ag_{0.5}Ga_{0.5}S_3$[105] $Ba_4MM'S_6$[105] (M = Cu, Ag; M'= Ga, In) **$Ba_4CuGa_5S_{12}$**[106]	$BaCu_6Ge_2S_8$[108] **$Ba_4Cu_2GeS_4$**[109] **$Ba_{1.5}Ag_{0.978}Sn_{1.005}S_4$**[110] **$Ba_{1.5}Ag_{0.798}Sn_{1.05}S_4$**[110] **$Ba_{1.5}Ag_{0.998}Sn_{1.00}S_4$**[110]	**$BaZnSnS_4$**[113]	**Ba_2InBiS_5**[114] Ba_2GaBiS_5[114] **$BaGa_2SiS_6$**[115] **$BaGa_2GeS_6$**[115,116] **$Ba_2Ga_8GeS_{16}$**[117] **$Ba_2Ga_8SiS_{16}$**[117] Ba_2GaSbS_5[118] **$Ba_{23}Ga_8Sb_2S_{38}$**[125]	$Ba_2GeSb_4S_{10}$[122] Ba_2BiGaS_5 **Ba_2BiInS_5**
Se	$Ba_4AgGa_5Se_{12}$[104] $Ba_4MM'Se_6$[105] (M = Cu, Ag; M'= Ga, In) **$Ba_4CuGa_5Se_{12}$**[106] $Ba_7AgGa_5Se_{15}$[107]	**$BaAg_2GeSe_4$**[111] $Ba_3Cu_2Sn_3Se_{10}$[112] $BaCu_2SnSe_4$[112] **$Ba_{1.5}Ag_{0.908}Sn_{1.022}Se_4$**[110] **$Ba_{1.5}Ag_{0.908}Sn_{1.022}Se_4$**[110] **$Ba_{1.5}Ag_{0.908}Sn_{1.022}Se_4$**[110]	**$BaCdSnSe_4$**[79]	$BaGa_2GeSe_6$[116] $Ba_2GaAsSe_5$[119] **Ba_2GaMSe_5**[120] (M = Sb, Bi;) $Ba_2InSbTe_5$[120] **$Ba_2InSbSe_5$**[120] $Ba_6Ga_2SnSe_{11}$[121] **$Ba_4Ga_4SnSe_{12}$**[121] $BaGa_2SiSe_6$[116] **$BaGa_2GeSe_6$**[115]	$Ba_3Sn_{0.87}Bi_{2.13}Se_8$[123] $Ba_3SnSb_2Se_8$[123] **$Ba_4SiSb_2Se_{11}$**[124] $Ba_3Bi_6PbSe_{13}$[100] $Ba_3Bi_6SnSe_{13}$[100]
Te				$Ba_2BiGaTe_4$[120] $Ba_2GaSbTe_5$[120]	

*Compounds in bold are noncentrosymmetric

1.5 Synthesis

Many solid-state compounds are synthesized at high temperatures (typically to as high as 1000 °C) and over long reaction times (few days to a few months) to ensure that diffusion takes place at reasonable rates. One challenge in preparing quaternary phases is that there may be other competing phases (binaries or ternaries) that may be formed in the first steps of the reaction and could be quite thermodynamically stable. Then it becomes necessary to regrind the samples, reload them into new ampoules, and reheat the samples to obtain the targeted compound. The choice of synthetic method, including starting materials, temperature, and containers, depends on

the class of compounds being prepared. In the simplest case, the reactants combined in stoichiometric amounts are finely ground to small pieces or powders to maximize the surface area, pressed into pellets, and heated according to a temperature profile, on the assumption that the reaction proceeds entirely through diffusion of atoms between solid phases (**Figure 1-5**). The choice of container is important and depends on the reactivity of the elements. Alkali and alkaline-earth metals react with fused silica whereas most rare-earth metals (other than Eu and Yb) and transition metals are less reactive. Binary alkali or alkaline-earth chalcogenides are a suitable alternative. Although alkali-metal chalcogenides such as Na_2S_2 and K_xS can be synthesized in liquid ammonia solution, it is more convenient to purchase these starting materials commercially. On the other hand, alkaline-earth metal chalcogenides such as SrS and BaS are easily prepared in thick-walled carbon-coated fused-silica tubes. Elemental chalcogens have relatively low boiling points (444 °C for S, 685 °C for Se, and 988 °C for Te) and high vapour pressures, which could result in volatilization losses (or worse, explosions) at the reaction temperatures used. To minimize these risks, care is taken to avoid filling the tubes to more than a quarter of their volumes, to use thick-walled tubing, and to heat gradually in the initial treatment.

Stoichiometric amount BaSe +ZnSe+M' (M' = Si, Ge), Se molar ratio of 1:1:1:2

Temperature Profile
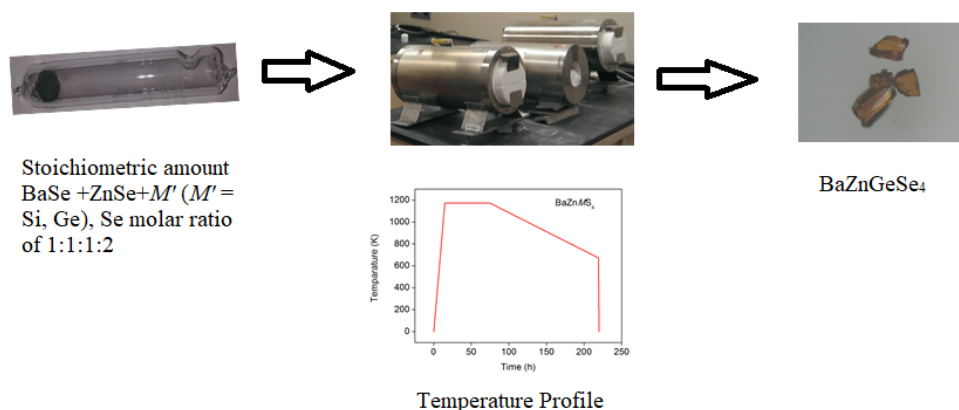
BaZnGeSe₄

Figure 1-5. Schematic showing the synthesis process for chalcogenides (BaZnGeSe$_4$ in this case).

A separate problem is the growth of sufficiently large single crystals for the purpose of structure determination. Although slow cooling of the melt may be successful in ideal cases, an alternative is to employ a flux, in the form of a low melting solid (e.g., Ga, Ge, In), a molten halide salt (e.g., NaCl, KCl, BaCl$_2$), or a molten polychalcogenide (Na$_2$Ch$_2$, K$_x$S), which acts as a solvent to allow the reactions to take place at lower temperatures. Eutectic mixtures of halide salts, such as NaCl–KCl, can also be useful in achieving low melting points, although in some cases, they may be incorporated into the final product.[63] The reactants are heated to above the melting point of the flux at which point the diffusion of other elements increases and then the sample is cooled down slowly, resulting in crystals formed through nucleation and precipitation. Since most salts are soluble in polar solvents, they can be easily washed away. Care must be taken if the resulting products are moisture-sensitive or contain residual alkali or alkaline-earth metals, which may react with polar solvents. Thus, in these cases, it is preferable to use binary or polychalcogenide starting materials, which are easier to handle.

Within the *RE–M–M′–Ch* systems, direct reactions of the elements were performed, and different heat treatments were optimized to obtain phase-pure samples. It must be mentioned that many reactions attempted with Te did not yield any new compounds. Within the Ba–*M–M′–Ch* systems, binary or ternary starting materials (Ba*Ch*, *M′*$_2$*Ch*$_3$ (*M′* = Ga, In), Ge*Ch*$_2$) were used to obtain phase-pure products. Reactions with Ca and Sr also did not yield any new compounds under the conditions tried. One of the important criteria to grow large single crystals is to know if the product melts congruently, which can be determined through differential scanning calorimetry. Although not performed in this thesis, very large single crystals can be grown using the Bridgman-

Stockbarger technique in which crystallization of the melt on a seed crystal occurs by virtue of a temperature gradient. For example, $BaGa_4S_7$ is a commercially used chalcogenide nonlinear optical material that has been grown using this method.

1.6 X-ray Diffraction

The most important technique to characterize the structures of solid state compounds is X-ray diffraction. When a series of waves encounter an obstacle of the comparable wavelength, it gets scattered in all directions. Interference then occurs between the resulting waves. If adjacent waves are in phase, they undergo constructive interference; if out of phase, they undergo destructive interference (**Figure 1–6**).

Constructive Interference   Destructive Interference
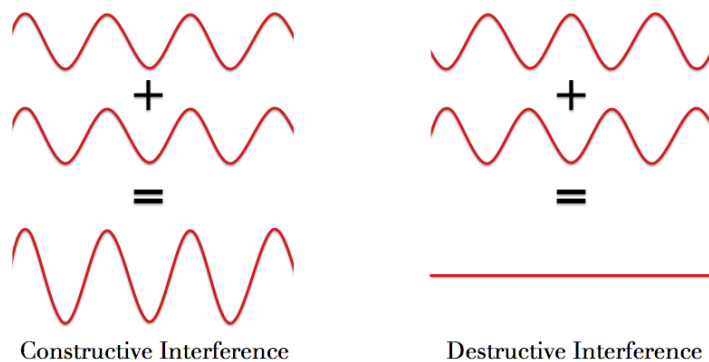
Figure 1-6. Schematic showing constructive and destructive interference in waves.

X-rays are a form of highly energetic electromagnetic radiation whose wavelengths are comparable to the distances between atoms (on the order of several Å). Hard X-rays with short wavelengths of 1–2 Å are produced when electrons are accelerated across an electrical potential and strike a metal target (e.g., normally Cu or Mo). The X-ray spectrum consists of a broad background called Bremsstrahlung or white radiation arising from inelastic collisions (incoming electrons with the nucleus of the target atoms). Superimposed on this background are sharp, intense peaks arising from elastic collisions (incoming electrons with the core electrons of the

target atoms) with wavelengths that are characteristic of the target element (**Figure 1–7**). The most intense of these sharp peaks are caused by ejection of electrons from the K ($n = 1$) shell and filling of the produced hole by electrons in the higher energy L ($n = 2$) or M ($n = 3$) shells, resulting in K_α and K_β lines, respectively. The less intense K_β lines are removed by a filter with an appropriate absorption edge (e.g., Ni for a Cu source, or Nb for a Mo source), while the most intense K_α lines are used for the X-ray diffraction experiment. X-ray diffraction patterns can be collected on powder samples, used primarily for phase identification, or single-crystal samples used to determine full crystal structures.[125, 126]
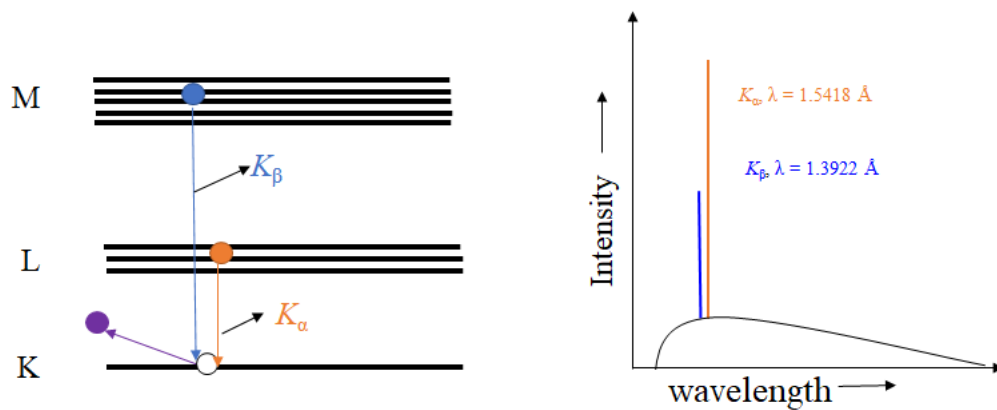
Figure 1-7. Schematic representation of (a) generation of X-ray and (b) the emission spectrum of copper.

1.6.1 Single-Crystal Diffraction

A crystal structure consists of a regular arrangement of atoms. This arrangement can be represented by a lattice (a set of imaginary points that defines the point and translational symmetry of the long-range arrangement) and a basis (the set of atoms associated with each lattice point). X-rays that strike the periodic arrangement of atoms within a crystal undergo diffraction, with constructive interference taking place only when the path differences between the scattered

17

wavelengths are integral numbers of wavelengths (**Figure 1–8**). The conditions described by these Laue equations, which are rather stringent to satisfy, can be interpreted as the intersection of diffraction cones oriented along each of the lattice directions.

$$a(cos\mu_a + cos\upsilon_a) = n_a\lambda = h\lambda$$
$$b(cos\mu_b + cos\upsilon_b) = n_b\lambda = k\lambda$$
$$c(cos\mu_c + cos\upsilon_c) = n_c\lambda = l\lambda$$
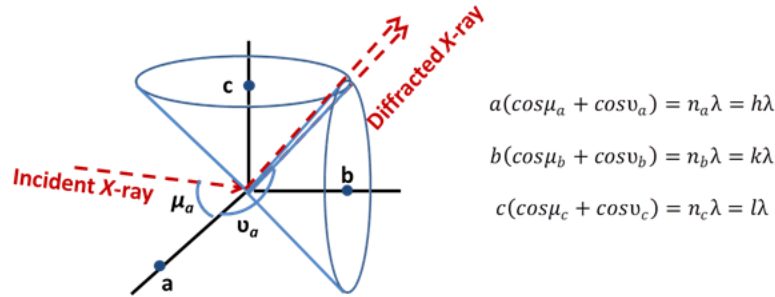
Figure 1-8. Laue conditions for X-ray diffraction. a, b, c are the distances between lattice points along x, y, z axes; μ and ν are the angles made by the incident and diffracted X-ray beam; λ is the wavelength; h, k, l are Miller indices.

The Laue conditions for the scattering of X-rays through a crystal can be modeled equivalently as specular reflection of X-rays by lattice planes in which the incident and reflected X-ray beams are oriented at equal angles (**Figure 1–9**). Known as Bragg's law, the condition for constructive interference is satisfied when the difference in path length made by X-rays striking parallel lattice planes is equal to integer multiples of wavelengths:[127]

$$2dsin\theta = n\lambda$$

where d is the spacing between adjacent lattice planes, θ is the angle of reflection, and n is the reflection order. By measuring the angles of the diffracted X-rays, the d-spacings of different lattice planes can be deduced, and thus the unit cell geometry can be obtained. It is important to realize that the physical phenomenon remains the scattering of X-rays by electron density of the atoms in a crystal.
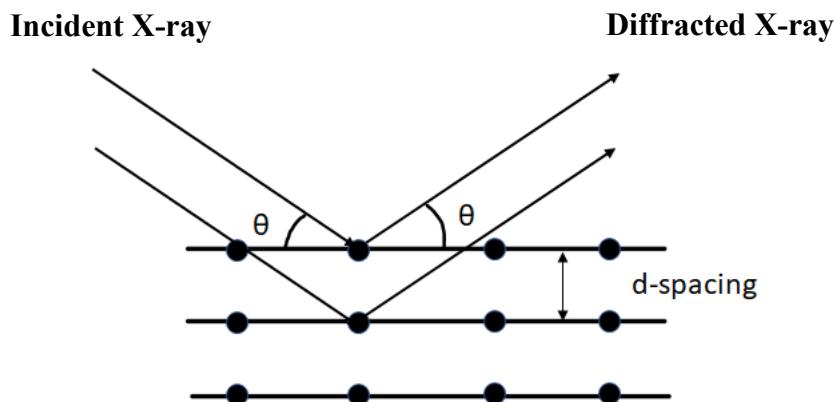
Figure 1-9. Principle of Bragg's law for X-ray diffraction.

There are many steps involved in the structure determination of a new compound, including growing suitable single crystals, selecting and mounting the crystal, collecting the intensity data, processing the data, determining the space group, solving the structure, and refining the structure. A suitable single crystal for data collection is typically 0.01 to 0.5 mm in its longest dimension. Choosing a larger crystal may increase the risk of additional reflections arising from attached smaller crystallites which could lead to difficulties in structure refinement. A suitable crystal is placed on the goniometer of a Bruker PLATFORM diffractometer equipped with a SMART APEX II CCD area detector and a Mo $K\alpha$ radiation source. Full sets of data are typically collected using ω scans at different ϕ angles. The data set consists of thousands of reflections containing information about the diffraction angles from specific lattice plane hkl and their intensities I_{hkl}. The intensity I_{hkl} is related to the square of the structure factor F_{hkl}, which reveals information about the electron density function of the crystal structure. In general, the structure factor F_{hkl} is a complex-numbered value that expresses both the amplitude and the phase of reflection. The Fourier transform of F_{hkl} (an image of the reciprocal space, **Figure 1–10**) into the electron density (real space) can be used to interpret the position of atoms in the unit cell. Unfortunately, the phases

of the structure factors cannot be measured experimentally, which is called the phase problem. Thus, the electron density cannot be directly evaluated because of this lack of phase information. Other techniques (e.g., direct methods, Patterson method) can be used to guess the phases of some structure factors to arrive at an initial model, which is then refined.
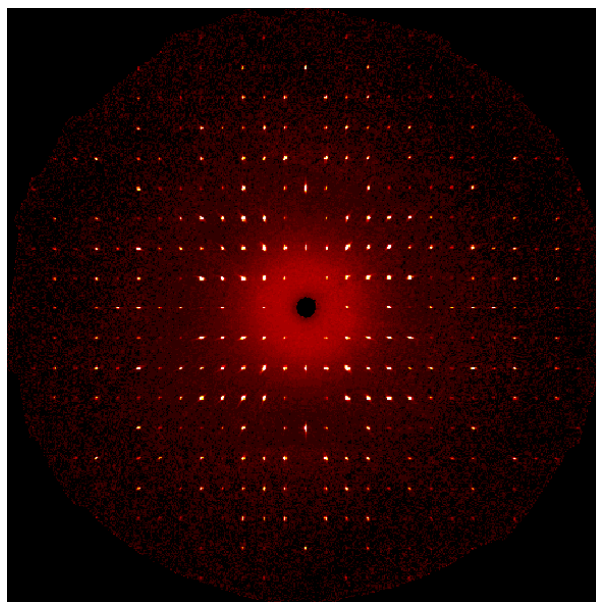
Figure 1-10. Reflections image of reciprocal crystal plane collected in single crystal diffractometer.

The structure is solved and refined through programs implemented in the SHELXTL program package. Because the compounds examined here contain many heavy atoms, numerical face-indexed absorption corrections are essential and were applied with the use of the SADABS program. Structural models are proposed by direct methods and their feasibility is evaluated by their chemical reasonableness. The models are then refined through least-square methods to improve the agreement between calculated and experimental intensities. A large part of this thesis deals with the refinement of noncentrosymmetric structures, for which it is important to determine the correct absolute configurations. Reflections related by inversion symmetry are known as

Friedel pairs (*hkl* and $\overline{hkl}$). Normally, the Friedel law states that the amplitude and phase of Friedel pairs are equal (**Figure 1-11**).

$F_{hkl} = F_{\overline{hkl}}$

When anomalous scattering is taken into account, Friedel's law still holds for centrosymmetric structures but becomes violated for noncentrosymmetric structures.
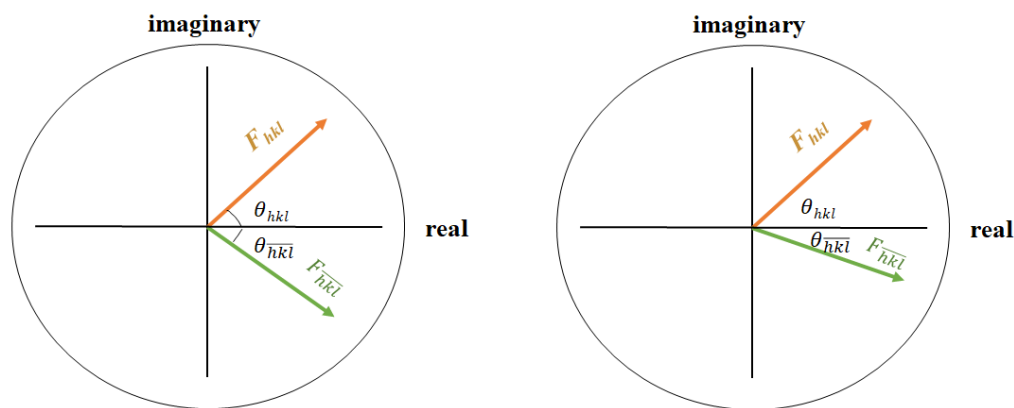
Figure 1-11. Friedel's law for (a) centrosymmetric; and (b) noncentrosymmetric (due to anomalous scattering).

$(hkl) = \overline{hkl}$). centrosymmetric

$(hkl) \neq \overline{hkl}$). non-centrosymmetric

Further, there are statistical relationships involving normalized structure factors (e.g., $\big| E^2-1 \big|$ statistics where $|E^2| = \frac{|F_{hkl}^2|}{\sum f^2}$ and Wilson plots) which can be suggest the likelihood of centrosymmetric vs noncentrosymmetric structures. Heavy atoms located at special positions and weak intensities may mislead or provide insufficient information to choose the correct space group. For example, in the structures of many $RE_3M_{1-x}M'Ch_7$ compounds, comparison of Friedel pairs and examination of $\big| E^2–1 \big|$ statistics were not always helpful; however, reference to prior structures established the correct space group choice. The quality of the proposed model is

estimated by the agreement to experimental data and to appeal of chemical reasonableness (bond distances, coordination environments, and displacement parameters). The refinement is monitored through the agreement factor R (= $\frac{\sum_{hkl}||F_o|-|F_c||}{\sum_{hkl}|F_c|}$, F_o = observed structure factor and F_c = calculated structure factor), goodness of fit S (= $\sqrt{\frac{\sum_{hkl}w(F_o^2-F_c^2)}{m-n}}$, w = $1/\sigma^2$, m = number of reflections, n = number of parameters), and inspection of the residual electron density map $\Delta\rho_{min,max}$. In well-refined structures, typically the agreement factors are small (R < 0.05 and wR_2 < 0.15), the goodness of fit is close to unity, and the residual electron density map is clean. Since X-ray diffraction provides a measure of electron density, it is sometimes hard to distinguish between atoms with similar electron density. For example, in the compound $La_3Sn_{0.5}InCh_7$, Sn (50 e$^-$) and In (49 e$^-$) cannot be easily differentiated. Moreover, both Sn and In could occupy tetrahedral and octahedral sites. In this instance, bond valence sum calculations and solid-state nuclear magnetic resonance spectroscopy were very useful in resolving the ambiguity.

1.6.2   Powder X-ray diffraction

A powder sample contains many small crystallites in random orientations. Instead of discrete reflections, X-rays striking a powder sample are diffracted according to interplanar distances of the lattice and give rise to lines at various angles 2θ that may be accidentally similar for more than one set of lattice planes. For this reason, structure determination is more difficult from powder X-ray data than from single-crystal X-ray data. The main use of powder X-ray diffraction patterns is for phase identification, in which simulated patterns of known phases are compared with the experimental pattern of a reaction product. In a multiphase sample, the relative amounts of the individual phases can be estimated from relative peak intensities (**Figure 1-12**).

The diffraction patterns were collected on an Inel powder diffractometer equipped with a

curved position-sensitive (CPS) detector, which allows peaks between 0 to 120° in 2θ to be detected simultaneously.
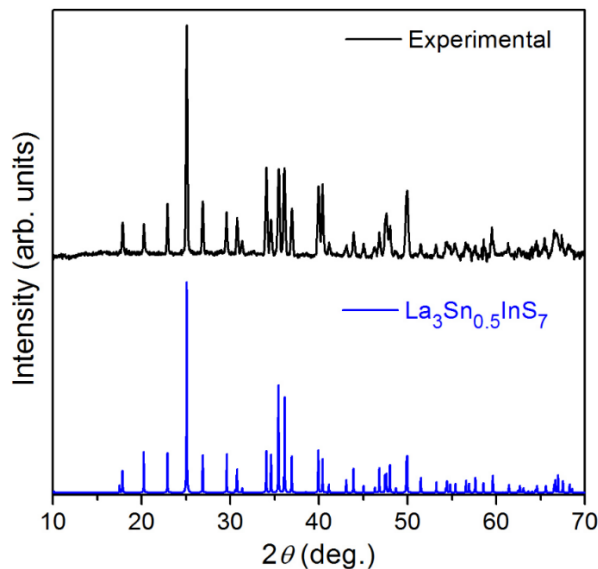
Figure 1-12. Powder diffraction pattern of $La_3Sn_{0.5}InS_7$; experimental pattern compared with simulated pattern.

1.7 Bond Valence

In early attempts to evaluate the stability of a crystalline solid, Pauling devised a set of rules that examined size and electronic factors. One of the most useful rules is the electroneutrality principle, in which, the electrostatic bond strength (s) to each coordinated anion is the ratio of the valence of the cation (number of electrons used in bonding) and coordination number of the cations (number of bonds that are formed). Similarly, the electrostatic bond strengths around a cation can be calculated. For a stable ionic structure, electroneutrality is maintained. A modern version of this rule is the concept of bond valence, v_{ij}, which can be thought of as a measure of the bond strength between two atoms i and j:

$$v_{ij} = \exp[(R_{ij} - d_{ij})/b]$$

where R_{ij} is the bond valence parameter (Å) for a specified contact between atoms i and j, d_{ij} is the experimentally observed distance (Å), and b is commonly taken as a constant value of 0.37.[129] The valence V_i of an atom i is equal to the sum of all the bond valences to it:

$$V_i = \Sigma v_{ij}$$

If the valence matches with the expected value for a given element, then the assignment is likely correct. Among several applications of bond valence sums, they can be used to differentiate between elements with similar atomic numbers. For example, **Table 1-6** shows bond valence sums for $LaSn_{0.5}InSe_7$ in various models to evaluate which sites, octahedral or tetrahedral, are most likely to be occupied by Sn vs. In atoms.

Table 1-6. Bond valence sums for $LaSn_{0.5}InSe_7$ for different models.

Model	As refined Sn oct, In tet	Reversed In oct, Sn tet	Disordered 0.33 Sn, 0.67 In in both sites
La	2.84	2.84	2.84
Oct site	3.14 for Sn	2.27 for In	3.14 for Sn 2.27 for In
Tet site	3.30 for In	4.56 for Sn	3.30 for In 4.56 for Sn
*Ch*1	1.81	1.67	1.71
*Ch*2	1.89	2.19	1.99
*Ch*3	2.28	2.63	2.40

1.8 Scanning electron microscopy (SEM) and energy dispersive X-ray (EDX) spectroscopy

For the compounds prepared in this thesis, the surface topography and morphology are examined by scanning electron microscopy and the chemical compositions are determined by energy-dispersive X-ray spectroscopy. A JEOL JSM-6010LA scanning electron microscope emits electrons accelerated through a voltage of 20 kV, which strike the surface of a sample. Secondary and backscattered electrons emitted in this process are used to generate an image and to detect the relative electron density (**Figure 1-13**). X-rays are also generated when the holes are filled by high-energy electrons. Because the wavelengths of these X-rays are characteristic of the type of element, an EDX spectrum provides a means of analyzing chemical compositions.[130]

Secondary electrons   Backscattered electrons   Characteristic X-rays
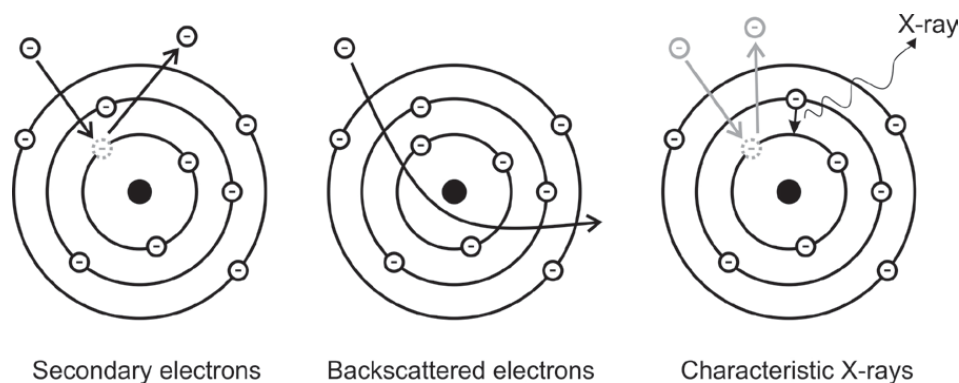
Figure 1-13. Secondary, backscattered electron, and characteristic x-ray phenomena observed in microscopy and X-ray spectroscopy.

A typical EDX spectrum contains several peaks whose integrated areas measure the relative amounts of each element in the sample (**Figure 1-14**). The relative molar amounts of each element can be measured to a precision of about 5%, depending on elements that are analyzed. EDX spectroscopy cannot be used to detect light elements, because the characteristic X-rays are too low in energy to be detected and it cannot easily distinguish between elements with a similar atomic number, because their X-ray wavelengths may overlap.
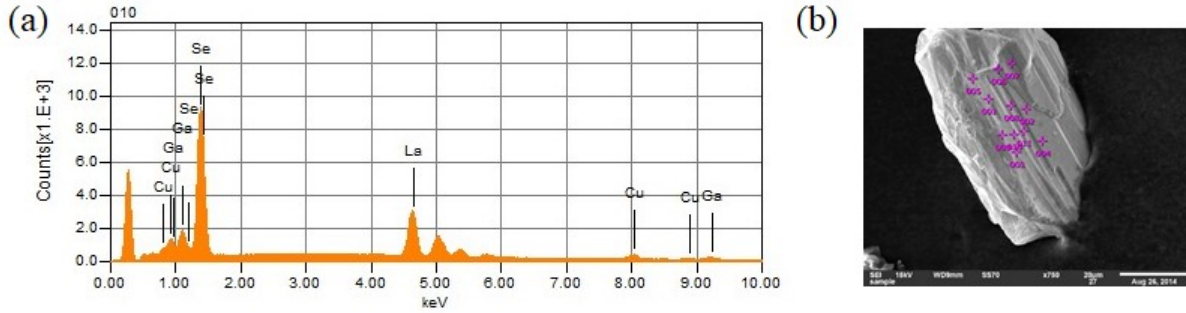
Figure 1-14. (a) X-ray spectrum of composition analysis on La₃CuGaSe₇ crystal (b) Secondary electron image of the same crystal.

1.9 Band structure calculations

As in molecules, the electronic structures of solids influence many of their properties. However, in contrast to molecules, which are composed of few atoms and have discrete energy levels, extended solids are composed of an extremely large number of atoms resulting in many energy levels so closely spaced that they constitute a continuum called a band. Just as for a molecule, the Schrödinger equation is used to evaluate the wavefunctions Ψ and energies E for an extended crystalline solid:

$$H\Psi = E\Psi$$

The Hamiltonian operator H contains two terms representing the kinetic energy and the potential energy:

$$(k + V)\Psi = E\Psi$$

A crystalline solid exhibits periodicity with lattice translations being one of the symmetry operations. The many electrons within a solid experience Coulombic attraction to the nuclei, and more complicated electron-electron interactions which are expressed via the exchange-correlation potential and the Hartree potential. Through the Kohn-Sham equation, this many-electron problem

can be reduced to a one-electron problem by combining the Coulomb, exchange correlation, and Hartree potentials.[131]

Just as atomic orbitals can be combined linearly to form molecular orbitals, they can also be combined in the same way in an extended solid where the translation symmetry can be used to simplify the calculations. The periodic representation of wavefunctions is a Bloch function. For a one-dimensional crystal with unit cell length a, the Bloch function ψ is expressed as a linear combination of atomic orbitals:

$$\psi(k) = \sum_{n=1}^{N} e^{ikna} \chi_n$$

Here, N is the total number of unit cells and k is a wavevector, which is quantized in reciprocal space. The unit cell in reciprocal space is called the first Brillouin zone and ranges over the values $-\frac{\pi}{a} \leq k \leq \frac{\pi}{a}$, but it suffices to plot the energies of these wavefunctions over positive values of k because the dependence is symmetric about the origin. A band dispersion diagram is a plot of E vs. k (**Figure 1-15**).

Although k is quantized, the bands are drawn as continuous lines because the energy levels are very close together (or, put another way, the increment in k is very small). It is convenient to plot instead the density of states (DOS), which measures the number of states within small energy increments, as a function of energy. Basically, DOS is inversely proportional to the slope of the band dispersion curve. The same ideas for a 1D crystal can be extrapolated to a real 3D crystal, in which energies of Bloch functions are plotted over different values of the wavevector within a volume of reciprocal space.[132]

$$\psi(0) = \sum_{n=1}^{N} e^0 \chi_n \qquad\qquad \psi\left(\frac{\pi}{a}\right) = \sum_{n=1}^{N} e^{i\pi n} \chi_n$$

$$\psi(0) = \chi_1 + \chi_2 + \chi_3 + \cdots \qquad\qquad \psi\left(\frac{\pi}{a}\right) = \chi_1 - \chi_2 + \chi_3 - \cdots$$
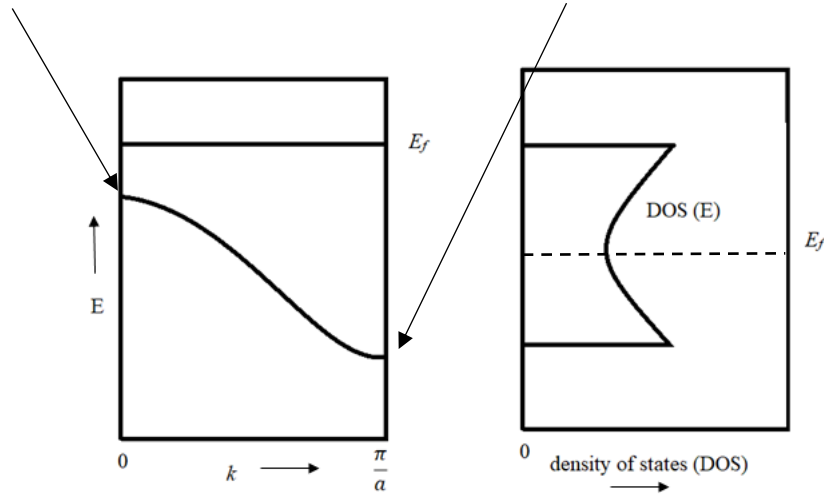
Figure 1-15. Schematic representation of located in a metal atom.

Band structure calculations were performed using the Stuttgart tight-binding linear muffin-tin orbital (TB-LMTO) program.[133] The infinite negative potential well is truncated to a finite value, thereby approximating the shape of muffin tins. An atomic spheres approximation is applied in which the potential function is ensured to be continuous by filling empty spaces between atoms as spheres with zero potential. The program then generates DOS curves. Electrons occupy states from the lowest energy upwards, up to the Fermi level, which can be arbitrarily set to 0 eV as a reference point. Where the Fermi level lies in the DOS curve gives information about the electrical properties: metallic (no gap), semimetallic (zero or small pseudogap), semiconducting (small gap, 0.5 to 3.0 eV), or insulating (large gap, >3.0 eV). For many chalcogenides, semiconducting behaviour is expected. It is also useful to take atomic projections of the DOS curve to ascertain the contribution of each atom in the structure. The bonding character of different interactions can be evaluated by crystal orbital Hamilton population (COHP) curves, which are

generated for a specific type of bond summed over all of them that are present within a unit cell. For example, these curves can be used to rationalize why $La_3Ga_{1.67}Ch_7$ is deficient in Ga, in order to avoid occupation of antibonding Ga–S levels (**Figure 1-16**).
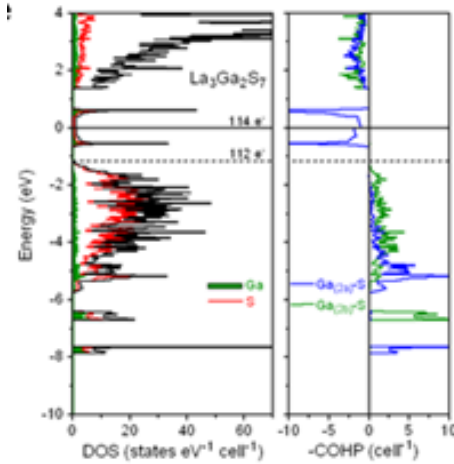
Figure 1-16. Schematic representation of COHP curve of the $La_3Ga_{1.67}Ch_7$.

1.10 Diffuse reflectance spectroscopy

Although electronic band gaps can be calculated from first principles, it is important to measure band gaps experimentally. A convenient method is through optical diffuse reflectance measurements. Reflection from a smooth surface such as a single crystal results in specular reflection, while reflection from an uneven surface (randomly oriented crystals) occurs in all directions. This phenomenon is known as diffuse reflectance. Scattered light has contributions from multiple effects, such as reflection, refraction, and diffraction, which are hard to separate. Kubelka and Munk developed an equation to relate these factors:

$$\frac{K}{S} = \frac{(1-R_\infty)^2}{2R_\infty} = F(R_\infty)$$

where R is reflectance, $F(R_\infty)$ is the Kubelka-Munk function, K is the absorption coefficient, and S is the scattering coefficient of the sample.[134]

Measuring the experimental band gap is part of the characterization of NLO materials. A compacted pellet of $BaSO_4$ was used as a 100% reflectance standard over the measured range from 300 nm (4.13 eV) to 2500 nm (0.5 eV). The absorption spectrum was then converted from the diffuse reflectance spectrum using the Kubelka-Munk function. The optical band gap was then estimated by extrapolating the absorption edge to the baseline. **Figure 1–17** shows a diffuse reflectance spectrum for the compound $Ba_5CdGa_6Se_{15}$.
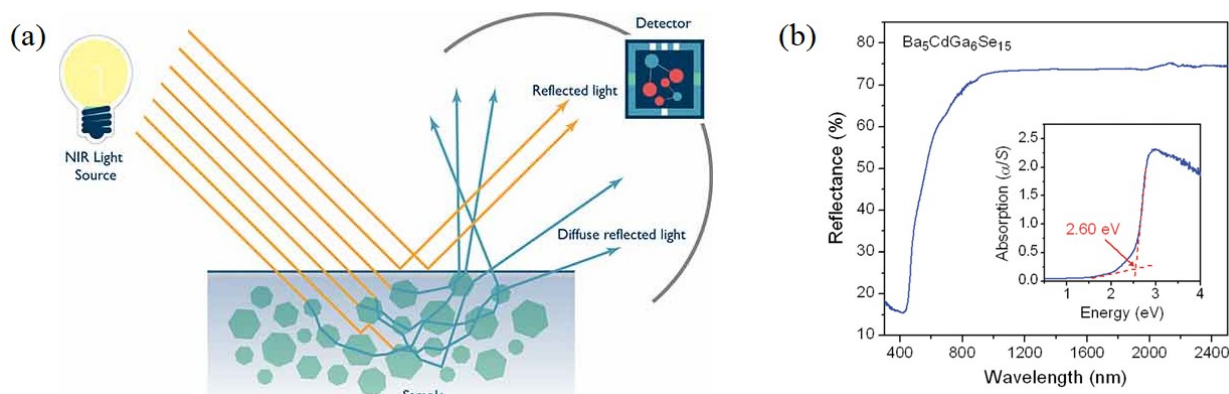
Figure 1-17. (a) Reflection of light due to uneven surface resulting in diffuse reflected light,[135] (b) Diffuse reflectance measurement of $Ba_5CdGa_6Se_{15}$.

1.11 Research motivation

Chalcogenides with noncentrosymmetric structures are attractive candidates for IR NLO materials, but the relatively few number of current materials that are commercially viable (which are all ternary chalcogenides) presents an exciting opportunity for solid state chemists to develop better materials. Ternary chalcogenides have now been heavily investigated over the past few decades. To date, over 8000 ternary chalcogenides have been structurally characterized, according

to crystallographic databases. Expanding to quaternary chalcogenides dramatically increases the number of potential new compounds; however, only ~4500 examples have been reported to date. This is an indication that much remains to be explored. Out of these examples, about 1200 contain rare-earth metals, and 250 contain Ba.

There are two major goals in this thesis. First, through systematic investigation of ternary and quaternary chalcogenide systems, we wish to prepare new compounds and determine their structures, in hopes of establishing patterns that allow us to relate structures and properties. Second, we specifically target the preparation of compounds adopting noncentrosymmetric structures because this is a prerequisite for obtaining NLO properties. Finding new examples of noncentrosymmetric structures also helps broaden our understanding to make better predictions of when such structures are likely to form.

The first part of this thesis examines the substitutional flexibility of the $RE_3M_{1-x}M'Ch_7$ family. These compounds comprise about 40% of all currently known quaternary RE-containing chalcogenides. Although general principles have been formulated that govern the types of components that can be substituted (e.g., electronic factors requiring charge balance and restriction of the sum of the valences of the M and M' components) and their site preferences, it is interesting to probe the limits of their validity. There are some unusual members within this family, and until recently, many of the properties of these compounds were unknown. In the last 10 years, some representatives ($Y_3Zn_{0.5}SiS_7$, $La_3In_{0.5}(Ge_{0.5}In_{0.5})S_7$) have demonstrated promising NLO behaviour. Ag-containing compounds in this family exhibiting large displacement parameters suggest the possibility of ionic conductivity. Compounds such as $La_3In_{0.5}(Ge_{0.5}In_{0.5})S_7$ and $La_3Ga_{0.5}(Ga_{0.5}Ge_{0.5})S_7$ are unusual because both M and M' components are p-block elements (in contrast to most other examples in which there is a combination of d- and p-block elements). We

are interested in finding further examples of such compounds. The only other examples in the *RE-M-M′-Ch* system which were reported to have a high SHG intensity are the compounds *RE*$_4$GaSbS$_9$ (*M* = Ga, In). The Se and Te analogs were not reported. Thus, it would be of interest to study the existence of other compounds and their nonlinear optical properties.

The second part of this thesis extends these investigations to Ba-containing chalcogenides. Although many alkali-metal-containing chalcogenides exhibit NLO materials, little is known about the corresponding alkaline-earth-containing chalcogenides, which should be expected to be more air-stable. Of the ~900 ternary and quaternary chalcogenides containing an alkaline-earth metal, about half contain Ba. Moreover, quaternary chalcogenides in the Ba–*M*–*M′*–*Ch* system have been particularly promising in revealing many noncentrosymmetric structures, compared to ternary chalcogenides in the Ba–*M*–*Ch* system. In general, sulfides have been more well studied than selenides, but it is natural to expect that isostructural compounds should be easy to obtain, given the chemical similarity of S and Se. However, this generalization sometimes fails, as observed in the different structures of BaGa$_2$S$_4$ (*Pa*$\bar{3}$) and BaGa$_2$Se$_4$ (*Cccm*), or of BaGa$_4$S$_7$ (*Pm*2$_1$) and BaGa$_4$Se$_7$ (*Pc*). Thus, it is worthwhile to examine new selenides.

1.12 References

[1]   Makovicky, E. *Rev. Mineral Geochem.* **2006**, *61*, 7–125.
[2]   Sunshine, S. A.; Keszler, D. A.; Ibers, J. A. *Acc. Chem. Res.* **1987**, *20*, 395–400.
[3]   Kadam, R. M.; Rajeswari, B.; Sengupta, A.; Achary, S. N.; Kshirsagar, R. J.; Natarajan, V. *Spectrochim. Acta, Part A* **2015**, *137*, 363–370.
[4]   McKelvy, M. J.; Glaunsinger, W. S. *Mat. Res. Bull.*, **1986**, *21*, 835–842.
[5]   Late, D. J.; Rout, C. S.; Chakravarty, D.; Ratha, S. *Can. Chem. Trans.* **2015**, *3*, 118–157.
[6]   Pachmayr, U.; Johrendt, D. *Chem. Commun.,* **2015**, *51*, 4689–4692.
[7]   Cotter, D.; Manning, R. J.; Blow, K. J.; Ellis, A. D.; Kelly, A. E.; Nesset, D.; Phillips, I. D.; Poustie, A. J.; Rogers, D. C. *Science* **1999**, *286*, 1523−1528.
[8]   Chung, I.; Kanatzidis, M. G. *Chem. Mater.* **2014**, *26*, 849–869.
[9]   Pushkarsky, M. B.; Webber, M. E.; Macdonald, T.; Patel, C. K. N. *Appl. Phys. Lett.* **2006**, *88*, 1–3.

[10] Pestov, D.; Wang, X.; Ariunbold, G. O.; Murawski, R. K.; Sautenkov, V. A.; Dogariu, A.; Sokolov, A. V.; Scully, M. O. *Proc. Natl. Acad. Sci*. U.S.A. **2008**, *105*, 422−427.

[11] Pushkarsky, M. B.; Dunayevskiy, I. G.; Prasanna, M.; Tsekoun, A. G.; Go, R.; Patel, C. K. N. *Proc. Natl. Acad. Sci.* U.S.A. **2006**, *103*, 19630−19634.

[12] Nikogosyan, D. N. *Nonlinear optical crystals: a complete survey*,1st ed.; Springer: New York, **2005**.

[13] Guang, S. H.; Song, H. L., *Physics of Nonlinear Optics*, 1st ed., World Scientific Publishing, Singapore, **1999**.

[14] Dougherty, J. P.; Kurtz, S. K. *J. Appl. Crystallogr.*, **1976**, *9*, 145.

[15] Boyd, R. Nonlinear Optics, 3rd ed.; Elsevier, New York, **2008**.

[16] Zhang, W.; Yu, H.; Wu, H.; Halasyamani, P. S. *Chem. Mater*. **2017**, *29*, 2655−2668.

[17] Halasyamani, P. S.; Poeppelmeier, K. R. *Chem. Mater.* **1998,** *10,* 2753–2769.

[18] Liang, F.; Kang, L.; Lin, Z.; Wu, Yicheng. *Cryst. Growth des.* **2017**, *17*, 2254–2289.

[19] Collin, G.; Étienne, J.; Flahaut, J.; Guittard, M.; Laruelle, P. *Rev. Chim. Miner.* **1973**, *10*, 225–238.

[20] Palazzi, M.; Carcaly, J.; Flahaut, J. *J. Solid State Chem.* **1980**, *35*, 150–155.

[21] Daszkiewicz, M.; Gulay, L. D.; Lychmanyuk; O. S. *Acta Crystallogr. B* **2009**, *65*, 126–133.

[22] Nanjundaswamy, K. S.; Gopalakrishnan, J. J. Solid State Chem. **1983**, *49*, 51–58.

[23] Gitzendanner R. L.; Spencer C. M.; DiSalvo F. J.; Pell M. A.; Ibers J. A. *J. Solid State Chem.* **1997**, *131*, 399–404.

[24] Abrahams, S. C. *Acta Crystallogr. B*, **1990**, *46*, 311–324.

[25] Guo S. P.; Guo G. C.; Wang M. S.; Zou J. P.; Xu G.; Wang G. J.; Long X. F.; Huang J. S. *Inorg. Chem.* **2009**, *48*, 7059–7065.

[26] Shi, Y. -F.; Chen, Y. -K.; Chen, M. -K.; Wu, L. -M.; Lin, H.; Zhou, L. -J.; Chen, L. *Chem. Mater.* **2015**, *27*, 1876–1884.

[27] Hartenbach, I.; Nilges, T.; Schleid T. *Z. Anorg. Allg. Chem.* **2007**, *633*, 2445–2452.

[28] Gulay, L. D.; Lychmanyuk, O. S; Olekseyuk; I. D.; Daszkiewicz; M.; Stępień-Damm, J.; Pietraszko, A. *J. Alloys Compd.* **2007**, *431*, 185–190.

[29] Hartenbach, I.; Müller, C.; Schleid T. *Z. Anorg. Allg. Chem.* **2006**, *632*, 2147.

[30] Gulay, L. D.; Lychmanyuk, O. S.; Wolcyrz, M.; Pietraszko, A.; Olekseyuk I. D. *J Alloys Compd.* **2006**, *425*, 159–163.

[31] Strok, O. M.; Daszkiewicz, M.; Gulay, L. D.; Kaczorowski D. *J. Alloys Compd*. **2010**, *493*, 47–49.

[32] Gulay, L. D.; Olekseyuk, I. D.; Wolcyrz, M.; Stępień-Damm, J. *Z. Anorg. Allg. Chem*. **2005**, *631*, 1919–1923.

[33] Daszkiewicz, M; Gulay, L. D.; Lychmanyuk, O. S; Pietraszko, A. *J. Alloys Compd*. **2008**, *460*, 201–205.

[34] Daszkiewicz, M; Gulay, L. D.; Lychmanyuk, O. S; Pietraszko, A. *J. Alloys Compd.* **2009**, *467*, 168–172.

[35] Daszkiewicz, M; Gulay, L. D.; Lychmanyuk, O. S. *Acta Crystallogr. B* **2009**, *65*, 126–133.

[36] Daszkiewicz, M; Gulay, L. D.; Lychmanyuk, O. S; Pietraszko, A. *J. Alloys Compd.* **2009**, *467*, 168–172.

[37] Daszkiewicz, M; Gulay, L. D.; M.; Pietraszko, A.; Shemet, V. Y. *J. Solid State Chem.* **2007**, *180*, 2053–2060.

[38] Choudhury, A.; Dorhout, P. K. *Inorg. Chem.* **2015**, *54*, 1055–1065.

[39] He, J.; Wang, Z.; Zhang, X.; Cheng, Y.; Gong, Y.; Lai, X.; Zheng C.; Lin J.; Huang F. *RSC Adv.* **2015**, *5*, 52629–52635.

[40] Rudyk, B. W.; Stoyko, S. S.; Oliynyk, A. O.; Mar, A. *J. Solid State Chem.* **2014**, *210*, 79–88.

[41] Yin, W.; Wang, W.; Kang, L.; Lin, Z.; Feng, K.; Shi, Y.; Hao, W.; Yao, J. L.; Wu, Y. *J. Solid State Chem.* **2013**, *202*, 269–275.

[42] Rudyk, B. W.; Stoyko, S. S.; Mar, A *J. Solid State Chem.* **2013**, *208*, 78–85.

[43] Huch, M. R.; Gulay, L. D.; Olekseyuk, I. D. *J. Alloys Compd.* **2006**, *424*, 114–118.

[44] Strok, O. M.; Daszkiewicz, M.; Gulay, L. D *Chem. Met. Alloys* **2015**, *8*, 16–21.

[45] Daszkiewicz, M.; Marchuk, O. V.; Gulay, L. D.; Kaczorowski, D. *J. Alloys Compd.* **2014**, *610*, 258–263.

[46] Daszkiewicz, M.; Pashynska, Y. O.; Marchuk, O. V.; Gulay, L. D.; Kaczorowski, D. *J. Alloys Compd.* **2014**, *616*, 243–249.

[47] Assoud A.; Sankar C. R.; Kleinke H. *Solid State Sci.* **2014**, *38*, 124–128.

[48] Zhao, H. J *J. Solid State Chem.* **2015**, *227*, 5–9.

[49] Zhao, H. J *Z. Anorg. Allg. Chem.* **2015**, *641*, 917–921.

[50] Zeng H. Y.; Zheng F. K.; Guo G. C.; Huang J. S. *J. Alloys Compd.* **2008**, *458*, 123–129

[51] Villars, P.; Cenzual, K. Pearson's Crystal Data - Crystal Structure Database for Inorganic Compounds, Release **2017/18**, ASM international, Materials Park, Ohio, USA.

[52] Chen, M. -C.; Li, L. -H.; Chen, Y. -B.; Chen, L. *J. Am. Chem. Soc.* **2011**, *133*, 4617–4624.

[53] Zhao, H. -J. *J. Solid State Chem.* **2016**, *237*, 99–104.

[54] Zhao, H. -J.; Zhang, Y. -F.; Chen, L. *J. Am. Chem. Soc.* **2012**, *134* 1993–1995.

[55] Zhao, H. -J. *Z. Anorg. Allg. Chem.* **2016**, *642*, 56–59.

[56] Huch, M. R.; Gulay, L. D.; Olekseyuk, I. D.; Pietraszko, A. *J. Alloys Compd.* **2006**, *425* 230–234.

[57] Huch, M. R.; Gulay, L. D.; Olekseyuk, I. D. *J. Alloys Compd.* **2007**, *439*, 156–161.

[58] Gulay, L. D.; Olekseyuk, I. D.; Wołcryz, M.; Stępień-Damm, J. *J. Alloys Compd.* **2005**, *399*, 189–195.

[59] Gulay, L. D.; Olekseyuk, I. D. *J. Alloys Compd.* **2005**, *387*, 160–164.

[60] Gulay, L. D.; Stępień-Damm, J.; Pietraszko, A.; Olekseyuk, I. D. *J. Alloys Compd.* **2006**, *413*, 90–95.

[61] Zhao, H. -J.; Li, L. -H.; Wu, L. -M.; Chen, L. *Inorg. Chem.* **2009**, *48*, 11518–11524.

[62] Daszkiewicz, M.; Marchuk, O. V.; Gulay, L. D.; Kaczorowski, D. *J. Alloys Compd.* **2012**, *519*, 85–91.

[63] Kanatzidis, M. G. *Inorg. Chem.* **2017**, *56*, 3158–3173.

[64] Donohue, P. C.; Hanlon, J. E. *J. Electrochem. Soc.* **1974**, *121*, 137–142.

[65] Lin, X.; Zhang, G.; Ye, N. *Cryst. Growth Des.* **2009**, *9*, 1186–1189.

[66] Yao, J. L.; Mei, D.; Bai, L.; Lin, Z.; Yin, W.; Fu, P.; Wu, Y. *Inorg. Chem.* **2010**, *49*, 9212.

[67] Eisenmann, B.; Jakowski, M.; Klee, W.; Schäfer, H. *Rev. Chim. Miner.* **1983**, *20*, 255–263.

[68] Mei, D.; Yin, W.; Bai, L.; Lin, Z.; Yao, J. L.; Fu, P.; Y. Wu *Dalton Trans.* **2011**, *40*, 3610–3615.

[69] Mei, D.; Yin, W.; Lin, Z.; Yao, J. L.; Fu, P.; Y. Wu *J. Alloys Compd.* **2011**, *509*, 2981–2985.

[70] Eisenmann, B.; Jakowski, M.; Schäfer, H. *Z. Naturforsch. B* **1984**, *39*, 27–30.

[71] Eisenmann, B.; Jakowski, M.; Schäfer, H. *Rev. Chim. Miner.* **1984**, *21*, 12–20.

[72] Eisenmann, B.; Jakowski, M.; Schäfer, H. *Z. Naturforsch. B* **1983**, *38*, 1581–1584.

[73] Eisenmann, B.; Jakowski, M.; Schäfer, H. *Mater. Res. Bull.* **1982**, *17*, 1169–1175.

[74] Klee, W.; Schäfer, H. *Z. Anorg. Allg. Chem.* **1981**, *479*, 125–133.

[75] Liu, J. W.; Wang, P.; Chen, L. *Inorg. Chem.* **2011**, *50*, 5706–5713.

[76] Yin, W.; Mei, D.; Feng, K.; Yao, J.; Fu, P.; Wu, Y. *Dalton Trans.* **2011**, *40*, 9159–9162.

[77] Lemely, J. T. *Acta Crystallogr. B* **1974**, *30*, 549–550.

[78] Wu, K.; Pan, S.; Yang, Z. *RSC Adv.* **2015**, *5*, 33646–33652.

[79]   Wu, K.; Su, X.; Yang, Z.; Pan, S. *Dalton Trans.* **2015**, *44*, 19856–19864.

[80]   Assoud, A.; Soheilnia, N.; Kleinke, H. *Z. Naturforsch. B* **2004**, *59*, 975–979.

[81]   Jumas, J. C.; Philippot E.; Vermot G. D. F.; Ribes M.; Maurin M. *J. Solid State Chem.* **1975**, *14*, 319–327.

[82]   Luo, Z. Z.; Lin, C. S.; Cheng, W. D.; Zhang, H.; Zhang, W. L.; He, Z. Z *Inorg. Chem.* **2013**, *52*, 273–279.

[83]   Ribes, M.; Olivier, F. J.; Philippot, E.; Maurin, M. *J. Solid State Chem.* **1973**, *8*, 195–205.

[84]   Luo, Z. Z.; Lin, C. S.; Zhang, W. L.; Zhang, H.; He, Z. Z.; Cheng, W.D. *Chem. Mater.* **2014**, *26*, 1093–1099.

[85]   Assoud, A.; Klienke, H. *Chem. Mater.* **2005**, *17*, 4509–4513.

[86]   Feng, K.; Jiang, X.; Kang, L.; Yin, W.; Hao, W.; Lin, Z.; Yao, J. L.; Wu, Y.; Chen, C. *Dalton Trans.* **2013**, *42*, 13635–13641.

[87]   Assoud, A.; Derakhshan S.; Soheilnia N.; Klienke, H. *Chem. Mater.*, **2004**, *16*, 4193–4198.

[88]   Assoud, A.; Soheilnia, N.; Kleinke, H. *J. Solid State Chem.* **2005**, *178*, 1087–1093.

[89]   Johrendt, D.; Tampier, M. *Chem. Eur. J.* **2000**, *6*, 994–998.

[90]   Brinkmann, C.; Eisenmann, B.; Schäfer, H. *Anorg. Allg. Chem.* **1984**, *517*, 143–148.

[91]   Pan, M. Y.; Xia, S. Q.; Liu X. C.; Tao X. T. *J. Solid State Chem.* **2014**, *219*, 74–79.

[92]   Jörgens, S.; Mewis, A. *Z. Anorg. Allg. Chem.* **2007**, *633*, 570–574.

[93]   Jörgens, S.; Mewis, A.; Hoffmann, R. D.; Pöttgen, R.; Mosel, B. D. *Z. Anorg. Allg. Chem.* **2003**, *629*, 429–433.

[94]   Wang, J.; Lee, K.; Kovnir, K. *Z. Anorg. Allg. Chem.* **2015**, *641*, 1087–1092.

[95]   Cordier, G.; Schwidetzky, C.; Schäfer, H. *J. Solid State Chem.* **1984**, *54*, 84–88.

[96]   Iordanidis, L.; Ghelani, N. A.; Hogan, T. P.; Kanatzidis, M. G.; Brazis, P. W.; Kyratsi, T.; Ireland, J. R.; Lane, M.; Chen, W.; Dyck, J. S.; Uher, C. *Chem. Mater.* **2001**, *13*, 622–633.

[97]   Cordier, G.; Schwidetzky, C.; Schäfer, H. *Rev. Chim. Miner.* **1983**, *20*, 877–883.

[98]   Cordier, G.; Schwidetzky, C.; Schäfer, H. *Rev. Chim. Miner.* **1985**, *22*, 93–100.

[99]   Wang, J.; Lee, K.; Kovnir, K. *J. Mater. Chem. C* **2015**, *3*, 9811–9818.

[100]   Wang, Y. C.; DiSalvo, F. J. *Chem. Mater.* **2000**, *12*, 1011–1017.

[101]   Chung, D. Y.; Jobic, S.; Hogan, T. P.; Kannewurf, C. R.; Brec, R.; Rouxel, J.; Kanatzidis, M. G. *J. Am. Chem. Soc.* **1997**, *119*, 2505–2515.

[102]   Jörgens, S.; Johrendt, D.; Mewis, A. *Chem. Eur. J.* **2003**, *9*, 2405–2410.

[103]   Dörrscheidt, W.; Schäfer, H. *Z. Naturforsch. B* **1981**, *36*, 410–414.

[104]   Yin, W.; Feng, K.; He, R.; Mei, D.; Lin, Z.; Yao, J.; Wu, Y. *Dalton Trans.* **2012**, *41*, 5653–5661.

[105]   Lei, X. W.; Yang, M.; Xia, S. Q.; Liu, X. C.; Pan, M. Y.; Li, X.; Tao, X. T. *Chem. Asian J.* **2014**, *9*, 1123-1131.

[106]   Kuo, S.-M.; Chang, Y.-M.; Chung, I.; Jang, J.-I.; Her, B.-H.; Yang, S.-H.; Ketterson, J. B.; Kanatzidis, M. G.; Hsu, K.-F. *Chem. Mater.* **2013**, *25,* 2427–2433.

[107]   Yin, W.; He, R.; Feng, K.; Hao, W.; Yao, J. L.; Wu, Y. *J. Alloys Compd.* **2013**, *565*, 115–119.

[108]   Tampier, M.; Johrendt, D. *Z. Naturforsch. B* **1998**, *53*, 1483–1488.

[109]   Teske, C. L. *Z. Naturforsch. B* **1979**, *34*, 386–389.

[110]   Frazer, L.; Chang, Y. -M.; Liu, T. -K.; Lin, J.-F.; Liang, I. -C.; Sheu, H. -S.; Ketterson, J. B.; Kanatzidis, M. G.; Hsu, K. -F. *Chem. Mater.* **2015**, *27*, 1316–1326.

[111]   Tampier, M.; Johrendt, D. *Z. Anorg. Allg. Chem.* **2001**, *627*, 312-320.

[112]   Assoud, A.; Soheilnia, N.; Kleinke, H. *Chem. Mater.* **2005**, *17*, 2255–2261.

[113]   Teske, C. L. *Z. Naturforsch. B* **1980**, *35*, 509–510.

[114]   Geng, L.; Cheng, W. D.; Lin, C. S.; Zhang, W. L.; Zhang, H.; He, Z. Z. *Inorg. Chem.* **2011**, *50*, 5679–5686.

[115] Lin, X.; Guo, Y.; Ye, N.; *J. Solid State Chem.* **2012**, *195*, 172–177.
[116] Yin, W.; Feng, K.; He, R.; Mei, D.; Lin, Z.; Yao, J. L.; Wu, Y. *Dalton Trans.* **2012**, *41*, 5653–5661.
[117] Liu B. W.; Zeng H. Y.; Zhang M. J.; Fan Y. H.; Guo G. C.; Huang J. S.; Dong Z. C. *Inorg. Chem.* **2015**, *54*, 976–981.
[118] Geng, L.; Zhang, H.; Cheng, W. D. *J. Struct. Chem*. **2013**, *32*, 538–544.
[119] Li, C.; Li, X.; Huang, H., Yao, J.; Wu, Y. *Inorg. Chem.* **2015**, *54*, 9785–9789.
[120] Hao, W.; Mei, D.; Yin, W.; Feng, K.; Yao, J. L.; Wu, Y. *J. Solid State Chem.* **2013**, *198*, 81–86.
[121] Yin, W.; Lin, Z.; Kang, L.; Kang, B.; Deng, J.; Lin, Z.; Yao, J.; Wu, Y. *Dalton Trans.* **2015**, *44*, 2259–2266.
[122] Geng L. *Acta Crystallogr. E* **2013**, *69*, i24.
[123] Chung, M. Y.; Lee, C. S. *Inorg. Chem.* **2012**, *51*, 13328–13333.
[124] Choi, K. S.; Kanatzidis, M. G. *Inorg. Chem.* **2001**, *40*, 101–104.
[125] Chen, M. C.; Wu, L. M.; Lin, H.; Zhou, L. J.; Chen, L. *J. Am.Chem. Soc.* **2012**, *134*, 6058−6060.
[126] Massa, W. *Crystal Structure Determination*, 2^(nd) ed., Springer–Verlag: Berlin, **2004**.
[127] West, A. R. *Basic Solid State Chemistry*, 2^(nd) ed., Wiley: New York, **1999**.
[128] Bragg, W. H.; Bragg W. L. *Proc. R. Soc. Lond. A* **1913**, *88*, 428–438.
[129] Brese, N. E.; O'Keeffe, M. *Acta. Crystallogr., Sect. B* **1991**, *47*, 192–197.
[130] Russ, J. C. *Fundamentals of energy dispersive X-ray analysis*, Butterworth: London, **1984**.
[131] Dronskowski, R. *Computational Chemistry of Solid State Materials*, Wiley-VCH, Weinheim, **2005**.
[132] Hoffman, R. *Angew. Chem.*, *Int. Ed. Engl*. **1987**, *26*, 846–878.
[133] Tank, R.; Jepsen, O.; Burkhardt, A.; Andersen, O. K. *TB-LMTO-ASA Program*, version 4.7; Max Planck Institut für Festkörperforschung: Stuttgart, Germany, **1998**.
[134] Kubelka, P.; Munk, F. *Z. Techn. Physik*. **1931***, 12*, 593.
[135] Abramowitz, M.; Sutter, R. T.; Davidson, M. W., accessed 5 May 2016 <http://www.olympusmicro.com/primer/java/reflection/specular/>.

Chapter 2

Noncentrosymmetric rare-earth copper gallium chalcogenides $RE_3CuGaCh_7$ (RE = La–Nd; Ch = S, Se): An unexpected combination

2.1 Introduction

Ternary and quaternary rare-earth chalcogenides serve as a rich source of new materials by virtue of the many possible combinations of components, including transition metals and p-block metalloids, that can be accommodated.[1] Many metal chalcogenides are often promising nonlinear optical materials.[2] First discovered more than 40 years ago,[3] the chalcogenides $RE_3MM'Ch_7$ (Ch = S, Se) form a large family of compounds now known with over 300 representatives,[4] despite what appears at first glance to be a restrictive electronic condition that the valences of M and M' must sum to five, to maintain overall charge balance in the formula.[5] Thus, fully stoichiometric compounds can be obtained for I-IV combinations (M = Na, Cu, Ag; M' = Si, Ge, Sn), which constitute the vast majority,[6] II-III combinations (M = alkaline-earth and divalent transition metals; M' = Al, Ga, In), which are growing in number following recent investigations,[5, 7–15] and III-II combinations such as RE_3CrBeS_7, which are still few.[5,8] Alternatively, substoichiometric compounds can satisfy the charge balance requirement through other combinations of M and M', provided that defects are introduced into the M site, as found in $Ce_3Al_{0.67}AlS_7$ (= $Ce_3Al_{1.67}S_7$), $La_3Mn_{0.5}SiS_7$, or $Sm_3Al_{0.33}SiS_7$.[16–18]

These chalcogenides $RE_3MM'Ch_7$ adopt a noncentrosymmetric hexagonal structure (space group $P6_3$, La_3CuSiS_7- or $Ce_3Al_{1.67}S_7$-type) containing one-dimensional chains and are expected to be small band gap semiconductors. They have often been proposed to be candidates for

materials applications that take advantage of measured or predicted properties pertaining to ferroelectricity (La_3MnGaS_7), nonlinear optical behaviour ($Y_3Zn_{0.5}SiS_7$), and ionic conductivity ($La_3Ag_{0.82}SnS_7$, $Ce_3Ag_{0.63}SiS_{6.63}Cl_{0.37}$).[19–21] Recent reports include strong second harmonic generation (SHG) effects for $La_3Ga_{0.5}(Ga_{0.5}Ge_{0.5})S_7$ and photovoltaic behaviour for $La_3CuGaSe_7$.[22–23] Among these compounds, $La_3Ag_{0.82}SnS_7$ is unusual because it does not satisfy the charge balance rule, and $La_3CuGaSe_7$ only does so if divalent Cu species are proposed, which would be uncharacteristic within a chalcogenide.

Here we present an investigation of the chalcogenides $RE_3CuGaCh_7$ (Ch = S, Se) to determine if other analogues to $La_3CuGaSe_7$ exist, and more importantly, to carefully evaluate the valence of Cu in these compounds through detailed consideration of structural and electronic evidence obtained through X-ray diffraction, magnetic measurements, and X-ray photoelectron spectroscopy.

2.2 Experimental

2.2.1 Synthesis

Starting materials were freshly filed RE pieces (RE = La–Nd, 99.9%, Hefa), Cu powder (99.9%, Cerac), Ga shot (99.99%, Cerac), S flakes (99.998%, Sigma-Aldrich), and Se powder (99.99%, Sigma-Aldrich). Stoichiometric mixtures of the elements with a total mass of 0.2 g were pressed into pellets (6 mm diameter, 1–3 mm thickness) and loaded into fused-silica tubes which were evacuated and sealed. The tubes were heated at either 1050 °C (for RE_3CuGaS_7) or 900 °C (for $RE_3CuGaSe_7$) for 5 d and then cooled to room temperature over 12 h. Powder X-ray diffraction patterns were collected on an Inel diffractometer equipped with a curved position-sensitive detector (CPS 120) and a Cu $K\alpha_1$ radiation source operated at 40 kV and 20 mA. The

quaternary chalcogenides $RE_3CuGaCh_7$ constituted the major phase in the products (>95% for RE = La, Ce; >90% for RE = Pr, Nd), the most common minor phases being binary chalcogenides such as RE_3Ch_4. After these phases were accounted for, there remained a few weak unidentified peaks in some XRD patterns that probably belong to multinary chalcogenides not yet characterized; more detailed investigation of these RE–Cu–Ga–Ch systems is ongoing. The homogeneity of the products was improved upon regrinding and reheating, but the minor phases could not be completely eliminated. **Figure. 2–1** shows representative powder XRD patterns for $La_3CuGaCh_7$. Reactions performed under the same conditions above were attempted for other trivalent RE components (Sm, Gd–Lu); these did not result in formation of the desired quaternary phase but rather of mixtures of binary phases including RE_3Ch_4. Energy-dispersive X-ray (EDX) analyses on selected crystals were performed on a JEOL JSM-6010LA InTouchScope scanning electron microscope. The average chemical compositions, determined from examination of multiple points (4–10) on each crystal, were 23(2)–27(4)% RE, 7(1)–9(1)% Cu, 7(2)–10(2)% Ga, and 53(4)–62(2)% Ch, consistent with the formula $RE_3CuGaCh_7$ (expected 25% RE, 8% Cu, 8% Ga, 58% Ch). Polycrystalline samples of $RE_3CuGaCh_7$ have a dark-grey appearance and are stable in air for several months.
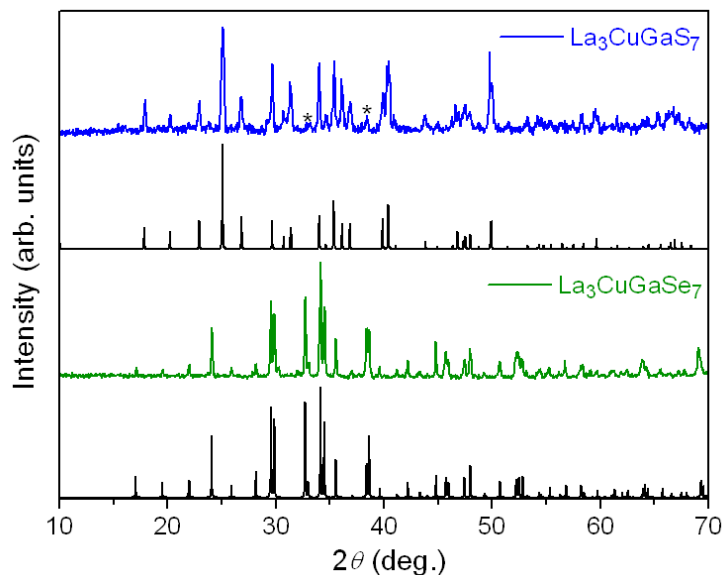
Figure 2-1. Powder XRD patterns for La$_3$CuGaS$_7$ (blue) and La$_3$CuGaSe$_7$ (green). Simulated patterns are shown in black. Peaks that do not belong to the simulated pattern for La$_3$CuGaS$_7$ are marked with asterisks.

2.2.1   Structure determination

Suitable single crystals were available for all members of the *RE*$_3$CuGa*Ch*$_7$ series. Intensity data were collected at room temperature on a Bruker PLATFORM diffractometer equipped with a SMART APEX II CCD detector and a graphite-monochromated Mo *K*α radiation source, using ω scans at 6–8 different ϕ angles with a frame width of 0.3º and an exposure time of 12–15 s per frame. Face-indexed absorption corrections were applied. Structure solution and refinement were carried out with use of the SHELXTL (version 6.12) program package[24]. The Laue symmetry (6/*m*) and systematic absences (00*l*; *l* = odd) indicated the hexagonal space groups *P*6$_3$ or *P*6$_3$/*m*. Although the intensity statistics were somewhat ambiguous for the sulfides (mean $|E^2–1| = 0.84$–0.86), they were strongly suggestive of noncentrosymmetry for the selenides (mean $|E^2–1| = 0.61$–0.80). The noncentrosymmetric space group *P*6$_3$ was chosen from these

considerations as well as from the precedent established by numerous other La_3CuSiS_7-type compounds. Direct methods confirmed models consistent with the La_3CuSiS_7-type structure. Atomic coordinates were standardized with the program STRUCTURE TIDY. [25] Given that this space group has a polar direction (along the c-axis), the z-coordinate of the Cu atom was fixed to be at the origin. Refinement of racemic twinning led to a Flack parameter close to zero for most crystals examined, indicating that the correct absolute configurations were chosen. For two of the crystals ($La_3CuGaSe_7$, $Pr_3CuGaSe_7$), which exhibited unusual intensity statistics, it was essential to invoke merohedral twinning (following the twin law $0\ 1\ 0\ /\ 1\ 0\ 0\ /\ 0\ 0\ -1$) for successful structure refinement.

In the structural models, it was assumed that Cu atoms occupy a trigonal planar site and Ga atoms a tetrahedral site. However, Cu and Ga atoms are difficult to distinguish because of their similar X-ray scattering factors. Nevertheless, if the site occupations are reversed, the refinements are consistently worse (e.g., R_1 increases from 0.030 to 0.032 for La_3CuGaS_7, and similar increases are observed for the other crystals). The possibility of disorder of Cu and Ga atoms within each site was also considered. Refinements in which disorder is introduced into the trigonal planar site were unstable, but tended towards full occupancy with Cu; analogous treatment of the tetrahedral site led to nearly full occupancy with Ga (e.g., 0.9(1) Ga / 0.1(2) Cu in La_3CuGaS_7). These results lend confidence that the atom assignments are correct, in conformity with the well-established observation in La_3CuSiS_7-type structures that the tetrahedral site is preferred by the higher-valent metal[5].

A pathological feature often encountered in $RE_3MM'Ch_7$ compounds, especially when M is Cu or Ag, is pronounced anisotropic displacement of the M atoms. [21,23,26–31] In $RE_3CuGaCh_7$, the displacement ellipsoids of the Cu atoms are highly elongated along the c-direction, with

41

U_{33}/U_{11} ranging from 9 to 16 (e.g., $U_{11} = 0.0103(6)$ Å^2 and $U_{33} = 0.120(4)$ Å^2 in La$_3$CuGaS$_7$). In accordance with the typical strategy to treat this problem,[23] the Cu site was split into two closely spaced ones with their displacement parameters set equal and their occupancies constrained to sum to unity. These refinements reduced the anistropy, with U_{33}/U_{11} now ranging from 3 to 6, and led to more reasonable displacement parameters (e.g., $U_{11} = 0.0104(5)$ Å^2 and $U_{33} = 0.039(3)$ Å^2 in La$_3$CuGaS$_7$).

For most of the structures determined here, the difference electron density maps were featureless. However, for La$_3$CuGaS$_7$, the maximum residual density ($\Delta\rho_{max} = 5.79$ e/Å^3) was 10% that of the heaviest atom in the formula ($0.10 \times 57 = 5.70$ e/Å^3), the threshold at which the checkCIF analysis flags an alert. This residual density is located in a general position ($6c$) at distances of 2.07, 2.10, 2.28, and 2.78 Å to surrounding S atoms; the two shortest distances verge on being physically unrealistic. Although it can be modeled as a Cu site that is partially occupied at rather low levels (0.110(2)), corresponding to a Cu-excessive formula La$_3$Cu$_{1.33}$GaS$_7$, additional evidence to be discussed later gives us reason to be skeptical about the validity of this model.

In the final refinements, fully stochiometric models were accepted for all RE_3CuGaCh_7 structures. **Table 2–1** lists crystal data and details of the data collections, **Table 2–2** lists positional and displacement parameters, and **Table 2–3** lists selected interatomic distances.

Table 2-1. Crystallographic data for $RE_3CuGaCh_7$ (RE = La–Nd; Ch = S, Se).

Formula	La$_3$CuGaS$_7$	Ce$_3$CuGaS$_7$	Pr$_3$CuGaS$_7$	Nd$_3$CuGaS$_7$
Formula mass (amu)	774.41	778.04	780.41	790.40
Space group	$P6_3$ (No. 173)	$P6_3$ (No. 173)	$P6_3$ (No. 173)	$P6_3$ (No. 173)
a (Å)	10.255(3)	10.128(3)	10.0371(6)	9.9622(11)
c (Å)	6.0706(15)	6.0518(19)	6.0834(4)	6.0936(7)
V (Å^3)	552.9(3)	537.6(4)	530.75(7)	523.74(13)
Z	2	2	2	2
ρ_{calcd} (g cm^{-3})	4.652	4.807	4.883	5.012
T (K)	296	296	296	296
Crystal dimensions (mm)	0.10 × 0.08 × 0.06	0.07 × 0.06 × 0.05	0.07 × 0.06 × 0.04	0.04 × 0.04 × 0.04
μ(Mo $K\alpha$) (mm^{-1})	16.90	18.16	19.30	20.47
Transmission factors	0.316–0.540	0.353–0.558	0.377–0.516	0.472–0.616
2θ limits	4.59–66.25°	4.64–66.19°	4.69–66.19°	4.72–66.11°
Data collected	$-15 \leq h \leq 15$, $-15 \leq k \leq 15$, $-9 \leq l \leq 9$	$-15 \leq h \leq 15$, $-15 \leq k \leq 15$, $-9 \leq l \leq 9$	$-15 \leq h \leq 15$, $-15 \leq k \leq 15$, $-9 \leq l \leq 9$	$-15 \leq h \leq 15$, $-15 \leq k \leq 15$, $-9 \leq l \leq 9$
No. of data collected	8105	7847	7607	7660
No. of unique data, including $F_o^2 < 0$	1419 (R_{int} = 0.028)	1362 (R_{int} = 0.033)	1343 (R_{int} = 0.041)	1331 (R_{int} = 0.075)
No. of unique data, with $F_o^2 > 2\sigma(F_o^2)$	1342	1289	1251	1098
No. of variables	41	41	41	41
Twin law	$-100/0-10/00-1$	$-100/0-10/00-1$	$-100/0-10/00-1$	$-100/0-10/00-1$
Flack parameter	$-0.00(4)$	0.03(3)	0.02(2)	$-0.02(4)$
$R(F)$ for $F_o^2 > 2\sigma(F_o^2)$ [a]	0.030	0.022	0.020	0.034
$R_w(F_o^2)$ [b]	0.086	0.051	0.034	0.074
Goodness of fit	1.14	1.07	1.06	1.04
$(\Delta\rho)_{max}$, $(\Delta\rho)_{min}$ (e Å^{-3})	5.79, -1.26	2.55, -1.26	0.87, -1.08	1.98, -1.95

Formula	La₃CuGaSe₇	Ce₃CuGaSe₇	Pr₃CuGaSe₇	Nd₃CuGaSe₇
Formula mass (amu)	1102.71	1106.34	1108.71	1118.70
Space group	$P6_3$ (No. 173)			
a (Å)	10.626(10)	10.6007(6)	10.4181(8)	10.3426(9)
c (Å)	6.392(6)	6.3775(4)	6.3743(5)	6.3869(6)
V (Å^3)	625.0(14)	620.65(8)	599.16(10)	591.67(12)
Z	2	2	2	2
ρ_{calcd} (g cm^{-3})	5.859	5.920	6.145	6.279
T (K)	296	296	296	296
Crystal dimensions (mm)	0.08 × 0.04 × 0.04	0.05 × 0.05 × 0.04	0.07 × 0.05 × 0.04	0.05 × 0.05 × 0.04
μ(Mo $K\alpha$) (mm^{-1})	34.16	35.08	37.14	38.42
Transmission factors	0.182–0.420	0.295–0.406	0.162–0.376	0.203–0.376
2θ limits	4.43–66.14°	4.44–66.19°	4.51–66.20°	4.55–66.18°
Data collected	$-16 \leq h \leq 15$, $-16 \leq k \leq 16$, $-9 \leq l \leq 9$	$-16 \leq h \leq 16$, $-16 \leq k \leq 16$, $-9 \leq l \leq 9$	$-15 \leq h \leq 16$, $-16 \leq k \leq 16$, $-9 \leq l \leq 9$	$-15 \leq h \leq 15$, $-15 \leq k \leq 15$, $-9 \leq l \leq 9$
No. of data collected	8781	9058	8787	8671
No. of unique data, including $F_o^2 < 0$	1548 (R_{int} = 0.084)	1575 (R_{int} = 0.050)	1526 (R_{int} = 0.049)	1507 (R_{int} = 0.060)
No. of unique data, with $F_o^2 > 2\sigma(F_o^2)$	1387	1422	1474	1371
No. of variables	41	41	41	41
Twin law	010/100/00–1	–100/0–10/00–1	010/100/00–1	–100/0–10/00–1
Flack parameter	–0.12(3)	0.00(5)	–0.06(4)	0.00(3)
$R(F)$ for $F_o^2 > 2\sigma(F_o^2)$ [a]	0.039	0.030	0.030	0.030
$R_w(F_o^2)$ [b]	0.095	0.071	0.069	0.063
Goodness of fit	1.06	1.06	1.11	1.13
$(\Delta\rho)_{max}$, $(\Delta\rho)_{min}$ (e Å^{-3})	2.59, –1.66	3.25, –1.48	1.28, –1.20	1.47, –1.36

[a] $R(F) = \sum||F_o| - |F_c|| / \sum|F_o|$ for $F_o^2 > 2\sigma(F_o^2)$.
[b] $R_w(F_o^2) = [\sum[w(F_o^2 - F_c^2)^2] / \sum wF_o^4]^{1/2}$; $w^{-1} = [\sigma^2(F_o^2) + (Ap)^2 + Bp]$, where $p = [\max(F_o^2,0) + 2F_c^2] / 3$.

Table 2-2. Positional and equivalent isotropic displacement parameters (Å^2) [a] for $RE_3CuGaCh_7$ (RE = La–Nd; Ch = S, Se).

	La$_3$CuGaS$_7$	Ce$_3$CuGaS$_7$	Pr$_3$CuGaS$_7$	Nd$_3$CuGaS$_7$
RE in 6*c* (*x*, *y*, *z*)				
x	0.1391(1)	0.1412(1)	0.1446(1)	0.1470(1)
y	0.3701(1)	0.3721(1)	0.3749(1)	0.3758(1)
z	0.4460(2)	0.4345(1)	0.0781(1)	0.4067(2)
U_{eq}	0.0156(2)	0.0151(1)	0.0153(1)	0.0183(2)
Cu1a in 2*a* (0, 0, *z*)				
occupancy	0.72(1)	0.71(1)	0.65(1)	0.68(3)
z	0.0000(11)	0.0000(10)	0.0000(8)	0.000(3)
U_{eq}	0.0199(11)	0.0284(12)	0.0229(9)	0.033(2)
Cu1b in 2*a* (0, 0, *z*)				
occupancy	0.28(1)	0.29(1)	0.35(1)	0.32(3)
z	0.091(3)	0.102(2)	–0.0955(12)	0.101(4)
U_{eq}	0.0199(11)	0.0284(12)	0.0229(9)	0.033(2)
Ga in 2*b* (1/3, 2/3, *z*)				
z	0.8643(3)	0.8544(2)	0.6579(2)	0.8278(3)
U_{eq}	0.0173(4)	0.0147(3)	0.0124(2)	0.0144(4)
S1 in 6*c* (*x*, *y*, *z*)				
x	0.2490(2)	0.2492(2)	0.2509(2)	0.2520(3)
y	0.1531(2)	0.1525(2)	0.1515(2)	0.1503(3)
z	0.4782(4)	0.4712(3)	0.0336(2)	0.4577(4)
U_{eq}	0.0142(4)	0.0158(3)	0.0153(3)	0.0191(6)
S2 in 6*c* (*x*, *y*, *z*)				
x	0.5198(3)	0.5192(2)	0.5197(2)	0.5199(3)
y	0.0985(3)	0.0966(2)	0.0950(2)	0.0938(3)
z	0.2154(4)	0.2033(3)	0.3091(2)	0.1756(4)
U_{eq}	0.0141(4)	0.0135(3)	0.0130(2)	0.0160(5)
S3 in 2*b* (1/3, 2/3, *z*)				
z	0.2319(6)	0.2229(5)	0.2905(4)	0.1949(7)
U_{eq}	0.0139(7)	0.0132(5)	0.0123(4)	0.0150(8)
	La$_3$CuGaSe$_7$	Ce$_3$CuGaSe$_7$	Pr$_3$CuGaSe$_7$	Nd$_3$CuGaSe$_7$
RE in 6*c* (*x*, *y*, *z*)				
x	0.1481(1)	0.1477(1)	0.1510(1)	0.1533(1)
y	0.3695(1)	0.3706(1)	0.3731(1)	0.3743(1)
z	0.0555(2)	0.0567(1)	0.0726(1)	0.4168(1)
U_{eq}	0.0230(2)	0.0197(2)	0.0194(2)	0.0218(2)
Cu1a in 2*a* (0, 0, *z*)				
occupancy	0.68(2)	0.670(11)	0.647(12)	0.659(13)
z	0.0000(18)	0.0000(11)	0.0000(12)	0.0000(14)
U_{eq}	0.0232(16)	0.0207(11)	0.0225(12)	0.0304(18)
Cu1b in 2*a* (0, 0, *z*)				

occupancy	0.32(2)	0.330(11)	0.353(12)	0.341(13)
z	−0.092(4)	−0.094(2)	−0.101(2)	0.107(3)
U_{eq}	0.0232(16)	0.0207(11)	0.0225(12)	0.0304(18)
Ga in $2b$ (1/3, 2/3, z)				
z	0.6421(6)	0.6432(3)	0.6575(4)	0.8334(4)
U_{eq}	0.0245(8)	0.0188(4)	0.0152(4)	0.0161(4)
Se1 in $6c$ (x, y, z)				
x	0.2544(2)	0.2540(1)	0.2562(1)	0.2567(1)
y	0.1501(2)	0.1506(1)	0.1497(2)	0.1484(1)
z	0.0177(3)	0.0195(2)	0.0259(2)	0.4693(2)
U_{eq}	0.0202(4)	0.0160(2)	0.0172(3)	0.0195(3)
Se2 in $6c$ (x, y, z)				
x	0.5219(2)	0.5214(1)	0.5211(1)	0.5219(1)
y	0.0919(2)	0.0921(1)	0.0895(1)	0.0886(1)
z	0.2881(3)	0.2891(2)	0.3063(2)	0.1834(2)
U_{eq}	0.0197(4)	0.0157(2)	0.0150(2)	0.0171(2)
Se3 in $2b$ (1/3, 2/3, z)				
z	0.2693(5)	0.2708(3)	0.2851(3)	0.2048(3)
U_{eq}	0.0168(6)	0.0136(3)	0.0136(4)	0.0154(4)

[a] U_{eq} is defined as one-third of the trace of the orthogonalized U_{ij} tensor.

Table 2-3. Selected interatomic distances (Å) in $RE_3CuGaCh_7$ (RE = La–Nd; Ch = S, Se).

Bonds	La₃CuGaS₇	Ce₃CuGaS₇	Pr₃CuGaS₇	Nd₃CuGaS₇
RE–S2	2.884(2)	2.849(2)	2.824(1)	2.812(3)
RE–S1	2.916(2)	2.895(2)	2.887(1)	2.869(3)
RE–S1	2.961(2)	2.936(2)	2.938(1)	2.931(3)
RE–S3	2.974(2)	2.919(2)	2.879(1)	2.852(2)
RE–S2	2.993(3)	2.956(2)	2.934(1)	2.913(3)
RE–S1	3.042(3)	3.009(2)	2.978(1)	2.931(3)
RE–S2	3.075(2)	3.042(2)	3.035(1)	3.032(3)
RE–S1	3.410(3)	3.426(2)	3.488(1)	3.527(3)
Cu1a–S1 (×3)	2.235(2)	2.210(2)	2.206(1)	2.202(3)
Cu1b–S1 (×3)	2.333(6)	2.341(5)	2.333(3)	2.354(10)
Ga–S3	2.231(4)	2.230(3)	2.235(2)	2.237(5)
Ga–S2 (×3)	2.293(3)	2.288(2)	2.284(1)	2.281(3)
Bonds	**La₃CuGaSe₇**	**Ce₃CuGaSe₇**	**Pr₃CuGaSe₇**	**Nd₃CuGaSe₇**
RE–Se2	3.015(3)	3.002(1)	2.955(1)	2.938(1)
RE–Se1	3.018(4)	3.020(1)	2.985(1)	2.972(1)
RE–Se1	3.067(4)	3.065(1)	3.043(1)	3.036(1)
RE–Se3	3.082(3)	3.067(1)	2.998(1)	2.969(1)
RE–Se2	3.109(3)	3.099(1)	3.050(2)	3.033(1)
RE–Se1	3.142(4)	3.143(1)	3.079(2)	3.049(1)
RE–Se2	3.281(3)	3.260(1)	3.224(1)	3.222(1)
RE–Se1	3.600(4)	3.592(1)	3.634(2)	3.686(2)
Cu1a–Se1 (×3)	2.357(3)	2.348(1)	2.329(1)	2.317(1)
Cu1b–Se1 (×3)	2.456(8)	2.455(5)	2.459(5)	2.471(6)
Ga–Se3	2.383(5)	2.375(3)	2.374(3)	2.372(3)
Ga–Se2 (×3)	2.424(3)	2.416(1)	2.409(2)	2.404(2)

2.2.2   Magnetic susceptibility measurements

Measurements of dc magnetic susceptibility were initially attempted for La₃CuGaS₇ on a Quantum Design Physical Property Measurement System (PPMS) equipped with the Model P500 option (ac/dc magnetometer system), but difficulties were encountered in centering the sample because the signal was very weak. Instead, this sample was analyzed on a more sensitive Quantum Design Dynacool PPMS equipped with the Model 525 option (vibrating sample magnetometer

(VSM)). Centering of the sample was performed at 1.8 K, at which a stronger signal could be detected than at 300 K. The sample (85 mg of La_3CuGaS_7 powder) was cooled in the absence of field down to 1.8 K and the dc magnetic susceptibility was measured under an applied field of 0.5 T with increasing temperature after stabilization at each increment. The measurements were repeated by cooling the sample under an applied field of 0.5 T.

2.2.3   XPS analysis

La_3CuGaS_7 and $Ce_3CuGaSe_7$ were chosen for analysis by X-ray photoelectron spectroscopy (XPS) as representative samples to probe the valence states of the *RE* and Cu atoms in these compounds. XPS spectra were collected on a Kratos AXIS Ultra spectrometer equipped with a monochromatic Al *K*α radiation source (1486.7 eV), operated at 12 kV and 12 mA, and a hybrid lens with a 700 μm × 400 μm spot size. The finely ground, air-stable samples were pressed onto 6-mm diameter pellets, mounted on a sample bar with double-sided tape, and transferred into the analysis chamber, which was maintained at a pressure between 10^{-7} and 10^{-9} Pa. The samples were sputter-cleaned with an Ar^+ ion beam (4 kV, 10 mA) until peaks associated with oxides (e.g., Cu satellite peaks) disappeared and the O 1s signal remained constant. Charge neutralization was required, with the settings adjusted (1 A filament current, 3.5 V charge balance, 1.1 V filament bias) until the signals were maximized and the peak widths were minimized. Survey spectra were collected between 1100 and 0 eV with a pass energy of 80 eV, a step size of 0.4 eV, and a dwell time of 0.1 s. High-resolution *RE* 3d and Cu 2p spectra were collected with a pass energy of 20 eV, a step size of 0.1 eV (except for the Cu 2p spectrum of $Ce_3CuGaSe_7$, which had a smaller step size of 0.05 eV), and a dwell time of 0.2 s. The spectra were calibrated to the C 1s peak at 284.8 eV arising from adventitious carbon. All spectra were analyzed with use of the CasaXPS software

package.[32] The background, fitted to a Shirley-type function, was removed. The core-lines were fitted to a pseudo-Voigt line shape (70% Gaussian and 30% Lorentzian) to account for instrumental and experimental broadening effects. On the basis of many previous measurements made on this spectrometer, we estimate the precision of the reported binding energies (BEs) to be better than ±0.1 eV.

2.2.4   Band structure calculations

Tight-binding linear muffin tin orbital band structure calculations were performed on an idealized model of La$_3$CuGaS$_7$, in which Cu atoms are placed entirely within the trigonal planar site, within the local density and atomic spheres approximation with use of the Stuttgart TB-LMTO-ASA program (version 4.7).[33] The basis set consisted of La 6s/6p/5d/4f, Cu 4s/4p/3d, Ga 4s/4p/4d, and S 3s/3p/3d orbitals, with the La 6p, Ga 4d, and S 3d orbitals being downfolded. Integrations in reciprocal space were carried out with an improved tetrahedron method over 208 irreducible k points within the first Brillouin zone.

2.2.5   Solid-state UV-visible spectroscopy

Optical diffuse reflectance measurements on La$_3$CuGaSe$_7$ were made on a Nicolet 8700 spectrometer at room temperature, over a scan range of 1110 to 300 nm. The powder sample was spread on a compacted base of BaSO$_4$, used as a 100% reflectance standard. Reflectance data were converted to absorbance data through the Kubelka-Munk function.

2.3   Results and discussion

The quaternary chalcogenides RE_3CuGaCh_7 (Ch = S, Se), which form for the earlier rare-earth components (RE = La–Nd), encompass the formerly unique representative, La$_3$CuGaSe$_7$,[23] known in this copper-containing series. They extend the transition-metal substitution in

RE_3MGaCh_7, previously limited to M = Mn–Ni.[9,13,15] The $RE_3CuGaCh_7$ compounds were prepared by direct reaction of the elements at 1050 °C (sulfides) or 900 °C (selenides), under identical conditions used to synthesize other RE_3MGaCh_7 compounds.[15] Use of a KI flux was reported to be beneficial for the crystal growth of $La_3CuGaSe_7$,[23] although in our hands, similarly sized crystals could be obtained without special treatment.

As the hexagonal La_3CuSiS_7-type structure adopted by $RE_3CuGaCh_7$ has been well described in the literature,[5] we focus on peculiarities. The structure has a one-dimensional character, consisting of two kinds of chains extended along the c-direction, with RE atoms located between them in a CN7+1 geometry (**Figure 2–2**). First, Ga-centred tetrahedra (surrounded by three basal $Ch2$ atoms and one apical $Ch3$ atom) are arranged in stacks extending along ⅓, ⅔, z and ⅔, ⅓, z, with their apical atoms all pointing in the same polar direction [001]. This feature is the primary source of noncentrosymmetry in the structure and is common to all La_3CuSiS_7-type compounds. Second, triangles of $Ch1$ atoms are arranged in staggered stacks so that they form confacial antiprisms extending along the c-axis. As in all other copper-containing La_3CuSiS_7-type compounds,[3,5,23,29,30] Cu atoms occupy the site strictly centred within the plane of these triangles to attain a CN of 3. In other cases, it is the antiprismatic site located halfway between these triangles that are occupied by metal atoms in an octahedral geometry (CN6), as in RE_3MGaCh_7 (M = Mn–Ni),[9,13,15] or it could be an intermediate site having an asymmetric coordination with three short and three long bonds, as experienced by deficient Al atoms in $Ce_3Al_{0.67}AlS_7$.[16]
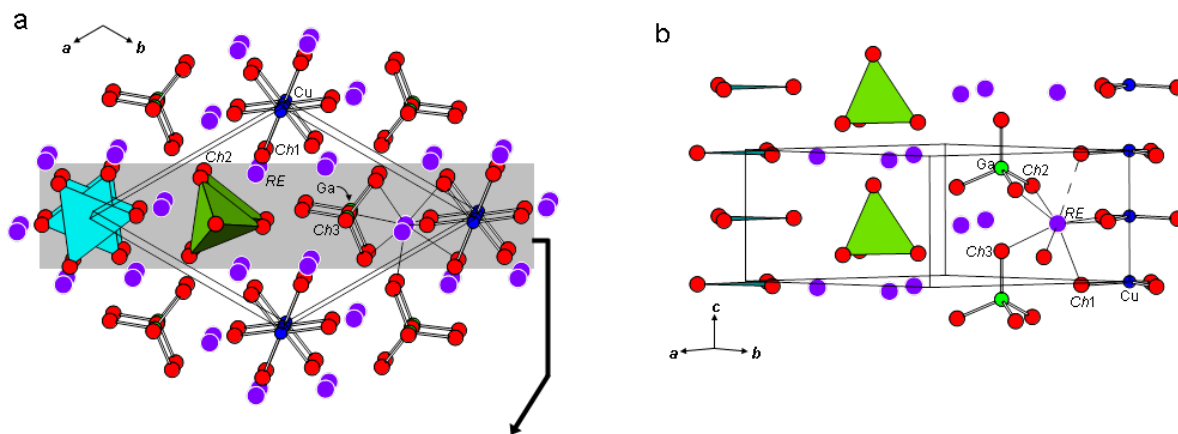
Figure 2-2. Structure of $RE_3CuGaCh_7$ (Ch = S, Se) viewed (a) down and (b) perpendicular to the c-direction, highlighting the stacks of Cu-centred trigonal planes (blue) and Ga-centred tetrahedra (green) separated by RE atoms (purple).

Plots of cell lengths and c/a ratios of these $RE_3CuGaCh_7$ compounds reveal trends that support the general crystal chemical principles developed for many La_3CuSiS_7-type structures (**Figure 2–3**).[5] The a-parameter depends strongly on RE but the c-parameter is nearly constant. In accordance with predictions, the structure responds flexibly within the ab-plane, contracting upon substitution with a smaller RE component, but it is quite rigid along the c-direction, whose repeat is fixed by space-filling requirements imposed by the choice of Ga and Ch atoms within the Ga-centred tetrahedra. For quaternary sulfides adopting the La_3CuSiS_7-type structure, c-parameters have been estimated based on the identity of the metal-centred tetrahedra. For compounds containing GaS_4 tetrahedra, the c-parameter is predicted to be 6.05±0.05 Å, in excellent agreement with the observed values in RE_3CuGaS_7 (c = 6.05–6.10 Å).[5] Data for the corresponding selenides are not as extensive, but the results for $RE_3CuGaSe_7$ (c = 6.37–6.40 Å) obtained here indicate that other La_3CuSiS_7-type compounds containing $GaSe_4$ tetrahedra should have a c-parameter close to 6.38±0.05 Å. For comparison, the c-parameters in RE_3MGaSe_7 (M =

Fe–Ni) are 6.35–6.43 Å.[15] The c/a ratio generally increases in the progression of *RE* from La to Nd, reflected by distortion of the *RE* coordination geometry in which the contact to an eighth surrounding *Ch* atom, roughly parallel to c (as shown by the dashed line in **Figure. 2–2**), becomes greatly elongated (over 3.4 Å in the sulphides or over 3.6 Å in the selenides), while the contacts to the remaining *Ch* atoms shrink.
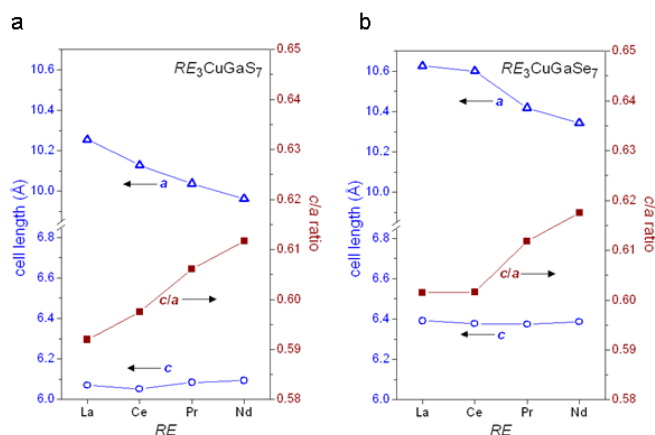
Figure 2-3. Plots of cell parameters and c/a ratios for (a) RE_3CuGaS_7 and (b) $RE_3CuGaSe_7$.

A graphical representation of bond distances clearly reveals this effect (**Figure 2–4**). At the other extreme, it is interesting that the trend in the c/a ratio reaches a plateau at the La-member in the $RE_3CuGaSe_7$ series, indicating that there are limits in compatible sizes of *RE* and Ga atoms, and that their effects on a and c are not entirely independent. Note that the *RE*–Se distances are similar in $La_3CuGaSe_7$ and $Ce_3CuGaSe_7$ despite the size differences between La and Ce atoms, implying that the insertion of a large *RE* atom such as La cannot be accommodated indefinitely through structural expansion within the *ab*-plane.
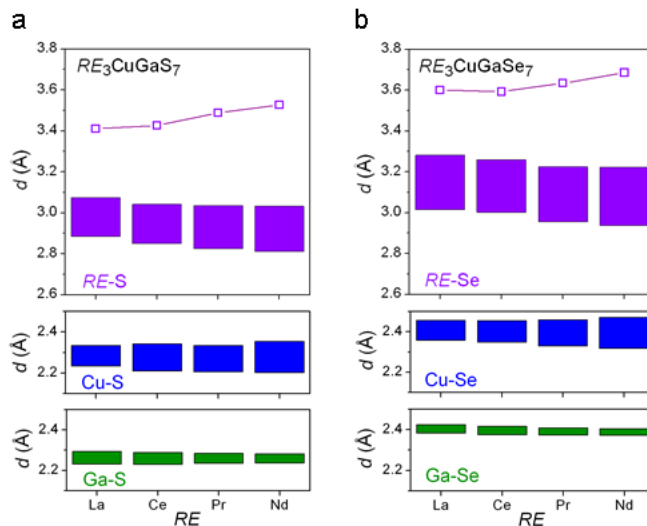
Figure 2-4. Ranges of bond distances in (a) RE_3CuGaS_7 and (b) $RE_3CuGaSe_7$. The long contacts to the eighth Ch atom around the RE atom are plotted separately in the top panels.

A noteworthy feature is the trigonal planar Cu site, which exhibits highly elongated displacement ellipsoids, but can be modeled as two split sites with more reasonable ellipsoids in favourable cases such as here (**Figure 2–5**). The main site residing strictly on the plane is about 70% occupied whereas the secondary site displaced slightly off (by ~0.6 Å) the plane is about 30% occupied.
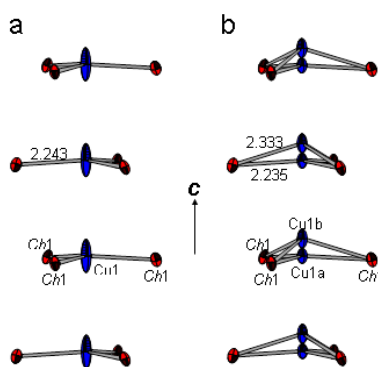
Figure 2-5. Stacks of three-coordinate Cu atoms in $RE_3CuGaCh_7$ modeled as (a) single sites and (b) closely spaced split sites. The distances shown are for La_3CuGaS_7, and the displacement ellipsoids are drawn at the 50% probability level.

As support for this model, it is helpful to cite previous temperature-dependent studies of related Ag-deficient compounds $RE_3Ag_{1-y}SnS_7$ (RE = La, Ce; y = 0.2) which have confirmed that two split sites can be resolved at low temperatures (12 K);[31] however, at high temperatures (400–500 K), the electron density becomes extremely diffuse within the channels enclosed by the surrounding chalcogen atoms, as also seen in $Ce_3Ag_{0.63}SiS_{6.63}Cl_{0.37}$.[21] Because this diffusion is promoted by the presence of defects within this site, we wish to establish whether Cu deficiencies are also possible in $RE_3CuGaCh_7$. Reactions were performed with the nominal compositions $La_3Cu_xGaS_7$ (x = 0.2 to 2.0 in increments of 0.2) under the same conditions as before, and the products were analyzed by powder XRD (**Figure. 2–6**). Although the control sample, La_3CuGaS_7 (x = 1.0), still contained small amounts of impurities, the important observation is that secondary phases become substantial in all the other samples. This evidence suggests that a solid solution does not form (or certainly not to the same degree as the Ag-containing phases) in La_3CuGaS_7.
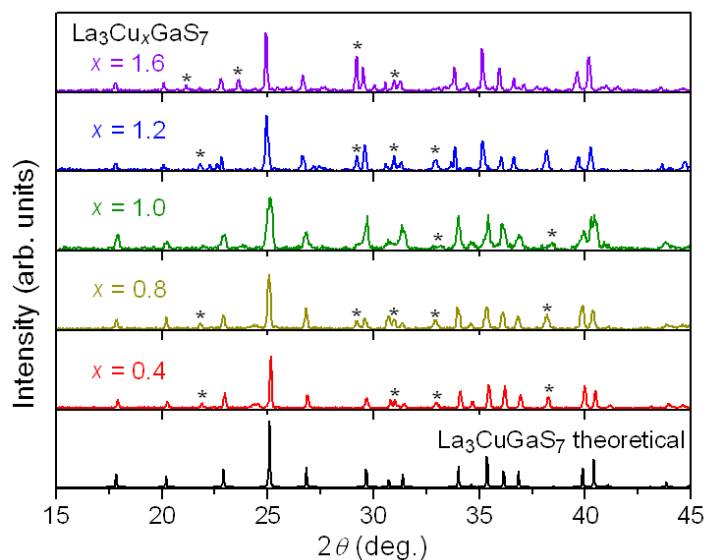
Figure 2-6. Powder XRD patterns for reactions performed with nominal compositions $La_3Cu_xGaS_7$ containing variable Cu content. Peaks that do not belong to the simulated pattern for La_3CuGaS_7 are marked with asterisks.

The combination of Cu and Ga atoms in $RE_3CuGaCh_7$ is unexpected. Given the presence of isolated Ch atoms and with the assumption of normal valences, the formula $(RE^{3+})_3(Cu^+)(Ga^{3+})(Ch^{2-})_7$ is one electron short of charge balance. In the previous report on La$_3$CuGaSe$_7$, the presence of divalent Cu atoms was proposed to recover a charge-balanced formula, on the basis of a calculated bond valence sum of 1.69 for the Cu atoms and the observation of paramagnetic behaviour.[23] **Table 2–4** lists bond valence sums evaluated for the RE, Cu, and Ga atoms in all $RE_3CuGaCh_7$ compounds characterized here.[34] They agree well with expectations of RE^{3+}, Cu^+, and Ga^{3+}. In particular, the Cu atoms placed within the strictly trigonal planar site have bond valence sums of 1.1–1.3 so that they are slightly overbonded; when they are displaced off-plane, the bond valence sums are reduced to 0.8–0.9. This analysis provides one possible explanation for the elongated displacement ellipsoids observed in these sites. Indeed, detailed inspection of the crystal structures reveals a nice correlation in which the trigonal planar site is less occupied and the displacement ellipsoid is more elongated as the degree of overbonding becomes more severe in the progression of RE from La to Nd. We do not understand the discrepancy in the bond valence sum analysis of La$_3$CuGaSe$_7$ because the structure redetermined by us agrees with the previously reported one (other than a small typographical error in the x-coordinate, which should be –0.1041(3), for the Se3 atom) and gives similar metrical parameters.[23] The Cu–Ch distances (2.20–2.35 Å in RE_3CuGaS_7; 2.32–2.47 Å in $RE_3CuGaSe_7$) fall within the normal ranges found around three-coordinate Cu atoms (2.2–2.4 Å in sulfides; 2.3–2.5 Å in selenides).[4] For example, CuS (covellite) contains among the shortest observed trigonal Cu–S bonds of 2.19 Å.[35–38]

Table 2-4. Bond valence sums in $RE_3CuGaCh_7$.[a]

	RE	**Cu1a / Cu1b**	**Ga**
La$_3$CuGaS$_7$	2.85	1.09 / 0.84	3.00
Ce$_3$CuGaS$_7$	2.96	1.16 / 0.82	3.03
Pr$_3$CuGaS$_7$	2.95	1.18 / 0.84	3.05
Nd$_3$CuGaS$_7$	3.02	1.19 / 0.79	3.06
La$_3$CuGaSe$_7$	2.70	1.20 / 0.92	2.95
La$_3$CuGaSe$_7$ [b]	2.75	1.22 / 0.85	2.98
Ce$_3$CuGaSe$_7$	2.75	1.24 / 0.93	3.01
Pr$_3$CuGaSe$_7$	2.95	1.30 / 0.92	3.06
Nd$_3$CuGaSe$_7$	3.01	1.34 / 0.89	3.09

[a] Evaluated from $V_i = \sum \exp[(R_{ij} - d_{ij})/0.37]$, with bond valence parameters R_{ij} taken from Ref. 34 and distances d_{ij} from crystal structures determined here. [b] Evaluated with distances taken from Ref. 23.

Magnetic measurements made on La$_3$CuGaS$_7$, which contains a nonmagnetic *RE* component, reveal rather low susceptibility values (**Figure. 2–7**). (The small kink near 60 K was confirmed to originate from trapped oxygen; it was not observed when the measurement was repeated by packing the sample more tightly and applying the extended purge option on the magnetometer.) A plot of the inverse susceptibility fitted to the Curie-Weiss law gives a small effective magnetic moment μ_{eff} of 0.63(1) μ_B. The appropriate comparison is to other binary copper sulfides, but there is inconsistency in their reported magnetic properties; for example, CuS (which contains monovalent Cu, notwithstanding its formula) has been reported to show either temperature-independent paramagnetism or a Curie-Weiss behaviour giving a small effective magnetic moment (~0.3 μ_B) that can been attributed to residual spin density on the S atoms.[37,39,40] Because the sample does contain a small amount of unidentified phase (**Figure 2–1**), it is quite likely that the temperature-dependent paramagnetism is not intrinsic to La$_3$CuGaS$_7$. Even if we assume that the sample is pure, it is clear that this small magnetic moment cannot be explained by

the presence of divalent Cu in La_3CuGaS_7, which would be expected to give rise to a much larger moment ($\mu_{eff} = 1.73\ \mu_B$).
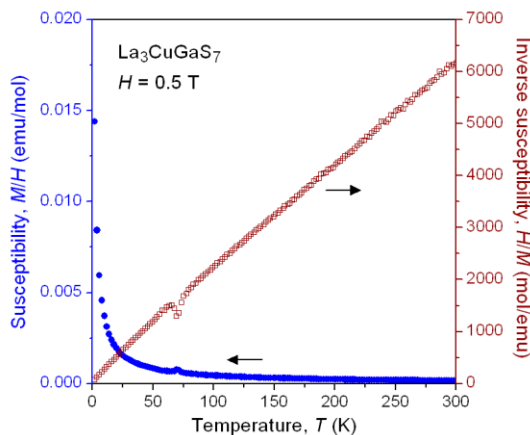
Figure 2-7. Magnetic susceptibility and its inverse for La_3CuGaS_7. The small kink near 60 K is attributed to residual oxygen.

To further address the question of the Cu valence state in $RE_3CuGaCh_7$, high-resolution XPS spectra of the Cu 2p core-lines were measured for La_3CuGaS_7 and $Ce_3CuGaSe_7$ (**Figure 2–8a**). The Cu $2p_{3/2}$ core-line peaks have binding energies (BE) of 932.6 eV in La_3CuGaS_7 and 931.9 eV in $Ce_3CuGaSe_7$. As has been well documented in previous work, Cu XPS spectra must be interpreted carefully because they can be strongly influenced by final state effects.[41–46] It is true that the Cu $2p_{3/2}$ BEs in La_3CuGaS_7 and $Ce_3CuGaSe_7$ agree well with those found in Cu^+-containing sulfides (932.7–932.9 eV) and selenides (931.8–932.7 eV) reported in the NIST X-ray database, and less than those found in Cu^{2+}-containing oxides and halides (>933.5 eV), but Cu metal also has a similar BE of 932.7 eV.[47] The most important diagnostic feature to identify is a satellite peak, which arises from a shake-up or shake-down process, that appears to the high-energy side (940–945 eV) of the $2p_{3/2}$ core-line peak in Cu^{2+} systems. The absence of this satellite peak in La_3CuGaS_7 and $Ce_3CuGaSe_7$ thus precludes the occurrence of Cu^{2+}. Moreover, final state

effects lead to broader peaks for Cu^{2+} (with full-width-at-half-maxima, FWHM, values of ~3 eV) than for Cu^+ and Cu^0 (with FWHM of 1.2–1.3 eV). The observed FWHM values are 1.5–1.7 eV, slightly greater than expected, but this may be an artefact of the low intensity of the spectra. This spectroscopic evidence thus strongly supports the assertion that $RE_3CuGaCh_7$ contains only monovalent Cu. Although sometimes disputed, the consensus established from most XPS measurements is that Cu is invariably monovalent in sulfides and selenides.[42,46]

Conceivably, but improbably, charge balance could be still recovered in $Ce_3CuGaSe_7$ if mixed-valence of the Ce atoms is invoked; thus, RE 3d XPS spectra were also measured for these two compounds. Such spectra are typically quite complicated because of the severe final state effects entailed by spin-orbit coupling with unpaired 4f electrons and by different relaxation processes. Along with the set of core-line peaks (A, B), intense satellite peaks (A′, B′) are also seen in the La 3d spectrum of La_3CuGaS_7 (**Figure 2–8b**). The BE of the La $3d_{5/2}$ core-line peak (A) is 833.4 eV (Figure 2–8b), similar to other La-containing chalcogenides such as La_3MInS_7 (M = Fe, Co, Ni; 833.6–833.8 eV) but higher than in La_2O_3 (831.9 eV)[14]. Characteristic of La^{3+} is the satellite peak (A′), induced by a ligand-to-metal shake-up process, located at 4 eV to higher BE of the core-line peak. The Ce 3d spectrum of $Ce_3CuGaSe_7$ exhibits considerable fine structure because of multiplet splitting and can be fitted with component peaks through a well-established procedure that takes into account the possibility of both Ce^{3+} and Ce^{4+} species (Figure 2–8c). [48–51] From the relative areas of these component peaks, we estimate that 90% of the signal arises from Ce^{3+}. Residual Ce^{4+}, which gives rise to the small peak at 916 eV, is often observed in Ce 3d XPS spectra and is most likely attributed to surface oxides (CeO_2) rather than being intrinsic to the bulk sample.
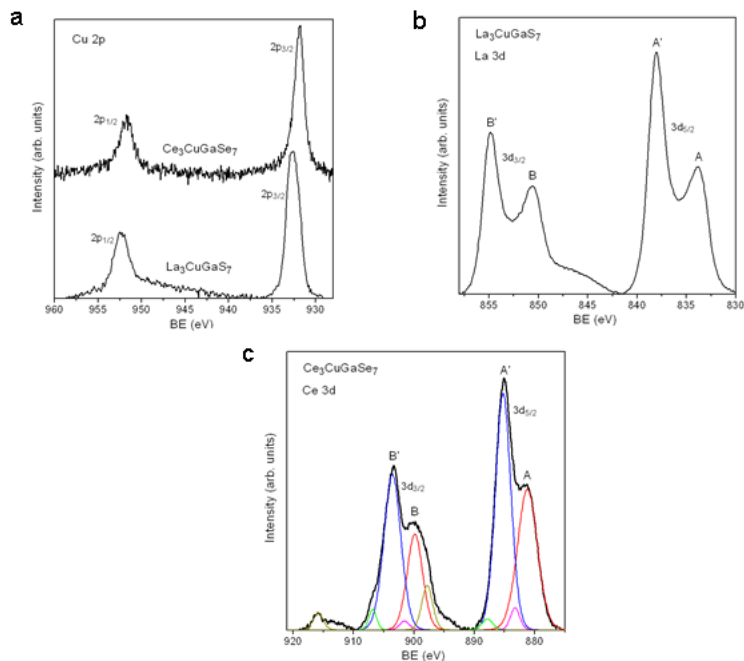
Figure 2-8. (a) Cu 2p, (b) La 3d, and (c) Ce 3d XPS spectra for La₃CuGaS₇ and Ce₃CuGaSe₇. In (c), the spectrum was fitted to ten component peaks, for which the most intense (blue, red) correspond to final states of Ce^{3+} and the remainder to those of Ce^{4+}.

The electronic band structure was calculated for La₃CuGaS₇ (**Figure 2–9**). Consistent with the one-electron deficiency relative to charge balance, the Fermi level is located just below the top of the valence band, which is separated by 2.3 eV from the conduction band higher in energy. The optical band gap for the corresponding selenide La₃CuGaSe₇ was obtained experimentally from the absorption edge in the diffuse reflectance spectrum and found to be 2.0 eV (**Figure 2–10**). Not shown are S 3s states, located at much lower energies (–12 to –11 eV), which are used for Cu–S and Ga–S bonding. The small peak just below –5 eV corresponds to bonding involving Ga 4s and S 3p states. The broad valence band is composed predominantly from mixing of Cu 3d and S 3p states, with small contributions from Ga 4p states. Although Cu 3d states extend from –4 eV up to the top of the valence band, they contribute much less than S 3p states to the density of states

(DOS) at the Fermi level. This situation is similar to CuS, for which both the calculated band structure and the experimental valence band spectrum show the Fermi level cutting the top of a valence band which is of mostly S-based character.[38,42] In other words, the electron deficiency in La_3CuGaS_7 is accommodated by holes in S-based bands rather than by the presence of Cu^{2+} species. There is no strong preference among S1, S2, and S3 atoms to accommodate the electron deficiency because they are chemically similar, as confirmed by inspection of QTOT values. The proposal that S-based spin density could be responsible for the paramagnetism observed in CuS, if this behaviour is assumed to be intrinsic,[37] could then also explain the same observation in La_3CuGaS_7.

Moreover, the dark grey colour of $RE_3CuGaCh_7$ compounds is consistent with this electronic structure. The optical band gap for the corresponding selenide $La_3CuGaSe_7$ was obtained experimentally from the absorption edge in the diffuse reflectance spectrum and found to be 2.0 eV. In other RE_3MGaCh_7 compounds containing earlier transition metals (M = Mn–Ni), the transition-metal d-band is located at higher energies and is partially occupied,[15] leading to the possibility of strong spin polarization, which cannot occur in the case of La_3CuGaS_7.
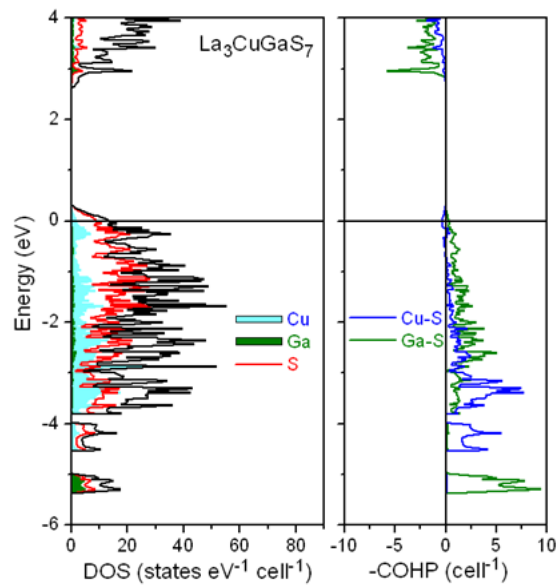
Figure 2-9. Density of states (DOS) and crystal orbital Hamilton population (–COHP) curves for La$_3$CuGaS$_7$.
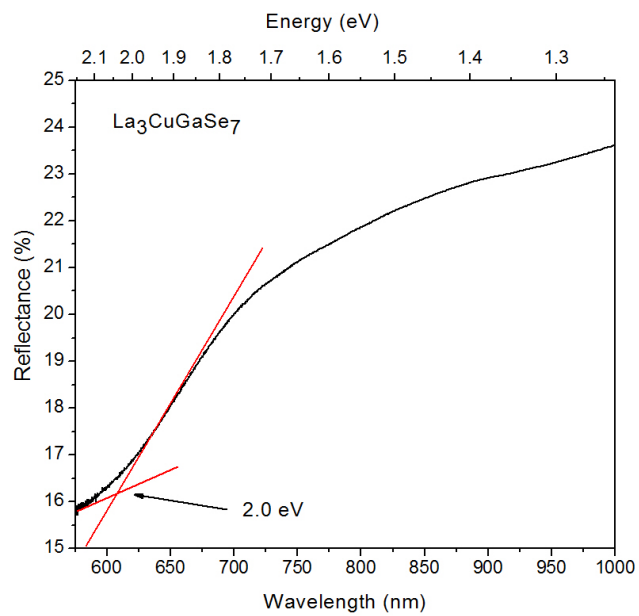
Figure 2-10. Optical diffuse reflectance spectrum of La$_3$CuGaSe$_7$.

As expected, Cu–S and Ga–S interactions provide most of the bonding stability in the structure, as seen in the optimized population of essentially all bonding levels in the crystal orbital Hamilton population (COHP) curves. These are strong bonds, as confirmed by their integrated COHP (–ICOHP) values of 2.50 eV/bond for Cu–S and 2.57 eV/bond for Ga–S contacts. In the crystal structure determination, there was a possible ambiguity about the occupation of Cu and Ga atoms within trigonal planar and tetrahedral sites, respectively. If the band structure calculation is repeated with the atom assignments are reversed, a destabilization of 4.57 eV/cell takes place, lending support to the principle that higher-valent metal prefers the higher coordination site. The contribution of La-based states to covalent bonding is not negligible, but it is small, giving an – ICOHP value of 0.77 eV/bond for La–S contacts.

2.4   Conclusions

Although the vast majority of compounds adopting the La_3CuSiS_7-type structure satisfy the requirement for charge balance, the quaternary Cu-containing chalcogenides $RE_3CuGaCh_7$ described here resemble Ag-containing representatives such as $La_3Ag_{0.82}SnS_7$ in exhibiting a small electron deficiency.[20] The unlikely situation of Cu^{2+} species in $RE_3CuGaCh_7$ is ruled out. Instead, bond valence sum analysis, magnetic susceptibility, and Cu XPS measurements provide convincing evidence that the Cu atoms in $RE_3CuGaCh_7$ are monovalent, and the electron deficiency is accommodated through S-based holes in the valence band. Thus, $RE_3CuGaCh_7$ may be considered to be hole-doped versions of the normally semiconducting La_3CuSiS_7-type phases, and it would be interesting to assess the optical behaviour of these compounds. The Cu atoms tend to exhibit anisotropic displacement but not as pronounced as for Ag atoms in related compounds. There does not appear to be a significant homogeneity range in La_3CuGaS_7. It would be

worthwhile to target the Ag-containing analogues $RE_3AgGaCh_7$, which are probably more amenable to solid solubility.

2.5 References

[1]   Mitchell, K.; Ibers, J. A. *Chem. Rev.* **2002**, *102*, 1929–1952.
[2]   Chung, I.; Kanatzidis, M. G. *Chem. Mater.* **2014**, *26*, 849–869.
[3]   Guittard, M.; Julien-Pouzol, M.; Laruelle, P.; Flahaut, J. *C. R. Acad. Sci., Ser. C* 1968, *267*, 767–769.
[4]   Villars, P.; Cenzual, K. Pearson's Crystal Data – Crystal Structure Database for Inorganic Compounds, ASM International, Materials Park, OH, 2010.
[5]   Collin, G.; Étienne, J.; Flahaut, J.; Guittard, M.; Laruelle, P. *Rev. Chim. Miner.* **1973**, *10*, 225–238.
[6]   Choudhury, A.; Dorhout, P. K. *Inorg. Chem.* **2015**, *54*, 1055–1065 and references therein.
[7]   Collin, G.; Flahaut, J. *C. R. Acad. Sci., Ser. C* **1970**, *270*, 488–490.
[8]   Collin, G.; Flahaut, J. *Bull. Soc. Chim. Fr.* **1972**, 2207–2209.
[9]   Rodier, N.; Guittard, M.; Flahaut, J. *C. R. Acad. Sci., Ser. 2* **1983**, *296,* 65–70.
[10]   Nanjundaswamy, K. S.; Gopalakrishnan, J. *J. Solid State Chem.* **1983**, *49*, 51–58.
[11]   Van Calcar, P. M.; Dorhout, P. K. *Mater. Sci. Forum* **1999**, *315*, 322–330.
[12]   Wu, L. -B.; Huang, F. -Q. *Z. Kristallogr. – New Cryst. Struct.* **2005**, *220*, 305–306.
[13]   Yin, W.; Wang, W.; Kang, L.; Lin, Z.; Feng, K.; Shi, Y.; Hao, W.; Yao, J. L.; Wu, Y. *J. Solid State Chem.* **2013**, *202*, 269–275.
[14]   Rudyk, B. W.; Stoyko, S. S.; Mar, A *J. Solid State Chem.* **2013**, *208*, 78–85.
[15]   Rudyk, B. W.; Stoyko, S. S.; Oliynyk, A. O.; Mar, A. *J. Solid State Chem.* **2014**, *210*, 79–88.
[16]   Patrie, M.; Guittard, M. *C. R. Acad. Sci., Ser. C* **1969**, *268,* 1136–1138.
[17]   Collin, G.; Laruelle, P. *C. R. Acad. Sci., Ser. C* **1970***, 270*,410–412.
[18]   Guo S. -P.; Guo G. -C.; Wang M. -S.; Zou J. -P.; Xu, G.; Wang, G. J.; Long, X. -F.; Huang, J. -S. *Inorg. Chem.* **2009**, *48*, 7059–7065.
[19]   Abrahams, S. C. *Acta Crystallogr., Sect. B* **1990**, *46*, 311–324.
[20]   Daszkiewicz, M.; Gulay, L. D. *Mater. Res. Bull.* **2012**, *47*, 497–499.
[21]   Hartenbach, I.; Nilges, T.; Schleid T. *Z. Anorg. Allg. Chem.* **2007**, *633*, 2445–2452.
[22]   Shi, Y. -F.; Chen, Y. -K.; Chen, M. -K.; Wu, L. -M.; Lin, H.; Zhou, L. -J.; Chen, L. *Chem. Mater.* **2015**, *27*, 1876–1884.
[23]   Zhang, X.; Chen, W.; Mei, D.; Zheng, C.; Liao, F.; Li, Y.; Lin, J.; Huang, F. *J. Alloys Compd.* **2014**, *610*, 671–675.
[24]   Sheldrick, G. M. *SHELXTL*, version 6.12; Bruker AXS Inc.: Madison, WI, **2001**.
[25]   Gelato, L. M.; Parthé, E. *J. Appl. Crystallogr.* **1987**, *20*, 139–143.
[26]   Hwu, S. -J.; Bucher, C. K.; Carpenter, J. D.; Taylor, S. P. *Inorg. Chem.* **1995**, *34*, 1979–1980.
[27]   Lin, S. -H.; Mao, J. -G.; Guo, G. -C.; Huang, J. -S. *J. Alloys Compd.* **1997**, *252*, L8–L11.
[28]   Wu, L. -B.; Huang, F. -Q. *Z. Kristallogr. – New Cryst. Struct.* **2005**, *220*, 307–308.
[29]   Gulay, L. D.; Lychmanyuk, O. S.; Wołcyrz, M.; Pietraszko, A.; Olekseyuk, I. D. *J. Alloys Compd.* **2006**, *425*, 159–163.
[30]   Gulay, L. D.; Lychmanyuk, O. S.; Olekseyuk, I. D.; Daszkiewicz, M.; Stępień-Damm, J.; Pietraszko, A. *J. Alloys Compd.* **2007** *431*, 185–190.
[31]   Daszkiewicz, M; Gulay, L. D.; M.; Pietraszko, A.; Shemet, V. Y. *J. Solid State Chem.* **2007**, *180*, 2053–2060
[32]   Fairley, N. CasaXPS, version 2.3.9, Casa Software Ltd., Teighnmouth, Devon, UK, **2003**, http://www.casaxps.com.

[33] Tank, R.; Jepsen, O.; Burkhardt, A.; Andersen, O. K. *TB-LMTO-ASA Program*, version 4.7; Max Planck Institut für Festkörperforschung: Stuttgart, Germany, **1998**.

[34] Brese, N. E.; O'Keeffe, M. *Acta. Crystallogr., Sect. B* **1991**, *47*, 192–197.

[35] Evans, Jr., H. T.; Konnert, J. A. *Am. Mineral.* **1976**, *61*, 996–1000.

[36] Ohmasa, M.; Suzuki, M.; Takeuchi, Y. *Mineral. J.* **1977**, *8*, 311–319.

[37] Fjellvåg, H.; Grønvold, F.; Stølen, S.; Andresen, A. F.; Müller-Käfer, R.; Simon, A. *Z. Kristallogr.* **1988**, *184*, 111–121.

[38] Gotsis, H. J.; Barnes, A. C.; Strange, P. *J. Phys.: Condens. Matter* **1992**, *4*, 10461–10468.

[39] Okamoto, K.; Kawai, S.; Kiriyama, R. *Jap. J. Appl. Phys.* **1969**, *8*, 718–724.

[40] Nozaki, H.; Shibata, K.; Ohhashi, N. *J. Solid State Chem.* **1991**, *91*, 306–311.

[41] Gaarenstroom, S. W.; Winograd, N. *J. Chem. Phys.* **1977**, *67*, 3500–3506.

[42] Folmer, J. C. W.; Jellinek, F. *J. Less-Common Met.* **1980**, *76*, 153–162.

[43] Folmer, J. C. W.; Jellinek, F.; Calis, G. H. M. *J. Solid State Chem.* **1988**, *72*, 137–144.

[44] Chawla, S. K.; Sankarraman, N.; Payer, J. H. *J. Electron Spectrosc. Relat. Phenom.* **1992**, *61*, 1–18.

[45] Patrick, R. A. D.; Mosselmans, J. F. W.; Charnock, J. M.; England, K. E. R.; Helz, G. R.; Gardner, C. D.; Vaughan, D. J. *Geochim. Cosmochim. Acta* **1997**, *61*, 2023–2036.

[46] Goh, S. W.; Buckley, A. N.; Lamb, R. N. *Miner. Eng.* **2006**, *19*, 204–208.

[47] Wagner, C. D.; Naumkin, A. V.; Kraut-Vass, A.; Allison, J. W.; Powell, C. J.; Rumble Jr., J. R. NIST X-ray Photoelectron Spectroscopy Database, version 3.5 (web version), National Institute of Standards and Technology, Gaithersburg, MD 2003, http://srdata.nist.gov/xps.

[48] Burroughs, P.; Hamnett, A.; Orchard, A. F.; Thornton, G. *J. Chem. Soc., Dalton Trans.* **1976**, 1686–1698.

[49] Kotani, A.; Jo, T.; Parlebas, J. C. *Adv. Phys.* **1988**, *37*, 37–85.

[50] LeNormand, F.; El Fallah, J.; Hilaire, L.; Légaré, P.; Kotani, A.; Parlebas, J. C. *Solid State Commun.* **1989**, *71*, 885–889.

[51] Bêche, E.; Charvin, P.; Perarnau, D.; Abanades, S.; Flamant, G. *Surf. Interface Anal.* **2008**, *40*, 264–267.

Chapter 3

Metal ion displacements in noncentrosymmetric chalcogenides $La_3Ga_{1.67}S_7$, $La_3Ag_{0.6}GaCh_7$ (Ch = S, Se), and La_3MGaSe_7 (M = Zn, Cd)

3.1 Introduction

A large class of chalcogenides have the general formula $RE_3M_{1-x}M'Ch_7$ (where RE = rare-earth metal; M, M' = metals and metalloids; Ch = S, Se). They adopt related noncentrosymmetric structures (in hexagonal space group $P6_3$) in which the occupation of the M site by a diverse range of elements with different valences accounts for the existence of an enormous number of representatives, well over 300 to date.[1] The prototype structure is termed the $Ce_3Al_{1.67}S_7$-type for ternary chalcogenides (when M and M' are the same element) or the La_3CuSiS_7-type for quaternary chalcogenides (when M and M' are different elements).[2,3] Most $RE_3M_{1-x}M'Ch_7$ compounds satisfy charge balance, which is met by the condition $3(3)+(1-x)V_M + V_{M'} + 7(-2) = 0$, where V_M and $V_{M'}$ are the valences of M and M', respectively.[4] For fully stoichiometric compounds $RE_3MM'Ch_7$, this condition simplifies to $V_M + V_{M'} = 5$, exemplified in numerous I–IV combinations (M = Na, Cu, Ag; M' = Si, Ge, Sn),[5] as found in the eponymous structure type itself, and II–III combinations (M = alkaline-earth and divalent transition metals; M' = Al, Ga, In),[6–14] and less commonly in III–II combinations.[4,7] For nonstoichiometric compounds $RE_3M_{1-x}M'Ch_7$, charge balance is preserved through the formation of an appropriate level of M deficiencies, as in $Ce_3Al_{0.67}AlS_7$ ($0.67(3) + 3 = 5$) and $La_3Mn_{0.5}SiS_7$ ($0.5(2) + 4 = 5$).[2,15,16] Conspicuous exceptions to the requirement of charge balance are seen in Cu- and Ag-containing compounds which are electron-deficient: $RE_3CuGaCh_7$ and $RE_3Ag_{1-x}M'Ch_7$ (M' = Si, Ge, Sn).[17, 18–22]

Given their noncentrosymmetric structures, the primary application that has been envisioned for these chalcogenides is as nonlinear optical materials. Although some early investigations seemed unpromising,[23] renewed efforts have revealed strong second harmonic generation effects for $Y_3Zn_{0.5}SiS_7$, $La_3Ga_{0.5}(Ga_{0.5}Ge_{0.5})S_7$, and $La_3In_{0.5}(Ge_{0.5}In_{0.5})S_7$.[24,25] An idiosyncratic feature in many of these structures is the occurrence of pronounced anisotropic displacement of the M cations, especially in Ag-containing compounds such as $RE_3Ag_{1-x}M'Ch_7$ (M = Si, Ge, Sn; Ch = S, Se), leading to the proposal that they could also be good ionic conductors.[22,26] These large displacements are correlated with the variable distribution of the M atoms within sites of different coordination geometries (ranging from CN3 to CN6). However, without full single-crystal structure determinations, the occupations of these sites are often only left assumed.

The five related compounds $La_3Ga_{1.67}S_7$, $La_3Ag_{0.6}GaS_7$, $La_3Ag_{0.6}GaSe_7$, $La_3ZnGaSe_7$, and $La_3CdGaSe_7$ were investigated here to establish the metal site distributions and to understand the coordination preferences. Their electronic structures were examined through X-ray photoelectron spectroscopy and band structure calculations.

3.2 Experimental

3.2.1 Synthesis

Starting materials were freshly filed La pieces (99.9%, Hefa), Ag powder (99.9%, Cerac), Zn shot (99.99%, Sigma-Aldrich), Cd powder (99.95%, Alfa-Aesar), Ga shot (99.99%, Cerac), S flakes (99.998%, Sigma-Aldrich), and Se powder (99.99%, Sigma-Aldrich). With the intent to synthesize quaternary chalcogenides, mixtures of the elements were initially prepared with a loading composition of "La_3MGaCh_7" (M = Ag, Zn, Cd; Ch = S, Se) and a total mass of 0.2 g. The mixtures were pressed into pellets (6 mm diameter, 1–3 mm thickness) and loaded into fused-silica tubes which were evacuated and sealed. The tubes were heated at 950 °C for 3 d and cooled to room temperature over 2 d. The samples were analyzed by powder X-ray diffraction (XRD)

patterns collected on an Inel diffractometer equipped with a curved position-sensitive detector (CPS 120) and a Cu $K\alpha_1$ radiation source operated at 40 kV and 20 mA.

After the initial heat treatment, the Ag-containing samples with nominal compositions La$_3$AgGaCh_7 contained significant amounts of other phases, including AgGaCh_2 and possibly La$_3$Ga$_{1.67}Ch_7$. Given that structure determination (see below) suggested that these Ag-containing chalcogenides are substoichiometric with the formula La$_3$Ag$_{0.6}$GaCh_7, additional reactions were performed to prepare sulfides with loading compositions La$_3$Ag$_y$GaS$_7$ (y = 0.2–1.0 in increments of 0.2) with the same heating profile as before. The La$_3$Ag$_{0.6}$GaS$_7$ sample consisted chiefly of the quaternary chalcogenide, whereas the other samples contained significant secondary phases, implying that any degree of solid solution is limited (i.e., La$_3$Ag$_{0.6(1)}$GaS$_7$) and assumed to be similar for the corresponding selenides. Regrinding and reheating improved the homogeneity so that both La$_3$Ag$_{0.6}$GaS$_7$ and La$_3$Ag$_{0.6}$GaSe$_7$ samples were >95% pure. The powdered samples are pale yellow for La$_3$Ag$_{0.6}$GaS$_7$ and light grey for La$_3$Ag$_{0.6}$GaSe$_7$. Single crystals of these compounds were extracted from these samples and examined by energy-dispersive X-ray (EDX) analysis on a JEOL JSM-6010LA InTouchScope scanning electron microscope. They contained 25(2)–28(2)% La, 2(1)–3(1)% Ag, 10(2)–14(2)% Ga, and 57(3)–62(3)% Ch, in reasonable agreement with the expected composition of 26% La, 5% Ag, 9% Ga, and 60% Ch.

With the same heat treatment as before, substitution of the M component led to the successful preparation of the selenides La$_3$ZnGaSe$_7$ and La$_3$CdGaSe$_7$, which are fully stoichiometric as confirmed by EDX analysis of single crystals. It was difficult to obtain pure phases in the powder samples because of unavoidable volatilization losses of elemental Zn and Cd, as evidenced by their deposition at the other end of the fused-silica tubes. In hopes of obtaining larger crystals for property measurements, crystal growth was attempted in the presence of NaCl/KCl flux, but these experiments were unsuccessful. The sulfides La$_3$ZnGaS$_7$ and La$_3$CdGaS$_7$

could not be obtained under the conditions described above. Rare-earth substitutions were attempted within all six series "RE_3MGaCh_7" (RE = all feasible trivalent rare-earth metals from Ce to Lu; M = Ag, Zn, Cd; Ch = S, Se), to no avail.

A potential ambiguity is that ternary chalcogenides $La_3Ga_{1.67}Ch_7$ present as a secondary phase would be difficult to distinguish from the quaternary chalcogenides from their powder XRD patterns because they adopt the same structure type. Thus, a sample of the ternary sulfide $La_3Ga_{1.67}S_7$ was prepared by stoichiometric reaction of the elements at the same conditions as above, in anticipation of a full structure determination, which is lacking for this compound[15]. The sample was pure according to the powder XRD pattern and the EDX analysis agreed with expectations. Although the powder XRD patterns for $La_3Ga_{1.67}S_7$ and $La_3Ag_{0.6}GaS_7$ are indeed very similar, they can be distinguished by small shifts in the peaks, more visible at higher angles, between the two compounds, consistent with their slightly different cell parameters (**Figure 3–1**).
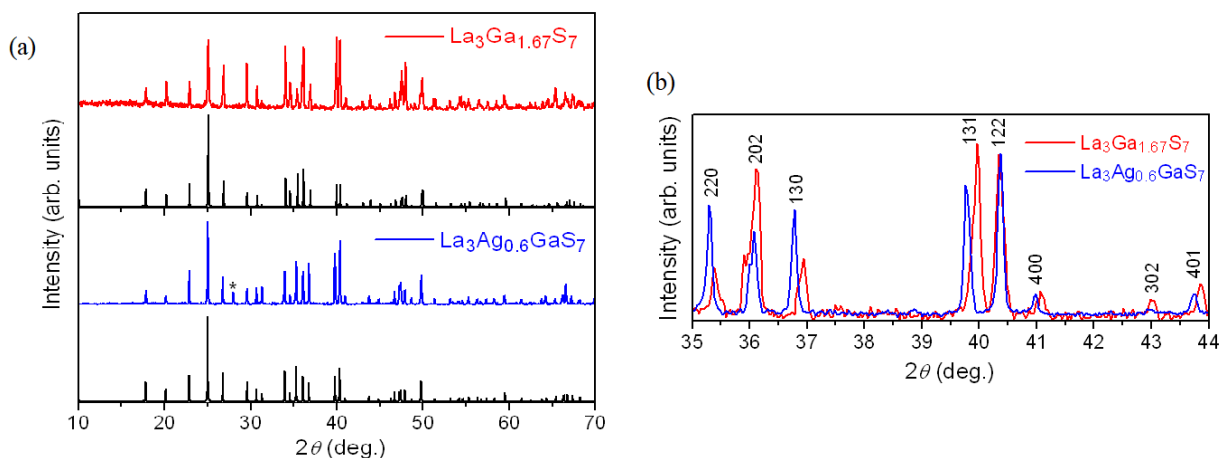
Figure 3-1. (a) Powder XRD patterns for $La_3Ga_{1.67}S_7$ and $La_3Ag_{0.6}GaS_7$. (b) Close-up showing slightly different peak positions.

3.2.2   Structure determination

Intensity data were collected for $La_3Ga_{1.67}S_7$, $La_3Ag_{0.6}GaS_7$, $La_3Ag_{0.6}GaSe_7$, $La_3ZnGaSe_7$, and $La_3CdGaSe_7$ at room temperature on a Bruker PLATFORM diffractometer equipped with a

SMART APEX II CCD area detector and a graphite-monochromated Mo $K\alpha$ radiation source, using ω scans at eight different ϕ angles with a frame width of 0.3º and an exposure time of 15 s per frame. Face-indexed numerical absorption corrections were applied. Structure solution and refinement were carried out with use of the SHELXTL (version 6.12) program package.[27] For all structures, the noncentrosymmetric hexagonal space group $P6_3$ was chosen on the basis of intensity statistics, Laue symmetry, and systematic absences. Atomic positions corresponding to the La_3CuSiS_7-type (or $Ce_3Al_{1.67}S_7$-type) structure were confirmed by direct methods. For consistency and ease of comparison, the atomic coordinates for all structures were standardized such that the M atom occupying the trigonal planar site is located at the origin with its z-coordinate set to zero along the polar c-axis. To establish the correct absolute configuration, the crystals were treated as inversion twins and a Flack parameter was refined.

For $La_3Ag_{0.6}GaS_7$ and $La_3Ag_{0.6}GaSe_7$, the Ag atoms were initially placed within a trigonal planar site at $2a$ (0, 0, ~0.00) and the Ga atoms within a tetrahedral site at $2b$ (1/3, 2/3, ~0.84). Refinements indicated that all sites were fully occupied except for the Ag sites, which were partially occupied at 0.60(1) in $La_3Ag_{0.6}GaS_7$ or 0.62(1) in $La_3Ag_{0.6}GaSe_7$. However, their displacement ellipsoids were highly elongated along the c-direction (U_{33} = 0.47(1) $Å^2$ vs. U_{11} = 0.019(1) $Å^2$ in $La_3Ag_{0.6}GaS_7$; U_{33} = 0.38(2) $Å^2$ vs. U_{11} = 0.028(2) $Å^2$ in $La_3AgGaSe_7$). These Ag sites were thus split into two – the first at 0, 0, 0 within the original trigonal planar site and the second at 0, 0, ~0.21 close to a trigonal antiprismatic site – with the constraint that their occupancies sum to 0.6 and their displacement parameters set equal. This split-site model has been commonly applied in refinements of many related La_3CuSiS_7-type structures exhibiting this feature.[22] In structures containing a large number of split sites with low occupancy and large anisotropic displacement parameters, an alternative approach that has been recommended (but not frequently implemented) is to attempt a non-harmonic refinement in which the structure factor

expression includes higher order tensors.[28] Such a refinement was carried out on the sulfide La$_3$Ag$_{0.6}$GaS$_7$ with use of the JANA2006 program package.[29] Third-order non-harmonic parameters were applied within the Gram-Charlier formalism for the temperature components, with the two different Ag positions in the harmonic refinement above modeled as one site. Harmonic and non-harmonic displacement parameters are listed in **Table A1–1** in the Appendix. Because the agreement factor, R_1 of 0.028 (for 678 observed data and 42 parameters), in the non-harmonic refinement was not an improvement over the harmonic one, we have opted to focus on the split-site model for this and the other structures presented here. Moreover, because there were no especially high correlation coefficients (>0.5) relating the displacement parameters with positional parameters of the Ag atoms, we consider the split-site model to be a satisfactory representation of the Ag atom displacements.

The structures of La$_3$ZnGaSe$_7$ and La$_3$CdGaSe$_7$ were refined in a similar manner as above, with Zn or Cd atoms initially placed within the trigonal planar site and Ga atoms within the tetrahedral site. Both types of sites were found to be fully occupied, and reversal of atom assignments within these sites led to worse agreement factors (e.g., R_1 increased from 0.046 to 0.053 in La$_3$CdGaSe$_7$). There was no evidence for disorder of Cd and Ga atoms, which can be distinguished by their X-ray scattering factors, in La$_3$CdGaSe$_7$ (e.g., the occupancies within the tetrahedral site refined to 1.00(4) Ga and 0.00(4) Cd), and this assumption was extended for the Zn and Ga atoms in La$_3$ZnGaSe$_7$. A split-site model was applied for the Zn or Cd atoms in these structures. The site preferences of these atoms are reversed in La$_3$ZnGaSe$_7$ and La$_3$CdGaSe$_7$, as discussed in detail later. The absolute configuration of the particular crystal of La$_3$CdGaSe$_7$ examined also happened to be opposite to those of the other crystals reported here; this is, of course, an aleatory outcome.

Refinement of the structure of $La_3Ga_{1.67}S_7$ proceeded without much complication. The tetrahedral Ga site was found to be fully occupied. The main point of interest is the partially occupied Ga site, which had been previously assumed, by analogy to the prototype structure ($Ce_3Al_{1.67}S_7$-type), to be located near but probably slightly displaced from the ideal trigonal antiprismatic site.[2,15] Without splitting, its occupation refined to 0.65(3), close to the expected value of 0.67. However, when a split-site model was attempted, a second site was found which is more aptly described as trigonal pyramidal rather than trigonal planar. The occupations of these split sites are close to each other: 0.32(1) in the trigonal pyramidal site and 0.35(1) in the trigonal antiprismatic site.

Crystal data and further details are listed in **Table 3–1**, positional and equivalent isotropic displacement parameters in **Table 3–2**, and interatomic distances in **Table 3–3**.

Table 3-1. Crystallographic data for $La_3Ga_{1.67}S_7$, $La_3Ag_{0.6}GaCh_7$ (Ch = S, Se), and La_3MGaSe_7 (M = Zn, Cd).

Formula	$La_3Ga_{1.67}S_7$	$La_3Ag_{0.6}GaS_7$	$La_3Ag_{0.6}GaSe_7$	$La_3ZnGaSe_7$	$La_3CdGaSe_7$
Formula mass (amu)	757.58	775.59	1103.89	1104.54	1151.57
Space group	$P6_3$ (No. 173)				
a (Å)	10.1772(8)	10.2290(8)	10.5879(17)	10.630(9)	10.606(5)
c (Å)	6.0648(5)	6.0529(5)	6.3766(10)	6.374(5)	6.380(3)
V (Å^3)	544.01(10)	548.48(10)	619.1(2)	623.7(12)	621.5(7)
Z	2				
ρ_{calcd} (g cm^{-3})	4.625	4.696	5.922	5.881	6.153
T (K)	296(2)	296(2)	296(2)	296(2)	296(2)
Crystal dimensions (mm)	0.07 × 0.07 × 0.06	0.12 × 0.09 × 0.08	0.05 × 0.04 × 0.04	0.07 × 0.04 × 0.04	0.07 × 0.04 × 0.04
μ(Mo $K\alpha$) (mm^{-1})	16.89	16.18	33.74	34.45	34.35
Transmission factors	0.383–0.533	0.306–0.444	0.275–0.453	0.229–0.406	0.222–0.391
2θ limits	4.62–66.20°	4.60–65.92°	4.44–67.05°	4.42–66.17°	4.43–66.31°
Data collected	$-15 \le h \le 15, -15 \le k$	$-15 \le h \le 15, -15 \le k \le 15, -9 \le l \le 9$	$-16 \le h \le 16, -16 \le k \le 16, -9 \le l \le 9$	$-16 \le h \le 16, -16 \le k \le 16, -9 \le l \le 9$	$-16 \le h \le 16, -16 \le k \le 16, -9 \le l \le 9$

	$\leq 15, -9 \leq l \leq 9$				
No. of data collected	7993	7971	9142	9076	9152
No. of unique data, including $F_o^2 < 0$	1385 ($R_{int} =$ 0.031)	1380 ($R_{int} =$ 0.025)	1610 ($R_{int} =$ 0.077)	1574 ($R_{int} =$ 0.066)	1587 ($R_{int} =$ 0.066)
No. of unique data, with $F_o^2 > 2\sigma(F_o^2)$	1312	1332	1263	1349	1328
No. of variables	41	41	40	40	40
Flack parameter	–0.02(3)	0.01(2)	–0.01(6)	0.01(6)	0.01(6)
$R(F)$ for $F_o^2 > 2\sigma(F_o^2)$ [a]	0.020	0.018	0.044	0.040	0.046
$R_w(F_o^2)$ [b]	0.045	0.040	0.110	0.099	0.136
Goodness of fit	1.124	1.093	1.057	1.083	1.075
$(\Delta\rho)_{max}$, $(\Delta\rho)_{min}$ (e Å^{-3})	2.76, –1.05	1.31, –1.48	2.47, –2.38	2.54, –3.24	3.34, –5.50

[a] $R(F) = \sum\|F_o| - |F_c\| / \sum|F_o|$.
[b] $R_w(F_o^2) = [\sum[w(F_o^2 - F_c^2)^2] / \sum wF_o^4]^{1/2}$; $w^{-1} = [\sigma^2(F_o^2) + (Ap)^2 + Bp]$, where $p = [\max(F_o^2,0) + 2F_c^2] / 3$.

Table 3-2. Atomic coordinates and equivalent isotropic displacement parameters (Å^2) [a] for La$_3$Ga$_{1.67}$S$_7$, La$_3$Ag$_{0.6}$GaCh$_7$ (Ch = S, Se), and La$_3$MGaSe$_7$ (M = Zn, Cd).

	La$_3$Ga$_{1.67}$S$_7$	La$_3$Ag$_{0.6}$GaS$_7$	La$_3$Ag$_{0.6}$GaSe$_7$	La$_3$ZnGaSe$_7$	La$_3$CdGaSe$_7$
La in 6c (x, y, z)					
x	0.1421(1)	0.1395(1)	0.1472(1)	0.1457(1)	0.1465(1)
y	0.3742(1)	0.3748(1)	0.3750(1)	0.3745(1)	0.3753(1)
z	0.4014(1)	0.4202(1)	0.4088(2)	0.4398(2)	0.0769(2)
U_{eq}	0.0150(1)	0.0147(1)	0.0244(2)	0.0198(2)	0.0191(2)
Ma in 2a (0, 0, z)					
Occupancy	0.319(6) Ga	0.363(3) Ag	0.460(9) Ag	0.737(12) Zn	0.179(8) Cd
z	0.101(2)	0.000(1)	0.000(2)	0.000(3)	0.001(4)
U_{eq}	0.030(1)	0.061(2)	0.080(4)	0.086(4)	0.045(1)
Mb in 2a (0, 0, z)					
Occupancy	0.348(6) Ga	0.237(3) Ag	0.140(9) Ag	0.263(12) Zn	0.821(8) Cd
z	0.215(2)	0.210(1)	0.205(8)	0.209(8)	0.307(1)
U_{eq}	0.030(1)	0.061(2)	0.080(4)	0.086(4)	0.045(1)
Ga in 2b (1/3, 2/3, z)					
z	0.8212(2)	0.8396(2)	0.8240(4)	0.8546(4)	0.6621(5)
U_{eq}	0.0138(2)	0.0116(2)	0.0197(5)	0.0180(5)	0.0173(6)
Ch1 in 6c (x, y, z)					
x	0.2372(2)	0.2440(2)	0.2520(2)	0.2512(2)	0.2537(2)

y	0.1458(2)	0.1517(2)	0.1512(2)	0.1520(2)	0.1528(2)
z	0.4392(3)	0.4509(3)	0.4457(3)	0.4722(3)	0.0401(3)
U_{eq}	0.0254(4)	0.0296(4)	0.0348(4)	0.0275(4)	0.0225(4)
*Ch*2 in 6*c* (*x*, *y*, *z*)					
x	0.5190(2)	0.5184(1)	0.5201(2)	0.5194(1)	0.5198(2)
y	0.0975(2)	0.0990(1)	0.0930(2)	0.0932(1)	0.0934(2)
z	0.1747(2)	0.1914(2)	0.1784(2)	0.2085(2)	0.3084(3)
U_{eq}	0.0148(2)	0.0134(2)	0.0212(3)	0.0185(3)	0.0176(3)
*Ch*3 in 2*b* (1/3, 2/3, *z*)					
z	0.1884(4)	0.2085(3)	0.1940(4)	0.2261(4)	0.2914(5)
U_{eq}	0.0128(4)	0.0117(3)	0.0211(5)	0.0183(4)	0.0173(5)

[a] U_{eq} is defined as one-third of the trace of the orthogonalized U_{ij} tensor.

Table 3-3. Selected interatomic distances (Å) in La$_3$Ga$_{1.67}$S$_7$, La$_3$Ag$_{0.6}$GaCh$_7$ (*Ch* = S, Se), and La$_3$*M*GaSe$_7$ (*M* = Zn, Cd).

	La₃Ga₁.₆₇S₇	**La₃Ag₀.₆GaS₇**	**La₃Ag₀.₆GaSe₇**	**La₃ZnGaSe₇**	**La₃CdGaSe₇**
La–*Ch*2	2.867(1)	2.860(1)	2.980(2)	2.986(2)	2.977(2)
La–*Ch*3	2.919(1)	2.927(1)	3.035(2)	3.047(3)	3.037(2)
La–*Ch*1	2.914(1)	2.941(1)	3.049(2)	3.059(3)	3.060(2)
La–*Ch*1	2.940(1)	2.970(1)	3.087(2)	3.090(3)	3.099(2)
La–*Ch*2	2.969(2)	2.973(1)	3.090(2)	3.099(3)	3.090(2)
La–*Ch*1	3.058(2)	3.073(2)	3.165(2)	3.193(3)	3.163(3)
La–*Ch*2	3.040(2)	3.032(1)	3.214(2)	3.213(3)	3.213(2)
La–*Ch*1	3.483(2)	3.420(2)	3.608(2)	3.582(3)	3.606(3)
Ma–*Ch*1 (×3)	2.326(4)	2.203(2)	2.352(3)	2.337(3)	2.360(3)
Mb–*Ch*1 (×3)	2.510(5)	2.626(5)	2.79(3)	2.78(3)	2.778(4)
Mb–*Ch*1 (×3)	2.690(6)	2.686(5)	2.85(3)	2.87(3)	2.900(4)
Ga–*Ch*3	2.227(3)	2.233(2)	2.359(4)	2.368(4)	2.365(5)
Ga–*Ch*2 (×3)	2.281(2)	2.284(1)	2.408(2)	2.416(2)	2.411(2)

73

3.2.3 XPS analysis

XPS spectra for $La_3Ag_{0.6}GaS_7$ were measured on a Kratos AXIS 165 spectrometer equipped with a monochromatic Al $K\alpha$ X-ray source (12 kV, 12 mA) and a hybrid lens with a spot size of $700 \times 400\ \mu m^2$. The air-stable samples were finely ground, loaded onto double-sided tape, mounted on a sample bar, and transferred into the analysis chamber via a load lock. The pressure inside the XPS instrument was maintained between 10^{-7} and 10^{-9} Pa. Samples were sputter-cleaned with an Ar^+ ion beam (4 kV, 10 mA) until no further changes were observed in the peak shoulders associated with surface oxides, which could not be completely removed. Core-line binding energies (BE) were, within standard uncertainties, the same before and after the sputtering procedure. The survey spectrum (collected in the range of 0–1100 eV with pass energy of 80 eV, step size of 0.4 eV, and dwell time of 100 ms) revealed the presence of all expected elements. However, all Ga core-lines overlapped with those of other elements, precluding the determination of exact composition. A qualitative examination indicated that of the three remaining components, S was most abundant, followed by La, then Ag, as expected. High-resolution spectra (collected with pass energy of 20 eV, step size of 0.05 eV, and dwell time of 200 ms) were measured in the appropriate BE ranges as determined from the survey scan for the Ag 3d and S 2p core lines. Charge neutralization was applied to all samples in varying degrees, with the best settings chosen (charge balance of 1.8–3.6 V, filament current of 1.6–2.0 A) to give the most intense and sharpest peaks. The spectra were calibrated to the C 1s line at 284.8 eV arising from adventitious carbon and were analyzed with use of the CasaXPS software package.[30] The background arising from energy loss was removed by applying a Shirley-type function and the peaks were fitted to pseudo-Voigt (70% Gaussian and 30% Lorentzian) line profiles to take into account spectrometer and

lifetime broadening effects. On the basis of many previous measurements made on this instrument, we estimate a precision of better than ±0.1 eV in the BEs.

3.2.4   Band structure calculations

Tight-binding linear muffin tin orbital band structure calculations were performed on within the local density and atomic spheres approximation with use of the Stuttgart TB-LMTO-ASA program (version 4.7).[31] Models for the five compounds examined with the ideal, fully stoichiometric formulas La_3MGaCh_7 were considered in which the M atoms were placed entirely within the more highly occupied site as determined from the split-site crystal structure refinements. The basis sets consisted of La 6s/(6p)/4d/(4f), Zn 4s/4p/3d, Ag/Cd 5s/5p/4d/(4f), Ga 4s/4p/(4d), S 3s/3p/(3d), and Se 4s/4p/(4d) orbitals, with the ones indicated in parentheses being downfolded. Integrations in reciprocal space were carried out with an improved tetrahedron method over 208 irreducible k points within the first Brillouin zone.

3.3   Results and discussion

The four quaternary chalcogenides $La_3Ag_{0.6}GaS_7$, $La_3Ag_{0.6}GaSe_7$, $La_3ZnGaSe_7$, and $La_3CdGaSe_7$ have been prepared by reaction of the elements at 950 °C. $La_3Ag_{0.6}GaS_7$ and $La_3Ag_{0.6}GaSe_7$ extend the series of rare-earth chalcogenides $RE_3M_{1-x}M'Ch_7$ containing I–III combinations of the M and M' components, which were previously limited to $RE_3CuGaCh_7$.[17] $La_3ZnGaSe_7$ and $La_3CdGaSe_7$ are new examples containing II–III combinations, which were also few.[6–14] Whereas Al-containing chalcogenides RE_3MAlCh_7 were known for a wide variety of divalent M components,[6] Ga-containing ones were previously found only in the series RE_3MGaCh_7 (M = Mn, Fe)[7,12] and In-containing ones RE_3MInS_7 (M = Fe, Co, Ni) were recently identified.[13]

Because ternary chalcogenides $La_3Ga_{1.67}Ch_7$ were a potential secondary phase in the reactions, the sulfide $La_3Ga_{1.67}S_7$ was also prepared to serve as a frame of reference.

The basic framework of the hexagonal La_3CuSiS_7-type structures of these compounds can be defined by two types of one-dimensional arrangements, extending parallel to the polar c-axis, of coordination polyhedra formed by the Ch atoms; the RE atoms lie in the intervening spaces between these chains (**Figure 3–2**). The first type of arrangement consists of isolated tetrahedra, each with three $Ch2$ atoms at the base and a $Ch3$ atom at the apex, which are centred by Ga atoms and which stack so that all point in the same direction. These Ga-centred tetrahedra are common to all five compounds presented here and are nearly invariant: the Ga–S distances are 2.23–2.28 Å in the sulfides $La_3Ga_{1.67}S_7$ and $La_3Ag_{0.6}GaS_7$, and similarly the Ga–Se distances are 2.36–2.42 Å in the selenides $La_3Ag_{0.6}GaSe_7$, $La_3ZnGaSe_7$, and $La_3CdGaSe_7$. The geometrical requirements imposed by these tetrahedra fix the value of the c-parameter, which is essentially constant at 6.05–6.06 Å for the sulfides and 6.37–6.38 Å for the selenides (in agreement with expected values of 6.05±0.05 Å and 6.38±0.05 Å, respectively, as found in RE_3CuGaS_7 and $RE_3CuGaSe_7$)[17]. The second type of arrangement consists of trigonal antiprisms, each formed by six $Ch1$ atoms, which share opposite faces to form columns colinear with the c-axis. (These trigonal antiprisms can be equally well regarded as octahedra that are compressed along the 6_3-axis which lies along c.) The filling of these trigonal antiprisms by the M atoms (where M = Ga, Ag, Zn, Cd) is highly variable as they can be displaced to multiple positions along the axis, ranging from the ideal centre of the trigonal antiprism (CN6) to coplanar with the triangular face (CN3).
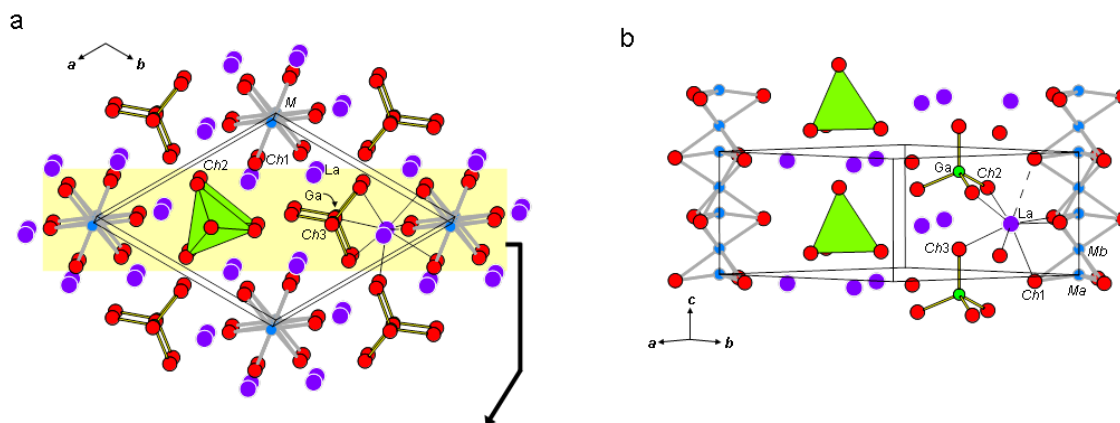
Figure 3-2. (a) Structure of La$_3M_{1-x}$GaCh_7 (M = Ag, Zn, Cd, Ga), viewed down the c-direction, with coordinates of La$_3$Ag$_{0.6}$GaS$_7$ used in this drawing. (b) A slice of the structure parallel to (110) showing stacks of tetrahedra centred by Ga atoms and stacks of trigonal antiprisms partially occupied by M atoms in approximately trigonal planar and trigonal antiprismatic sites.

The variable location of the M site is reflected by their large displacement parameters, which are highly elongated along c. To illustrate the pathological nature of these displacements, the difference electron density map of La$_3$Ag$_{0.6}$GaS$_7$, after refinement of a model excluding the Ag atoms, shows a continuum of electron density extending along the channels within the confacial columns of trigonal antiprisms (**Figure 3–3**).

Although this feature has been previously noted to be especially pronounced in Ag-containing compounds with the La$_3$CuSiS$_7$-type structure,[18–22] this may be a more general phenomenon than recognized. A simplified model consisting of two closely spaced split sites with equal displacement parameters – Ma with nearly trigonal planar geometry and Mb with nearly trigonal antiprismatic geometry – was invoked for the five chalcogenides examined here (**Figure 3–4**).
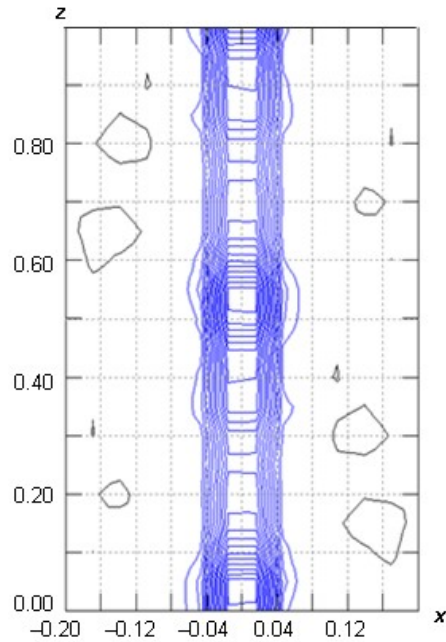
Figure 3-3. Difference electron density map after refinement of model in $La_3Ag_{0.6}GaS_7$ with Ag atoms excluded. The section is parallel to (010) and shows a nearly continuous distribution of electron density within a channel along the c-axis.
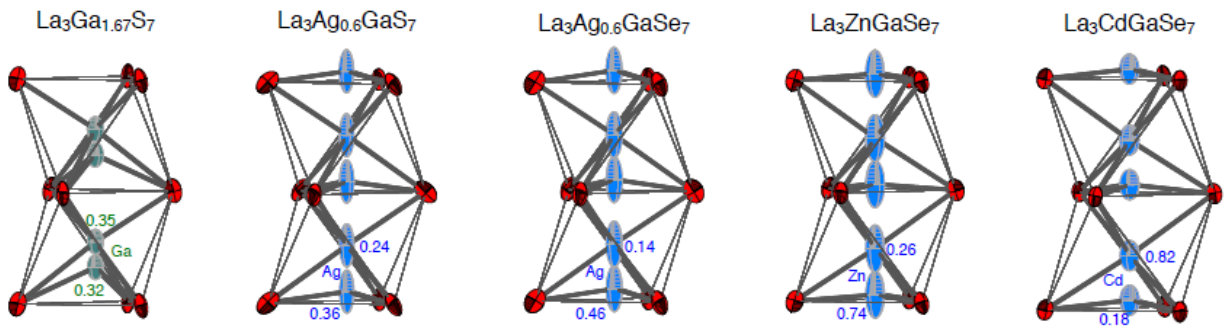
Figure 3-4. Occupation of M atoms in $La_3M_{1-x}GaCh_7$ (M = Ag, Zn, Cd, Ga) within columns of confacial trigonal antiprisms of Ch atoms. The displacement ellipsoids are drawn at the 50% probability level.

A classification scheme of $RE_3M_{1-x}M'Ch_7$ structures into three groups has been proposed depending on the occupation of the M site in (1) only the trigonal planar site, (2) both trigonal planar and trigonal antiprismatic sites, and (3) only the trigonal antiprismatic site.[22] According to this scheme, the title compounds belong to the second group. Within the split-site model, the occupancies of the trigonal planar vs. trigonal antiprismatic sites are 0.36 vs. 0.24 in $La_3Ag_{0.6}GaS_7$ and 0.46 vs. 0.14 in $La_3Ag_{0.6}GaSe_7$, suggesting a preference of Ag atoms for the trigonal planar site which is consistent with what is found in other Ag-containing chalcogenides.[18–22] However, given that the electron density is really continuous within the channel and that the occupancies of closely spaced split sites with such large displacements can be correlated, this interpretation should perhaps be accepted cautiously. The comparison between the selenides $La_3ZnGaSe_7$ and $La_3CdGaSe_7$ is interesting. The Al-containing sulfides RE_3ZnAlS_7 and RE_3CdAlS_7 were previously assumed, without direct confirmation, to contain Zn and Cd atoms in trigonal antiprismatic sites, by analogy to RE_3MnAlS_7 and other RE_3MAlS_7 compounds containing divalent M components[6]. However, the results here reveal that both types of sites can be occupied, with a marked preference for Zn in the trigonal planar site (occupancy of 0.74) in $La_3ZnGaSe_7$ in contrast to a preference for Cd in the trigonal antiprismatic site (occupancy of 0.82) in $La_3CdGaSe_7$. Finally, even the ternary sulfide $La_3Ga_{1.67}S_7$ exhibits significant displacement of Ga atoms which can be modeled as almost equal occupation of slightly off-centred (occupancy of 0.32) and nearly ideal trigonal antiprismatic sites (occupancy of 0.35), the former perhaps more appropriately described as trigonal pyramidal.

The trigonal planar and trigonal antiprismatic sites are too close to each other (about ¼ of the c-repeat, corresponding to 1.5 Å for the sulfides and 1.6 Å for the selenides, which would be unphysical bond distances) for both to be simultaneously occupied. Thus, on a local level, the

occupation of one of these sites affects the location of neighbouring M atoms along the channel, which can be interpreted as motion of ions, as has been proposed for many Ag-containing chalcogenides $RE_3Ag_{1-x}M'Ch_7$ (M = Si, Ge, Sn) and related to the low energy barriers to motion between these sites.[22]

To seek an understanding of the different site occupations of the M atoms in these compounds, bond valence sums[32] were evaluated (**Table 3–4**). In agreement with expected values, the bond valence sums are 2.8–3.1 for the La atoms, 3.0–3.1 for the Ga atoms, and 1.8–2.2 for the Ch atoms. However, significant deviations are observed for the M atoms depending on which site – trigonal planar (Ma, CN3) vs. trigonal antiprismatic (Mb, CN6) – is occupied. A stark contrast is seen in the selenides $La_3ZnGaSe_7$ and $La_3CdGaSe_7$, which contain divalent M atoms.

Table 3-4. Bond valence sums for $La_3Ga_{1.67}S_7$, $La_3Ag_{0.6}GaCh_7$ (Ch = S, Se), and La_3MGaSe_7 (M = Zn, Cd).

	La₃Ga₁.₆₇S₇	**La₃Ag₀.₆GaS₇**	**La₃Ag₀.₆GaSe₇**	**La₃ZnGaSe₇**	**La₃CdGaSe₇**
La	3.11	3.05	2.88	2.81	2.86
Ma	2.34	2.60	2.34	2.19	3.34
Mb	1.93	1.53	1.32	1.18	1.86
Ga	3.08	3.05	3.09	3.02	3.06
Ch1	1.82	2.01	1.94	1.85	1.92
Ch2	2.03	2.04	1.94	1.90	1.93
Ch3	2.23	2.22	2.21	2.14	2.18

In $La_3ZnGaSe_7$, occupation of Zn atoms in the Ma site allows reasonable but slightly short Zn–Se bonds (2.337(3) Å) to form so that an appropriate bond valence sum of 2.2 is attained, whereas occupation in the Mb site leads to rather long Zn–Se bonds (2.510(5)–2.690(6) Å) so that the Zn atoms are underbonded to give a low bond valence sum of 1.2. Conversely, in $La_3CdGaSe_7$, occupation of Cd atoms in the Ma site leads to rather short Cd–Se bonds (2.360(3) Å) so that they are overbonded with a bond valence sum of 3.3, whereas occupation in the Mb site gives longer

Cd–Se bonds (2.778(4)–2.900(4) Å) to lower the bond valence sum to 1.9. (For comparison, typical Zn–Se bond lengths are 2.3–2.6 Å and typical Cd–Se bond lengths are 2.4–2.8 Å.[1]) Although both CN3 and CN6 are possible coordinations for Zn-triad elements, CN6 is usually preferred by Cd. In the Ag-containing compounds $La_3Ag_{0.6}GaS_7$ and $La_3Ag_{0.6}GaSe_7$, occupation of monovalent Ag atoms in either site results in overbonding, though it is more severe in *Ma* than in *Mb*, corresponding to bond valence sums of 2.3–2.6 and 1.3–1.5, respectively. The Ag–*Ch* distances in these compounds are similar to literature values for Ag–S (2.2–3.0 Å) and Ag–Se bonds (2.3–3.1 Å), which fall in extremely broad ranges, as is found in the well-known superionic conductors Ag_2S and Ag_2Se.[1, 33] In the ternary sulfide $La_3Ga_{1.67}S_7$, occupation of trivalent Ga atoms in *Ma* (no longer trigonal planar but rather trigonal pyramidal with CN3+3) or *Mb* sites leads to underbonding, with bond valence sums of 2.3 and 1.9, respectively. This observation seems puzzling, because an obvious solution to this underbonding problem is for the Ga atoms to shorten their distances to the surrounding S atoms by approaching the ideal, flat trigonal planar site.

An extension of the bond valence sum argument provides valuable insight. When *M* atoms are displaced within the channel, the surrounding *Ch*1 atoms are also affected. Thus, the bond valence sums of both the *M* and *Ch*1 atoms are correlated. Model structures were considered in which one *M* atom is displaced from 0 to 0.5 in increments of 0.1 (in fractional coordinates) along *z*, with the *Ch*1 atoms located at $z = 0$ to simplify the interpretation. We then evaluated bond valences (up to a cutoff of 4.0 Å for *M*–*Ch*1 distances, beyond which the values are insignificant at <0.01) and tracked how the bond valence sums vary as the *M* atom is shifted from the ideal trigonal planar site ($z = 0$) to the ideal trigonal antiprismatic site ($z = 0.25$) and then to the next ideal trigonal planar site ($z = 0.50$) along the channel. (At $z = 0$, there are three short and six very

long M–$Ch1$ distances, giving effectively CN3; at $z = 0.25$, there are six equidistant M–$Ch1$ distances, giving CN6; at intermediate values of z, there are three shorter and three longer M–$Ch1$ distances, giving an asymmetric environment with CN3+3.) The bond valence sums for the M and $Ch1$ atoms are plotted as a function of z for all five compounds (**Figure 3–5**).
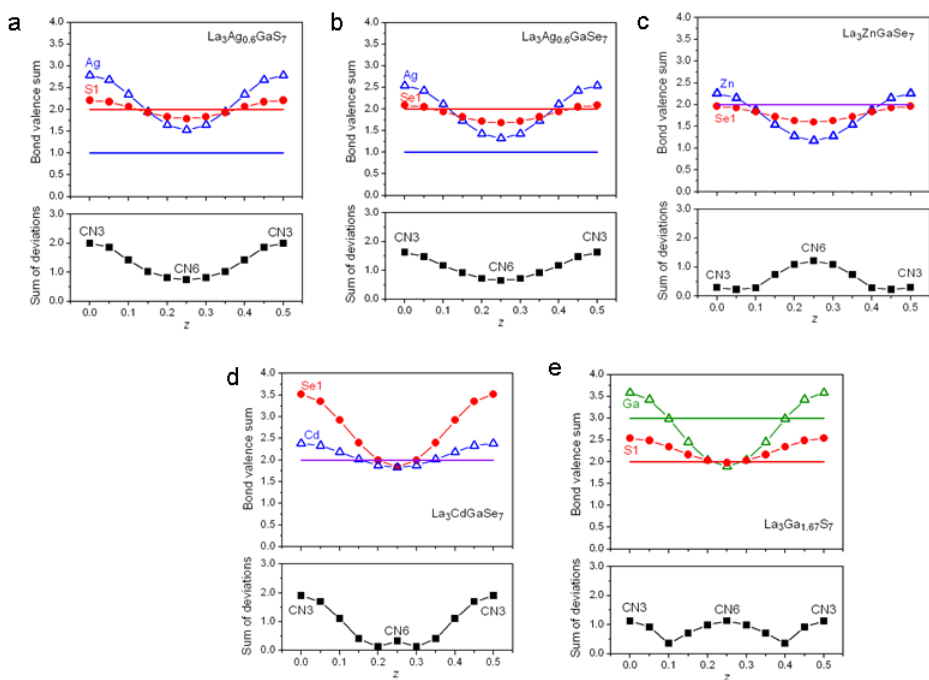
Figure 3-5. Bond valence sums (top panel) and deviations of these sums from their expected values (bottom panel) for M and $Ch1$ atoms, as the M atom is shifted along the channel enclosed by the $Ch1$ atoms in (a) $La_3Ag_{0.6}GaS_7$, (b) $La_3Ag_{0.6}GaSe_7$, (c) $La_3ZnGaSe_7$, (d) $La_3CdGaSe_7$, and (e) $La_3Ga_{1.67}S_7$.

To provide a frame of reference, these sums should be compared with the expected values, shown as horizontal lines (1 for monovalent Ag, 2 for divalent Zn and Cd, 3 for trivalent Ga, and 2 for divalent S or Se). That is, an atom is overbonded if its bond valence sum lies above these lines, or underbonded if it lies below. Furthermore, the combined deviations (in absolute values) of the bond valence sums for the M and $Ch1$ atoms from their expected values are plotted. The

contrast in coordination preferences between $La_3ZnGaSe_7$ and $La_3CdGaSe_7$ is reinforced even more clearly. The *M* atoms prefer the trigonal planar site in $La_3ZnGaSe_7$ and the trigonal antiprismatic site in $La_3CdGaSe_7$ because the bond valence sums for both *M* and Se1 atoms are best satisfied under these circumstances and the deviations of these bond valence sums from their expected values are close to zero. Moreover, in $La_3CdGaSe_7$, straying away from the trigonal antiprismatic site leads to severe overbonding of the Se1 atoms. In $La_3Ag_{0.6}GaS_7$ and $La_3Ag_{0.6}GaSe_7$, the Ag atoms are always overbonded no matter where they are located whereas the S or Se atoms remain well-behaved. This inability to satisfy the bonding requirements is a possible explanation for the especially large displacements experienced by the Ag atoms. The preferred site for the Ag atoms is predicted to be the trigonal antiprismatic one, which disagrees with observation; this discrepancy could be attributed to oversimplifications in this model, which neglects longer-range bonding interactions, or to the unreliability of occupancy refinements of split sites to mimic continuous electron density, as discussed earlier. Lastly, in $La_3Ga_{1.67}S_7$, the deviations of bond valence sums are minimized when Ga atoms are located in an intermediate position, in agreement with the observed off-centred coordination (CN3+3).

As in most other $RE_3M_{1-x}M'Ch_7$ compounds, charge balance is attained in $La_3ZnGaSe_7$, $La_3CdGaSe_7$, and $La_3Ga_{1.67}S_7$, with all atoms exhibiting their normal valences. However, $La_3Ag_{0.6}GaS_7$ and $La_3Ag_{0.6}GaSe_7$ are electron-deficient, even more so than $RE_3CuGaCh_7$ because of the occurrence of Ag deficiencies, as implied by the formula $(La^{3+})_3(Ag^{1+})_{0.6}(Ga^{3+})(Ch^{2-})_7$, which is not charge-balanced. Proposals invoking the presence of more highly oxidized Ag species (like Ag^{2+} or Ag^{3+}) to recover charge balance are simply untenable in a sulfide or selenide. To rule out such species, XPS spectra were collected on $La_3Ag_{0.6}GaS_7$ (**Figure 3–6**).
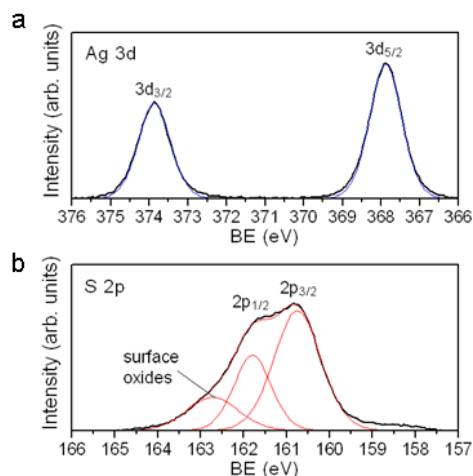
Figure 3-6. (a) Ag 3d and (b) S 2p XPS sepctra for $La_3Ag_{0.6}GaS_7$.

The Ag 3d spectrum consists of two spin-orbit-split $3d_{5/2}$ and $3d_{3/2}$ peaks at BEs of 367.9 and 373.9 eV, respectively, with widths (FWHM) of 1.0 eV and in the expected intensity ratio of 3:2. Similar to Cu spectra, Ag 3d spectra are difficult to interpret because they experience severe final-state effects[34,35]. The Ag $3d_{5/2}$ core-line peak is estimated to have a BE of 368.2±0.1 eV in the elemental metal, but contrary to normal expectations, it is found at similar or even lower BEs in compounds containing monovalent (or higher-valent) Ag species (e.g., 367.9(3) eV in Ag_2O, 367.6(4) eV in AgO).[36] In $La_3Ag_{0.6}GaS_7$, the measured BE of 367.9 eV for the Ag $3d_{5/2}$ peak falls within the range found for most other monovalent Ag compounds (367.7–368.4 eV, with an average of 368.0 eV);[36] it is slightly lower relative to the binary sulfide Ag_2S (368.0–368.2 eV)[34] and the ternary arsenide $BaAg_2As_2$ (368.3 eV)[36]. The small negative shift suggests an increased shielding of the core electrons, perhaps reflecting the continuum of electron density in the Ag channels described earlier. The S 2p spectra are well-behaved and straightforward to interpret. The S $2p_{3/2}$ peak in $La_3Ag_{0.6}GaS_7$ is shifted to a significantly lower BE (160.8 eV) relative to elemental sulfur (163.8 eV), confirming that the S atoms are anionic. It is similar to those found

in other binary transition-metal sulfides (e.g., 160.8–161.4 eV in FeS) or related quaternary sulfides (e.g., 161.2–161.3 eV in La$_3$MInS$_7$ (M = Fe, Co, Ni)). [36, 13]

The electronic band structures were evaluated for models of all five compounds adopting idealized, fully stoichiometric structures with M atoms occupying the trigonal planar site (in La$_3$AgGaS$_7$, La$_3$AgGaSe$_7$, and La$_3$ZnGaSe$_7$) or the trigonal antiprismatic site (in La$_3$CdGaSe$_7$ and La$_3$Ga$_2$S$_7$), as shown in density of states (DOS) and crystal orbital Hamilton population (COHP) curves (**Figure 3–7**).
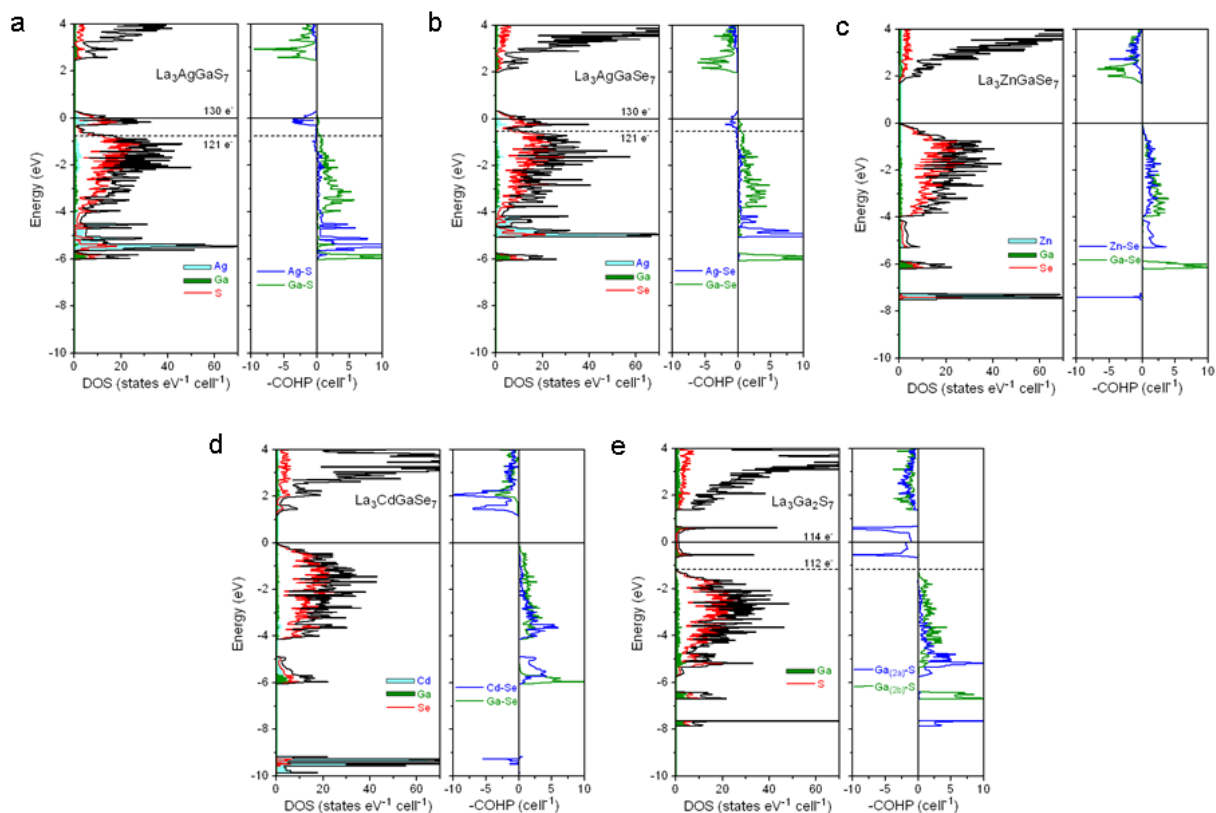
Figure 3-7. Density of states (DOS) and crystal orbital Hamilton population (–COHP) curves for (a) La$_3$AgGaS$_7$, (b) La$_3$AgGaSe$_7$, (c) La$_3$ZnGaSe$_7$, (d) La$_3$CdGaSe$_7$, and (e) La$_3$Ga$_2$S$_7$ with hypothetical fully stoichiometric and ordered structures.

Bond strengths for La–Ch, M–Ch, and Ga–Ch interactions can be gauged by their integrated COHP (–ICOHP) values (**Table 3–5**). In general, the DOS curves for all models consist of a filled valence band derived largely from Ch-based orbitals (mixed with M and Ga orbitals) separated from an empty conduction band derived largely from La-based orbitals. The Ga–Ch bonds within the Ga-centred tetrahedra common to all compounds result from overlap between Ch p orbitals with Ga s- and p-orbitals, corresponding to the narrow spike near –6 eV and the wide manifold extending up to the Fermi level, respectively. With all bonding and no antibonding levels filled, these bonds are optimized and strong (with –ICOHP values of 2.5–2.9 eV/bond), and they provide the dominant contribution (40–46%) to the covalent bonding energy of the structure.

Table 3-5. Integrated crystal orbital Hamilton populations for $La_3Ga_{1.67}S_7$, $La_3Ag_{0.6}GaCh_7$ (Ch = S, Se), and La_3MGaSe_7 (M = Zn, Cd).

	La–Ch			M–Ch			Ga–Ch		
	eV/bond	eV/cell	%	eV/bond	eV/cell	%	eV/bond	eV/cell	%
$La_3Ga_{1.67}S_7$	0.70	5.57	20.9	1.74	10.43	39.2	2.66	10.62	39.9
$La_3Ag_{0.6}GaS_7$	0.70	5.63	21.8	2.90	8.71	33.6	2.89	11.55	44.6
$La_3Ag_{0.6}GaSe_7$	0.74	5.88	25.4	2.30	6.90	29.8	2.59	10.37	44.8
$La_3ZnGaSe_7$	0.73	5.82	24.9	2.25	6.76	28.9	2.70	10.80	46.2
$La_3CdGaSe_7$	0.68	5.48	23.4	1.35	8.10	34.6	2.46	9.83	42.0

The identity of the M component leads to interesting differences in the band structures. In $La_3ZnGaSe_7$ and $La_3CdGaSe_7$, all components attain filled-shell configurations as implied by the electron-precise formulations $(La^{3+})_3(M^{2+})(Ga^{3+})(Se^{2-})_7$ of these compounds, leading to the occurrence of band gaps of 1.67 eV and 1.12 eV, respectively, at the Fermi level. Most of the Zn–Se or Cd–Se bonding originates from overlap between Zn or Cd s/p orbitals with Se p orbitals.

The Zn–Se bonds are stronger (–ICOHP of 2.2 eV/bond) than the Cd–Se bonds (–ICOHP of 1.4 eV/bond), but when scaled by the coordination numbers (CN3 around Zn vs. CN6 around Cd), both types of bonds contribute roughly the same contribution (29–34%) to bonding energy in the overall structure. The extremely narrow spikes in the DOS (at –7.6 eV and –9.5 eV, respectively, in $La_3ZnGaSe_7$ and $La_3CdGaSe_7$) are derived nearly entirely of Zn or Cd d-orbitals, which are highly localized and contribute little to bonding. In contrast, Ag d-orbitals participate significantly in bonding with chalcogen p-orbitals in La_3AgGaS_7 and $La_3AgGaSe_7$. Under normal circumstances, overlap to metal d-orbitals is less effective than to s- or p-orbitals. Because the distances from Ag atoms to the surrounding chalcogen atoms are rather short in these compounds, this overlap now becomes important. The splitting between bonding and antibonding Ag–*Ch* levels resulting from this overlap with Ag d-orbitals is small, to the extent that the antibonding levels are actually found near the Fermi level, as clearly seen in the –COHP curves. (Antibonding Ag–*Ch* levels involving Ag s- and p-orbitals are found much higher in energy, starting at +3 eV.) On proceeding from the fully stoichiometric formulas to the observed substoichiometric ones, $La_3Ag_{0.6}GaS_7$ and $La_3Ag_{0.6}GaSe_7$, the electron count is lowered from 130 e^- to 121.2 e^- in the unit cell. The Ag–*Ch* antibonding levels can then depopulated by lowering the Fermi level slightly to a pseudogap near –0.5 eV, without adversely affecting Ga–*Ch* bonding. In other words, the problem of severe "overbonding" experienced by the Ag atoms in the bond valence sum argument described earlier is overcome by the introduction of Ag deficiencies. This analysis provides a satisfying explanation for why the fully stoichiometric models La_3AgGaS_7 and $La_3AgGaSe_7$, which are already electron-deficient, would undergo even further depletion of electrons. Similarly, we propose that this explanation can be extended for other $RE_3Ag_{1-x}M'Ch_7$ (M' = Si, Ge, Sn) compounds which also suffer from problems of overbonding to the Ag atoms. [18–22] The specific

level of Ag substoichiometry experimentally observed (typically with $x = 0.1–0.5$) then results from the competition between avoiding Ag–Ch antibonding and maintaining good M'–Ch bonding character, which will depend on a case-by-case basis on the detailed structures and combinations of elements. For example, the degree of Ag deficiency tends to be enhanced upon substitution with smaller RE components in other $RE_3Ag_{1-x}M'Ch_7$ (M' = Si, Ge, Sn) series, consistent with the more severe steric problems that would be entailed when the crystal structure becomes more contracted. For comparison, the previously reported Cu-containing analogues $RE_3CuGaCh_7$ do not exhibit substoichiometry because the Cu atoms do not experience the same degree of overbonding as in the Ag-containing compounds.[17] Of course, the introduction of Ag vacancies and the ensuing disorder will modify the band structure significantly. Notwithstanding the location of the Fermi level within finite DOS in the hypothetical stoichiometric or substoichiometric model of the Ag-containing compounds, the pale yellow colour observed in $La_3Ag_{0.6}GaS_7$ implies a large band gap.

The band structure of hypothetically fully stoichiometric $La_3Ga_2S_7$ is a superposition of bands involving interaction of S-based states with those of the tetrahedrally coordinated Ga atom (labeled Ga_{2b} to indicate its Wyckoff site) and of the Ga atom placed near the trigonal antiprismatic site within the channels (labeled Ga_{2a}) in this model. The prominent feature in the DOS curve is a band (from –0.7 to +0.7 eV) that has strongly Ga_{2a}–S antibonding character. Clearly, filling of this band can be avoided by lowering the electron count from 114 e⁻ to 112 e⁻, achieved by introducing defects in the Ga sites within the channels and bringing the fully stoichiometric formula $La_3Ga_2S_7$ to the electron-precise one $La_3Ga_{1.67}S_7$, which now has a band gap of 0.50 eV.

3.4 Conclusions

Large displacements of the metal atom M are inherent in many $RE_3M_{1-x}M'Ch_7$ compounds, and as demonstrated by the results presented here, they have to be evaluated on a case-by-case basis through careful single-crystal X-ray diffraction experiments. Given that only cell parameters have been reported for many of these compounds, assumptions about the site occupations of the M atoms may be completely unwarranted, as shown in the ternary sulfide $La_3Ga_{1.67}S_7$. Even in presumably well-behaved compounds, such as $La_3ZnGaSe_7$ and $La_3CdGaSe_7$, where preferred coordination geometries may be strongly dictated by the M atom, there is the possibility for partial occupancy of more than one site. There is growing recognition that the $RE_3M_{1-x}M'Ch_7$ compounds represent not a single structure, as could be misleadingly inferred by the name of the structure type (La_3CuSiS_7-type), but rather as a family of "quasi-isostructural" compounds.[22] We have offered here a simple explanation for why such displacements occur in the form of a bond valence sum argument in which both M and Ch atoms strive to achieve optimum bonding environments. These displacements become especially severe if good M–Ch bonding cannot be attained, as seen in $La_3Ag_{0.6}GaS_7$ and $La_3Ag_{0.6}GaSe_7$, in which Ag–Ch antibonding interactions can only be relieved through removal of Ag atoms. These deficient Ag-containing compounds are the most electron-deficient examples, even more so than the Cu-containing analogues $RE_3CuGaCh_7$, ever observed in the versatile $RE_3M_{1-x}M'Ch_7$ series. Efforts are underway to improve the yields of these compounds and to grow larger crystals for optical property measurement

3.5 References

[1]   Villars, P.; Cenzual, K. Pearson's Crystal Data – Crystal Structure Database for Inorganic Compounds (on DVD), Release 2015/16, ASM International, Materials Park, OH, USA.

[2]   de Saint-Giniez, D.; Laruelle, P.; Flahaut, J. *C. R. Acad. Sci., Ser. C* **1968**, *267*, 1029–1032.

[3]   Collin, G.; Laruelle, P. *Bull. Soc. Fr. Mineral. Cristallogr.* **1971**, *94*, 175–176.

[4]   Collin, G.; Étienne, J.; Flahaut, J.; Guittard, M.; Laruelle, P. *Rev. Chim. Miner.* **1973**, *10*, 225–238.

[5]   Choudhury, A.; Dorhout, P. K. *Inorg. Chem.* **2015**, *54*, 1055–1065 and references therein.

[6]   Collin, G.; Flahaut, J. *C. R. Acad. Sci., Ser. C* **1970**, *270*, 488–490.

[7]   Collin, G.; Flahaut, J. *Bull. Soc. Chim. Fr.* **1972**, 2207–2209.

[8]   Rodier, N.; Guittard, M.; Flahaut, J. *C. R. Acad. Sci., Ser. 2* **1983**, *296,* 65–70.

[9]   Nanjundaswamy, K. S.; Gopalakrishnan, J. *J. Solid State Chem.* **1983**, *49*, 51–58.

[10]   Van Calcar, P. M.; Dorhout, P. K. *Mater. Sci. Forum* **1999**, *315*, 322–330.

[11]   Wu, L. -B.; Huang, F. -Q. *Z. Kristallogr. – New Cryst. Struct.* **2005**, *220*, 305–306.

[12]   Yin, W.; Wang, W.; Kang, L.; Lin, Z.; Feng, K.; Shi, Y.; Hao, W.; Yao, J. L.; Wu Y. *J. Solid State Chem.* **2013**, *202*, 269–275.

[13]   Rudyk, B. W.; Stoyko, S. S.; Mar, A *J. Solid State Chem.* **2013**, *208*, 78–85.

[14]   Rudyk, B. W.; Stoyko, S. S.; Oliynyk, A. O.; Mar, A. *J. Solid State Chem.* **2014**, *210*, 79–88.

[15]   Patrie, M.; Guittard, M. *C. R. Acad. Sci., Ser. C* **1969**, *268,* 1136–1138.

[16]   Collin, G.; Laruelle, P. *C. R. Acad. Sci., Ser. C* **1970***, 270*,410–412.

[17]   Iyer, A. K.; Rudyk, B. W.; Lin, X.; Singh, H.; Sharma, A. Z.; Wiebe, C. R.; Mar, A. *J. Solid State Chem.* **2015**, *229*, 150–159.

[18]   Daszkiewicz, M; Gulay, L. D.; Pietraszko, A.; Shemet, V. Y. *J. Solid State Chem.* **2007**, *180*, 2053–2060.

[19]   Daszkiewicz, M; Gulay, L. D.; Lychmanyuk; O. S; Pietraszko, A. *J. Alloys Compd.* **2008**, *460*, 201–205.

[20]   Daszkiewicz, M; Gulay, L. D.; Lychmanyuk; O. S; Pietraszko, A. *J. Alloys Compd.* **2009**, *467*, 168–172.

[21]   Daszkiewicz, M.; Gulay, L. D. *Mater. Res. Bull.* **2012**, *47*, 497–499.

[22]   Daszkiewicz, M; Gulay, L. D.; Lychmanyuk; O. S. *Acta Crystallogr. B* **2009**, *65*, 126–133.

[23]   Poduska, K. M.; DiSalvo, F. J.; Min, K.; Halasyamani, P. S. *J. Alloys Compd.* **2002**, *335*, L5–L9.

[24]   Guo S. -P.; Guo G. -C.; Wang M. -S.; Zou J. -P.; Xu, G.; Wang, G. J.; Long, X. -F.; Huang, J. -S. *Inorg. Chem.* **2009**, *48*, 7059–7065.

[25]   Shi, Y. -F.; Chen, Y. -K.; Chen, M. -K.; Wu, L. -M.; Lin, H.; Zhou, L. -J; Chen, L. *Chem. Mater.* **2015**, *27*, 1876–1884.

[26]   Hartenbach, I.; Nilges, T.; Schleid T. *Z. Anorg. Allg. Chem.* **2007**, *633*, 2445–2452.

[27]   Sheldrick, G. M. *SHELXTL*, version 6.12; Bruker AXS Inc.: Madison, WI, 2001.

[28]   Bindi, L.; Evain, M. *Am. Mineral.* **2007**, *92*, 886–891.

[29]   Petřiček, V.; Dušek, M.; Palatinus, L. *Z. Kristallogr.* **2014**, *229*, 345–352.

[30]   Fairley, N. CasaXPS, version 2.3.9, Casa Software Ltd., Teighnmouth, Devon, UK, **2003**, http://www.casaxps.com.

[31]   Tank, R.; Jepsen, O.; Burkhardt, A.; Andersen, O. K. *TB-LMTO-ASA Program*, version 4.7; Max Planck Institut für Festkörperforschung: Stuttgart, Germany, 1998.

[32]   Brese, N. E.; O'Keeffe, M. *Acta Crystallogr., Sect. B* **1991**, *47*, 192–197.

[33]   Hull, S. *Rep. Prog. Phys.* **2004**, *67*, 1233–1314.

[34]   Kaushik, V. K. *J. Electron Spectrosc. Relat. Phenom.* **1991**, *56*, 273–277.

[35]   Ferraria, A. M.; Carapeto, A. P.; Botelho do Rego, A. M. *Vacuum* **2012**, *86*, 1988–1991.

[36]   Wagner, C. D.; Naumkin, A. V.; Kraut-Vass, A.; Allison, J. W.; Powell, C. J.; Rumble Jr., J. R. NIST X-ray Photoelectron Spectroscopy Database, version 3.5 (web version), National Institute of Standards and Technology, Gaithersburg, MD **2003**, http://srdata.nist.gov/xps

Chapter 4

Quaternary rare-earth sulfides $RE_3M_{0.5}GeS_7$ (RE = La–Nd, Sm; M = Co, Ni) and $Y_3Pd_{0.5}SiS_7$

4.1 Introduction

Rare-earth transition-metal chalcogenides are an important and numerous class of solid state compounds.[1] Among these is a family of quaternary chalcogenides $RE_3M_{1-x}M'Ch_7$ (RE = trivalent rare-earth metal; M, M' = metals, metalloids; Ch = S, Se) which was first discovered about 50 years ago and already recognized at that time to be a potentially rich source of new compounds given the large number of substituents possible for the four components.[2–11] To date, several hundred examples of these compounds have now been identified[12]. The great majority of these compounds are charge-balanced, satisfying the condition that the valences of M and M' must sum to five. For fully stoichiometric compounds $RE_3MM'Ch_7$, the most common are I–IV (M = Na, Cu, Ag; M' = Si, Ge, Sn), followed by II–III (M = alkaline-earth and divalent transition metals; M' = Al, Ga, In) and III–II (M = trivalent transition metals; M' = Be) combinations. [5,8,13–20] For nonstoichiometric compounds $RE_3M_{1-x}M'Ch_7$, the condition of charge balance can be maintained through formation of deficiencies in the M site, allowing the combinations of M and M' to be expanded. For example, these include $RE_3M_{0.5}M'Ch_7$ for II–IV (M = Mg and divalent transition metals; M' = Si, Ge), $RE_3M_{0.33}M'Ch_7$ for III–IV (M = Al, In, Sb; M' = Si, Ge), and $RE_3M_{0.25}M'Ch_7$ for IV–IV (M = Sn; M' = Si) combinations. [3,4,10,21–32] Ternary representatives such as $Ce_3Al_{1.67}S_7$ can also be regarded in this manner if reformulated as $Ce_3Al_{0.67}AlS_7$.[34,35] The breadth is further extended by allowing divalent Eu atoms in the RE site, [11] alkali metals or other main-group

elements in the *M* site, or halogens in the *Ch* site; or by relaxing the charge-balance condition to yield electron-deficient compounds often found with $M = $ Cu, Ag.[13, 36–44]

These chalcogenides exhibit considerable versatility in their structures and properties. As a result of their noncentrosymmetric hexagonal structure (in space group $P6_3$) and small band gaps, some of these compounds have now been found to show nonlinear optical properties (e.g., $La_3Ga_{0.5}(Ge_{0.5}Ga_{0.5})S_7$, $La_3In_{0.5}(Ge_{0.5}In_{0.5})S_7$, $Y_3Zn_{0.5}SiS_7$, $La_3Sb_{0.33}SiS_7$) and photoconductivity (e.g. $Ce_3Fe_{0.5}SiSe_7$, $La_3CuGaSe_7$).[33, 26, 45, 31, 46] Ferroelectric properties have been proposed but have yet to be demonstrated[47]. If the *M* components contain transition metals with electron configurations that are not closed-shell, then interesting magnetic properties may be anticipated (e.g., La_3MAlS_7 ($M = $ Mn, Fe, Co), La_3MInS_7 ($M = $ Fe, Co, Ni), RE_3MGaCh_7 ($M = $ Fe, Co, Ni; *Ch* = S, Se), $RE_3M_{0.5}M'Se_7$ ($M = $ Mn, Fe; $M' = $ Si, Ge)). [15, 18, 19, 31] The *M* atoms can occupy a trigonal planar (CN3) or octahedral (CN6) site, or intermediate sites between these extremes.[11,42,44] Ionic conductivity has been proposed to potentially occur in some deficient Ag-containing compounds (e.g., $RE_3Ag_{1-x}M'Ch_7$ ($M' = $ Si, Ge, Sn; *Ch* = S, Se)), in which the occupation of the Ag atoms within these sites is highly variable.[37,42]

In continuation of our investigations on these chalcogenides, we report here the synthesis of eleven new quaternary sulfides $RE_3M_{0.5}GeS_7$ ($RE = $ La–Nd, Sm; $M = $ Co, Ni) and $Y_3Pd_{0.5}SiS_7$, paying careful attention to the metal site distributions, which are often taken for granted without experimental support, through single-crystal structure determinations on all members. Their electronic structures were determined through band structure calculations. Magnetic properties were probed on $RE_3Co_{0.5}GeS_7$ ($RE = $ Ce, Pr, Sm), which could be obtained as pure phases.

4.2 Experimental

4.2.1 Synthesis

Starting materials were freshly filed RE pieces (La–Nd, Sm; 99.9%, Hefa), Co powder (99.9%, Cerac), Ni powder (99.99%, Sigma-Aldrich), Pd powder (99.95%, Alfa-Aesar), Ge shot (99.99%, Cerac), and S flakes (99.998%, Sigma-Aldrich). Mixtures of the elements with the loading composition "$RE_3M_{0.5}GeS_7$" (M = Co, Ni) and a total mass of 0.2 g were pressed into pellets (6 mm diameter, 1–3 mm thickness) and loaded into fused-silica tubes, which were evacuated and sealed. The tubes were heated at 1050 ºC for 4 d and cooled to 600 ºC over 4 d, and then the furnace was turned off. Heating at temperatures lower than 1050 ºC resulted in poorer quality crystals, and heating for less than 4 d at 1050 ºC resulted in greater amounts of secondary phases. Powder X-ray diffraction (XRD) patterns were collected on an Inel diffractometer equipped with a curved position-sensitive detector (CPS 120) and a Cu $K\alpha_1$ radiation source operated at 40 kV and 20 mA. The samples consisted of the desired quaternary sulfides as the major phase (>95% for La members, and >80% for the Ce–Nd, Sm members); the most common secondary phases were binary sulfides CoS and NiS. Representative powder XRD patterns are shown for the La members (**Figure 4–1**). By regrinding the samples and repeating the heat treatment, $RE_3Co_{0.5}GeS_7$ (RE = Ce, Pr, Sm) could also be obtained with >95% purity. Attempts to extend the range of RE substitution beyond Sm (all the way to Lu) using the same preparative conditions were unsuccessful. Substitutions were also attemped for the M component to prepare $RE_3M_{0.5}M'S_7$ (RE = La, Y; M = Rh, Pd; M' = Si, Ge). The compound $Y_3Pd_{0.5}SiS_7$ could be obtained, but only with the use of KI flux and in the presence of secondary phases. Regrinding and reheating did not improve the phase purity.

Black, irregular-shaped crystals of the quaternary sulfides were examined on a JEOL JSM-6010LA InTouchScope scanning electron microscope. Energy-dispersive X-ray (EDX) analysis was performed on the crystals chosen for structure determination (see below). The compositions averaged over multiple points (8–10) on each crystal were 26(1)–30(1)% RE, 4(1)–5(1)% M, 7(1)–9(1)% Ge, and 55(2)–62(2)% S, in agreement with the expected composition of 26% RE, 4% M, 9% Ge, and 61% S for $RE_3M_{0.5}GeS_7$ (M = Co, Ni). Similarly, the average composition for $Y_3Pd_{0.5}SiS_7$ was found to be 26(1)% Y, 3(1)% Pd, 8(1)% Si, and 59(1)% S. These compositions were also confirmed for a random selection of 3–5 crystals of each compound.
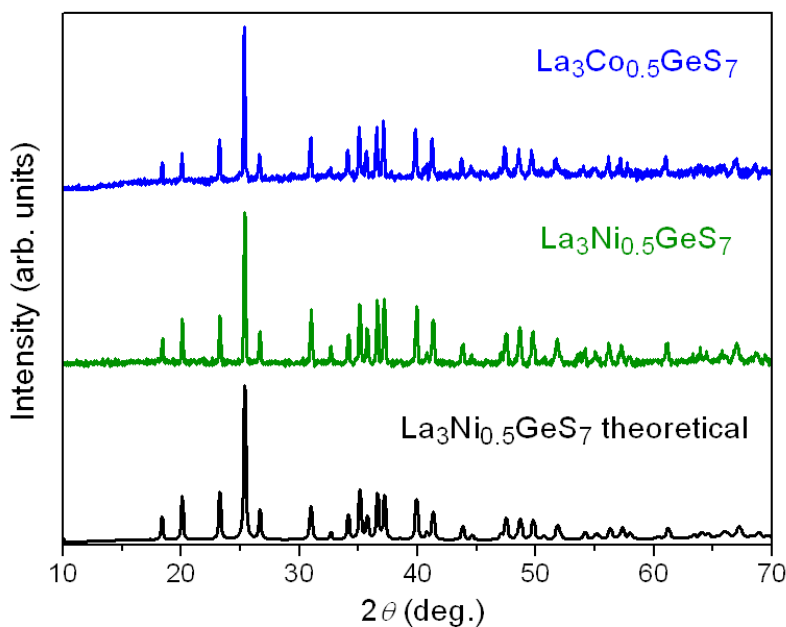
Figure 4-1. Powder XRD patterns of $La_3Co_{0.5}GeS_7$ and $La_3Ni_{0.5}GeS_7$, in comparison with the simulated pattern for $La_3Ni_{0.5}GeS_7$.

4.2.2 Structure determination

Intensity data were collected for all eleven compounds $RE_3M_{0.5}GeS_7$ (RE = La–Nd, Sm; M = Co, Ni) and $Y_3Pd_{0.5}SiS_7$ at room temperature on a Bruker PLATFORM diffractometer equipped

with a SMART APEX II CCD detector and a graphite-monochromated Mo $K\alpha$ radiation source, using ω scans at 5–8 different ϕ angles with a frame width of 0.3° and an exposure time of 12–20 s per frame. Face-indexed numerical absorption corrections were applied. Structure solution and refinement were carried out with use of the SHELXTL (version 6.12) program package[48]. The noncentrosymmetric space group $P6_3$ was chosen and direct methods revealed initial positions of all atoms in structural models consistent with previous $RE_3M_{1-x}M'Ch_7$ compounds: RE in $6c$, M in $2a$, M' in $2b$, and three Ch sites in $6c$, $6c$, and $2b$. The atomic coordinates were standardized with the program STRUCTURE TIDY[49], which places the M atom at the origin, with its z-coordinate fixed to zero along the polar c-axis. However, to facilitate comparison, we prefer to translate the structure to place the S1 atoms at $z = 0$ (and 0.5). This allows the coordination geometry of the M atoms to be readily identified by its z-coordinate: ideally trigonal planar at $z = 0$ and 0.5, ideally octahedral at $z = 0.25$ and 0.75, or intermediate situations at other values. The absolute configurations of each crystal were established by refining a Flack parameter, with inversion twinning being assumed.

For all compounds, there is an M site with octahedral geometry (located near 0, 0, ~0.25 and 0, 0, ~0.75) that exhibits displacement parameters which are too large if fully occupied but attain more reasonable values if half occupied. For example, in $La_3Co_{0.5}GeS_7$, the Co site has U_{eq} of 0.050(1) Å^3 if it is fully occupied. When freely refined, the occupancy of the Co site converges to 0.51(2) and the value of U_{eq} becomes 0.015(1) Å^3, in line with the other atoms. All other sites were confirmed to be fully occupied.

For some compounds, there remained a small amount of residual electron density in the difference map near 0, 0, ~0.00 (and 0, 0, ~0.50), corresponding to what would be a trigonal planar site for M. For example, in $Pr_3Co_{0.5}GeS_7$, the difference map $((\Delta\rho)_{max}, (\Delta\rho)_{min} = 8.5, -1.3$ e$^-$ Å$^3)$

clearly shows a peak near 0, 0, ~0.50. Thus, Co atoms were distributed into two split sites, a primary octahedral one labeled Co-*a* at 0, 0, ~0.25 and a secondary trigonal planar one labeled Co-*b* at 0, 0, ~0.50, with the constraint that their occupancies must sum to 0.50 and their displacement parameters set to be equal. This refinement resulted in occupancies of 0.442(3) in Co-*a* and 0.058(3) in Co-*b*, accompanied by a meaningful improvement in agreement factors (conventional R_1 reduced from 0.027 to 0.023). In most other cases, this residual density is not as prominent. Nevertheless, the split site model was attempted for all compounds, and if convergence was attained, it was accepted.

Crystal data and further details are listed in **Tables 4–1**, **4–2** and **4–3** positional and equivalent isotropic displacement parameters in **Tables 4–4**, **4–5** and **4–6** and selected interatomic distances in **Tables 4–7**, **4–8** and **4–9**.

Table 4-1. Crystallographic data for $RE_3Co_{0.5}GeS_7$ (RE = La–Nd, Sm).

Formula	La₃Co₀.₅GeS₇	Ce₃Co₀.₅GeS₇	Pr₃Co₀.₅GeS₇	Nd₃Co₀.₅GeS₇	Sm₃Co₀.₅GeS₇
Formula mass (amu)	743.21	746.83	749.21	759.20	777.53
Space group	$P6_3$ (No. 173)				
a (Å)	10.3179(7)	10.206(3)	10.1306(6)	10.0775(6)	9.9742(14)
c (Å)	5.8107(4)	5.7906(17)	5.7785(4)	5.7704(3)	5.7393(8)
V (Å³)	535.72(8)	522.4(3)	513.59(7)	507.51(7)	494.48(15)
Z	2				
ρ_{calcd} (g cm⁻³)	4.607	4.748	4.845	4.968	5.222
T (K)	296(2)	296(2)	296(2)	296(2)	296(2)
Crystal dimensions (mm)	0.06 × 0.05 × 0.04	0.05 × 0.04 × 0.04	0.05 × 0.04 × 0.04	0.06 × 0.05 × 0.04	0.05 × 0.05 × 0.04
μ(Mo $K\alpha$) (mm⁻¹)	16.54	17.77	19.01	20.18	22.78
Transmission factors	0.478–0.620	0.542–0.610	0.510–0.566	0.395–0.578	0.416–0.553
2θ limits	4.56–66.58°	4.61–66.37°	4.64–66.45°	4.67–66.35°	4.72–66.24°
Data collected	$-15 \le h \le 15, -15 \le k \le 15, -8 \le l \le 8$	$-15 \le h \le 15, -15 \le k \le 15, -8 \le l \le 8$	$-15 \le h \le 15, -15 \le k \le 15, -8 \le l \le 8$	$-15 \le h \le 15, -15 \le k \le 15, -8 \le l \le 8$	$-15 \le h \le 15, -15 \le k \le 15, -8 \le l \le 8$
No. of data collected	7801	7595	7422	7304	6985
No. of unique data, including $F_o^2 < 0$	1367 (R_{int} = 0.042)	1335 (R_{int} = 0.099)	1310 (R_{int} = 0.042)	1295 (R_{int} = 0.034)	1260 (R_{int} = 0.042)
No. of unique data, with $F_o^2 > 2\sigma(F_o^2)$	1287	1064	1239	1235	1169
No. of variables	39	38	40	38	39
Flack parameter	–0.02(3)	0.01(6)	–0.01(3)	0.00(3)	0.01(2)
$R(F)$ for $F_o^2 > 2\sigma(F_o^2)$ [a]	0.024	0.043	0.023	0.021	0.020
$R_w(F_o^2)$ [b]	0.045	0.092	0.048	0.044	0.034
Goodness of fit	1.100	1.084	1.136	1.107	1.074
$(\Delta\rho)_{max}$, $(\Delta\rho)_{min}$ (e Å⁻³)	2.90, –1.30	3.20, –2.09	2.44, –1.26	2.13, –1.34	1.35, –1.02

[a] $R(F) = \sum ||F_o| - |F_c|| / \sum |F_o|$ for $F_o^2 > 2\sigma(F_o^2)$. [b] $R_w(F_o^2) = [\sum[w(F_o^2 - F_c^2)^2] / \sum wF_o^4]^{1/2}$; $w^{-1} = [\sigma^2(F_o^2) + (Ap)^2 + Bp]$, where $p = [\max(F_o^2,0) + 2F_c^2] / 3$.

Table 4-2. Crystallographic data for $RE_3Ni_{0.5}GeS_7$ (RE = La–Nd, Sm).

Formula	La₃Ni₀.₅GeS₇	Ce₃Ni₀.₅GeS₇	Pr₃Ni₀.₅GeS₇	Nd₃Ni₀.₅GeS₇	Sm₃Ni₀.₅GeS₇
Formula mass (amu)	743.09	746.72	749.09	759.09	777.42
Space group			$P6_3$ (No. 173)		
a (Å)	10.2983(4)	10.2052(13)	10.1303(4)	10.0760(3)	9.9642(8)
c (Å)	5.8078(2)	5.7921(7)	5.7752(2)	5.7605(2)	5.7436(5)
V (Å³)	533.42(5)	522.41(15)	513.27(4)	506.49(3)	493.86(9)
Z			2		
ρ_{calcd} (g cm⁻³)	4.626	4.747	4.847	4.977	5.228
T (K)	296(2)	296(2)	296(2)	296(2)	296(2)
Crystal dimensions (mm)	0.05 × 0.05 × 0.04	0.08 × 0.06 × 0.05	0.06 × 0.05 × 0.04	0.08 × 0.06 × 0.06	0.05 × 0.04 × 0.04
μ(Mo $K\alpha$) (mm⁻¹)	16.72	17.88	19.13	20.33	22.92
Transmission factors	0.552–0.653	0.395–0.557	0.440–0.527	0.361–0.461	0.431–0.572
2θ limits	4.57–66.02°	4.61–66.17°	4.64–66.19°	4.66–66.27°	4.72–66.30°
Data collected	$-15 \le h \le 15$, $-15 \le k \le 15$, $-8 \le l \le 8$	$-15 \le h \le 15$, $-15 \le k \le 15$, $-8 \le l \le 8$	$-15 \le h \le 15$, $-15 \le k \le 15$, $-8 \le l \le 8$	$-15 \le h \le 15$, $-15 \le k \le 15$, $-8 \le l \le 8$	$-15 \le h \le 15$, $-15 \le k \le 14$, $-8 \le l \le 8$
No. of data collected	7786	7574	7378	7287	7111
No. of unique data, including $F_o^2 < 0$	1341 (R_{int} = 0.036)	1318 (R_{int} = 0.080)	1303 (R_{int} = 0.036)	1286 (R_{int} = 0.025)	1263 (R_{int} = 0.060)
No. of unique data, with $F_o^2 > 2\sigma(F_o^2)$	1282	1134	1255	1270	1128
No. of variables	41	39	41	41	40
Flack parameter	–0.02(3)	–0.02(4)	–0.01(3)	0.01(2)	–0.01(4)
$R(F)$ for $F_o^2 > 2\sigma(F_o^2)$ [a]	0.021	0.033	0.020	0.013	0.030
$R_w(F_o^2)$ [b]	0.041	0.064	0.040	0.030	0.060
Goodness of fit	1.175	1.068	1.088	1.104	1.137
$(\Delta\rho)_{max}$, $(\Delta\rho)_{min}$ (e Å⁻³)	2.28, –0.98	2.70, –1.57	2.01, –1.01	1.17, –0.70	4.30, –1.41

[a] $R(F) = \sum ||F_o| - |F_c|| / \sum |F_o|$ for $F_o^2 > 2\sigma(F_o^2)$. [b] $R_w(F_o^2) = [\sum[w(F_o^2 - F_c^2)^2] / \sum wF_o^4]^{1/2}$; $w^{-1} = [\sigma^2(F_o^2) + (Ap)^2 + Bp]$, where $p = [\max(F_o^2,0) + 2F_c^2] / 3$

Table 4-3. Crystallographic data for $Y_3Pd_{0.5}SiS_7$.

Formula	$\mathbf{Y_3Pd_{0.5}SiS_7}$
Formula mass (amu)	572.44
Space group	$P6_3$ (No. 173)
a (Å)	9.7891(3)
c (Å)	5.6840(4)
V (Å^3)	471.70(4)
Z	2
ρ_{calcd} (g cm^{-3})	4.030
T (K)	296(2)
Crystal dimensions (mm)	$0.05 \times 0.05 \times 0.05$
μ(Mo $K\alpha$) (mm^{-1})	20.82
Transmission factors	0.418–0.524
2θ limits	4.80–66.26°
Data collected	$-15 \le h \le 15, -14 \le k \le 15, -8 \le l \le 8$
No. of data collected	6928
No. of unique data, including $F_o^2 < 0$	1197 ($R_{int} = 0.064$)
No. of unique data, with $F_o^2 > 2\sigma(F_o^2)$	989
No. of variables	40
Flack parameter	–0.04(2)
$R(F)$ for $F_o^2 > 2\sigma(F_o^2)$ [a]	0.041
$R_w(F_o^2)$ [b]	0.108
Goodness of fit	1.117
$(\Delta\rho)_{max}, (\Delta\rho)_{min}$ (e Å^{-3})	0.95, –1.84

[a] $R(F) = \sum||F_o| - |F_c|| / \sum|F_o|$ for $F_o^2 > 2\sigma(F_o^2)$. [b] $R_w(F_o^2) = [\sum[w(F_o^2 - F_c^2)^2] / \sum wF_o^4]^{1/2}$; $w^{-1} = [\sigma^2(F_o^2) + (Ap)^2 + Bp]$, where $p = [\max(F_o^2, 0) + 2F_c^2] / 3$.

Table 4-4. Atomic coordinates and equivalent isotropic displacement parameters (Å^2) [a] for $RE_3Co_{0.5}GeS_7$ (RE = La–Nd, Sm).

	La$_3$Co$_{0.5}$GeS$_7$	Ce$_3$Co$_{0.5}$GeS$_7$	Pr$_3$Co$_{0.5}$GeS$_7$	Nd$_3$Co$_{0.5}$GeS$_7$	Sm$_3$Co$_{0.5}$GeS$_7$
RE in 6c (x, y, z)					
x	0.12637(3)	0.12822(7)	0.12820(3)	0.12989(3)	0.12974(3)
y	0.35619(3)	0.35708(7)	0.35593(3)	0.35740(3)	0.35628(3)
z	0.48700(13)	0.0160(3)	0.48389(13)	0.48002(11)	0.02297(10)
U_{eq}	0.00996(9)	0.01239(17)	0.00993(8)	0.01008(7)	0.00861(7)
Co-a in 2a (0, 0, z)					
Occupancy	0.5	0.5	0.442(3)	0.5	0.5
z	0.2484(10)	0.2499(18)	0.2515(10)	0.2493(8)	0.2524(8)
U_{eq}	0.0139(5)	0.0098(10)	0.0067(6)	0.0093(5)	0.0119(5)
Co-b in 2a (0, 0, z)					
Occupancy			0.058(3)		
z			0.490(8)		
U_{eq}			0.0067(6)		
Ge in 2b (1/3, 2/3, z)					
z	0.9050(2)	0.5976(4)	0.9022(2)	0.89831(19)	0.60441(17)
U_{eq}	0.0103(2)	0.0125(5)	0.0107(2)	0.0097(2)	0.0078(2)
S1 in 6c (x, y, z)					
x	0.24240(17)	0.2421(4)	0.24252(18)	0.24448(16)	0.24657(16)
y	0.15652(16)	0.1551(3)	0.15493(17)	0.15520(15)	0.15604(16)
z	0.5000(5)	0.0000(9)	0.5000(5)	0.5000(4)	0.0000(3)
U_{eq}	0.0146(3)	0.0161(6)	0.0146(3)	0.0136(3)	0.0117(3)
S2 in 6c (x, y, z)					
x	0.52140(18)	0.5200(4)	0.52023(19)	0.51986(17)	0.51932(17)
y	0.10670(18)	0.1041(4)	0.10276(19)	0.10158(17)	0.10037(18)
z	0.2579(3)	0.2467(6)	0.2517(3)	0.2463(3)	0.2592(2)
U_{eq}	0.0114(3)	0.0136(6)	0.0111(3)	0.0104(2)	0.0089(3)
S3 in 2b (1/3, 2/3, z)					
z	0.2787(5)	0.2225(10)	0.2783(5)	0.2748(5)	0.2270(4)
U_{eq}	0.0120(5)	0.0138(11)	0.0117(5)	0.0109(5)	0.0095(5)

[a] U_{eq} is defined as one-third of the trace of the orthogonalized U_{ij} tensor.

Table 4-5. Atomic coordinates and equivalent isotropic displacement parameters (Å^2) [a] for $RE_3Ni_{0.5}GeS_7$ (RE = La–Nd, Sm).

	La$_3$Ni$_{0.5}$GeS$_7$	Ce$_3$Ni$_{0.5}$GeS$_7$	Pr$_3$Ni$_{0.5}$GeS$_7$	Nd$_3$Ni$_{0.5}$GeS$_7$	Sm$_3$Ni$_{0.5}$GeS$_7$
RE in 6*c* (*x*, *y*, *z*)					
x	0.12671(3)	0.12838(5)	0.12804(3)	0.12870(2)	0.12991(4)
y	0.35582(3)	0.35722(5)	0.35566(3)	0.35583(2)	0.35587(4)
z	0.01251(11)	0.48249(18)	0.01598(11)	0.01764(8)	0.02096(18)
U_{eq}	0.00969(8)	0.01197(13)	0.00962(8)	0.00860(6)	0.01061(11)
Ni-*a* in 2*a* (0, 0, *z*)					
Occupancy	0.478(3)	0.5	0.478(3)	0.474(2)	0.475(5)
z	0.2489(9)	0.2479(13)	0.2492(9)	0.2490(5)	0.2483(12)
U_{eq}	0.0116(5)	0.0125(7)	0.0126(6)	0.0094(4)	0.0109(10)
Ni-*b* in 2*a* (0, 0, *z*)					
Occupancy	0.022(3)		0.022(3)	0.026(2)	0.025(5)
z	0.020(18)		–0.007(14)	–0.002(8)	0.03(2)
U_{eq}	0.0116(5)		0.0126(6)	0.0094(4)	0.0109(10)
Ge in 2*b* (1/3, 2/3, *z*)					
z	0.59400(19)	0.9012(3)	0.59784(18)	0.59932(13)	0.6019(3)
U_{eq}	0.0103(2)	0.0123(4)	0.0097(2)	0.00835(14)	0.0108(3)
S1 in 6*c* (*x*, *y*, *z*)					
x	0.24042(15)	0.2422(3)	0.24272(15)	0.24320(10)	0.2442(2)
y	0.15496(15)	0.1551(2)	0.15521(14)	0.15487(10)	0.1544(2)
z	0.0000(4)	0.5000(6)	0.0000(4)	0.0000(3)	0.0000(6)
U_{eq}	0.0149(3)	0.0155(4)	0.0143(3)	0.01269(18)	0.0151(4)
S2 in 6*c* (*x*, *y*, *z*)					
x	0.52159(17)	0.5206(3)	0.52039(16)	0.51982(11)	0.5195(3)
y	0.10625(17)	0.1044(3)	0.10305(16)	0.10186(11)	0.1000(3)
z	0.2408(3)	0.2523(4)	0.2483(3)	0.25117(18)	0.2570(4)
U_{eq}	0.0116(3)	0.0132(5)	0.0106(2)	0.00949(17)	0.0120(4)
S3 in 2*b* (1/3, 2/3, *z*)					
Z	0.2202(5)	0.2763(7)	0.2217(4)	0.2227(3)	0.2248(7)
U_{eq}	0.0121(5)	0.0131(8)	0.0114(4)	0.0096(3)	0.0115(7)

[a] U_{eq} is defined as one-third of the trace of the orthogonalized U_{ij} tensor.

Table 4-6. Atomic coordinates and equivalent isotropic displacement parameters ($Å^2$) [a] for $Y_3Pd_{0.5}SiS_7$.

	$Y_3Pd_{0.5}SiS_7$
Y in $6c$ (x, y, z)	
x	0.13099(9)
y	0.35711(9)
z	0.0286(2)
U_{eq}	0.0256(2)
Pd-a in $2a$ $(0, 0, z)$	
Occupancy	0.443(3)
z	0.2459(6)
U_{eq}	0.0269(6)
Pd-b in $2a$ $(0, 0, z)$	
Occupancy	0.057(3)
z	–0.063(5)
U_{eq}	0.0269(6)
Si in $2b$ $(1/3, 2/3, z)$	
z	0.6140(7)
U_{eq}	0.0202(8)
S1 in $6c$ (x, y, z)	
x	0.2524(3)
y	0.1591(3)
z	0.0000(6)
U_{eq}	0.0382(6)
S2 in $6c$ (x, y, z)	
x	0.5233(3)
y	0.1048(3)
z	0.2631(4)
U_{eq}	0.0226(4)
S3 in $2b$ $(1/3, 2/3, z)$	
z	0.2455(7)
U_{eq}	0.0239(7)

[a] U_{eq} is defined as one-third of the trace of the orthogonalized U_{ij} tensor.

Table 4-7. Selected interatomic distances (Å) in $RE_3Co_{0.5}GeS_7$ (RE = La–Nd, Sm).

	La$_3$Co$_{0.5}$GeS$_7$	Ce$_3$Co$_{0.5}$GeS$_7$	Pr$_3$Co$_{0.5}$GeS$_7$	Nd$_3$Co$_{0.5}$GeS$_7$	Sm$_3$Co$_{0.5}$GeS$_7$
RE–S1	2.8548(14)	2.830(3)	2.8026(15)	2.8021(14)	2.7734(14)
RE–S1	2.8571(15)	2.828(3)	2.7979(15)	2.7937(14)	2.7590(14)
RE–S2	2.9303(17)	2.904(4)	2.8848(17)	2.8633(15)	2.8392(15)
RE–S1	3.012(3)	2.986(5)	2.972(3)	2.944(2)	2.901(2)
RE–S2	3.0270(17)	2.990(4)	2.9791(18)	2.9547(16)	2.9269(16)
RE–S2	3.0613(17)	3.031(4)	3.0203(17)	3.0112(15)	2.9885(15)
RE–S3	3.0736(12)	3.030(3)	3.0161(13)	2.9882(11)	2.9651(11)
RE–S1	3.154(3)	3.160(5)	3.148(3)	3.162(2)	3.151(2)
Co-a–S1 (×3)	2.628(4)	2.607(7)	2.599(4)	2.595(3)	2.581(3)
Co-a–S1 (×3)	2.638(4)	2.608(7)	2.589(4)	2.599(3)	2.596(3)
Co-b–S1 (×3)			2.156(2)		
Ge–S3	2.171(3)	2.172(6)	2.173(3)	2.173(3)	2.166(3)
Ge–S2 (×3)	2.2226(17)	2.227(4)	2.2246(18)	2.2265(16)	2.2211(16)

Table 4-8. Selected interatomic distances (Å) in $RE_3Ni_{0.5}GeS_7$ (RE = La–Nd, Sm).

	La₃Ni₀.₅GeS₇	Ce₃Ni₀.₅GeS₇	Pr₃Ni₀.₅GeS₇	Nd₃Ni₀.₅GeS₇	Sm₃Ni₀.₅GeS₇
RE–S1	2.8420(13)	2.830(2)	2.8001(13)	2.7889(9)	2.762(2)
RE–S1	2.8452(13)	2.829(2)	2.7976(13)	2.7817(9)	2.749(2)
RE–S2	2.9300(15)	2.901(2)	2.8852(14)	2.8707(10)	2.840(2)
RE–S1	3.017(3)	2.978(3)	2.970(2)	2.9517(15)	2.919(3)
RE–S2	3.0273(16)	2.992(3)	2.9788(15)	2.9607(11)	2.929(2)
RE–S2	3.0594(15)	3.035(3)	3.0221(14)	3.0087(10)	2.990(2)
RE–S3	3.0690(11)	3.0279(18)	3.0185(11)	2.9997(7)	2.9652(18)
RE–S1	3.154(3)	3.169(3)	3.144(2)	3.1438(15)	3.147(3)
Ni-*a*–S1 (×3)	2.611(3)	2.601(5)	2.593(3)	2.583(2)	2.565(5)
Ni-*a*–S1 (×3)	2.618(3)	2.614(5)	2.598(3)	2.590(2)	2.576(5)
Ni-*b*–S1 (×3)	2.177(6)		2.157(2)	2.1485(9)	2.138(11)
Ge–S3	2.171(3)	2.173(4)	2.172(3)	2.1695(18)	2.166(4)
Ge–S2 (×3)	2.2214(16)	2.223(3)	2.2217(15)	2.2234(10)	2.222(3)

Table 4-9. Selected interatomic distances (Å) in Y₃Pd₀.₅SiS₇.

	Y₃Pd₀.₅SiS₇
Y–S1	2.725(3)
Y–S1	2.739(3)
Y–S2	2.781(2)
Y–S1	2.827(3)
Y–S2	2.875(2)
Y–S2	2.975(2)
Y–S3	2.9366(18)
Y–S1	3.136(4)
Pd-*a*–S1 (×3)	2.576(3)
Pd-*a*–S1 (×3)	2.601(4)
Pd-*b*–S1 (×3)	2.193(5)
Si–S3	2.094(5)
Si–S2 (×3)	2.134(3)

4.2.3 Magnetic susceptibility measurements

Measurements of dc magnetic susceptibility were made on $RE_3Co_{0.5}GeS_7$ (RE = Ce, Pr, Sm) between 2 and 300 K under zero-field-cooled conditions with an applied field of 0.5 T on a Quantum Design 9T PPMS magnetometer. Susceptibility values were corrected for contributions from the holder and sample diamagnetism.

4.2.4 Band structure calculations

Tight-binding linear muffin tin orbital band structure calculations on $La_3Co_{0.5}GeS_7$ and $La_3Ni_{0.5}GeS_7$ were performed within the local density and atomic spheres approximation with use of the Stuttgart TB-LMTO-ASA program (version 4.7).[50] The half-occupancy of the Co or Ni atoms was modeled by imposing an ordered distribution in which the metal atoms alternately occupy every other centre along chains of confacial octahedra; the space group symmetry is lowered to $P3$ but the cell parameters remain the same. The basis set consisted of La 6s/(6p)/5d/4f, Co or Ni 4s/4p/3d, Ge 4s/4p/(4d), and S 3s/3p/(3d) orbitals, with the orbitals shown in parentheses being downfolded. Integrations in reciprocal space were carried out with an improved tetrahedron method over 400 irreducible k points within the first Brillouin zone.

4.3 Results and discussion

The new quaternary rare-earth transition-metal germanium sulfides $RE_3M_{0.5}GeS_7$ (RE = La–Nd, Sm; M = Co, Ni), as well as $Y_3Pd_{0.5}SiS_7$, were prepared by reactions at 1050 °C. The previously known sulfides $RE_3M_{0.5}SiS_7$ and $RE_3M_{0.5}GeS_7$ were limited to M = Mg, Cr, Mn, Fe, Zn, and Cd, with only cell parameters known for many of them and the ranges of RE substitution not entirely elucidated yet. [3,4,10,21–28,32] The compounds $La_3Co_{0.5}SiS_7$ and $La_3Ni_{0.5}SiS_7$ have also been reported but the series have not been extended further. [21,22] Only a few of the corresponding

selenides $RE_3M_{0.5}SiSe_7$ and $RE_3M_{0.5}GeSe_7$ (M = Mg, Mn, Fe) have been found so far[30,31]. For simplicity, the discussion below focuses on $RE_3M_{0.5}GeS_7$ (M = Co, Ni) but most points pertain equally to $Y_3Pd_{0.5}SiS_7$.

The hexagonal structure of $RE_3M_{0.5}GeS_7$ (M = Co, Ni) consists of anionic chains of confacial M-centred octahedra $[M_{0.5}S_{6/2}]^{5-}$ and stacks of Ge-centred tetrahedra $[GeS_4]^{4-}$, both aligned parallel to the polar c-axis (**Figure 4–2**). The sites containing the divalent M atoms are half-occupied to maintain charge neutrality. To avoid confusion, it is worthwhile distinguishing the names of the structure types that have now proliferated to describe the large family of chalcogenides $RE_3M_{1-x}M'Ch_7$ and related compounds. Within Pearson's database, there are currently >600 entries of chalcogenides with the Wyckoff sequence $c^3 b^2 a$ in space group $P6_3$ (no. 173), which belong to five structure types named $U_3Cu_2S_7$, $Ce_3Al_{1.67}S_7$, La_3CuSiS_7, $La_3Mn_{0.5}SiS_7$, and $La_3Ag_{0.82}SnS_7$.[12] In all these structures, there are triangles of chalcogen atoms stacked in a staggered fashion along the c-axis (or, these could be regarded as forming columns of trigonal antiprisms); it is useful to fix the z-coordinate of these atoms at the origin so that the triangles lie parallel to $z = 0$ and $z = \frac{1}{2}$. The $2b$ site (at 1/3, 2/3, z) is always fully occupied by M' atoms in tetrahedral coordination geometry. However, the $2a$ site (at 0, 0, z) lying along the c-axis varies in its location and can be fully or partially occupied by M atoms in different coordination geometries: (i) trigonal planar if the M atoms (at 0, 0, ~0) are coplanar with the chalcogen triangles, designated as the La_3CuSiS_7-type structure, (ii) octahedral (strictly, trigonal antiprismatic) if the M atoms (at 0, 0, ~0.25) are midway between the chalcogen triangles, designated as the $La_3Mn_{0.5}SiS_7$-type structure, or (iii) both trigonal planar and octahedral, designated as the $La_3Ag_{0.82}SnS_7$-type structure. Ternary compounds result when M and M' atoms are identical, corresponding to the $U_3Cu_2S_7$-type structure (when M adopts trigonal planar geometry) or the

$Ce_3Al_{1.67}S_7$-type structure (when M adopts octahedral geometry). From these descriptions, the quaternary sulfides $RE_3M_{0.5}GeS_7$ (M = Co, Ni) can be classified as adopting essentially the $La_3Mn_{0.5}SiS_7$-type structure because the M atoms half-occupy the octahedral site. However, for some members of these series (especially the Ni-containing compounds), as well as for $Y_3Pd_{0.5}SiS_7$, it appears that the trigonal planar site may accommodate a very low occupancy of M atoms (about 0.05 or less).
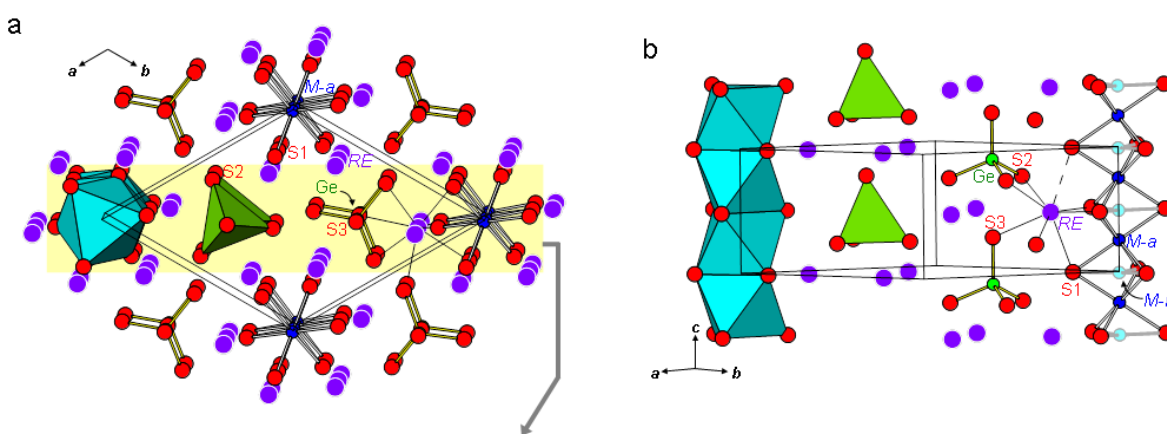
Figure 4-2. (a) Structure of $RE_3M_{0.5}GeS_7$ (M = Co, Ni) viewed down the c-direction. (b) A slice parallel to (110) showing chains of confacial M-centred octahedral and stacks of Ge-centred tetrahedra. For some compounds, a trigonal planar site contains M atoms at very low occupancy.

The RE^{3+} cations are located between these two types of one-dimensional arrangements and are surrounded by S atoms in a [7+1] coordination with roughly bicapped trigonal prismatic geometry. Substitution with smaller RE components within a given $RE_3M_{0.5}GeS_7$ series contracts the structure much more within the ab-plane than along the c-direction, as seen in plots of the cell parameters, so that the overall effect is to increase the c/a ratio (**Figure 4–3**).
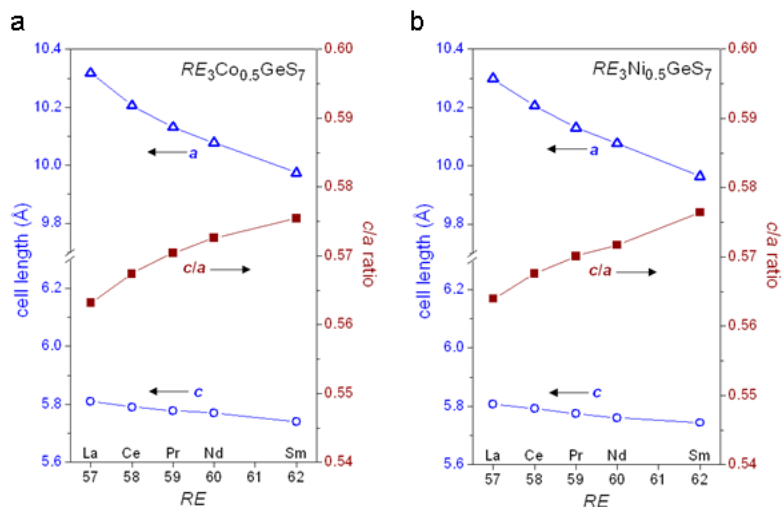
Figure 4-3. Plots of cell parameters and c/a ratios for (a) $RE_3Co_{0.5}GeS_7$ and (b) $RE_3Ni_{0.5}GeS_7$.

Close inspection of the RE–S, M–S, and Ge–S bond distances reveals in detail how the structure responds upon this RE substitution (Figure 4–4). The range of Ge–S bonds remains essentially constant at 2.17–2.22 Å. This implies that the Ge-centred tetrahedra are rigid and thus fix the value of the c-parameter to be close to 5.80 ± 0.05 Å, consistent with other Ge-containing series of related quaternary chalcogenides.[11] The M–S bonds also do not vary much upon RE substitution. Within a given compound, the two sets of three M–S distances are nearly identical, implying that the coordination geometry of the M atoms is accurately described as being octahedral as opposed to compressed or elongated trigonal antiprismatic, as found in other quaternary chalcogenides; for example, in $La_3Co_{0.5}GeS_7$, the Co–S distances are 2.63–2.64 Å and the S–Co–S angles are 87.5–92.3°. In contrast, the RE–S bonds are highly flexible. The seven shorter RE–S bonds contract significantly while they become more disparate from the eight long RE–S bond, which remains invariant at ~3.15 Å.
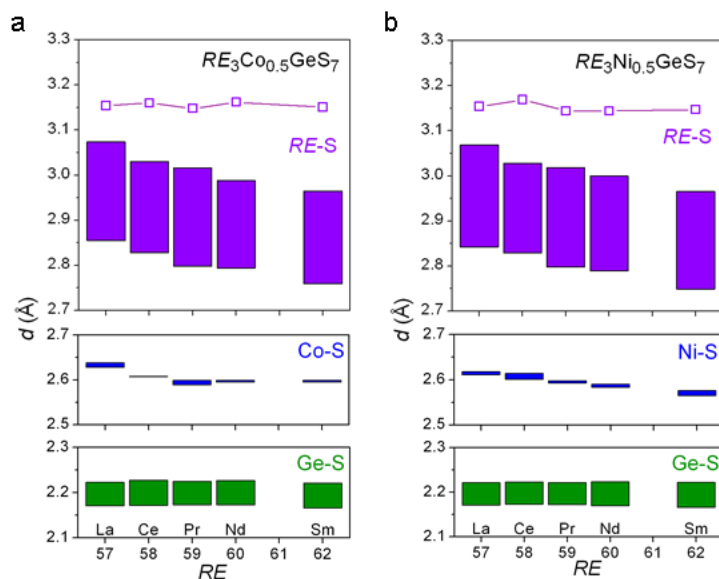
Figure 4-4. Ranges of *RE*–S, *M*–S, and Ge–S distances for (a) $RE_3Co_{0.5}GeS_7$ and (b) $RE_3Ni_{0.5}GeS_7$.

The site distribution of *M* atoms within octahedral sites and Ge atoms in tetrahedral sites in $RE_3M_{0.5}GeS_7$ (M = Co, Ni) agrees with that proposed in related chalcogenides $RE_3M_{0.5}SiS_7$ and $RE_3M_{0.5}GeS_7$ containing other types of divalent *M* atoms,[3,4,10,21–32] and is consistent with the charge-balanced formulation $(RE^{3+})_3(M^{2+})_{0.5}(Ge^{4+})(S^{2–})_7$. However, it is useful to examine this assumption more closely. In particular, there exist ternary chalcogenides $RE_3Ge_{1+x}S_7$ and $RE_3Ge_{1+x}Se_7$ in which Ge atoms occupy both the octahedral and tetrahedral sites,[6,51–54] raising the possibility that $RE_3M_{0.5}GeS_7$ may also contain Ge atoms in octahedral sites. Where single-crystal structures have been determined, the refined formulas for the ternary chalcogenides $RE_3Ge_{1+x}S_7$ have been found with the occupancy, *x*, of the octahedral site varying from 0.25 to 0.49, corresponding to assignments of tetravalent or divalent Ge, respectively, if charge balance is respected.[52–54] Bond valence sums[55] for all atoms have been evaluated for $RE_3M_{0.5}GeS_7$ (M = Co, Ni), as well as for $Y_3Pd_{0.5}SiS_7$ (**Table 4–10**). They appear to be reasonable for all except the *M*

atoms in octahedral sites, which are somewhat underbonded with values of 1.3–1.6. If the occupations are reversed, with Ge atoms placed in octahedral sites and M atoms in tetrahedral sites, the bond valence sums become 2.0–2.3 for Ge and 2.5–2.7 for M.

Table 4-10. Bond valence sums for $RE_3M_{0.5}GeS_7$ (M = Co, Ni) and $Y_3Pd_{0.5}SiS_7$.

	RE	*M-a*	*M-b*	Ge or Si	S1	S2	S3
La$_3$Co$_{0.5}$GeS$_7$	3.17	1.28		4.12	1.94	2.12	2.07
Ce$_3$Co$_{0.5}$GeS$_7$	3.23	1.37		4.08	1.97	2.14	2.13
Pr$_3$Co$_{0.5}$GeS$_7$	3.22	1.42	2.31	4.10	1.99	2.13	2.11
Nd$_3$Co$_{0.5}$GeS$_7$	3.25	1.41		4.08	1.97	2.15	2.16
Sm$_3$Co$_{0.5}$GeS$_7$	3.15	1.44		4.15	1.94	2.12	2.14
La$_3$Ni$_{0.5}$GeS$_7$	3.21	1.27	2.07	4.13	1.98	2.13	2.08
Ce$_3$Ni$_{0.5}$GeS$_7$	3.23	1.30		4.11	1.96	2.15	2.13
Pr$_3$Ni$_{0.5}$GeS$_7$	3.23	1.34	2.19	4.12	1.99	2.14	2.11
Nd$_3$Ni$_{0.5}$GeS$_7$	3.27	1.37	2.24	4.12	2.01	2.15	2.14
Sm$_3$Ni$_{0.5}$GeS$_7$	3.16	1.43	2.30	4.14	1.96	2.12	2.14
Y$_3$Pd$_{0.5}$SiS$_7$	2.91	1.60	2.33	4.07	1.86	2.04	1.98

We consider an assignment of divalent Ge, which would contain a lone pair, to be rather unusual, especially given that its octahedral coordination environment is highly symmetrical. This reversed model also leads to overbonding of the M atoms, and correspondingly, underbonding of the surrounding S atoms (which now have bond valence sums of 1.6–1.7). Moreover, the formula "$RE_3Ge_{0.5}MS_7$" disagrees with the compositions determined by the EDX analysis. Thus, we are inclined to retain the standard structural model. An alternative way to counteract the problem of underbonding of M atoms in the octahedral sites is to place them instead in trigonal planar sites at low occupancies, as observed for some members of these quaternary chalcogenides. However, this results in rather short M–S distances of 2.14–2.18 Å, at the lower bound of observed Co–S and Ni–S distances in the literature, [12] and the opposite problem of overbonding (with bond valence sums of 2.1–2.3 for the M atoms). Similar conclusions can be made for $Y_3Pd_{0.5}SiS_7$, although the underbonding of the octahedral Pd sites is not as severe. While the rather low CN of these

secondary sites is certainly unusual, it is not unprecedented. Trigonal planar MS_3 units (CN3) occur in $A_9Co_2S_7$ (A = K, Rb, Cs) and high-pressure $Ni_{3-x}S$, and linear MS_2 units (CN2) occur in $M_3M'_2Ch_2$ (M = Co, Ni, Pd; M' = In, Tl, Sn) with shandite-type structures.[56–58]

Magnetic susceptibility measurements were made on $RE_3Co_{0.5}GeS_7$ (RE = Ce, Pr, Sm), which could be obtained as essentially pure phase **(Figure 4–5)**. The Ce and Pr members exhibit paramagnetic behaviour and showed no transitions down to 5 K, whereas the Sm member undergoes a downturn in its magnetic susceptibility near 14 K suggestive of an antiferromagnetic transition.
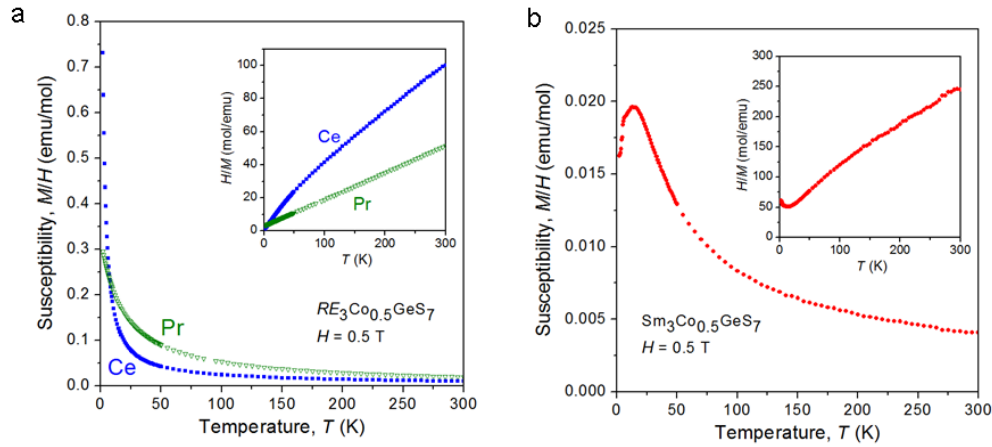
Figure 4-5. Magnetic susceptibility and its inverse (insets) for $RE_3Co_{0.5}GeS_7$ (RE = Ce, Pr, Sm).

The inverse magnetic susceptibility curves could be fitted well to the Curie-Weiss law, $\chi = C/(T-\theta_p)$, over the linear portions from 50 to 300 K for the Ce member and from 5 to 300 K for the Pr member. However, the inverse magnetic susceptibility for the Sm member shows a noticeable curvature over the entire temperature range, and could be better fitted to the modified Curie-Weiss law, $\chi = C/(T-\theta_p) + \chi_o$, from 50 to 300 K with a small temperature independent term ($\chi_o = 1 \times 10^{-3}$ emu/mol). The effective magnetic moments μ_{eff} were evaluated from the Curie

constants ($\mu_{\text{eff}} = (8C)^{1/2}$). These experimental values agree well with theoretical values derived from RE^{3+} and Co^{2+} species, the latter assumed to be in high-spin configuration within an octahedral crystal field, as obtained through $\mu_{\text{eff}} = \left(3\mu_{RE}^2 + 0.5\mu_{Co}^2\right)^{1/2}$ (Table 4–11). (In the case of $Pr_3Co_{0.5}GeS_7$, the Co^{2+} species partially occupying the trigonal planar site, which gives rise to a two-below-one-below-two crystal-field splitting, would lead to the same number of unpaired electrons.) The experimental values are larger than what would be expected if only RE^{3+} species alone contribute to the effective magnetic moment. Thus, these magnetic measurements support the assignments of RE^{3+} and Co^{2+} assumed in the charge-balanced formulations presented earlier. The relatively large negative values of θ_p imply antiferromagnetic coupling interactions, but no long-range magnetic ordering is seen except for the Sm member. Note, however, that the Ce member exhibits a slight curvature in its inverse magnetic susceptibility below 50 K, suggesting that ordering may be possible at very low temperatures. The magnetic behaviour of this Co-containing series is similar to other $RE_3M_{0.5}GeS_7$ (M = Mn, Fe) series, where negative θ_p values are also found but long-range antiferromagnetic ordering is clearly seen only in a few cases ($Dy_3Mn_{0.5}GeS_7$, $Sm_3Fe_{0.5}GeS_7$).[27,28] In particular, the behaviour of $Sm_3Co_{0.5}GeS_7$ resembles that of $Sm_3Fe_{0.5}GeS_7$ except that additional transitions are seen at even lower temperatures for the latter[28]. In general, the θ_p and μ_{eff} values tend to be smaller in magnitude in these metal-deficient compounds $RE_3M_{0.5}GeS_7$ compared to related stoichiometric compounds like RE_3MGaS_7.[19] For example, weaker magnetic interactions are implicated in $Pr_3Co_{0.5}GeS_7$ (θ_p = −19 K, μ_{eff} = 7.0 μ_B/f.u.) relative to Pr_3CoGaS_7 (θ_p = −35 K, μ_{eff} = 7.6 μ_B/f.u.).[19] The detailed magnetic structures of these and related compounds remain unresolved pending neutron diffraction experiments.

Table 4-11. Magnetic data for $RE_3Co_{0.5}GeS_7$ (RE = Ce, Pr, Sm).

Compound	$Ce_3Co_{0.5}GeS_7$	$Pr_3Co_{0.5}GeS_7$	$Sm_3Co_{0.5}GeS_7$ [a]
θ_p (K)	−36	−19	−39
$\mu_{eff,meas}$ (μ_B/f.u.)	5.1	7.0	2.9
$\mu_{eff,theor}$ (RE + Co) (μ_B/f.u.)	5.2	6.8	3.1
$\mu_{eff,theor}$ (RE only) (μ_B/f.u.)	4.4	6.2	1.4

[a] Fitted to modified Curie-Weiss law with $\chi_o = 1 \times 10^{-3}$ emu/mol.

Band structure calculations were performed on ordered models of $La_3M_{0.5}GeS_7$ (M = Co, Ni), resulting in the density of states (DOS) and crystal orbital Hamilton population (COHP) curves shown (**Figure 4–6**). The DOS curves for both compounds show a valence band composed of mostly S 3p states mixed with Ge 4p states (near −5 eV) and M 3d states (from −3 eV upwards), and an empty conduction band composed of mostly La states. At the electron counts corresponding to these compounds (119 e⁻/cell for $La_3Co_{0.5}GeS_7$ and 120 e⁻/cell for $La_3Ni_{0.5}GeS_7$), the Fermi level cuts through a narrow band contributed mostly by the M 3d states, which separate into crystal-field-split t_{2g} and e_g levels in accordance with the octahedral geometry. Although the calculations were performed without spin polarization, consideration of on-site electron-electron repulsions (Hubbard U) may lead to further splitting causing a gap to open. Inspection of the COHP curves shows that the Ge–S interactions are dominant and perfectly optimized with all bonding and no antibonding levels filled. The integrated COHP values (–ICOHP) for the Ge–S contacts are the same (3.5 eV/bond) in both compounds. The M–S interactions involve occupation of some antibonding levels and lead to –ICOHP values of 1.6 eV/bond in $La_3Co_{0.5}GeS_7$ and 1.4 eV/bond in $La_3Ni_{0.5}GeS_7$. The valence band does have a small contribution of La states, leading to partial covalent character in the La–S interactions corresponding to an –ICOHP value of 0.6 eV in both compounds.
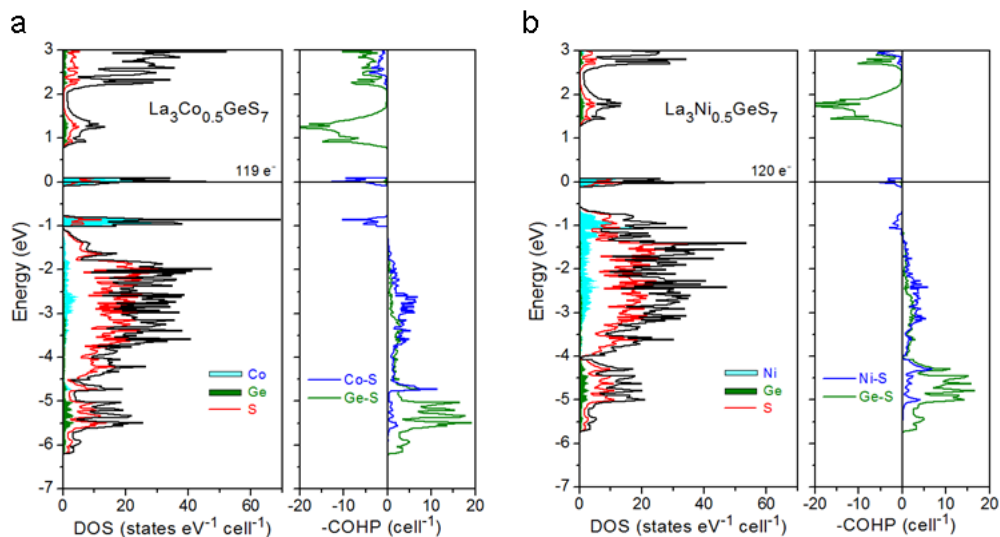
Figure 4-6. Density of states (DOS) and crystal orbital Hamilton population (–COHP) curves for ordered models of (a) La$_3$Co$_{0.5}$GeS$_7$ and (b) La$_3$Ni$_{0.5}$GeS$_7$.

4.4 Conclusions

The new compounds RE_3Co$_{0.5}$GeS$_7$ and RE_3Ni$_{0.5}$GeS$_7$ (RE = La–Nd, Sm) complete the missing series of quaternary sulfides $RE_3M_{0.5}$GeS$_7$ containing a divalent transition metal, previously known for M = Cr, Mn, Fe, Zn, and Cd. Among first- and second-row transition metals, other members are probably unlikely to be found. Although Y$_3$Pd$_{0.5}$SiS$_7$ was also discovered, the analogous compound "Y$_3$Pd$_{0.5}$GeS$_7$" did not form under similar preparative conditions, suggesting that there may be restrictions on the relative sizes of the RE, M, and tetrel components. Among third-row transition metals, perhaps the Pt and Hg members may be feasible targets. The possibility that the M atoms can occupy not only the octahedral site (corresponding to the La$_3$Mn$_{0.5}$SiS$_7$-type structure) but also the trigonal planar site (corresponding to the La$_3$CuSiS$_7$-type structure), even at a very low level, reinforces the notion that there is a continuum of "quasi-isostructural" structures possible for $RE_3M_{1-x}M'Ch_7$ compounds.[42]

4.5   References

[1]   Mitchell, K.; Ibers, J. A. *Chem. Rev.* **2002**, *102*, 1929–1952.
[2]   Guittard, M.; Julien-Pouzol, M.; Laruelle, P.; Flahaut, J. *C. R. Acad. Sci., Ser. C* **1968**, *267*, 767–769.
[3]   Michelet, A.; Flahaut, J. *C. R. Acad. Sci., Ser. C* **1969**, *269*, 1203–1205.
[4]   Collin, G.; Flahaut, J. *C. R. Acad. Sci., Ser. C* **1970**, *270*, 410–412.
[5]   Collin, G.; Flahaut, J. *C. R. Acad. Sci., Ser. C* **1970**, *270*, 488–490.
[6]   Guittard, M.; Julien-Pouzol *Bull. Soc. Chim. Fr.* **1970**, 2467–2469.
[7]   Collin, G.; Laruelle, P. *Bull. Soc. Fr. Mineral. Cristallogr.***1971**, *94*, 175–176.
[8]   Collin, G.; Flahaut, J. *Bull. Soc. Chim. Fr.* **1972**, 2207–2209.
[9]   Collin, G.; Étienne, J.; Laruelle, P. *Bull. Soc. Fr. Mineral. Cristallogr.* **1973**, *96*, 12–17.
[10]   Perez, G.; Darriet-Duale, M.; Hagenmuller, P. *J. Solid State Chem.* **1970**, *2*, 42–48.
[11]   Collin, G.; Étienne, J.; Flahaut, J.; Guittard, M.; Laruelle, P. *Rev. Chim. Miner.* **1973**, *10*, 225–238.
[12]   Villars, P.; Cenzual, K. Pearson's Crystal Data – Crystal Structure Database for Inorganic Compounds (on DVD), Release 2015/16, ASM International, Materials Park, OH, USA.
[13]   Choudhury, A.; Dorhout, P. K. *Inorg. Chem.* **2015**, *54*, 1055–1065 and references therein.
[14]   Rodier, N.; Guittard, M.; Flahaut, J. *C. R. Acad. Sci., Ser. 2* **1983**, *296,* 65–70.
[15]   Nanjundaswamy, K. S.; Gopalakrishnan, J. *J. Solid State Chem.* **1983**, *49*, 51–58.
[16]   Van Calcar, P. M.; Dorhout, P. K. *Mater. Sci. Forum* **1999**, *315*, 322–330.
[17]   Yin, W.; Wang, W.; Kang, L.; Lin, Z.; Feng, K.; Shi, Y.; Hao, W.; Yao, J. L.; Wu Y. *J. Solid State Chem.* **2013**, *202*, 269–275.
[18]   Rudyk, B. W.; Stoyko, S. S.; Mar, A *J. Solid State Chem.* **2013**, *208*, 78–85.
[19]   Rudyk, B. W.; Stoyko, S. S.; Oliynyk, A. O.; Mar, A. *J. Solid State Chem.* **2014**, *210*, 79–88.
[20]   Yin, W.; Shi, Y.; Kang, B.; Deng, J.; Yao, J.; Wu, Y. *J. Solid State Chem.* **2014**, *213*, 87–92.
[21]   Jin, Z.; Li, Z.; Du, Y. *Yingyong Huaxue* **1985**, *2*, 42–46.
[22]   Meng, Y.; Fan, Y.; Lu, R.; Cui, Q.; Zou, G. *Physica* **1986**, *139&140B,* 337–340.
[23]   Gitzendanner, R. L.; Spencer, C. M.; DiSalvo, F. J.; Pell, M. A.; Ibers, J. A. *J. Solid State Chem.* **1996**, *131*, 399–404.
[24]   Huch, M. R.; Gulay, L. D.; Olekseyuk, I. D. *J. Alloys Compd.* **2006**, *424*, 114–118.
[25]   Gulay, L. D; Daszkiewicz, M.; Huch, M. R.; Pietraszko, A. *Acta Crystallogr., Sect. E*, **2007**, *63*, i187.
[26]   Guo S. P.; Guo G. C.; Wang M. S.; Zou J. P.; Xu G.; Wang G. J.; Long X. F.; Huang J.S. *Inorg. Chem.* **2009**, 48, 7059–7065.
[27]   Daszkiewicz, M.; Marchuk, O. V.; Gulay, L. D.; Kaczorowski, D. *J. Alloys Compd.* **2014**, 610, 258–263.
[28]   Daszkiewicz, M.; Pashynska, Y. O.; Marchuk, O. V.; Gulay, L. D.; Kaczorowski, D. *J. Alloys Compd.* **2014,** 616, 243–249
[29]   Assoud A.; Sankar C. R.; Kleinke H. *Solid State Sci.* **2014**, *38*, 124–128.
[30]   Strok, O. M.; Daszkiewicz, M.; Gulay, L. D. *Chem. Met. Alloys* **2015**, *8*, 16–21.
[31]   He, J.; Wang, Z.; Zhang, X.; Cheng, Y.; Gong, Y.; Lai, X.; Zheng C.; Lin J.; Huang F. *RSC Adv.* **2015**, *5*, 52629–52635
[32]   Sun, Y. -L.; Chi, Y.; Guo, S. -P. *Jiegou Huaxue* **2016**, *35*, 1369–1375.
[33]   Shi, Y. -F.; Chen, Y. -K.; Chen, M. -K.; Wu, L. -M.; Lin, H.; Zhou, L. -J; Chen, L. *Chem. Mater.* **2015**, *27*, 1876–1884.
[34]   de Saint-Giniez, D.; Laruelle, P.; Flahaut, J. *C. R. Acad. Sci., Ser. C* **1968**, *267*, 1029–1032.
[35]   Patrie, M.; Guittard, M. *C. R. Acad. Sci., Ser. C* **1969,** *268*, 1136–1138.
[36]   Jaulmes, S.; Palazzi, M.; Laruelle, P. *Mater. Res. Bull.* **1988**, *23*, 831–835.

[37]   Hartenbach, I.; Nilges, T.; Schleid T. *Z. Anorg. Allg. Chem.* **2007**, *633*, 2445–2452.

[38]   Daszkiewicz, M; Gulay, L. D.; M.; Pietraszko, A.; Shemet, V. Y. *J. Solid State Chem.* **2007**, *180*, 2053–2060.

[39]   Daszkiewicz, M; Gulay, L. D.; Lychmanyuk; O. S; Pietraszko, A. *J. Alloys Compd*. **2008**, *460*, 201–205.

[40]   Daszkiewicz, M; Gulay, L. D.; Lychmanyuk; O. S; Pietraszko, A. *J. Alloys Compd.* **2009**, *467*, 168–172

[41]   Daszkiewicz, M; Gulay, L. D. *Mater. Res. Bull.* **2012**, *47*, 497–499.

[42]   Daszkiewicz, M; Gulay, L. D.; Lychmanyuk; O. S. *Acta Crystallogr. B* **2009**, *65*, 126–133.

[43]   Iyer, A. K.; Rudyk, B. W.; Lin, X; Singh, H.; Sharma, A. Z.; Wiebe, C. R.; Mar, A. *J. Solid State Chem.* **2015**, *229*, 150–159.

[44]   Iyer, A. K.; Yin, W.; Rudyk, B. W.; Lin, X; Nilges, T.; Mar, A. *J. Solid State Chem.* **2016**, *243*, 221–231.

[45]   Zhao, H. -J. *J. Solid State Chem.* **2015**, *227*, 5–9.

[46]   Zhang, X.; Chen, W.; Mei, D.; Zheng, C.; Liao, F.; Li, Y.; Lin, J.; Huang, F. *J. Alloys Compd.* **2014**, *610*, 671–675.

[47]   Abrahams, S. C. *Acta Crystallogr. B*, **1990**, *46*, 311–324.

[48]   Sheldrick, G. M. *SHELXTL*, version 6.12; Bruker AXS Inc.: Madison, WI, **2001**.

[49]   Gelato, L. M.; Parthé, E. *J. Appl. Crystallogr.* **1987**, *20*, 139–143.

[50]   Tank, R.; Jepsen, O.; Burkhardt, A.; Andersen, O. K. *TB-LMTO-ASA Program*, version 4.7; Max Planck Institut für Festkörperforschung: Stuttgart, Germany, 1998.

[51]   Michelet, A.; Flahaut, J. *C. R. Acad. Sci., Ser. C* **1969**, *268*, 326–329.

[52]   Michelet, A.; Mazurier, A.; Collin, G.; Laruelle, P.; Flahaut, J. *J. Solid State Chem.* **1975**, *13*, 65–76.

[53]   Zeng H. Y.; Zheng F. K.; Guo G. C.; Huang J. S. *J. Alloys Compd.* **2008**, *458*, 123–129.

[54]   Daszkiewicz, M.; Strok, O. M.; Gulay, L. D.; Kaczorowski, D. *J. Alloys Compd.* **2010**, *508*, 258–261.

[55]   Brese, N. E.; O'Keeffe, M. *Acta Crystallogr., Sect. B* **1991**, *47*, 192–197.

[56]   Bronger, W.; Koelman, W.; Schmitz, D. *Z. Anorg. Allg. Chem.* **1995**, *621*, 405–408.

[57]   Chareev, D. A.; Kurnosov, A. V.; Dubrovinsky, L. S.; Narygina, O. V.; Gavrilenko, P. G.; Zarechnaya, E. Yu.; Dubrovinskaya, N. A.; Litvin, Yu. A.; Osadchii, E. G. *Dokl. Earth Sci.* **2010**, *432*, 771–774.

[58]   Zabel, M.; Wandinger, S.; Range, K. -J. *Z. Naturforsch. B* **1979**, *34*, 238–241.

Chapter 5

Quaternary chalcogenides La$_3$Sn$_{0.5}$InS$_7$ and La$_3$Sn$_{0.5}$InSe$_7$

5.1   Introduction

Among complex rare-earth chalcogenides, there exists an unusually rich family having the general formula $RE_3M_{1-x}M'Ch_7$, whose versatility was already recognized when they were first discovered 50 years ago.[1,2] Given their noncentrosymmetric hexagonal structures, their potential application as nonlinear optical materials (e.g., La$_3$In$_{0.5}$(Ge$_{0.5}$In$_{0.5}$)S$_7$) has only begun to be explored.[3] An attractive feature of these chalcogenides that could enable tuning of properties is that they are highly amenable to substitution. The components M and M' can be taken from a wide range of metals or metalloids from Groups 1 to 14. These atoms can occupy several possible sites: along one stack in the structure are M atoms in sites having trigonal planar (CN3), octahedral (CN6), or intermediate geometries, and along another stack are M' atoms in sites having tetrahedral geometry (CN4).[4,5] Several hundred representatives have now been prepared to date, most of them being fully stoichiometric compounds with the ideal formula $RE_3MM'Ch_7$ and satisfying the restriction that the valences of M and M' must sum to five to attain a charge balanced formulation.[6] However, a growing number of nonstoichiometric compounds $RE_3M_{1-x}M'Ch_7$ are now known: $RE_3M_{0.5}M'Ch_7$ (M = Mg and divalent transition metals; M' = Si, Ge),[2,7–22] $RE_3M_{0.33}M'Ch_7$ (M = Al, In, Sb; M' = Si, Ge),[3,14,17,23–25] and $RE_3M_{0.25}M'Ch_7$ (M = Sn; M' = Si).[23] The site distributions of the M and M' components in these compounds are not necessarily obvious, and many of the subtler details can only be revealed through single-crystal structure determinations. Some simple crystal

chemical principles were proposed in the early investigations of these compounds to rationalize the site preferences,[4] but it is important to find cases that test their limits of applicability.

Here we report the preparation of two quaternary chalcogenides $La_3Sn_{0.5}InS_7$ and $La_3Sn_{0.5}InSe_7$, which are nonstoichiometric $RE_3M_{1-x}M'Ch_7$ compounds having a new combination of M and M' components. We evaluate the evidence for the site distributions of Sn and In atoms within these compounds through single-crystal X-ray diffraction, bond valence sum analyses, and ^{119}Sn magic-angle spinning nuclear magnetic resonance (MAS NMR) spectroscopy. Electronic band structures were also calculated and optical band gaps were measured.

5.2 Experimental

5.2.1 Synthesis

Starting materials were freshly filed La pieces (99.9%, Hefa), Sn powder (99.9%, Cerac), In powder (99.99%, Sigma-Aldrich), S flakes (99.998%, Sigma-Aldrich), and Se powder (99.99%, Sigma-Aldrich) (check). Stoichiometric mixtures of the elements with a total mass of 0.2 g were pressed into pellets (6 mm diameter, 1–3 mm thickness) and loaded into fused-silica tubes, which were evacuated and sealed. The tubes were heated at 1050º C (for $La_3Sn_{0.5}InS_7$) or 950 ºC (for $La_3Sn_{0.5}InSe_7$) for 4 d and cooled to 600 ºC over 4 d, and then the furnace was turned off. Powder X-ray diffraction (XRD) patterns were collected on an Inel diffractometer equipped with a curved position-sensitive detector (CPS 120) and a Cu $K\alpha_1$ radiation source operated at 40 kV and 20 mA. The sulfide sample contained only the $La_3Sn_{0.5}InS_7$ and no other detectable crystalline phases (**Figure 5–1**). When the loading composition was changed to "La_3SnInS_7," significant amounts of other phases were observed in the powder XRD pattern. The selenide sample consisted of about 80% $La_3Sn_{0.5}InSe_7$, with SnSe and In_2Se_3 as the other phases present; regrinding and reheating this

sample at the same temperature as before did not improve its homogeneity. In both cases, heating temperatures below 900 ℃ tended to result in greater amounts of secondary phases and poorer crystal quality. The colour of the two samples was observed to be dark grey. The single crystals obtained were irregular in shape and appeared grey in colour. Substitutions of La with other *RE* components (Ce, Pr, Nd, Sm) were attempted but were unsuccessful under the reaction conditions used above.

Single crystals present in the samples above were examined on a JEOL JSM-6010LA InTouchScope scanning electron microscope. Energy-dispersive X-ray (EDX) analyses on these crystals, averaged over multiple points, revealed compositions (30(2)% La, 5(1)% Sn, 8(1)% In, 58(2)% S for $La_3Sn_{0.5}InS_7$; 25(2)% La, 5(1)% Sn, 9(1)% In, 61(2)% Se for $La_3Sn_{0.5}InSe_7$) in good agreement with expectations (26% La, 4% Sn, 9% In, 61% *Ch*).
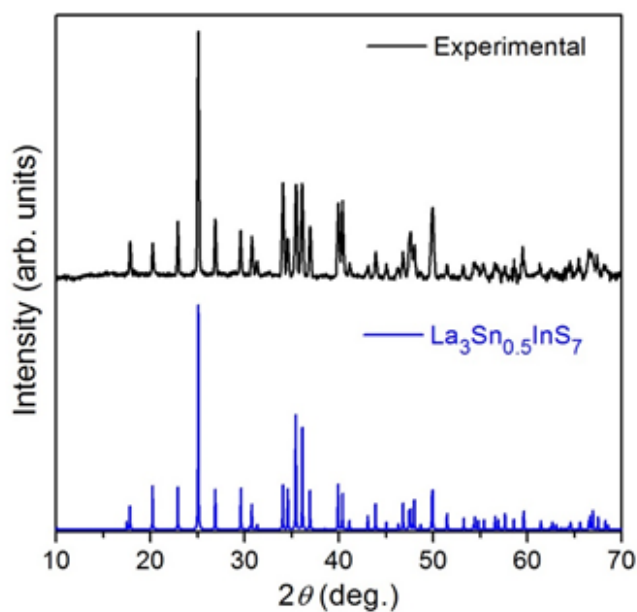
Figure 5-1. Powder XRD pattern of $La_3Sn_{0.5}InS_7$

5.2.2 Structure determination

Intensity data were collected at room temperature for $La_3Sn_{0.5}InS_7$ and $La_3Sn_{0.5}InSe_7$ on a Bruker PLATFORM diffractometer equipped with a SMART APEX II CCD detector and a graphite-monochromated Mo $K\alpha$ radiation source, using ω scans at 8 different ϕ angles with a frame width of 0.3° and an exposure time of 20 s per frame. Face-indexed numerical absorption corrections were applied. Structure solution and refinement were carried out with use of the SHELXTL (version 6.12) program package.[36] Direct methods provided a structural model in the noncentrosymmetric space group $P6_3$ consisting of La in $6c$, an octahedral site in $2a$ tentatively assigned as Sn, a tetrahedral site in $2b$ tentatively assigned as In, and three Ch sites in $6c$, $6c$, and $2b$. In lieu of the standardized coordinates obtained with the program STRUCTURE TIDY,[37] we translate along the polar c-direction so that the z-coordinate of the $Ch1$ atoms is at 0 (or 0.5). This choice has the advantage of immediately revealing the coordination of the M site in $RE_3M_{1-x}M'Ch_7$ structures as ideally trigonal planar (at $z = 0$ or 0.5) or ideally octahedral (at $z = 0.25$ or 0.75). A Flack parameter was refined to determine the absolute configuration of each crystal.

In the initial model, the octahedral site at $2a$ (0, 0, z) was fully occupied by Sn and the tetrahedral site at $2b$ (1/3, 2/3, z) was fully occupied by In atoms, corresponding to the stoichiometric formula $La_3SnInCh_7$. In both sulfide and selenide, the displacement parameters for the octahedral site were significantly higher than for the other sites ($U_{eq} = 0.047(1)$ Å^2 for Sn relative to 0.011(1)–0.017(1) Å^2 for other sites in La_3SnInS_7; $U_{eq} = 0.069(2)$ Å^2 for Sn relative to 0.015(1)–0.022(1) Å^2 for other sites in $La_3SnInSe_7$). Half-occupation of these sites resulted in more reasonable displacement parameters, as confirmed in subsequent refinements in which the occupancy was freed (occ = 0.49(1), $U_{eq} = 0.016(1)$ Å^2 for $La_3Sn_{0.5}InS_7$; occ = 0.56(1), $U_{eq} = 0.036(1)$ Å^2 for $La_3Sn_{0.5}InSe_7$). Because Sn and In are indistinguishable from their X-ray

scattering factors, additional evidence (discussed elsewhere) is needed to support this model over one in which the site assignments are reversed.

Table 5–1 lists crystal data and details of the data collections, Table 5–2 lists positional and displacement parameters, and Table 5–3 lists selected interatomic distances.

Table 5-1. Crystallographic data for $La_3Sn_{0.5}InS_7$ and $La_3Sn_{0.5}InSe_7$.

Formula	$La_3Sn_{0.5}InS_7$	$La_3Sn_{0.5}InSe_7$
Formula mass (amu)	815.32	1143.61
Space group	\multicolumn{2}{c}{$P6_3$ (No. 173)}	
a (Å)	10.2993(11)	10.6533(7)
c (Å)	6.0921(6)	6.4245(4)
V (Å^3)	559.65(13)	631.45(9)
Z	\multicolumn{2}{c}{2}	
ρ_{calcd} (g cm^{-3})	4.838	6.015
T (K)	296(2)	296(2)
Crystal dimensions (mm)	$0.09 \times 0.05 \times 0.03$	$0.06 \times 0.06 \times 0.05$
μ(Mo $K\alpha$) (mm^{-1})	15.58	32.83
Transmission factors	0.414–0.693	0.280–0.369
2θ limits	4.57–66.46°	4.41–66.38°
Data collected	$-15 \le h \le 15, -15 \le k \le 15, -9 \le l \le 9$	$-16 \le h \le 16, -16 \le k \le 16, -9 \le l \le 9$
No. of data collected	8303	9367
No. of unique data, including $F_o^2 < 0$	1442 ($R_{int} = 0.032$)	1617 ($R_{int} = 0.046$)
No. of unique data, with $F_o^2 > 2\sigma(F_o^2)$	1388	1476
No. of variables	39	39
Flack parameter	0.03(3)	0.01(3)
$R(F)$ for $F_o^2 > 2\sigma(F_o^2)$ [a]	0.019	0.028
$R_w(F_o^2)$ [b]	0.041	0.063
Goodness of fit	1.091	1.078
$(\Delta\rho)_{max}, (\Delta\rho)_{min}$ (e Å^{-3})	1.67, –0.93	1.87, –1.53

[a] $R(F) = \sum ||F_o| - |F_c|| / \sum |F_o|$ for $F_o^2 > 2\sigma(F_o^2)$. [b] $R_w(F_o^2) = [\sum[w(F_o^2 - F_c^2)^2] / \sum wF_o^4]^{1/2}$; $w^{-1} = [\sigma^2(F_o^2) + (Ap)^2 + Bp]$, where $p = [\max(F_o^2,0) + 2F_c^2] / 3$.

Table 5-2. Atomic coordinates and equivalent isotropic displacement parameters (Å^2) [a] for $La_3Sn_{0.5}InS_7$ and $La_3Sn_{0.5}InSe_7$.

	$La_3Sn_{0.5}InS_7$	$La_3Sn_{0.5}InSe_7$
La in 6c (x, y, z)		
x	0.13877(3)	0.14670(5)
y	0.36582(3)	0.36921(5)
z	0.02762(7)	0.46364(12)
U_{eq}	0.01336(8)	0.01986(13)
Sn in 2a (0, 0, z)		
Occupancy	0.5	0.5
z	0.2514(3)	0.2443(7)
U_{eq}	0.0172(3)	0.0305(7)
In in 2b (1/3, 2/3, z)		
z	0.60389(10)	0.88293(17)
U_{eq}	0.01265(13)	0.0166(2)
Ch1 in 6c (x, y, z)		
x	0.24811(14)	0.25117(11)
y	0.15190(14)	0.14899(10)
z	0.0000(3)	0.50000(19)
U_{eq}	0.0177(3)	0.0231(2)
Ch2 in 6c (x, y, z)		
x	0.51433(14)	0.51458(10)
y	0.08838(14)	0.08219(10)
z	0.2686(2)	0.22030(17)
U_{eq}	0.0130(2)	0.01756(18)
Ch3 in 2b (1/3, 2/3, z)		
z	0.2168(3)	0.2718(2)
U_{eq}	0.0122(4)	0.0159(3)

[a] U_{eq} is defined as one-third of the trace of the orthogonalized U_{ij} tensor.

Table 5-3. Selected interatomic distances (Å) in $La_3Sn_{0.5}InS_7$ and $La_3Sn_{0.5}InSe_7$.

	$La_3Sn_{0.5}InS_7$	$La_3Sn_{0.5}InSe_7$
La–Ch1	2.896(1)	3.018(1)
La–Ch2	2.910(1)	3.018(1)
La–Ch1	2.938(1)	3.067(1)
La–Ch3	2.956(1)	3.035(1)
La–Ch2	3.009(1)	3.109(1)
La–Ch1	3.068(2)	3.175(1)
La–Ch2	3.076(1)	3.238(1)
La–Ch1	3.386(2)	3.617(1)
Sn–Ch1 (×3)	2.697(2)	2.810(3)
Sn–Ch1 (×3)	2.707(2)	2.851(3)
In–Ch3	2.358(2)	2.498(2)
In–Ch2 (×3)	2.424(1)	2.557(1)

5.2.3 ^{119}Sn NMR spectroscopy

^{119}Sn MAS NMR spectra were acquired on a Bruker Avance 500 NMR spectrometer, operating at 186.6 MHz for ^{119}Sn. Powdered samples were packed into 4 mm (o.d.) zirconia rotors and placed into a Bruker double-channel (H/X) MAS NMR probe. Spectra were acquired at spinning frequencies ranging from 5.0 to 14.0 kHz, using a Bloch pulse ($\pi/2 = 4$ μs, $\gamma B_1/2\pi = 62.5$ kHz), a relaxation delay of 2.0 s, and between 8,192 and 76,000 co-added transients. All spectra were referenced to tetramethyltin ($\delta(^{119}\text{Sn}) = 0$ ppm) by setting the isotropic ^{119}Sn NMR peak of tetracyclohexyltin to -97.35 ppm. [38]

5.2.4 Diffuse reflectance spectroscopy

The optical spectrum of $La_3Sn_{0.5}InS_7$ was measured from 350 nm (3.54 eV) to 2500 nm (0.50 eV) on a Cary 5000 UV-vis-NIR spectrophotometer equipped with a diffuse reflectance accessory. A compacted pellet of $BaSO_4$ was used as a 100% reflectance standard. The optical absorption spectrum was converted from the diffuse reflectance spectrum using the Kubelka-Munk function, $\alpha/S = (1-R)^2/2R$, where α is the Kubelka–Munk absorption coefficient, S is the scattering coefficient, and R is the reflectance.[39]

5.2.5 Band structure calculations

Tight-binding linear muffin tin orbital band structure calculations on $La_3Sn_{0.5}InS_7$ were performed within the local density and atomic spheres approximation with use of the Stuttgart TB-LMTO-ASA program (version 4.7).[40] An ordered superstructure model was considered in which Sn atoms were placed in every second octahedral site within chains extending along the c-axis, lowering the space group symmetry to $P3$. The basis set consisted of La 6s/(6p)/5d/4f, Sn 5s/5p/(4d)/(4f), In 5s/5p/(4d)/(4f), and S 3s/3p/(3d) orbitals, with the orbitals shown in parentheses

being downfolded. Integrations in reciprocal space were carried out with an improved tetrahedron method over 400 irreducible k points within the first Brillouin zone.

5.3 Results and discussion

The compounds $La_3Sn_{0.5}InS_7$ and $La_3Sn_{0.5}InSe_7$ were obtained by stoichiometric reactions of the elements at 1050 °C and 950 °C, respectively, in high yield, as illustrated by the powder X-ray diffraction (XRD) pattern of the sulfide (Figure 5–1). They are new members belonging to the family of quaternary rare-earth chalcogenides $RE_3M_{1-x}M'Ch_7$ (Ch = S, Se). Representatives of such chalcogenides with M and M' components consisting of only p-block elements are not as common as those consisting of a combination of d- and p-block elements. Other examples that have been confirmed by single-crystal X-ray diffraction include $RE_3Al_{0.33}SiS_7$,[14] $Sm_3Al_{0.33}GeS_7$,[24] and $RE_3Sb_{0.33}SiS_7$.[25] The existence of $La_3In_{0.33}SiS_7$ and $La_3Sn_{0.25}SiS_7$ has been reported but structural characterization is lacking.[23] When the M and M' components are identical, the related ternary chalcogenides $RE_3M_{1.67}Ch_7$ (M = Al, Ga, In) and $RE_3M_{1.25}Ch_7$ (M = Si, Ge, Sn) are known, adopting the $Ce_3Al_{1.67}S_7$-type structure.[26,27]

Within the hexagonal structure of $La_3Sn_{0.5}InCh_7$ (Ch = S, Se) (in space group $P6_3$), one-dimensional stacks parallel to the c-direction are separated by the La atoms (**Figure 5–2**). One stack extends along the c-axis, built up of triangles of $Ch1$ atoms lying at $z = 0$ and $z = \frac{1}{2}$ which are arranged in a staggered fashion. The sites located midway, $2a$ (0, 0, ~0.25), between these triangles are half-occupied by Sn atoms in essentially octahedral coordination geometry. Another stack extends along 1/3, 2/3, z (or 2/3, 1/3, z), built up of triangles of $Ch2$ atoms and single $Ch3$ atoms, with In atoms occupying tetrahedral sites. The La atoms lying between these stacks are surrounded by Ch atoms in approximately bicapped trigonal prismatic geometry in [7+1]

coordination with a distinctly longer distance to one of the Ch atoms. Among the various structural branches of the $RE_3M_{1-x}M'Ch_7$ family,[5] $La_3Sn_{0.5}InCh_7$ adopts the $La_3Mn_{0.5}SiS_7$-type structure.

The distribution of Sn atoms in octahedral and In atoms in tetrahedral sites in $La_3Sn_{0.5}InCh_7$ is reversed from that in other $RE_3M_{1-x}M'Ch_7$ compounds containing a combination of group 13 and 14 elements, such as $RE_3Al_{0.33}SiS_7$, which contains Al in octahedral and Si in tetrahedral sites.[14] Strong evidence supports the structural model proposed for $La_3Sn_{0.5}InCh_7$. Although it is true that Sn and In cannot be distinguished on the basis of their X-ray scattering factors, the structure refinement clearly indicates that the octahedral site is half-occupied and the tetrahedral site is fully occupied, resulting in the formula $La_3M_{0.5}M'Ch_7$, irrespective of the assignments of these sites. The energy-dispersive X-ray (EDX) analyses unequivocally reveal the presence of twice as much In as Sn, consistent with the composition $La_3Sn_{0.5}InCh_7$. Reaction of the elements in this nominal stoichiometry results in $La_3Sn_{0.5}InS_7$ as phase-pure material and $La_3Sn_{0.5}InSe_7$ as major (80%) product. Finally, this composition gives a formulation $(La^{3+})(Sn^{4+})_{0.5}(In^{3+})(Ch^{2-})_7$ that is charge-balanced, as is found in the overwhelming number of $RE_3M_{1-x}M'Ch_7$ compounds.

Nevertheless, this structural model is unusual because it appears to run counter to the general observation that the tetrahedral site M' is normally preferred by higher-valent elements in $RE_3M_{1-x}M'Ch_7$ compounds. Thus, it is worthwhile to examine the structural details more closely, focusing on the sulfide $La_3Sn_{0.5}InS_7$ for concreteness and then extending the conclusions to the selenide $La_3Sn_{0.5}InSe_7$. In $La_3Sn_{0.5}InS_7$, the bond lengths are 2.697(2)–2.707(2) Å around octahedral Sn sites and 2.358(2)–2.424(1) Å around tetrahedral In sites.
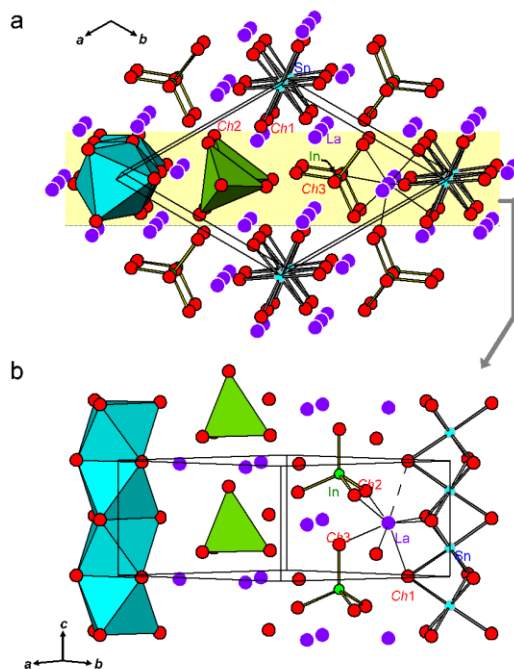
Figure 5-2. (a) Structure of $La_3Sn_{0.5}InCh_7$ (Ch = S, Se) viewed down the c-direction. (b) A slice

A good basis for comparison is to the ternary sulfides $La_3Sn_{1.25}S_7$ (or $La_3Sn_{0.25}SnS_7$) and

$La_3In_{1.67}S_7$ (or $La_3In_{0.67}InS_7$) which contain Sn or In atoms in both types of sites. In $La_3Sn_{1.25}S_7$,

the bond lengths are 2.664(4)–2.672(4) Å around octahedral Sn sites and 2.343(4)–2.392(2) Å

around tetrahedral Sn sites. In $La_3In_{1.67}S_7$, the bond lengths are 2.658(1)–2.722(1) Å around

octahedral In sites and 2.392(1)–2.451(1) Å around tetrahedral In sites. All of these distances are

typical of Sn–S (2.35–2.80 Å) and In–S (2.35–2.85 Å) bonds found in other sulfides as listed in

Pearson's Crystal Data. Although the ranges of bond lengths do overlap, comparison of these

three structures suggests that the assignment of octahedral Sn and tetrahedral In in $La_3Sn_{0.5}InS_7$

may be up for question. However, bond valence sum calculations permit a more critical analysis

to be made (Table 5–4).[30] In the as-refined model ($La_3Sn_{0.5}InS_7$), the bond valence sums are 3.04

around the octahedral site occupied by Sn atoms and 3.53 around the tetrahedral site occupied by

In atoms. If the assignments are reversed ($La_3In_{0.5}SnS_7$), the bond valence sums become 2.38

127

around the octahedral site occupied by In atoms and 4.50 around the tetrahedral site occupied by

Sn atoms. In other words, the octahedral site is underbonded and the tetrahedral site is overbonded

in either scenario. (Note that this observation also applies to the ternary compounds $La_3Sn_{1.25}S_7$,

with bond valence sums of 3.33 around octahedral and 4.84 around tetrahedral sites, and

$La_3In_{1.67}S_7$, with bond valence sums of 2.47 around octahedral and 3.26 around tetrahedral sites.)

It is important to appreciate that bond valence sums for all atoms, not just one or two, must be

examined to evaluate the stability of a structure. In particular, changing the occupation of the

octahedral and tetrahedral sites also affects the bond valence sums of the surrounding chalcogen

atoms. The bond valence sums are close to 2 for all S atoms in the as-refined model $La_3Sn_{0.5}InS_7$,

but deviate significantly in the reversed model $La_3In_{0.5}SnS_7$. The same conclusions apply to the

selenide $La_3Sn_{0.5}InSe_7$.

Table 5-4. Bond valence sums for $La_3Sn_{0.5}InS_7$ and $La_3Sn_{0.5}InSe_7$ in different models.

	$La_3Sn_{0.5}InS_7$			$La_3Sn_{0.5}InSe_7$		
Model	as refined Sn oct, In tet	reversed In oct, Sn tet	disordered 0.33 Sn, 0.67 In in both sites	as refined Sn oct, In tet	reversed In oct, Sn tet	disordered 0.33 Sn, 0.67 In in both sites
La	2.98	2.98	2.98	2.84	2.84	2.84
oct site	3.04 for Sn	2.38 for In	3.04 for Sn 2.38 for In	3.14 for Sn	2.27 for In	3.14 for Sn 2.27 for In
tet site	3.53 for In	4.50 for Sn	3.53 for In 4.50 for Sn	3.30 for In	4.56 for Sn	3.30 for In 4.56 for Sn
*Ch*1	1.90	1.79	1.83	1.81	1.67	1.71
*Ch*2	2.00	2.23	2.08	1.89	2.19	1.99
*Ch*3	2.28	2.56	2.37	2.28	2.63	2.40

Even with the constraint of a charge-balanced formulation, there exists the possibility that

the Sn and In atoms could be disordered over both the octahedral and tetrahedral sites, viz.

$La(Sn_{0.33}In_{0.67})_{0.5}(Sn_{0.33}In_{0.67})Ch_7$. The bond valence sums around the chalcogen atoms then

become intermediate between those in the as-refined and the reversed models (**Table 5–4**). To

distinguish between the ordered vs. disordered site distributions, the ^{119}Sn MAS NMR spectrum of $La_3Sn_{0.5}InS_7$ was collected (**Figure 5–3**). Although ^{119}Sn NMR spectra of tin-containing sulfides remain relatively sparse, the wide ranges of isotropic chemical shifts (δ_{iso}) and chemical shift anisotropy (CSA) observed suggest that they can be useful in providing information about chemical environments of Sn atoms.[31–34] The presence of only one resonance in $La_3Sn_{0.5}InS_7$ with an isotropic chemical shift of –44 ppm implies that the Sn atoms reside in one site, supporting the ordered structural model. An NMR spectrum of this sample (not shown) was also acquired at a lower spinning frequency (8.0 kHz) to ascertain that the spinning sideband peaks were not obscuring another NMR site. From the one set of visible spinning sidebands, the CSA is found to be relatively small (span, $\Omega \approx 200$ ppm), suggesting that the Sn atoms are in a highly symmetric environment. Within the structure, the octahedral sites are nearly regular with similar distances (2.697(2)–2.707(2) Å) to all six surrounding S atoms and bond angles (88.66(2)–91.55(6)°) that are close to ideal, whereas the tetrahedral sites are quite distorted with one short (2.358(2) Å) and three long (2.424(1) Å) distances. Among sulfides containing nominally Sn^{4+} species, [119]Sn isotropic chemical shifts vary from –770 ppm (SnS_2 and Na_2SnS_3 both with Sn-centred octahedra) to 68 ppm (Na_4SnS_4 with Sn-centred tetrahedra); SnS containing nominally Sn^{2+} species in a [3+3] coordination has a [119]Sn δ_{iso} of –300 ppm and a very wide span of 641 ppm.[31] On balance, the NMR evidence supports the occupation of Sn^{4+} species within the octahedral sites exclusively.

Another interesting feature of the ^{119}Sn NMR spectrum of $La_3Sn_{0.5}InS_7$ is that the main resonance peak is asymmetric and quite broad (3 kHz at half-height); such broadening is typically attributed to short-range structural disorder. The most likely explanation is that the nonstoichiometry in $La_3Sn_{0.5}InS_7$ still entails local disorder around the Sn atoms, which statistically occupy octahedral sites at 0.50.
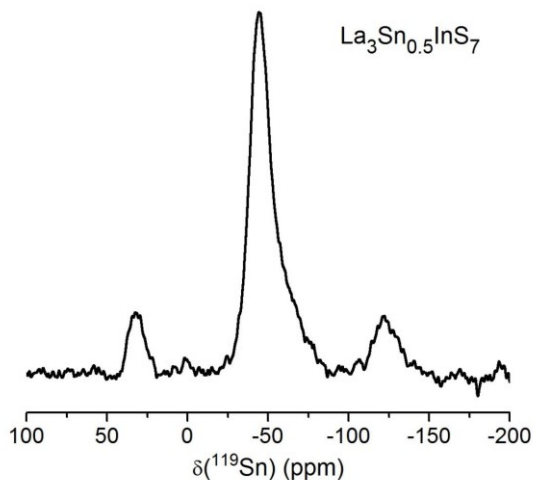
Figure 5-3. ^{119}Sn MAS NMR spectrum of $La_3Sn_{0.5}InS_7$ acquired at a spinning frequency of 14.0 kHz.

The optical absorption spectrum of $La_3Sn_{0.5}InS_7$, for which pure samples were available, indicates a band gap of 1.45 eV as estimated through an extrapolation method (**Figure 5–4**). This band gap lies in the infrared region and is consistent with the dark grey colour of bulk powders of $La_3Sn_{0.5}InS_7$. For comparison, a related $RE_3M_{1-x}M'Ch_7$ compound containing p-block components for M and M' such as $La_3Sb_{0.33}SiS_7$ has a band gap of 1.9 eV.[25]
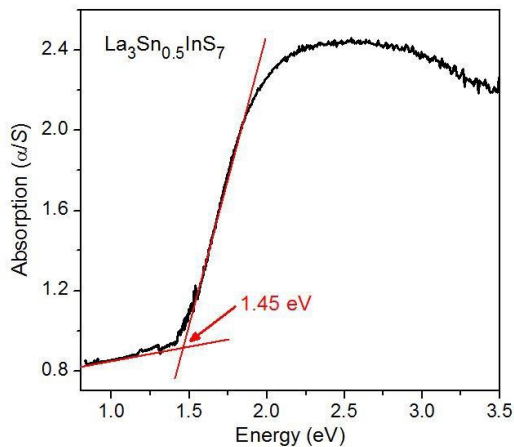
Figure 5-4. Diffuse reflectance spectrum for $La_3Sn_{0.5}InS_7$.

The electronic structure of an ordered superstructure model of $La_3Sn_{0.5}InS_7$ was obtained through band structure calculations (**Figure 5–5**). The density of states (DOS) curve shows a wide valence band, derived mainly from mixing of S 3p states with Sn 5p (mostly centred around –4 eV but also extending up to –1 eV) and In 5s/5p states (centred near –5 eV and extending from –4 to –0.5 eV, respectively), and an empty conduction band derived mostly from La states from 2.1 eV upwards. Energy gaps extracted from the DOS cannot be directly compared with the experimental optical band gap because the material is inherently disordered. Additionally, there is a small spike in the DOS near 0.5 eV above the Fermi level that involves mixing of Sn 5s and S 3p states. As shown in the crystal orbital Hamilton population (–COHP) curves, occupation of these states is strongly disfavoured because they are highly Sn–S antibonding. A separate band structure calculation (not shown here) performed on a fully stoichiometric model La_3SnInS_7 reveals that these states would be completely occupied. Thus, despite the apparent underbonding of the octahedral site if filled by Sn atoms, as suggested by the bond valence sum analysis presented earlier, there is a strong electronic driving force for the Sn substoichiometry. At the electron count corresponding to $La_3Sn_{0.5}InS_7$, both Sn–S and In–S bonding interactions are completely optimized, with only bonding and no antibonding levels being occupied. The integrated COHP values (–ICOHP) are 1.90 eV/bond for the Sn–S contacts and 2.09 eV/bond for the In–S contacts. A small contribution of La states within the valence band also gives rise to an –ICOHP value of 0.76 eV/bond for the La–S contacts, which have partial covalent character.
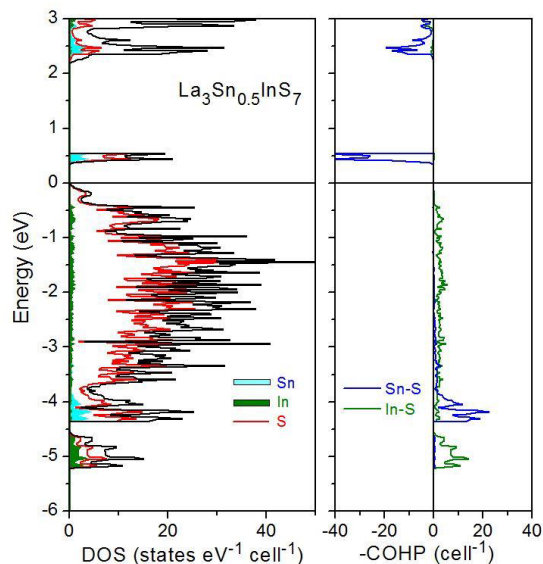
Figure 5-5. Density of states (DOS) and crystal orbital Hamilton populations (–COHP) for an ordered model of $La_3Sn_{0.5}InS_7$.

5.4 Conclusions

Given the previously reported existence of the ternary chalcogenides $La_3Sn_{1.25}Ch_7$ and $La_3In_{1.67}Ch_7$,[28,29] in which Sn or In atoms are capable of occupying both octahedral and tetrahedral sites, the preparation of $La_3Sn_{0.5}InCh_7$ provides an interesting case for the potential occurrence of charge ordering of the Sn and In atoms and for testing the assertion that higher-valent elements prefer the tetrahedral M' site in quaternary chalcogenides $RE_3M_{1-x}M'Ch_7$.[4] Although the elemental composition suggests that the Sn atoms should occupy the octahedral site, which permits deficiencies, it is possible to imagine other site distributions consistent with the formula $La_3Sn_{0.5}InCh_7$. Bond valence sum analyses reveal that whatever model is chosen, the octahedral site is underbonded and the tetrahedral site is overbonded; however, the as-refined model of Sn in octahedral and In in tetrahedral sites results in the lowest deviations of bond valence sums from their ideal values for the surrounding chalcogen atoms. The occurrence of Sn^{4+} species within

octahedral sites was confirmed by ^{119}Sn NMR spectroscopy of $La_3Sn_{0.5}InS_7$. This site distribution, reversed from the typical scenario observed in other $RE_3M_{1-x}M'Ch_7$ compounds, suggests that the general rule of higher-valent elements preferring the tetrahedral site can be violated. As in other $RE_3M_{1-x}M'Ch_7$ compounds, charge balance is attained through an appropriate combination of the valences of the M and M' components but in $La_3Sn_{0.5}InS_7$, avoidance of Sn–S antibonding levels is also important.

5.5 References

[1]   Guittard, M.; Julien-Pouzol, M.; Laruelle, P.; Flahaut, J. *C. R. Acad. Sci., Ser. C* **1968**, *267*, 767–769.

[2]   Michelet, A.; Flahaut, J. *C. R. Acad. Sci., Ser. C* **1969**, *269*, 1203–1205.

[3]   Shi, Y. -F.; Chen, Y. -K.; Chen, M. -K.; Wu, L. -M.; Lin, H.; Zhou, L. -J; Chen, L. *Chem. Mater.* **2015**, *27*, 1876–1884.

[4]   Collin, G.; Étienne, J.; Flahaut, J.; Guittard, M.; Laruelle, P. *Rev. Chim. Miner.* **1973**, *10*, 225–238.

[5]   Daszkiewicz, M; Gulay, L. D.; Lychmanyuk; O. S. *Acta Crystallogr. B* **2009**, *65*, 126–13.

[6]   Villars, P.; Cenzual, K. Pearson's Crystal Data – Crystal Structure Database for Inorganic Compounds (on DVD), Release 2015/16, ASM International, Materials Park, OH, USA.

[7]   Collin, G.; Flahaut, J. *C. R. Acad. Sci., Ser. C* **1970**, *270*, 488–490.

[8]   Perez, G.; Darriet-Duale, M.; Hagenmuller, P. *J. Solid State Chem.* **1970**, *2*, 42–48.

[9]   Jin, Z.; Li, Z.; Du, Y. *Yingyong Huaxue* **1985**, *2*, 42–46.

[10]   Meng, Y.; Fan, Y.; Lu, R.; Cui, Q.; Zou, G. *Physica* **1986**, *139&140B,* 337–340.

[11]   Gitzendanner, R. L.; Spencer, C. M.; DiSalvo, F. J.; Pell, M. A.; Ibers, J. A. *J. Solid State Chem.* **1996**, *131*, 399–404.

[12]   Huch, M. R.; Gulay, L. D.; Olekseyuk, I. D. *J. Alloys Compd.* **2006**, *424*, 114–118.

[13]   Gulay, L. D; Daszkiewicz, M.; Huch, M. R.; Pietraszko, A. *Acta Crystallogr., Sect. E*, **2007**, *63*, i187.

[14]   Guo S. P.; Guo G. C.; Wang M. S.; Zou J. P.; Xu G.; Wang G. J.; Long X. F.; Huang J.S. *Inorg. Chem.* **2009**, 48, 7059–7065.

[15]   Daszkiewicz, M.; Marchuk, O. V.; Gulay, L. D.; Kaczorowski, D. *J. Alloys Compd.* **2014**, 610, 258–263.

[16]   Daszkiewicz, M.; Pashynska, Y. O.; Marchuk, O. V.; Gulay, L. D.; Kaczorowski, D. *J. Alloys Compd.* **2014,** *616*, 243–249.

[17]   Assoud A.; Sankar C. R.; Kleinke H. *Solid State Sci.* **2014**, *38*, 124–128.

[18]   Strok, O. M.; Daszkiewicz, M.; Gulay, L. D. *Chem. Met. Alloys* **2015**, *8*, 16–21.

[19]   Daszkiewicz, M.; Pashynska, Y. O.; Marchuk, O. V.; Gulay, L. D.; Kaczorowski, D. *J. Alloys Compd* **2015**, *647*, 445–455.

[20]   He, J.; Wang, Z.; Zhang, X.; Cheng, Y.; Gong, Y.; Lai, X.; Zheng C.; Lin J.; Huang F. *RSC Adv.* **2015**, *5*, 52629–52635

[21]   Sun, Y. -L.; Chi, Y.; Guo, S. -P. *Jiegou Huaxue* **2016**, *35*, 1369–1375.

[22]   Iyer, A. K.; Yin, W.; Lee, E. J.; Lin, X; Mar, A. *J. Solid State Chem.* **2017**, *250*, 14–23.

[23]   Collin, G.; Étienne, J.; Laruelle, P. *Bull. Soc. Fr. Mineral. Cristallogr.* **1973**, *96*, 12–17.

[24]   Guo, S. P.; Zeng, H. Y.; Jiang, X. M.; Guo, G. C. *Jiegou Huaxue* **2009**, *28*, 1448–1452.

[25]   Zhao, H.-J. *J. Solid State Chem.* **2015**, *227*, 5–9.

[26]   de Saint-Giniez, D.; Laruelle, P.; Flahaut, J. *C. R. Acad. Sci., Ser. C* **1968**, *267*, 1029–1032.

[27]   Patrie, M.; Guittard, M. *C. R. Acad. Sci., Ser. C* **1969**, *268,* 1136–1138

[28]   Zeng, H. Y.; Zheng, F. K.; Guo, G. C.; Huang, J. S. *J. Alloys Compd.* **2008**, *458*, 123–129.

[29]   Gulay, L. D.; Daszkiewicz, M; Huch, M. R. *J. Solid State Chem.* **2008**, *181*, 2626–2632

[30]   Brese, N. E.; O'Keeffe, M. *Acta Crystallogr., Sect. B* **1991**, *47*, 192–197.

[31]   Mundus, C.; Taillades, G.; Pradel, A.; Ribes, M. *Solid State Nucl. Magn. Reson.* **1996**, *7*, 141–146.

[32]   Pietrass, T.; Taulelle, F. *Magn. Reson. Chem.* **1997**, *35*, 363–366.

[33]   Jiang, T.; Ozin, G. A.; Bedard, R. L. *J. Mater. Chem.* **1998**, *8*, 1641–1648.

[34]   MacKenzie, K.; Smith, M. E. *Multinuclear Solid-State Nuclear Magnetic Resonance of Inorganic Materials*, Elsevier, Oxford, **2002**.

[35]   Schevciv, O.; White, W. B. *Mater. Res. Bull.* **1983**, *18*, 1059–1068.

[36]   Sheldrick, G. M. *SHELXTL*, version 6.12; Bruker AXS Inc.: Madison, WI, 2001.

[37]   Gelato, L. M.; Parthé, E. *J. Appl. Crystallogr.* **1987**, *20*, 139–143

[38]   Harris, R. K.; Sebald, A. *Magn. Reson. Chem.* **1987**, *25*, 1058–1062.

[39]   Kortüm, G. *Reflectance Spectroscopy*, Springer, New York, **1969**.

[40]   Tank, R.; Jepsen, O.; Burkhardt, A.; Andersen, O. K. *TB-LMTO-ASA Program*, version 4.7; Max Planck Institut für Festkörperforschung: Stuttgart, Germany, **1998**.

Chapter 6

Noncentrosymmetric rare-earth selenides $RE_4InSbSe_9$ (RE = La–Nd)

6.1 Introduction

Quaternary chalcogenides containing rare-earth (RE) metals form a potentially large class of compounds given the numerous combinations possible with other components, frequently electropositive alkali or alkaline-earth metals.[1] Because they exhibit small band gaps, they have been identified as potential candidates for new optical semiconductors. For example, $AREMCh_3$ (A = alkali or alkaline-earth metal; RE = rare-earth metal; M = d-block metal; Ch = S, Se, Te) form a particularly rich series with optical band gaps that are typically less than 2.5 eV.[2] A more recent application of such chalcogenides is as thermoelectric materials, as exemplified by $Cs_xRE_2Cu_{6-x}Te_6$.[3] The RE–M–M'–Ch (M = d-block metal; M' = p-block metalloid; Ch = S, Se, Te) systems may be expected to be equally rich. Indeed, hundreds of representatives are known with the general formula $RE_3M_{1-x}M'Ch_7$.[4] However, unique structure types within these systems remain relatively limited. Two other series of compounds with identical compositions but different noncentrosymmetric structures, RE_4GaSbS_9 ($Aba2$) and RE_4InSbS_9 ($P4_12_12$), have been discovered recently and investigated for their nonlinear optical properties that originate from the asymmetric alignment of four-coordinate SbS_4 seesaw units exhibiting a stereochemically active lone pair.[5–8] Sm_4GaSbS_9 shows a large powder second harmonic generation (SHG) effect (with intensity 3.8 times that of $AgGaS_2$ in the same particle size range) but unfortunately it is not type-I phase matchable.[5] On the other hand, La_4InSbS_9 is type-I phase matchable but shows a weaker SHG effect (with intensity 1.5 times that of $AgGaS_2$).[6] Note that these RE_4MSbS_9 (M = Ga, In)

compounds are exclusively sulfides. It would thus be interesting to ascertain if the corresponding selenides RE_4MSbSe_9 could be prepared and to determine their physical properties.

In the course of systematically investigating the RE–M–Sb–Ch (M = Al, Ga, In; Ch = S, Se, Te) systems, we have prepared the new compounds $RE_4InSbSe_9$ (RE = La–Nd) which are the selenide analogues of RE_4InSbS_9. We report here the syntheses, crystal structures, optical spectra, and magnetic properties of these compounds.

6.2   Experimental

6.2.1   Synthesis

Freshly filed RE pieces (RE = La–Nd, 99.9%, Hefa), In powder (99.99%, Sigma-Aldrich), Sb powder (99.995%, Alfa-Aesar), and Se powder (99.99%, Sigma-Aldrich) were used as obtained. Binary starting materials Sb_2Se_3 and In_2Se_3 were prepared by stoichiometric reaction of the elements at 623 K and 873 K, respectively, in sealed fused-silica tubes. Crystals of $RE_4InSbSe_9$ (RE = La–Nd) were initially identified in reactions of mixtures of RE, In_2Se_3, Sb_2Se_3, and Se in a molar ratio of 8:1:1:12 and a total mass of ~0.3 g, which were pressed into pellets and loaded into fused-silica tubes, which were evacuated, sealed, and placed in a computer-controlled furnace. The tubes were heated to 1123 K over 30 h, kept at that temperature for 72 h, cooled to 573 K over 72 h, and then slowly cooled to room temperature by shutting off the furnace. Small black block-shaped air-stable crystals were obtained, but in low yields. Energy-dispersive X-ray (EDX) analyses, carried out on a JEOL JSM-6010LA scanning electron microscope, revealed that these crystals have a composition of 25(4)–32(3)% RE, 6(1)–7(1)% In, 6(1)–7(1)% Sb, and 53(3)–62(5)% Se, in reasonable agreement with the expected composition of 27% RE, 7% In, 7% Sb, and 60% Se. Attempts were made to extend the $RE_4InSbSe_9$ series to other trivalent RE metals (from Sm to Lu), using the same heating conditions as above, but these were unsuccessful.

Polycrystalline samples of $RE_4InSbSe_9$ (RE = La–Nd) were obtained in an optimized synthesis using a slightly different heat treatment. As before, mixtures of RE, In_2Se_3, Sb_2Se_3, and Se in a molar ratio of 8:1:1:12 were placed in evacuated and sealed fused-silica tubes. The tubes were heated to 1073 K over 24 h and kept there for 72 h, after which the furnace was turned off. The samples were reground, loaded into new tubes, and reheated at 1023 K for 96 h. Powder X-ray diffraction (XRD) patterns, collected on an Inel diffractometer equipped with a curved position-sensitive detector (CPS 120) and a Cu $K\alpha_1$ radiation source operated at 40 kV and 20 mA, revealed that the samples are essentially single-phase, within the limits of detection of crystalline phases by this technique (**Figure 6–1**).
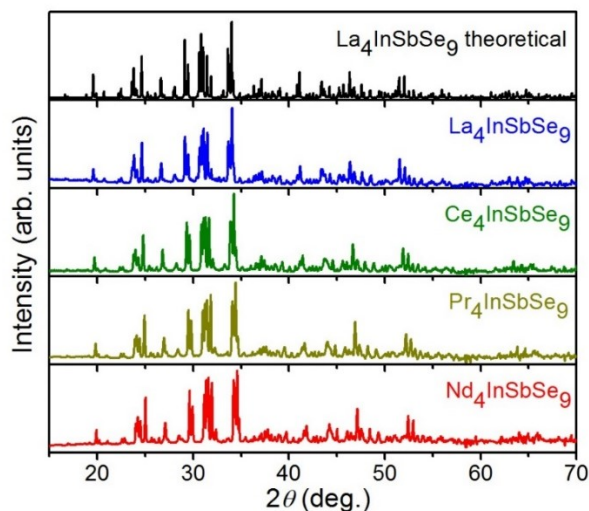
Figure 6-1. Powder XRD patterns of $RE_4InSbSe_9$ (RE = La–Nd).

6.2.2 Structure determination

Single crystals of suitable size and quality were available for all members of $RE_4InSbSe_9$ (RE = La–Nd). Intensity data were collected at room temperature on a Bruker PLATFORM diffractometer equipped with a SMART APEX II CCD area detector and a graphite-monochromated Mo $K\alpha$ radiation source, using ω scans at 5–7 different ϕ angles with a frame

width of 0.3º and an exposure time of 15–20 s per frame. Face-indexed numerical absorption corrections were applied. Structure solution and refinement were carried out with use of the SHELXTL (version 6.12) program package.[9] The Laue symmetry (4/m) and reflection conditions (00l, $l = 4n$; 0k0, $k = 2n$) established the chiral tetragonal space group $P4_12_12$ (or its enantiomorphic counterpart $P4_32_12$) as the only possibility. Direct methods revealed initial positions for all atoms, consistent with the La$_4$InSbS$_9$-type structure[7] in which In atoms occupy a tetrahedral site and Sb atoms occupy a more irregular site with seesaw coordination geometry. Refinements proceeded in a straightforward manner. The absolute configuration was determined by refining a Flack parameter, with inversion twinning being assumed. For the Nd-containing crystal, the Flack parameter of 0.04(3) indicated that the absolute configuration was correct in space group $P4_12_12$. For the other three crystals, the Flack parameter is close to 0.8, indicating that the majority twin component was in the opposite configuration. Instead of inverting the structure, which requires transformation to space group $P4_32_12$, we have opted to retain the structure description in $P4_12_12$ in accordance with standardization requirements recommended by the program STRUCTURE TIDY and consistent with earlier reports of this structure type listed in Pearson's Crystal Data. [10–11] This choice also facilitates comparison among the different compounds.

Crystal data and further details are listed in **Table 6–1**, positional and equivalent isotropic displacement parameters in **Table 6–2**, and interatomic distances in **Table 6–3**.

Table 6-1. Crystallographic data for $RE_4InSbSe_9$ (RE = La–Nd).

	La$_4$InSbSe$_9$	Ce$_4$InSbSe$_9$	Pr$_4$InSbSe$_9$	Nd$_4$InSbSe$_9$
Formula mass (amu)	1502.85	1507.69	1510.85	1524.17
Space group	$P4_12_12$ (No. 92)			
a (Å)	10.6499(4)	10.5725(4)	10.5208(7)	10.4777(4)
c (Å)	29.4790(12)	29.2989(11)	29.152(2)	29.0384(11)
V (Å^3)	3343.5(3)	3275.0(3)	3226.8(5)	3187.9(3)
Z	8			
ρ_{calcd} (g cm^{-3})	5.971	6.116	6.220	6.351
T (K)	296(2)	296(2)	296(2)	296(2)
Crystal dimensions (mm)	$0.06 \times 0.06 \times 0.05$	$0.06 \times 0.06 \times 0.05$	$0.04 \times 0.04 \times 0.04$	$0.05 \times 0.04 \times 0.04$
μ(Mo $K\alpha$) (mm^{-1})	32.50	33.87	35.17	36.40
Transmission factors	0.179–0.361	0.221–0.347	0.326–0.451	0.237–0.436
2θ limits	4.07–66.42°	4.10–66.45°	4.12–66.48°	4.13–66.31°
Data collected	$-16 \le h \le 16$, $-16 \le k \le 16$, $-45 \le l \le 45$	$-16 \le h \le 16$, $-16 \le k \le 16$, $-45 \le l \le 44$	$-16 \le h \le 16$, $-15 \le k \le 16$, $-44 \le l \le 44$	$-16 \le h \le 16$, $-15 \le k \le 16$, $-44 \le l \le 44$
No. of data collected	48694	47652	46534	46626
No. of unique data, including $F_o^2 < 0$	6394 (R_{int} = 0.104)	6273 (R_{int} = 0.094)	6190 (R_{int} = 0.154)	6074 (R_{int} = 0.121)
No. of unique data, with $F_o^2 > 2\sigma(F_o^2)$	5016	5086	4340	4659
No. of variables	138	138	138	138
Flack parameter	0.78(3)	0.84(2)	0.76(4)	0.04(3)
$R(F)$ for $F_o^2 > 2\sigma(F_o^2)$ [a]	0.043	0.039	0.052	0.046
$R_w(F_o^2)$ [b]	0.107	0.088	0.136	0.110
Goodness of fit	1.055	1.061	1.022	1.046
$(\Delta\rho)_{max}$, $(\Delta\rho)_{min}$ (e Å^{-3})	2.35, –1.94	2.10, –1.91	3.87, –2.43	2.69, –2.37

[a] $R(F) = \sum||F_o| - |F_c|| / \sum|F_o|$ for $F_o^2 > 2\sigma(F_o^2)$. [b] $R_w(F_o^2) = [\sum[w(F_o^2 - F_c^2)^2] / \sum wF_o^4]^{1/2}$; $w^{-1} = [\sigma^2(F_o^2) + (Ap)^2 + Bp]$, where $p = [\max(F_o^2,0) + 2F_c^2] / 3$.

Table 6-2. Atomic coordinates and equivalent isotropic displacement parameters (Å^2) for RE_4InSbSe$_9$ (RE = La–Nd).

Atom	Wyck. site	x	y	z	U_{eq} (Å^2) [a]
La$_4$InSbSe$_9$					
La1	8b	0.05647(8)	0.27147(8)	0.34087(3)	0.01666(16)
La2	8b	0.22240(8)	0.43929(8)	0.08696(3)	0.01675(16)
La3	8b	0.49038(8)	0.14964(7)	0.05327(2)	0.01754(16)
La4	8b	0.49636(9)	0.26872(7)	0.19914(2)	0.01862(15)
In	8b	0.01323(10)	0.19852(9)	0.20251(3)	0.0194(2)
Sb	8b	0.35947(10)	0.49085(12)	0.30433(4)	0.0288(2)
Se1	8b	0.00216(14)	0.39316(12)	0.15091(4)	0.0170(2)
Se2	8b	0.00470(13)	0.49529(13)	0.28044(4)	0.0156(2)
Se3	8b	0.00591(13)	0.00646(15)	0.14830(4)	0.0205(3)
Se4	8b	0.01949(14)	0.19050(13)	0.44989(4)	0.0190(3)
Se5	8b	0.20839(15)	0.19765(15)	0.25346(5)	0.0215(3)
Se6	8b	0.29826(14)	0.17795(14)	0.37692(4)	0.0172(3)
Se7	8b	0.30775(14)	0.20007(14)	0.12785(4)	0.0166(3)
Se8	8b	0.31968(14)	0.49210(16)	0.21181(4)	0.0218(3)
Se9	4a	0.31535(16)	0.31535(16)	0	0.0222(4)
Se10	4a	0.69157(17)	0.69157(17)	0	0.0393(7)
Ce$_4$InSbSe$_9$					
Ce1	8b	0.05756(7)	0.27190(6)	0.34126(2)	0.01642(14)
Ce2	8b	0.22235(6)	0.43844(7)	0.08702(2)	0.01603(13)
Ce3	8b	0.48969(7)	0.14984(6)	0.05333(2)	0.01706(14)
Ce4	8b	0.49644(7)	0.26807(6)	0.19932(2)	0.01787(13)
In	8b	0.01357(9)	0.19818(8)	0.20277(3)	0.01872(17)
Sb	8b	0.35887(8)	0.49094(10)	0.30454(3)	0.0269(2)
Se1	8b	0.00282(12)	0.39413(11)	0.15080(4)	0.0163(2)
Se2	8b	0.00491(11)	0.49606(11)	0.28054(4)	0.0151(2)
Se3	8b	0.00584(11)	0.00395(13)	0.14872(4)	0.0196(2)
Se4	8b	0.02106(12)	0.19076(12)	0.44994(4)	0.0181(2)
Se5	8b	0.20938(13)	0.19840(13)	0.25448(4)	0.0201(3)
Se6	8b	0.29930(12)	0.17726(12)	0.37691(4)	0.0163(2)
Se7	8b	0.30758(12)	0.19942(12)	0.12805(4)	0.0159(2)
Se8	8b	0.31907(12)	0.49060(13)	0.21170(4)	0.0200(2)
Se9	4a	0.31507(14)	0.31507(14)	0	0.0210(4)

Se10	4*a*	0.69285(15)	0.69285(15)	0	0.0412(6)
Pr₄InSbSe₉					
Pr1	8*b*	0.05774(11)	0.27239(10)	0.34146(3)	0.0177(2)
Pr2	8*b*	0.22254(10)	0.43863(11)	0.08700(3)	0.0177(2)
Pr3	8*b*	0.48942(11)	0.15035(10)	0.05347(3)	0.0188(2)
Pr4	8*b*	0.49665(12)	0.26757(10)	0.19942(3)	0.0190(2)
In	8*b*	0.01362(14)	0.19867(13)	0.20290(4)	0.0200(3)
Sb	8*b*	0.35812(13)	0.49063(17)	0.30464(5)	0.0272(3)
Se1	8*b*	0.0033(2)	0.39521(17)	0.15066(6)	0.0175(4)
Se2	8*b*	0.00494(18)	0.49665(18)	0.28049(6)	0.0160(3)
Se3	8*b*	0.00555(18)	0.0032(2)	0.14904(6)	0.0200(4)
Se4	8*b*	0.02179(19)	0.19097(19)	0.45006(6)	0.0189(4)
Se5	8*b*	0.2095(2)	0.1989(2)	0.25515(7)	0.0212(4)
Se6	8*b*	0.2995(2)	0.1770(2)	0.37695(6)	0.0174(4)
Se7	8*b*	0.3076(2)	0.19975(19)	0.12821(6)	0.0170(4)
Se8	8*b*	0.31878(19)	0.4896(2)	0.21151(6)	0.0209(4)
Se9	4*a*	0.3149(2)	0.3149(2)	0	0.0223(6)
Se10	4*a*	0.6941(2)	0.6941(2)	0	0.0429(10)
Nd₄InSbSe₉					
Nd1	8*b*	0.05798(9)	0.27283(8)	0.34172(3)	0.01730(17)
Nd2	8*b*	0.22281(8)	0.43856(9)	0.08696(3)	0.01658(17)
Nd3	8*b*	0.48889(9)	0.15071(8)	0.05353(3)	0.01790(17)
Nd4	8*b*	0.49688(10)	0.26695(8)	0.19950(3)	0.01839(16)
In	8*b*	0.01381(12)	0.19900(11)	0.20300(4)	0.0193(2)
Sb	8*b*	0.35777(11)	0.49047(14)	0.30483(4)	0.0254(3)
Se1	8*b*	0.00393(17)	0.39603(15)	0.15051(5)	0.0169(3)
Se2	8*b*	0.00507(15)	0.49725(15)	0.28041(5)	0.0154(3)
Se3	8*b*	0.00521(15)	0.00235(17)	0.14918(5)	0.0191(3)
Se4	8*b*	0.02291(16)	0.19119(16)	0.45006(5)	0.0180(3)
Se5	8*b*	0.20963(17)	0.19919(17)	0.25571(6)	0.0204(3)
Se6	8*b*	0.29969(16)	0.17706(17)	0.37693(5)	0.0166(3)
Se7	8*b*	0.30722(17)	0.19977(16)	0.12830(5)	0.0164(3)
Se8	8*b*	0.31905(16)	0.48873(18)	0.21136(5)	0.0199(3)
Se9	4*a*	0.31438(19)	0.31438(19)	0	0.0214(5)
Se10	4*a*	0.6948(2)	0.6948(2)	0	0.0431(9)

[a] Ueq is defined as one-third of the trace of the orthogonalized U_{ij} tensor.

Table 6-3. Interatomic distances (Å) for $RE_4InSbSe_9$ (RE = La–Nd).

	La$_4$InSbSe$_9$	Ce$_4$InSbSe$_9$	Pr$_4$InSbSe$_9$	Nd$_4$InSbSe$_9$
RE1–Se6	2.958(2)	2.937(2)	2.923(2)	2.910(2)
RE1–Se6	2.959(2)	2.935(2)	2.918(2)	2.903(2)
RE1–Se2	3.026(2)	3.015(1)	3.006(2)	3.001(2)
RE1–Se3	3.046(2)	3.022(1)	3.006(2)	2.993(2)
RE1–Se1	3.075(2)	3.044(1)	3.021(2)	3.002(2)
RE1–Se5	3.142(2)	3.106(2)	3.079(2)	3.059(2)
RE1–Se4	3.351(2)	3.320(1)	3.302(2)	3.281(2)
RE2–Se7	2.961(2)	2.940(1)	2.926(2)	2.913(2)
RE2–Se7	2.982(2)	2.960(1)	2.946(2)	2.934(2)
RE2–Se2	2.997(2)	2.970(1)	2.952(2)	2.938(2)
RE2–Se3	3.012(2)	2.986(1)	2.968(2)	2.955(2)
RE2–Se9	3.0486(8)	3.0270(7)	3.012(1)	2.9984(9)
RE2–Se1	3.049(2)	3.016(1)	2.995(2)	2.977(2)
RE3–Se2	2.965(1)	2.947(1)	2.934(2)	2.921(2)
RE3–Se7	2.984(2)	2.962(1)	2.946(2)	2.933(2)
RE3–Se6	3.002(2)	2.978(1)	2.960(2)	2.950(2)
RE3–Se9	3.0092(8)	2.9836(7)	2.966(1)	2.9497(9)
RE3–Se1	3.048(2)	3.020(1)	3.000(2)	2.984(2)
RE3–Se5	3.052(2)	3.022(2)	3.003(2)	2.988(2)
RE4–Se6	2.963(2)	2.943(1)	2.926(2)	2.914(2)
RE4–Se2	2.975(2)	2.947(1)	2.927(2)	2.910(2)
RE4–Se7	2.998(2)	2.979(1)	2.962(2)	2.953(2)
RE4–Se4	3.018(1)	2.995(1)	2.974(2)	2.962(2)
RE4–Se8	3.056(2)	3.030(2)	3.013(2)	2.998(2)
RE4–Se4	3.060(2)	3.032(1)	3.015(2)	2.999(2)
In–Se5	2.564(2)	2.565(2)	2.563(2)	2.560(2)
In–Se1	2.574(2)	2.574(1)	2.570(2)	2.568(2)
In–Se10	2.593(2)	2.585(2)	2.581(3)	2.577(2)
In–Se3	2.597(2)	2.594(2)	2.589(2)	2.588(2)
Sb–Se4	2.579(2)	2.578(2)	2.576(3)	2.576(2)
Sb–Se8	2.607(2)	2.606(2)	2.610(3)	2.606(2)
Sb–Se8	2.760(2)	2.752(2)	2.746(2)	2.744(2)
Sb–Se3	3.120(2)	3.121(2)	3.119(2)	3.111(2)

6.2.3 Diffuse reflectance spectroscopy

Spectra for $RE_4InSbSe_9$ (RE = La–Nd) were measured from 350 nm (3.54 eV) to 2000 nm (0.62 eV) on a Cary 5000 UV-vis-NIR spectrophotometer equipped with a diffuse reflectance accessory. A compacted pellet of $BaSO_4$ was used as a 100% reflectance standard. The optical absorption spectra were converted from the diffuse reflectance spectra using the Kubelka-Munk function, $\alpha/S = (1-R)^2/2R$, where α is the Kubelka–Munk absorption coefficient, S is the scattering coefficient, and R is the reflectance.[12]

6.2.4 Magnetic susceptibility measurements

Measurements of dc magnetic susceptibility were made on $RE_4InSbSe_9$ (RE = Pr, Nd) between 2 and 300 K under zero-field-cooled conditions with an applied field of 0.5 T on a Quantum Design 9T PPMS magnetometer equipped with the Model P500 option (ac/dc magnetometer system). The measurements were repeated by cooling the sample under an applied field of 0.5 T. Susceptibility values were corrected for contributions from the holder and sample diamagnetism.

6.3 Results and discussion

The compounds $RE_4InSbSe_9$ (RE = La–Nd) are the first quaternary phases found in the RE–In–Sb–Se system. They are the selenide analogues of RE_4InSbS_9 (RE = La, Pr, Nd, Sm).[7,8] The selenides were obtained in quantitative yield by reactions of RE, In_2Se_3, Sb_2Se_3, and Se at 1073 K followed by regrinding and reheating at 1023 K, whereas the sulfides were obtained by reactions of the elements at 1223 K. The occurrence of $Ce_4InSbSe_9$ suggests that Ce_4InSbS_9 also likely exists; on the other hand, attempts to substitute other RE components beyond Nd in $RE_4InSbSe_9$ were unsuccessful and the Sm member was not found. The selenides are black,

suggesting a smaller band gap than the sulfides, which are yellow. The tetragonal unit cell parameters in $RE_4InSbSe_9$ decrease regularly on proceeding to the smaller RE components, in accordance with the lanthanide contraction (**Figure 6–2**). The c/a ratios are essentially unchanged in both the sulfides (2.76) and the selenides (2.77), indicating that the structural expansion on proceeding to the larger selenides is isotropic.
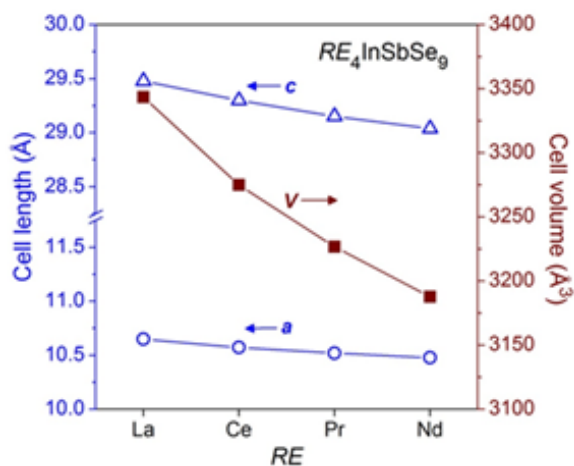
Figure 6-2. Unit cell lengths and volumes for $RE_4InSbSe_9$.

$RE_4InSbSe_9$ adopts the La_4InSbS_9-type structure[7], a unique one is so far limited to the eight compounds within the two series indicated above. The structure is quite complex, containing four RE, one In, one Sb, and ten Se sites, within the chiral space group $P4_12_12$. One-dimensional anionic chains $^1_\infty[In_2Sb_2Se_{11}]^{10-}$ spiral around the 2_1-axes parallel to the c-direction, and these chains are separated by the RE^{3+} cations as well as isolated Se^{2-} anions (**Figure 6–3**). Similar $[Ga_2Sb_2S_{11}]$ chains but with slightly different conformation are found in the closely related compounds RE_4GaSbS_9 (RE = Pr, Nd, Sm, Gd–Ho), which adopt the orthorhombic Sm_4GaSbS_9-type structure.[5,6]

144
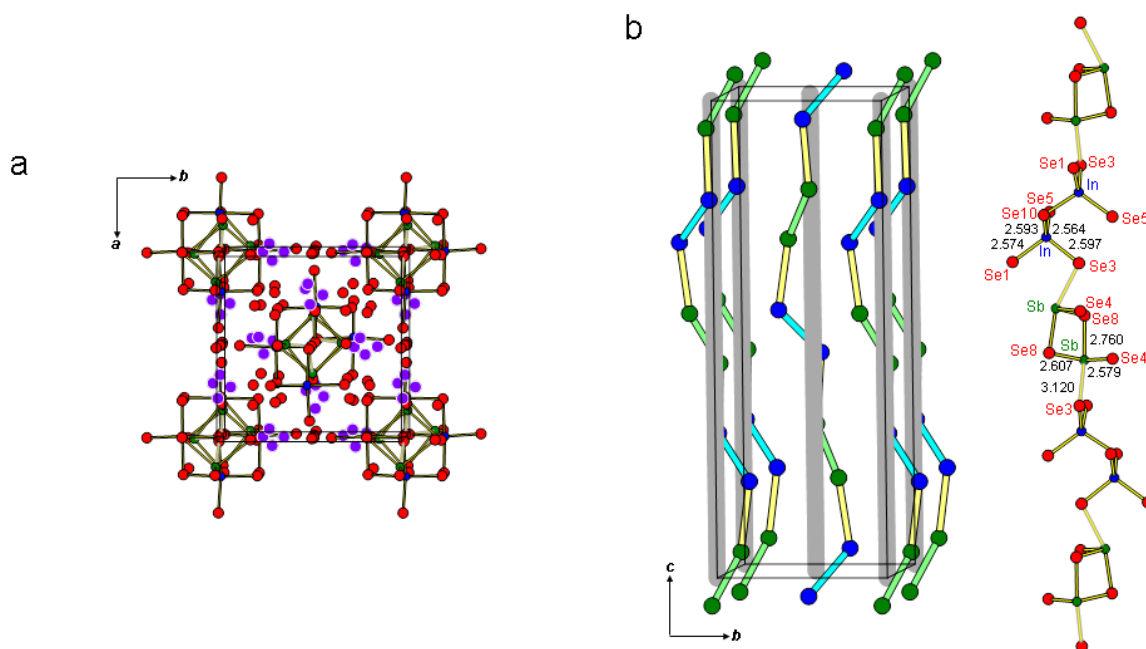
Figure 6-3. Structure of $RE_4InSbSe_9$ (RE = La–Nd) viewed (a) down the c-direction and (b) down the a-direction, highlighting the [$In_2Sb_2Se_{11}$] chains spiraling around 2_1-axes (grey) with only the In and Sb atoms shown (left), and an individual chain with bond lengths indicated for the La member (right).

In $RE_4InSbSe_9$, adjacent [$In_2Sb_2Se_{11}$] chains are related by 4_1-axes located along (0, ½, z) and (½, 0, z). These chains are built by linking two types of units (through corner-sharing of the Se3 atoms common to both units) in an alternating fashion: In_2Se_7 units formed by a pair of corner-sharing In-centred tetrahedra, and Sb_2Se_6 units formed by a pair of edge-sharing Sb-centred seesaws. The In-centred tetrahedra are fairly regular with In–Se bonds that are nearly equidistant (2.56–2.60 Å) and Se–In–Se angles that are close to ideal (106–113°, with an average of 109.4°). The In–Se distances agree well with those found in other structures containing corner-sharing $InSe_4$ tetrahedra (e.g., 2.55–2.58 Å in $CsInSe_2$, 2.51–2.63 Å in $Ba_2In_2Se_5$). [13–14] In contrast, the Sb-centred seesaws are highly irregular; the three shorter Sb–Se distances (2.58–2.76 Å) define a trigonal pyramid with narrow Se–Sb–Se angles (85–100°, with an average of 92°), and the fourth

Sb–Se distance is much longer (3.11–3.12 Å). This geometry (with CN3+1) is also found in the structure of Sb_2Se_3, with similar bond lengths and angles.[15] Both In–Se and Sb–Se distances are little changed upon *RE* substitution, which contracts the structure regularly. The *RE* atoms are surrounded by Se atoms in either monocapped trigonal prismatic (CN7 for *RE*1) or octahedral (CN6 for *RE*2, *RE*3, and *RE*4) coordination (**Figure 6–4**).
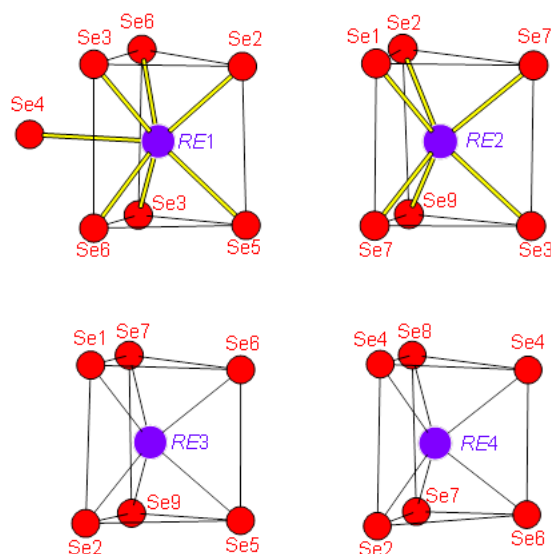
Figure 6-4. *RE* coordination polyhedra in $RE_4InSbSe_9$ (*RE* = La–Nd)

These compounds conform to the charge-balanced formulation $(RE^{3+})_4(In^{3+})(Sb^{3+})(Se^{2-})_9$. Bond valence sum calculations generally support the charge assignments (**Table 6–4**), although two of the Se atoms (Se5 and Se10) are somewhat underbonded. [16]

The occurrence of Sb^{3+} species is supported by the distorted geometry around these atoms associated with a stereochemically active lone pair. A narrower band gap is expected in these selenides compared to the corresponding sulfides. Accordingly, the optical absorption spectrum of $La_4InSbSe_9$ (**Figure 6–5**), converted from the UV-vis-NIR diffuse reflectance spectrum, reveals a band gap of 1.76(2) eV, which is about 0.3 eV smaller than that found in La_4InSbS_9 (2.07 eV).[7] The spectra for other members of $RE_4InSbSe_9$ are more complex because they contain additional

features arising from f-f transitions, but they indicate similar band gaps of 1.69 eV for $Ce_4InSbSe_9$, 1.89 eV for $Pr_4InSbSe_9$, and 1.57 eV for $Nd_4InSbSe_9$.

Table 6-4. Bond valence sums for $RE_4InSbSe_9$ (RE = La–Nd).

	La₄InSbSe₉	Ce₄InSbSe₉	Pr₄InSbSe₉	Nd₄InSbSe₉
*RE*1	2.9	3.1	3.1	3.2
*RE*2	2.9	3.1	3.1	3.1
*RE*3	2.9	3.1	3.1	3.1
*RE*4	2.9	3.1	3.1	3.1
In	3.0	3.0	3.0	3.0
Sb	2.7	2.7	2.7	2.8
Se1	2.0	2.1	2.2	2.2
Se2	2.0	2.2	2.1	2.1
Se3	1.8	1.9	1.9	1.9
Se4	2.1	2.1	2.1	2.2
Se5	1.5	1.6	1.6	1.6
Se6	2.2	2.3	2.3	2.3
Se7	2.1	2.2	2.2	2.2
Se8	1.9	2.0	2.0	2.0
Se9	1.8	2.0	1.9	2.0
Se10	1.4	1.5	1.5	1.5
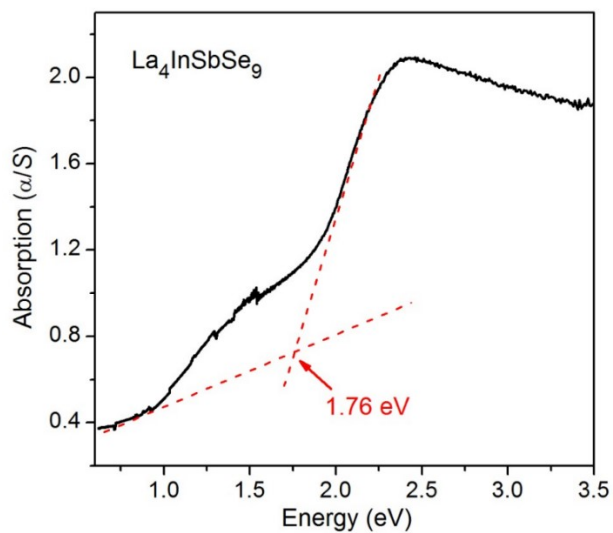
Figure 6-5. Diffuse reflectance spectrum for $La_4InSbSe_9$.

Some of the previously reported sulfides RE_4InSbS_9 are remarkable for exhibiting strong SHG effects despite crystallizing in a space group where such effects should be symmetry-forbidden.[7,8] However, among these sulfides, only the La and Sm members exhibit significant SHG effects, whereas the Pr and Nd members do not. Preliminary optical SHG measurements attempted on the corresponding selenides $RE_4InSbSe_9$ prepared here indicate that they only exhibit weak SHG effects. These observations suggest that the violation of symmetry requirements to permit SHG effects in these two series is highly sensitive to small changes in structure.

The temperature dependence of the magnetic susceptibility for $Pr_4InSbSe_9$ and $Nd_4InSbSe_9$ indicates paramagnetic behaviour with no transitions down to 2 K (**Figure 6–6**). The inverse magnetic susceptibility is linear for the Pr member and only shows a very slight curvature below 5 K for the Nd member. The inverse magnetic susceptibility curves were fit to the Curie-Weiss law ($\chi = C/(T-\theta_p)$). The effective magnetic moments ($\mu_{eff} = (8C)^{1/2}$) were found to be 7.25 μ_{eff}/f.u. (or 3.62 μ_B/Pr) for $Pr_4InSbSe_9$ and 7.28 μ_{eff}/f.u. (or 3.64 μ_B/Nd) for $Nd_4InSbSe_9$, in agreement with the expected free-ion values for trivalent RE (3.58 μ_B/Pr^{3+} and 3.62 μ_B/Nd^{3+}). The θ_p values are small and negative (–16 K for $Pr_4InSbSe_9$ and –10 K for $Nd_4InSbSe_9$), suggesting weak antiferromagnetic coupling between the RE atoms.
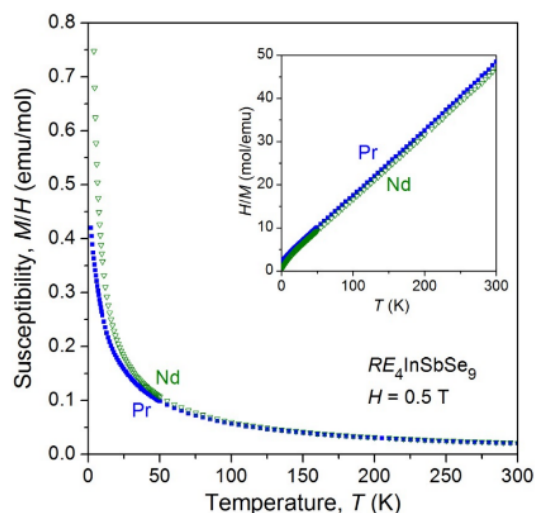
Figure 6-6. Magnetic susceptibility and its inverse (inset) for $RE_4InSbSe_9$ (RE = Pr, Nd).

6.4 Conclusions

The selenides $RE_4InSbSe_9$ adopt an unusual noncentrosymmetric structure type containing anionic helical chains $[In_2Sb_2Se_{11}]^{10-}$ all spiraling in the same direction. They possess smaller band gaps (by about 0.3 eV) than the isostructural sulfide analogues RE_4InSbS_9. Further substitutions (perhaps Bi for Sb) would be worthwhile attempting in hopes of improving the nonlinear optical properties of these compounds.

6.5 References

[1] Mitchell, K. A.; Ibers, J. A. *Chem. Rev.* **2002**, *102*, 1929–1952.
[2] Koscielski, L. A.; Ibers, J. A. *Z. Anorg. Allg. Chem.* **2012**, *638*, 2585–2593.
[3] Meng, C. -Y.; Chen, H.; Wang, P.; Chen, L. *Chem. Mater.* **2011**, *23*, 4910–4919.
[4] Iyer, A. K.; Yin, W.; Rudyk, B. W.; Lin, X.; Nilges, T.; Mar, A. *J. Solid State Chem.* **2016**, *243*, 221–231 and references therein.
[5] Chen, M. -C.; Li, L. -H.; Chen, Y.-B.; Chen, L. *J. Am. Chem. Soc.* **2011**, *133*, 4617–4624.
[6] Zhao, H. -J. *J. Solid State Chem.* **2016**, *237*, 99–104.
[7] Zhao, H. -J.; Zhang, Y. -F.; Chen, L. *J. Am. Chem. Soc.* **2012**, *134*, 1993–1995.
[8] Zhao, H. -J. *Z. Anorg. Allg. Chem.* **2016**, *642*. 56–59.
[9] Sheldrick, G. M. *SHELXTL*, version 6.12; Bruker AXS Inc.: Madison, WI, **2001**.
[10] Gelato, L. M.; Parthé, E. *J. Appl. Crystallogr.* **1987**, *20*, 139–143.
[11] Villars, P.; Cenzual, K. Pearson's Crystal Data – Crystal Structure Database for Inorganic Compounds (on DVD), release 2015/16, ASM International, Materials Park, OH, 2016.
[12] Kortüm, G. Reflectance Spectroscopy, Springer, New York, **1969**.

[13]   Ward, M. D.; Pozzi, E. A.; Van Duyne, R. P.; Ibers, J. A. *J. Solid State Chem.* **2014**, *212*, 191–196.

[14]   Eisenmann, B.; Hofmann, A.; *Z. Anorg. Allg. Chem.* **1990**, *580*, 151–159.

[15]   Tideswell, N. W.; Kruse, F. H.; McCullough, J. D. *Acta Crystallogr.* **1957**, *10*, 99–102.

[16]   Brese, N. E.; O'Keeffe, M. *Acta. Crystallogr., Sect. B* **1991**, *47*, 192–197.

Chapter 7

Quaternary rare-earth sulfides Nd$_7$FeInS$_{13}$ and Pr$_7$CoInS$_{13}$

7.1 Introduction

Rare-earth transition-metal chalcogenides adopt a diverse range of structures and exhibit interesting physical properties, including semiconducting behaviour and magnetic interactions.[1] Ternary phases among this family of chalcogenides have been well investigated, with thousands of representatives now reported.[2] Quaternary phases are potentially much more numerous, but only a small fraction of the combinations of components have been explored. Most of the known quaternary phases contain alkali or alkaline-earth metals, having been prepared through use of reactive chalcogenide fluxes containing these electropositive components.[3] Quaternary phases within the *RE–M–M′–Ch* (*M* = d-block metal; *M′* = p-block metal or metalloid; *Ch* = S, Se, Te) systems have so far been limited to only a few unique structure types. Among the ~550 entries in Pearson's database within these systems,[2] the vast majority belong to the *RE*$_3$*M*$_{1–x}$*M′Ch*$_7$ series (adopting the closely related La$_3$CuSiS$_7$, La$_3$Mn$_{0.5}$SiS$_7$, and La$_3$Ag$_{0.82}$SnS$_7$ hexagonal structure types).[4] Other series include *RE*$_2$CuIn*Ch*$_5$ (*Ch* = S, Se; La$_2$CuInS$_5$- or La$_2$CuInSe$_5$-type), *RE*CuPb*Ch*$_3$ (*Ch* = S, Se; HoCuPbS$_3$- or BaLaCuSe$_3$-type), *RE*$_5$CuPb$_3$Se$_{11}$ (Er$_5$CuPb$_3$Se$_{11}$-type), and *RE*$_2$Mn$_3$Sb$_4$S$_{12}$ (Pr$_2$Mn$_3$Sb$_4$S$_{12}$-type).[5–10]

Within the *RE–M*–In–S (*M* = first-row transition metal) systems, we recently identified the compounds *RE*$_3$FeInS$_7$ (*RE* = La–Pr), *RE*$_3$CoInS$_7$ (*RE* = La, Ce), and La$_3$NiInS$_7$ with hexagonal structures.[11] In the course of attempts to extend the range of *RE* substitution in this series, two

new quaternary phases, Nd_7FeInS_{13} and Pr_7CoInS_{13}, were discovered. We present here their crystal structures, which are of a new type, and draw relationships to other structures. Magnetic properties of Pr_7CoInS_{13} are also reported.

7.2 Experimental

7.2.1 Synthesis

Starting materials were freshly filed RE pieces (RE = Nd, Pr; 99.9%, Hefa), Fe powder (99.9%, Cerac), Co powder (99.9%, Sigma-Aldrich), In shot (99.99%, Cerac), and S flakes (99.998%, Sigma-Aldrich). Nd_7FeInS_{13} and Pr_7CoInS_{13} were originally identified as minor phases in reactions intended to prepare RE_3MInS_7 (M = Fe, Co) compounds.[11] Subsequently, reactions were performed using stoichiometric mixtures of the elements with the loading composition "RE_7MInS_{13}" and a total mass of 0.3 g. The mixtures were pressed into pellets (6 mm diameter, 1–3 mm thickness) and loaded into fused-silica tubes, which were evacuated and sealed. The tubes were heated at 1050 ºC for 3 d and cooled to room temperature over 30 h. The products were examined by powder X-ray diffraction (XRD) patterns (**Figure 7–1**), collected on an Inel diffractometer equipped with a curved position-sensitive detector (CPS 120) and a Cu $K\alpha_1$ radiation source operated at 40 kV and 20 mA. Regrinding and reheating eventually led to a sufficiently pure sample of Pr_7CoInS_{13} to enable magnetic measurements (see below). In the case of Nd_7FeInS_{13}, repeating this procedure up to five cycles did improve phase purity; however, the magnetic measurements on this sample appeared to suggest residual magnetic impurities that were not detected by XRD and are thus not reported because we are not confident about the reliability of these data. Attempts to substitute other trivalent RE components (all the way to Lu) using the same preparative conditions as above were unsuccessful. Lower heating temperatures led to

decomposition of RE_7MInS$_{13}$ into other phases. Grey prismatic crystals of Nd$_7$FeInS$_{13}$ and Pr$_7$CoInS$_{13}$ were examined on a JEOL JSM-6010LA InTouchScope scanning electron microscope (**Figure A2-1**). Energy-dispersive X-ray (EDX) analysis, averaged over 10 points on each crystal, indicated compositions of 31(2)–31(1)% RE, 3(2)–5(1)% M, 4(1)–5(1)% In, and 59(2)–62(3)% S, in good agreement with the expected composition of 31% RE, 5% M, 5% In and 59% S for RE_7MInS$_{13}$.
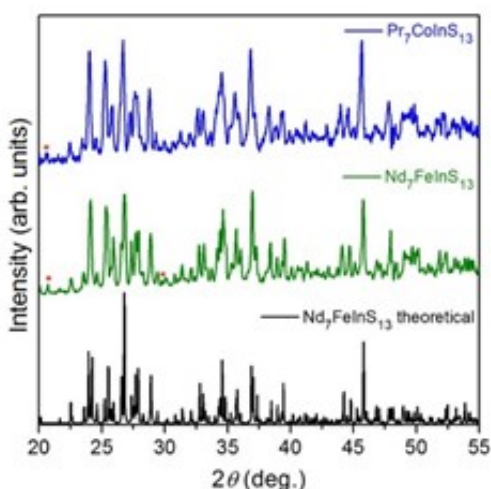
Figure 7-1. Powder XRD of Nd$_7$FeInS$_{13}$ and Pr$_7$CoInS$_{13}$.

7.2.2 Structure determination

Intensity data were collected for Nd$_7$FeInS$_{13}$ and Pr$_7$CoInS$_{13}$ on a Bruker PLATFORM diffractometer equipped with a SMART APEX II CCD detector and a graphite-monochromated Mo $K\alpha$ radiation source, using ω scans at 6–7 different ϕ angles with a frame width of 0.3º and an exposure time of 10–20 s per frame. Face-indexed numerical absorption corrections were applied. Structure solution and refinement were carried out with use of the SHELXTL (version 6.12) program package.[12] Laue symmetry, reflection conditions, and intensity statistics clearly established the centrosymmetric orthorhombic space group *Pnma* (No. 62). Direct methods

offered a sensible model consisting of seven *RE*, one *M*, one In, and thirteen Se sites, all in Wyckoff position 4*c*. The atomic coordinates were standardized with the program STRUCTURE TIDY. [13] Refinements proceeded smoothly, resulting in reasonable displacement parameters for all atoms, good agreement factors, and difference electron density maps that were reasonably clean considering the large number of heavy atoms in the structure; small residual peaks in the difference maps are likely attributed to absorption effects. The only possible ambiguity lies in the assignment of the *M* atoms within a tetrahedral site near 0.06, ¼, 0.15 and In atoms within an octahedral site near 0.05, ¼, 0.29. Additional refinements were performed in which each of these sites was allowed to contain a disordered mixture of both *M* and In atoms. In Nd_7FeInS_{13}, for example, the occupancies converged to 0.84(1) Fe / 0.16(1) In in the tetrahedral site and 0.00(1) Fe / 1.00(1) In in the octahedral site. Combined with the condition of a charge-balanced formula, these results favour an ordered model in which Fe atoms are found exclusively in the tetrahedral site and In atoms in the octahedral site. Additional support for this ordered model comes from a bond valence sum argument, discussed later.

Crystal data and further details are listed in **Table 7–1**, positional and equivalent isotropic displacement parameters in **Table 7–2**, and selected interatomic distances in **Table 7–3**.

Table 7-1. Crystallographic data for Nd_7FeInS_{13} and Pr_7CoInS_{13}.

Formula	**Nd_7FeInS_{13}**	**Pr_7CoInS_{13}**
Formula mass (amu)	1597.13	1576.90
Space group	*Pnma* (No. 62)	
a (Å)	11.2079(5)	11.2303(6)
b (Å)	3.9686(2)	3.9876(2)
c (Å)	44.1642(18)	44.506(2)
V (Å^3)	1964.41(15)	1993.07(18)
Z	4	
ρ_{calcd} (g cm^{-3})	5.400	5.255
T (K)	173(2)	296(2)
Crystal dimensions (mm)	$0.21 \times 0.04 \times 0.03$	$0.07 \times 0.02 \times 0.02$
μ(Mo $K\alpha$) (mm^{-1})	21.37	20.04
Transmission factors	0.086–0.669	0.411–0.757
2θ limits	3.69–66.40°	3.66–66.54°
Data collected	$-16 \le h \le 17$, $-6 \le k \le 6$, -67 $\le l \le 67$	$-17 \le h \le 17$, $-6 \le k \le 6$, -68 $\le l \le 68$
No. of data collected	27310	27381
No. of unique data, including $F_o^2 < 0$	4189 ($R_{int} = 0.048$)	4241 ($R_{int} = 0.125$)
No. of unique data, with $F_o^2 > 2\sigma(F_o^2)$	3642	2857
No. of variables	134	134
$R(F)$ for $F_o^2 > 2\sigma(F_o^2)$ [a]	0.029	0.042
$R_w(F_o^2)$ [b]	0.067	0.085
Goodness of fit	1.110	1.008
$(\Delta\rho)_{max}$, $(\Delta\rho)_{min}$ (e Å^{-3})	5.70, –4.81	4.55, –2.68

[a] $R(F) = \sum||F_o| - |F_c|| / \sum|F_o|$ for $F_o^2 > 2\sigma(F_o^2)$. [b] $R_w(F_o^2) = [\sum[w(F_o^2 - F_c^2)^2] / \sum wF_o^4]^{1/2}$; $w^{-1} = [\sigma^2(F_o^2) + (Ap)^2 + Bp]$, where $p = [\max(F_o^2, 0) + 2F_c^2] / 3$.

Table 7-2. Atomic coordinates and equivalent isotropic displacement parameters (Å^2) for Nd_7FeInS_{13} and Pr_7CoInS_{13}.

Atom	x	y	z	U_{eq} (Å^2) [b]
		Nd_7FeInS_{13}		
Nd1	0.00621(3)	¼	0.45657(2)	0.00703(8)
Nd2	0.08525(3)	¼	0.63062(2)	0.00690(8)
Nd3	0.12525(3)	¼	0.79936(2)	0.00616(7)
Nd4	0.22945(3)	¼	0.88878(2)	0.00797(8)
Nd5	0.26414(3)	¼	0.71647(2)	0.00741(8)
Nd6	0.34543(3)	¼	0.47732(2)	0.00871(8)
Nd7	0.35534(4)	¼	0.56801(2)	0.01214(9)
Fe	0.06305(9)	¼	0.14591(2)	0.00815(19)
In	0.05488(4)	¼	0.29451(2)	0.00705(9)
S1	0.02065(15)	¼	0.73885(4)	0.0075(3)
S2	0.06529(15)	¼	0.20123(4)	0.0080(3)
S3	0.08343(16)	¼	0.39315(4)	0.0077(3)
S4	0.10227(16)	¼	0.02075(4)	0.0082(3)
S5	0.13016(16)	¼	0.51718(4)	0.0091(3)
S6	0.25405(15)	¼	0.26437(4)	0.0065(3)
S7	0.31318(16)	¼	0.08666(4)	0.0082(3)
S8	0.34689(17)	¼	0.63231(4)	0.0118(3)
S9	0.35375(15)	¼	0.17632(4)	0.0070(3)
S10	0.35346(16)	¼	0.34682(4)	0.0085(3)
S11	0.37088(15)	¼	0.82879(4)	0.0068(3)
S12	0.44162(18)	¼	0.41787(4)	0.0149(4)
S13	0.80348(16)	¼	0.54854(4)	0.0080(3)

Atom	x	y	z	U_{eq} (Å^2) [b]
		Pr_7CoInS_{13}		
Pr1	0.00536(6)	¼	0.45629(2)	0.01114(13)
Pr2	0.08557(6)	¼	0.63070(2)	0.01061(13)
Pr3	0.12493(6)	¼	0.79952(2)	0.00949(13)
Pr4	0.22763(6)	¼	0.88915(2)	0.01093(13)
Pr5	0.26238(6)	¼	0.71664(2)	0.01136(13)
Pr6	0.34514(6)	¼	0.47760(2)	0.01230(14)
Pr7	0.35679(7)	¼	0.56821(2)	0.01684(15)
Co	0.06535(14)	¼	0.14744(4)	0.0112(3)
In	0.05619(7)	¼	0.29450(2)	0.01139(17)
S1	0.0178(3)	¼	0.73899(7)	0.0122(6)
S2	0.0663(2)	¼	0.20164(7)	0.0106(5)
S3	0.0841(3)	¼	0.39269(7)	0.0116(5)
S4	0.1022(3)	¼	0.02110(7)	0.0114(5)
S5	0.1302(3)	¼	0.51729(7)	0.0133(6)
S6	0.2551(3)	¼	0.26447(6)	0.0097(5)
S7	0.3118(3)	¼	0.08729(7)	0.0124(6)
S8	0.3495(3)	¼	0.63272(7)	0.0164(6)
S9	0.3547(3)	¼	0.17660(6)	0.0108(5)
S10	0.3578(3)	¼	0.34699(6)	0.0116(6)
S11	0.3696(3)	¼	0.82863(6)	0.0102(5)
S12	0.4404(3)	¼	0.41800(7)	0.0183(7)
S13	0.8045(3)	¼	0.54863(6)	0.0108(5)

[a] U_{eq} is defined as one-third of the trace of the orthogonalized U_{ij} tensor.

Table 7-3. Selected interatomic distances (Å) in Nd$_7$FeInS$_{13}$ and Pr$_7$CoInS$_{13}$.

	Nd$_7$FeInS$_{13}$	Pr$_7$CoInS$_{13}$
*RE*1–S5 (×2)	2.760(1)	2.770(2)
*RE*1–S7	2.886(2)	2.914(3)
*RE*1–S13 (×2)	2.922(1)	2.930(2)
*RE*1–S3	2.932(2)	2.965(3)
*RE*1–S5	3.016(2)	3.056(3)
*RE*2–S9 (×2)	2.912(1)	2.932(2)
*RE*2–S8	2.934(2)	2.965(3)
*RE*2–S3 (×2)	2.935(1)	2.948(2)
*RE*2–S11	2.998(2)	3.026(3)
*RE*2–S7 (×2)	3.000(1)	3.006(2)
*RE*3–S6 (×2)	2.856(1)	2.868(2)
*RE*3–S10 (×2)	2.896(1)	2.912(2)
*RE*3–S2 (×2)	2.915(1)	2.931(2)
*RE*3–S1	2.918(2)	2.950(3)
*RE*3–S11	3.044(2)	3.038(3)
*RE*4–S10 (×2)	2.870(1)	2.901(2)
*RE*4–S13	2.890(2)	2.901(3)
*RE*4–S3 (×2)	2.894(1)	2.910(2)
*RE*4–S12 (×2)	3.044(2)	3.031(3)
*RE*4–S11	3.088(2)	3.130(3)
*RE*5–S2 (×2)	2.836(1)	2.850(2)
*RE*5–S1	2.903(2)	2.921(3)
*RE*5–S6 (×2)	2.908(1)	2.923(2)
*RE*5–S9 (×2)	2.971(1)	2.980(2)
*RE*6–S4 (×2)	2.821(1)	2.841(2)
*RE*6–S13 (×2)	2.833(1)	2.857(2)
*RE*6–S12	2.838(2)	2.860(3)
*RE*6–S4	2.880(2)	2.887(3)
*RE*6–S5	2.987(2)	2.992(3)
*RE*7–S8	2.841(2)	2.872(3)
*RE*7–S7 (×2)	2.861(1)	2.877(2)
*RE*7–S4 (×2)	2.919(1)	2.930(2)
*RE*7–S12 (×2)	3.083(2)	3.088(3)
M–S8 (×2)	2.306(1)	2.306(2)
M–S10	2.371(2)	2.344(4)
M–S2	2.443(2)	2.412(3)
In–S9	2.596(2)	2.602(3)
In–S6	2.599(2)	2.603(3)
In–S1 (×2)	2.612(1)	2.624(2)
In–S11 (×2)	2.631(1)	2.641(2)

7.2.3 Magnetic susceptibility measurements

Measurements of dc magnetic susceptibility were made on Pr_7CoInS_{13} between 2 and 300 K under zero-field-cooled conditions with an applied field of 0.5 T on a Quantum Design 9T PPMS magnetometer. Susceptibility values were corrected for contributions from the holder and sample diamagnetism.

7.3 Results and discussion

Nd_7FeInS_{13} and Pr_7CoInS_{13} are new quaternary sulfides that are close in composition to the previously known compounds RE_3FeInS_7 (RE = La–Pr) and RE_3CoInS_7 (RE = La, Ce), which were also prepared at a similar temperature of 1050 ºC.[11] The range of RE substitution appears to be rather limited, with the RE_3MInS_7 series being restricted to the few largest RE components, and the RE_7MInS_{13} series to only one possible RE component, suggesting that their stability is primarily influenced by size factors. Indeed, RE_7MInS_{13} is not easy to synthesize, requiring multiple regrinding and reheating steps to achieve good phase purity.

An orthorhombic structure of a new type in space group $Pnma$ is adopted by Nd_7FeInS_{13} and Pr_7CoInS_{13}. For concreteness, we focus on Nd_7FeInS_{13} in the discussion below and arbitrarily designate it to be the name of this new structure type. In an ionic description, the structure consists of isolated Nd^{3+} cations, isolated S^{2-} anions, and two types of one-dimensional anionic chains extending along the b-direction (**Figure 7–2**).
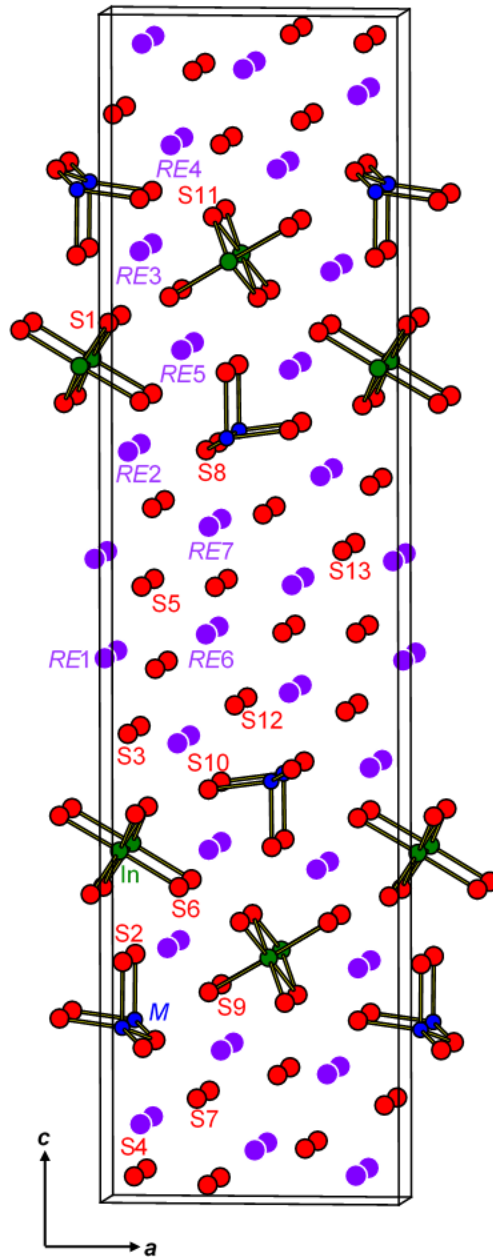
Figure 7-2. Structure of Nd_7FeInS_{13} and Pr_7CoInS_{13} viewed down the *b*-direction.

One chain is built of corner-sharing Fe-centred tetrahedra, $[FeS_2S_{2/2}]$, and another chain is built of edge-sharing In-centred octahedra, $[InS_2S_{4/2}]$ (**Figure 7–3**). The charge-balanced formulation is thus $(Nd^{3+})_7(Fe^{2+})(In^{3+})(S^{2-})_{13}$, or to emphasize the distinction between S atoms belonging to the chains and those that are isolated, it can be expressed as $(Nd^{3+})_7[FeS_3]^{4-}[InS_4]^{5-}$

$(S^{2-})_6$. Similar chains of corner-sharing M-centred tetrahedra are found in Ba_2FeS_3 and Ba_2CoS_3 (K_2CuCl_3-type) ,[14–21] and chains of edge-sharing In-centred octahedra are found in RE_3InS_6 ($RE =$ trivalent rare-earth metals; La_3InS_6-type).[22,23]
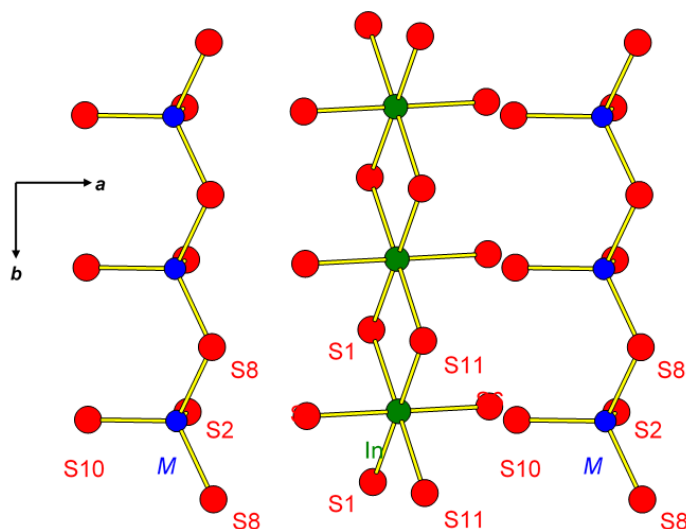
Figure 7-3. Chains of corner-sharing M-centred tetrahedra and edge-sharing In-centred tetrahedra in Nd_7FeInS_{13} and Pr_7CoInS_{13}

It is interesting to note that the occupations of the tetrahedral and octahedral sites are reversed in Nd_7FeInS_{13} (Fe tet, In oct) and RE_3FeInS_7 (Fe oct, In tet). Because both types of coordination geometries are suitable for Fe or In atoms, it is worthwhile examining the evidence more carefully to evaluate these assignments. In Nd_7FeInS_{13}, the bond distances to the surrounding S atoms are 2.31–2.44 Å around the tetrahedral Fe sites and 2.60–2.63 Å around the octahedral In sites. In RE_3FeInS_7 ($RE =$ La–Pr), the bond lengths are 2.53–2.61 Å around the octahedral Fe sites and 2.37–2.45 Å around the tetrahedral In sites.[11] The ranges of distances around the tetrahedral

sites overlap in both types of structures, raising the possibility that perhaps some disorder may be present. As a good benchmark, the structure of La_3InS_6 contains In atoms in both types of sites, the In–S distances being 2.44–2.50 Å around tetrahedral and 2.61–2.69 Å around octahedral sites.[22] Similarly, the structure of $La_2Fe_2S_5$ contains divalent Fe atoms in both types of sites, the Fe–S distances being 2.30–2.37 Å around tetrahedral and 2.45–2.67 Å around octahedral sites.[24] Comparison to the observed distances in Nd_7FeInS_{13} favours the existing assignment, on balance. Bond valence sum calculations provide further support.[25] In Nd_7FeInS_{13}, the bond valence sums are 2.4 around tetrahedral Fe sites and 3.0 around octahedral In sites, reasonably consistent with divalent Fe and trivalent In found in the charge-balanced formulation. If the site assignments are reversed, the bond valence sums become 1.8 around octahedral Fe sites and 4.1 around tetrahedral In sites, the latter value being unacceptably large. Lastly, given that Fe and In should be distinguishable from their X-ray scattering factors, refinements of the X-ray diffraction data on models allowing site disorder clearly showed a strong preference for Fe atoms within tetrahedral and In atoms within octahedral sites in Nd_7FeInS_{13}. As a check, refinements of the diffraction data for previously reported RE_3FeInS_7 confirmed the reverse preference.[11] The same conclusions hold for Pr_7CoInS_{13} vs. RE_3CoInS_7.

The Nd^{3+} cations in Nd_7FeInS_{13} are coordinated by S atoms in monocapped (CN7) or bicapped (CN8) trigonal prismatic geometry. Focusing on these Nd-centred trigonal prisms reveals that Nd_7FeInS_{13} contains fragments of two other sulfide structures (**Figure 7–4**). First, trigonal prisms extend as confacial columns which connect to neighbouring columns through edge-sharing to form characteristic channels defined by six-membered rings similar to the structure of Y_2HfS_5 (an antitype of Ce_5RuGe_2, which in turn is an ordered variant of β-Yb_5Sb_3).[26–28] These channels are filled with In and S atoms in Nd_7FeInS_{13}, or with Hf and S atoms in Y_2HfS_5. Second,

four trigonal prisms are grouped in tetrameric clusters such that two prisms are oriented perpendicular to the other two. Similar clusters are found in the structure of binary sulfides RE_2S_3 with the β-Cr_3C_2-type structure.[29] The connection of these two types of fragments generates additional trigonal prisms centred by Nd atoms and channels outlined by five-membered rings which are filled by Fe and S atoms.
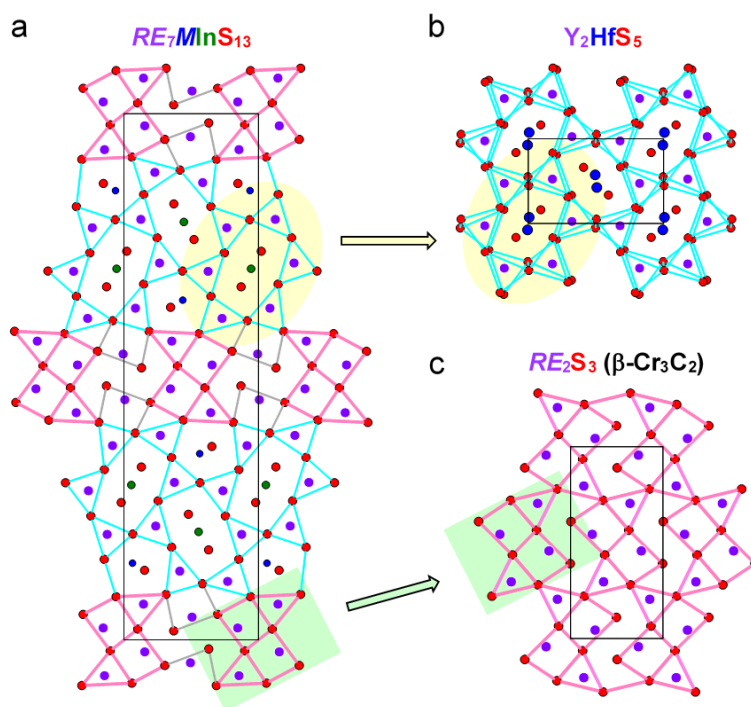
Figure 7-4. Structure of (a) Nd_7FeInS_{13} and Pr_7CoInS_{13} in terms of RE-centred trigonal prisms arrangements that are fragments of (b) Y_2HfS_5 and (c) RE_2S_3 (β-Cr_3C_2-type).

Temperature-dependent magnetic susceptibility measurements on Pr_7CoInS_{13} revealed paramagnetic behaviour (**Figure 7–5**). The inverse magnetic susceptibility is essentially linear, with only a small curvature barely noticeable below 50 K. Fitting of the inverse magnetic susceptibility from 50 to 300 K to the Curie-Weiss law, $\chi = C/(T-\theta_p)$, gave an effective magnetic moment $\mu_{eff} = 10.12(2)$ μ_B/f.u. (evaluated from the Curie constant through $\mu_{eff} = (8C)^{1/2}$) and a

paramagnetic Weiss temperature $\theta_p = -24(1)$ K. If free-ion values are taken for the magnetic moments of Pr^{3+} (3.58 μ_B) and Co^{2+} (3.87 μ_B, spin-only value), the expected effective magnetic moments for Pr_7CoInS_{13} calculated from $\mu_{eff} = \left(7\mu_{Pr}^2 + \mu_{Co}^2\right)^{1/2}$ would be 10.23 μ_B/f.u. if both types of moments contribute or 9.47 μ_B/f.u. if only Pr^{3+} moments contribute. Thus, the observed effective magnetic moment supports the assignment of Pr^{3+} and Co^{2+} with the magnetic moments of both species contributing. The negative Weiss temperature indicates nearest-neighbour antiferromagnetic coupling interactions, but no long-range ordering transitions are apparent in the magnetic susceptibility down to 2 K. An interesting comparison can be made to Ba_2CoS_3, [16–21] which also contains chains of corner-sharing Co-centred tetrahedra similar to those in Pr_7CoInS_{13}. The magnetic susceptibility of Ba_2CoS_3 shows a broad maximum in its magnetic susceptibility near 120 K and a highly negative Weiss temperature of –143 K, initially leading to proposals of low-dimensional (1D) antiferromagnetism.[17] While neutron diffraction experiments confirmed an antiparallel alignment of Co atoms within the chains, they also revealed significant interchain interactions.[20] In Pr_7CoInS_{13}, the intrachain Co–Co antiferromagnetic interactions appear to be suppressed, likely through additional coupling with the neighbouring Pr moments.
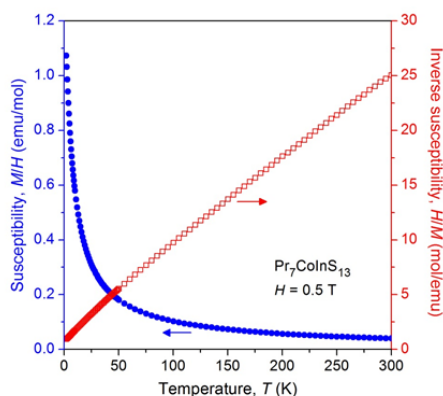
Figure 7-5. Magnetic susceptibility and its inverse for Pr_7CoInS_{13}.

7.4 Conclusions

Previously, we had proposed that the hexagonal RE_3FeInS_7 (RE = La–Pr) and RE_3CoInS_7 (RE = La, Ce) series was restricted to only the largest RE components because their structures were dominated by the size requirements of the large InS_4 tetrahedra present, which are isolated but must be stacked in registry with columns of face-sharing MS_6 octahedra.[11] Substitution with smaller RE components leads to the formation of Nd_7FeInS_{13} and Pr_7CoInS_{13} with close compositions but different structures in which the coordination geometries of M and In atoms are interchanged from those in RE_3FeInS_7 and RE_3CoInS_7. In both cases, it is interesting that the M-centred and In-centred polyhedra remain disconnected from each other.

7.5 References

[1]   Mitchell, K.; Ibers, J. A. *Chem. Rev.* **2002**, *102*, 1929–1952.
[2]   Villars, P.; Cenzual, K. Pearson's Crystal Data – Crystal Structure Database for Inorganic Compounds (on DVD), Release 2015/16, ASM International, Materials Park, OH, USA.
[3]   Kanatzidis, M. G.; Sutorik, A. C. *Prog. Inorg. Chem.* **1995**, *43*, 151–265.
[4]   Daszkiewicz, M; Gulay, L. D.; Lychmanyuk; O. S. *Acta Crystallogr. B* **2009**, *65*, 126–133.
[5]   Huch, M. R.; Gulay, L. D.; Olekseyuk, I. D.; Pietraszko, A. *J. Alloys Compd.* **2006**, *425* 230–234.
[6]   Huch, M. R.; Gulay, L. D.; Olekseyuk, I. D. *J. Alloys Compd.* **2007**, *439*, 156–161.
[7]   Gulay, L. D.; Olekseyuk, I. D.; Wołcryz, M.; Stępień-Damm, J. *J. Alloys Compd.* **2005**, *399*, 189–195.
[8]   Gulay, L. D.; Olekseyuk, I. D. *J. Alloys Compd.* **2005**, *387*, 160–164.
[9]   Gulay, L. D.; Stępień-Damm, J.; Pietraszko, A.; Olekseyuk, I. D. *J. Alloys Compd.* **2006**, *413*, 90–95.
[10]   Zhao, H. -J.; Li, L. -H.; Wu, L. -M.; Chen, L. *Inorg. Chem.* **2010**, *49*, 5811–5817.
[11]   Rudyk, B. W.; Stoyko, S. S.; Mar, A *J. Solid State Chem.* **2013**, *208*, 78–85.
[12]   Sheldrick, G. M. *SHELXTL*, version 6.12; Bruker AXS Inc.: Madison, WI, 2001.
[13]   Gelato, L. M.; Parthé, E. *J. Appl. Crystallogr.* **1987**, *20*, 139–143.
[14]   Hong, H. Y.; Steinfink, H. J. Solid State Chem. **1972**, *5*, 93–104.
[15]   Reiff, W. M.; Grey, I. E.; Fan, A.; Eliezer, Z.; Steinfink, H. *J. Solid State Chem.* **1975**, *13*, 32–40.
[16]   Nakayama, N.; Kosuge, K.; Kachi, S.; Shinjo, T.; Takada, T. *J. Solid State Chem.* **1980**, *33*, 351–356.
[17]   Baikie, T.; Maignan, A.; Francesconi, M. G. *Chem. Commun* **2004**, 836–837.
[18]   Baikie, T.; Hardy, V.; Maignan, A.; Francesconi, M. G. *Chem. Commun* **2005**, 5077–5079.
[19]   Barnes, A. D. J.; Baikie, T.; Hardy, V.; Lepetit, M. -B.; Maignan, A.; Young, N. A.; Francesconi, M. G. *J. Mater. Chem.* **2006**, *16*, 3489–3502.
[20]   Headspith, D. A.; Battle, P. D.; Francesconi, M. G. *J. Solid State Chem.* **2007**, *180*, 2859-2863.
[21]   Mezzadri, F.; Gilioli, E.; Calestani, G.; Migliori, A.; Harrison, M. R.; Headspith, D. A.;

Francesconi, M. G. *Inorg. Chem.* **2012**, *51*, 397–404.

[22]   Carré, D.; Guittard, M.; Adolphe, C. *Acta Cryst. Sect. B* **1978**, *34*, 3499–3501.

[23]   Aliev, O. M. *Inorg. Mater.* **1980**,*16*, 1027–1031 (Transl. *Neorg. Mater.* **1980**, *16*, 1514–1518.

[24]   Besrest, F.; Collin, G. *J. Solid State Chem.* **1977**, *21*, 161–170.

[25]   Brese, N. E.; O'Keeffe, M. *Acta. Crystallogr., Sect. B* **1991**, *47*, 192–197.

[26]   Donohue, P. C.; Jeitschko, W. *Mater. Res. Bull.* **1974**, *9*, 1333–1336.

[27]   Jeitschko, W.; Donohue, P.C. *Acta Crystallogr. Sect. B* **1975**, *31*, 1890–1895.

[28]   Gladyshevskii, R. E.; Cenzual, K.; Zhao, J. T.; Parthé, E. *Acta Cryst. Sect. C* **1992**, *48*, 221–225.

[29]   Sleight, A. W.; Prewitt, C. T. *Inorg. Chem.* **1968**, *7*, 2282–2288.

Chapter 8

Quaternary chalcogenides Ba*RE*₂In₂*Ch*₇ (*RE* = La–Nd; *Ch* = S, Se) containing In*Ch*₅ trigonal bipyramids

A version of this chapter has been published. Yin, W.; Iyer, A. K; Li, C.; Yao, J.; Mar, A. Dalton

*Trans. **2017**, 45, 12329–12337. Copyright (2016) by Royal Society of Chemistry.*

8.1 Introduction

Quaternary chalcogenides A–RE–M–Ch (where A = alkali or alkaline-earth metal; RE = rare-earth metal; M = d- or p-block metal or metalloid; Ch = S, Se, Te) exhibit considerable compositional and structural diversity arising from the nearly limitless ways of connecting coordination polyhedra.[1–5] They have provided many new candidates for materials applications resulting from several attractive features: they are usually semiconductors whose band gaps can be modified by judicious control of composition, they often contain magnetically active species in complex arrangements, and they are typically air-stable and thermodynamically robust. Some notable past examples include $Cs_xRE_2Cu_{6-x}Te_6$ as thermoelectric materials,[6] $AREMCh_3$ (A = Rb, Cs; M = divalent transition metals) as semiconductors with variable band gaps,[7–11] and $BaRE_2MS_5$ (M = Mn–Co) as antiferromagnets.[12–16]

Until recently, the systems A–RE–M–Ch (A = alkaline-earth metal; M = Ga, In) were poorly investigated. The few quaternary chalcogenides known in these systems were $AREGa_3S_7$ (A = Ca, Sr; RE = La, Ce),[17,18] $A_{1-x}Eu_xGa_2S_4$ (A = Sr, Ba),[19,20] and $CaYbInCh_4$ (Ch = S, Se),[21] with only the latter having ordered structures. Renewed efforts have led to the identification of many more compounds. Most of these compounds belong to five series having the same composition but adopting three different structure types containing Ga- or In-centred tetrahedra: Ba_2REGaS_5 ($I4/mcm$),[22] $Ba_2REGaSe_5$ ($P\bar{1}$),[23] $Ba_2REGaTe_5$ ($P\bar{1}$ and $Cmc2_1$),[24] $Ba_2REInSe_5$ ($Cmc2_1$),[23,25] and

Ba$_2$REInTe_5 ($Cmc2_1$).[22–24] A sixth series is Ba$_3$REInS$_6$ ($R\overline{3}c$), whose structure contains In-centred octahedra.[22] Among these compounds, Ba$_2$YInSe$_5$ exhibits a strong second harmonic generation (SHG) response close to that of AgGaSe$_2$, and Ba$_2$YInTe$_5$ is predicted to be a potentially good thermoelectric material.[23, 26]

In continuation of these efforts, we report here the new series of quaternary chalcogenides BaRE$_2$In$_2$Ch$_7$ (RE = La–Nd; Ch = S, Se) and the characterization of their crystal and electronic structures. We discuss structural relationships and examine the interesting coordination environment of the In atoms in these compounds.

8.2 Experimental

8.2.1 Synthesis

Ba rods (99%, Alfa-Aesar), freshly filed RE pieces (99.9%, Hefa), In powder (99.99%, Sigma-Aldrich), S flakes (99.998%, Sigma-Aldrich), Se powder (99.99%, Sigma-Aldrich), and BaS powder (99%, Alfa-Aesar) were used as obtained. Binary starting materials BaSe, In$_2$S$_3$, and In$_2$Se$_3$ were prepared by stoichiometric reaction of the elements at high temperatures (1173 K for BaSe, 1273 K for In$_2$S$_3$, and 873 K for In$_2$Se$_3$) in sealed fused-silica tubes.

Exploratory syntheses were initially carried out in the Ba–La–In–S system. The starting materials BaS, La, In$_2$S$_3$, and S were combined in the appropriate molar ratios to target the loading compositions BaLaInS$_4$, BaLaIn$_3$S$_7$, BaLa$_3$InS$_7$, and BaLa$_2$In$_2$S$_7$, each with a total mass of 0.3 g. The mixtures were pressed into pellets, loaded into fused-silica tubes which were evacuated and sealed, and placed into a computer-controlled furnace. The tubes were heated to 1323 K over 30 h, held at this temperature for 72 h, cooled slowly to 973 K over 96 h, cooled to 873 K over 24 h, and then cooled to room temperature over 24 h. Small black needle-shaped crystals were obtained

in low yield from the reactions with loading compositions $BaLaInS_4$ and $BaLaIn_3S_7$. These crystals were examined on a JEOL JSM-6010 LA scanning electron microscope and found by energy-dispersive X-ray (EDX) analysis to have the composition $BaLa_2In_2S_7$, as subsequently established by the structure determination. Attempts were made to substitute La with all other feasible trivalent RE metals (from Ce to Lu), using analogous loading compositions and temperature profiles as above. As confirmed by EDX analyses, crystals of $BaRE_2In_2S_7$ were obtained only for RE = Ce, Pr, and Nd from the reactions with loading compositions $BaREInS_4$ and $BaREIn_3S_7$. For other RE substitutions (RE = Sm, Gd–Lu), the desired $BaRE_2In_2S_7$ phase was not obtained under similar conditions. The reactions were extended to prepare the selenides using analogous loading compositions as before but with the temperature profile modified slightly so that the first step involves heating to 1273 K (instead of 1323 K) and with RE substitutions attempted for La–Dy. Crystals of $BaRE_2In_2Se_7$ were obtained from reactions with loading compositions $BaREIn_3Se_7$ for RE = La–Nd. Crystals of all $BaRE_2In_2Ch_7$ compounds are stable in air for months. EDX analyses of these crystals agreed well with expectations (**Table A3–1**).

Polycrystalline samples of $BaRE_2In_2Ch_7$ (RE = La–Nd; Ch = S, Se) were prepared by stoichiometric reaction of $BaCh$, RE, In_2Ch_3, and Ch in the molar ratio of 1:2:1:3. The mixtures were heated to 1073 K over 24 h and kept there for 48 h, after which the furnace was turned off. The samples were reground, loaded into new tubes, and reheated at 1073 K for 72 h. Powder X-ray diffraction (XRD) patterns were collected on an Inel diffractometer equipped with a curved position-sensitive detector (CPS 120) and a Cu $K\alpha_1$ radiation source operated at 40 kV and 20 mA (**Figure 8–1**). The samples contained the desired quaternary chalcogenides with varying amounts of $BaIn_2S_4$ or $BaIn_2Se_4$ as a byproduct. (**Figure A3–1**)
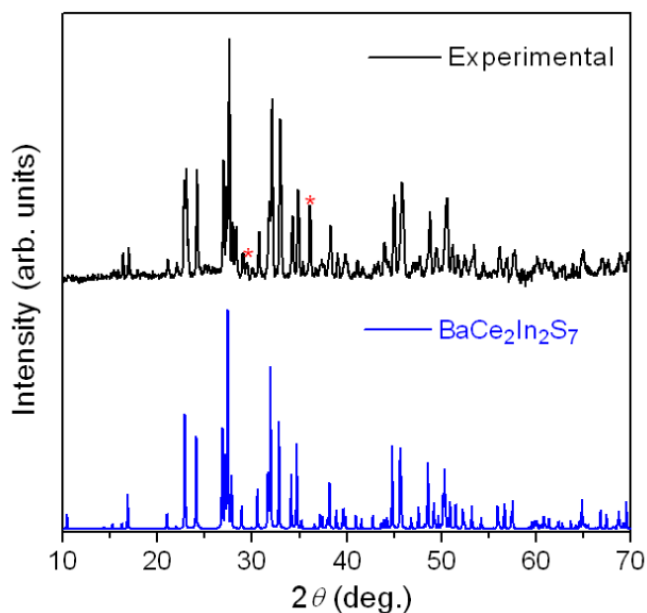
Figure 8-1. Powder XRD pattern of $BaCe_2In_2S_7$.

8.2.2 Structure determination

Single crystals of high quality and suitable size were available for the entire series $BaRE_2In_2Ch_7$ (RE = La–Nd; Ch = S, Se). Intensity data were collcted at room temperature on a Bruker PLATFORM diffractometer equipped with a SMART APEX II CCD area detector and a graphite-monochromated Mo $K\alpha$ radiation source, using ω scans at 5–8 different ϕ angles with a frame width of 0.3° and an exposure time of 15–20 s per frame. Face-indexed numerical absorption corrections were applied. Structure solution and refinement were carried out with use of the SHELXTL (version 6.12) program package.[27] The centrosymmetric orthorhombic space group *Pbam* was chosen on the basis of Laue symmetry and intensity statistics. Initial locations of all atoms were found by direct methods. The structure refinements for all compounds were straightforward, leading to excellent agreement factors (with conventional $R(F)$ values of 0.03–0.04) and featureless difference electron density maps (with $(\Delta\rho)_{max}$, $(\Delta\rho)_{min}$ values generally

around 3 and –3 e/Å^3, respectively). All atoms had reasonable displacement parameters and were confirmed to be fully occupied. Atom positions and labels were standardized with the program STRUCTURE TIDY.[28] Crystal data and further details are listed in **Table 8–1**, positional and equivalent isotropic displacement parameters Table 8–2, and interatomic distances in **Table 8–3**.

Table 8-1. Crystallographic data for BaRE_2In$_2Ch_7$ (RE = La–Nd; Ch = S, Se)

	BaLa$_2$In$_2$S$_7$	BaCe$_2$In$_2$S$_7$	BaPr$_2$In$_2$S$_7$	BaNd$_2$In$_2$S$_7$
Formula mass (amu)	869.22	871.64	873.22	879.88
Space group		*Pbam* (No. 55)		
a (Å)	11.6300(8)	11.5947(7)	11.5920(6)	11.5895(7)
b (Å)	12.4202(9)	12.3439(8)	12.3232(7)	12.3001(8)
c (Å)	4.0689(3)	4.0413(3)	4.0210(2)	4.0028(2)
V (Å^3)	587.74(7)	578.41(7)	574.40(5)	570.61(6)
Z		2		
ρ_{calcd} (g cm^{-3})	4.912	5.005	5.049	5.121
T (K)	296(2)	296(2)	296(2)	296(2)
Crystal dimensions (mm)	0.08 × 0.03 × 0.03	0.07 × 0.03 × 0.02	0.06 × 0.04 × 0.03	0.05 × 0.04 × 0.03
μ(Mo $K\alpha$) (mm^{-1})	15.46	16.19	16.86	17.54
Transmission factors	0.453–0.752	0.515–0.738	0.464–0.719	0.461–0.647
2θ limits	4.80–66.62°	4.82–66.58°	4.82–66.38°	4.83–66.55°
Data collected	$-17 \le h \le 17, -18 \le k \le 19, -6 \le l \le 6$	$-17 \le h \le 17, -18 \le k \le 19, -6 \le l \le 6$	$-17 \le h \le 17, -18 \le k \le 19, -6 \le l \le 6$	$-17 \le h \le 17, -18 \le k \le 18, -6 \le l \le 6$
No. of data collected	8324	8083	7994	8131
No. of unique data, including $F_o^2 < 0$	1261 (R_{int} = 0.052)	1239 (R_{int} = 0.060)	1228 (R_{int} = 0.060)	1228 (R_{int} = 0.046)
No. of unique data, with $F_o^2 > 2\sigma(F_o^2)$	1090	1022	1022	1061
No. of variables	40	39	39	40
$R(F)$ for $F_o^2 > 2\sigma(F_o^2)$ [a]	0.027	0.033	0.030	0.028
$R_w(F_o^2)$ [b]	0.058	0.075	0.063	0.062
Goodness of fit	1.104	1.127	1.141	1.186
$(\Delta\rho)_{max}$, $(\Delta\rho)_{min}$ (e Å^{-3})	1.91, −1.90	2.27, −1.89	2.21, −2.00	2.11, −1.91
	BaLa$_2$In$_2$Se$_7$	BaCe$_2$In$_2$Se$_7$	BaPr$_2$In$_2$Se$_7$	BaNd$_2$In$_2$Se$_7$
Formula mass (amu)	1197.52	1199.94	1201.52	1208.18
Space group	*Pbam* (No. 55)	*Pbam* (No. 55)	*Pbam* (No. 55)	*Pbam* (No. 55)
a (Å)	12.1515(6)	12.1364(7)	12.1433(8)	12.1358(10)

b (Å)	12.9367(7)	12.8927(8)	12.8798(9)	12.8510(11)
c (Å)	4.1966(2)	4.1741(3)	4.1547(3)	4.1363(4)
V (Å^3)	659.71(6)	653.13(7)	649.81(8)	645.09(10)
Z	2	2	2	2
ρ_{calcd} (g cm^{-3})	6.029	6.102	6.141	6.220
T (K)	296(2)	296(2)	296(2)	296(2)
Crystal dimensions (mm)	0.09 × 0.04 × 0.03	0.06 × 0.04 × 0.04	0.08 × 0.04 × 0.03	0.06 × 0.03 × 0.03
μ(Mo $K\alpha$) (mm^{-1})	31.98	32.73	33.39	34.13
Transmission factors	0.113–0.532	0.274–0.377	0.119–0.517	0.283–0.551
2θ limits	4.60–66.30°	4.61–66.50°	4.61–66.45°	4.62–66.49°
Data collected	$-18 \le h \le 18, -19 \le k \le 19, -6 \le l \le 6$	$-18 \le h \le 18, -19 \le k \le 19, -6 \le l \le 6$	$-18 \le h \le 18, -19 \le k \le 19, -6 \le l \le 6$	$-18 \le h \le 18, -19 \le k \le 19, -6 \le l \le 6$
No. of data collected	9266	9158	9108	9005
No. of unique data, including $F_o^2 < 0$	1407 (R_{int} = 0.053)	1403 (R_{int} = 0.054)	1392 (R_{int} = 0.059)	1391 (R_{int} = 0.089)
No. of unique data, with $F_o^2 > 2\sigma(F_o^2)$	1207	1195	1161	1062
No. of variables	40	40	40	39
$R(F)$ for $F_o^2 > 2\sigma(F_o^2)$ [a]	0.028	0.027	0.034	0.039
$R_w(F_o^2)$ [b]	0.060	0.059	0.077	0.085
Goodness of fit	1.144	1.148	1.136	1.119
$(\Delta\rho)_{max}, (\Delta\rho)_{min}$ (e Å^{-3})	1.72, −1.99	1.79, −2.33	4.52, −2.30	2.97, −2.43

[a] $R(F) = \sum||F_o| - |F_c|| / \sum|F_o|$ for $F_o^2 > 2\sigma(F_o^2)$. [b] $R_w(F_o^2) = [\sum[w(F_o^2 - F_c^2)^2] / \sum wF_o^4]^{1/2}$; $w^{-1} = [\sigma^2(F_o^2) + (Ap)^2 + Bp]$, where $p = [\max(F_o^2,0) + 2F_c^2] / 3$.

Table 8-2. Atomic coordinates and equivalent isotropic displacement parameters (Å^2) ^{a} for BaRE_2In$_2$Ch$_7$ (RE = La–Nd; Ch = S, Se)

	BaLa$_2$In$_2$S$_7$	BaCe$_2$In$_2$S$_7$	BaPr$_2$In$_2$S$_7$	BaNd$_2$In$_2$S$_7$
Ba in 2d (0, ½, ½)				
U_{eq}	0.01715(13)	0.01785(15)	0.01825(14)	0.01737(13)
RE in 4h (x, y, ½)				
x	0.11888(3)	0.11884(4)	0.11859(3)	0.11828(3)
y	0.14360(3)	0.14306(3)	0.14280(3)	0.14265(3)
U_{eq}	0.01111(9)	0.01228(11)	0.01274(9)	0.01186(10)
In in 4g (x, y, 0)				
x	0.28787(4)	0.28925(5)	0.29017(4)	0.29083(4)
y	0.37759(3)	0.37649(4)	0.37587(4)	0.37542(3)
U_{eq}	0.01363(11)	0.01501(13)	0.01475(11)	0.01297(11)
S1 in 4h (x, y, ½)				
x	0.35795(13)	0.36016(17)	0.36144(16)	0.36283(14)
y	0.28606(12)	0.28423(16)	0.28313(14)	0.28200(13)
U_{eq}	0.0138(3)	0.0157(3)	0.0161(3)	0.0144(3)
S2 in 4g (x, y, 0)				
x	0.08293(12)	0.08445(16)	0.08519(15)	0.08574(13)
y	0.30578(11)	0.30450(14)	0.30338(13)	0.30275(12)
U_{eq}	0.0123(3)	0.0133(3)	0.0136(3)	0.0119(3)
S3 in 4g (x, y, 0)				
x	0.28700(12)	0.28563(15)	0.28456(14)	0.28383(12)
y	0.06262(11)	0.06262(14)	0.06234(13)	0.06236(12)
U_{eq}	0.0123(3)	0.0131(3)	0.0132(3)	0.0125(3)
S4 in 2a (0, 0, 0)				
U_{eq}	0.0134(4)	0.0155(5)	0.0148(4)	0.0134(4)
	BaLa$_2$In$_2$Se$_7$	BaCe$_2$In$_2$Se$_7$	BaPr$_2$In$_2$Se$_7$	BaNd$_2$In$_2$Se$_7$
Ba in 2d (0, ½, ½)				
U_{eq}	0.01872(13)	0.01983(14)	0.02140(18)	0.0226(2)
RE in 4h (x, y, ½)				
x	0.11764(3)	0.11734(3)	0.11675(4)	0.11659(5)
y	0.14234(3)	0.14183(3)	0.14146(4)	0.14121(4)
U_{eq}	0.01258(10)	0.01350(10)	0.01438(12)	0.01612(14)
In in 4g (x, y, 0)				
x	0.28359(4)	0.28480(4)	0.28528(5)	0.28615(6)
y	0.37792(4)	0.37729(4)	0.37700(5)	0.37645(6)
U_{eq}	0.01523(11)	0.01579(11)	0.01570(14)	0.01717(17)
Se1 in 4h (x, y, ½)				
x	0.35742(6)	0.35925(6)	0.36031(8)	0.36180(9)
y	0.28372(5)	0.28261(5)	0.28194(7)	0.28109(8)
U_{eq}	0.01423(14)	0.01563(14)	0.01607(18)	0.0180(2)
Se2 in 4g (x, y, 0)				
x	0.07792(5)	0.07923(5)	0.07991(7)	0.08085(9)
y	0.30564(5)	0.30446(5)	0.30361(7)	0.30288(8)
U_{eq}	0.01326(14)	0.01393(14)	0.01423(18)	0.0155(2)
Se3 in 4g (x, y, 0)				

x	0.28859(5)	0.28731(5)	0.28621(7)	0.28535(9)
y	0.06481(5)	0.06478(5)	0.06491(7)	0.06494(8)
U_{eq}	0.01331(14)	0.01417(14)	0.01464(17)	0.0161(2)
Se4 in 2a (0, 0, 0)				
U_{eq}	0.01340(18)	0.01467(18)	0.0147(2)	0.0164(3)

Table 8-8-3. Interatomic distances (Å) for BaRE_2In$_2Ch_7$ (RE = La–Nd; Ch = S, Se)

	BaLa$_2$In$_2$S$_7$	BaCe$_2$In$_2$S$_7$	BaPr$_2$In$_2$S$_7$	BaNd$_2$In$_2$S$_7$
Ba–S3 (×4)	3.2986(11)	3.2952(14)	3.2968(13)	3.2971(12)
Ba–S2 (×4)	3.2997(11)	3.2963(14)	3.2998(13)	3.2984(12)
RE–S2 (×2)	2.8933(10)	2.8659(13)	2.8474(12)	2.8330(11)
RE–S3 (×2)	2.9955(10)	2.9679(13)	2.9541(12)	2.9431(11)
RE–S4 (×2)	3.0384(3)	3.0167(3)	3.0047(3)	2.9939(3)
RE–S1	3.1579(16)	3.131(2)	3.1175(19)	3.1022(17)
RE–S1	3.2956(16)	3.296(2)	3.3039(19)	3.3122(17)
In–S3	2.4576(15)	2.4562(19)	2.4558(17)	2.4568(16)
In–S1 (×2)	2.4689(9)	2.4609(12)	2.4558(11)	2.4540(10)
In–S2	2.5449(15)	2.5355(19)	2.5385(17)	2.5394(16)
In–S4	2.8979(5)	2.8801(6)	2.8734(5)	2.8679(5)
	BaLa$_2$In$_2$Se$_7$	BaCe$_2$In$_2$Se$_7$	BaPr$_2$In$_2$Se$_7$	BaNd$_2$In$_2$Se$_7$
Ba–Se2 (×4)	3.4089(5)	3.4112(5)	3.4139(7)	3.4142(9)
Ba–Se3 (×4)	3.4213(5)	3.4229(5)	3.4284(7)	3.4292(9)
RE–Se2 (×2)	3.0164(6)	2.9943(6)	2.9795(7)	2.9635(9)
RE–Se3 (×2)	3.1183(6)	3.0980(6)	3.0857(7)	3.0712(9)
RE–Se4 (×2)	3.1364(3)	3.1189(3)	3.1056(4)	3.0939(5)
RE–Se1	3.3036(8)	3.2802(8)	3.2666(11)	3.2493(13)
RE–Se1	3.4402(8)	3.4517(8)	3.4672(11)	3.4767(13)
In–Se3	2.5720(8)	2.5708(8)	2.5712(11)	2.5731(13)
In–Se1 (×2)	2.5870(5)	2.5811(5)	2.5777(6)	2.5732(8)
In–Se2	2.6684(8)	2.6657(8)	2.6670(11)	2.6648(13)
In–Se4	3.0675(5)	3.0536(5)	3.0509(7)	3.0424(8)

8.2.3 Diffuse reflectance spectroscopy

A compacted pellet of BaSO$_4$ was used as a 100% reflectance standard. Spectra for BaLa$_2$In$_2$S$_7$ and BaLa$_2$In$_2$Se$_7$ were collected from 300 nm (4.13 eV) to 2500 nm (0.50 eV) on a Cary 5000 UV-vis-NIR spectrophotometer equipped with a diffuse reflectance accessory. Optical absorption spectra were converted from the diffuse reflectance spectra using the Kubelka-Munk function,

$F(R) = \alpha/S = (1-R)^2/2R$, where α is the Kubelka-Munk absorption coefficient, S is the scattering coefficient, and R is the reflectance.[29]

8.2.4 Band structure calculations

Tight-binding linear muffin tin orbital band structure calculations on $BaLa_2In_2S_7$ and $BaLa_2In_2Se_7$ were performed within the local density and atomic spheres approximation with use of the Stuttgart TB-LMTO-ASA program (version 4.7).[30] The basis set consisted of Ba 6s/(6p)/5d/(4f), La 6s/(6p)/5d/(4f), In 5s/5p/(5d), and S 3s/3p/(3d) or Se 4s/4p/(4d) orbitals, with the orbitals shown in parentheses being downfolded. Integrations in reciprocal space were carried out with an improved tetrahedron method over 63 irreducible k points within the first Brillouin zone.

8.3 Results and discussion

The quaternary chalcogenides $BaRE_2In_2Ch_7$ (RE = La–Nd; Ch = S, Se) were obtained from high-temperature reactions of $BaCh$, RE, In_2Ch_3, and Ch. It was difficult to avoid formation of $BaIn_2Ch_4$ in polycrystalline samples prepared from reactions at 1073 K, even after regrinding and reheating; the best results were found for the La-containing samples, which contained ~5% of $BaIn_2Ch_4$. These compounds represent new series of quaternary chalcogenides found in the A–RE–In–(S, Se) systems (where A = alkaline-earth metal), in which Ba_3REInS_6 (RE = Pr, Sm, Gd, Yb),[22] $Ba_2REInSe_5$ (RE = Y, Nd, Sm, Gd, Dy, Er, Yb),[23,25] and $CaYbInCh_4$ (Ch = S, Se)[21] were previously known.

These chalcogenides adopt a new orthorhombic structure type (in space group $Pbam$) which can be considered to be an ordered variant of the $Eu_3Sn_2S_7$-type,[31] an exceedingly rare one that has been found for only three examples ($Eu_3Sn_2S_7$,[31,32] $Sr_3Sn_2S_7$,[33] and $Tl_3Cd_2I_7$ [34]). The unit

cell volumes decrease quite regularly on proceeding from La to Nd for the *RE* component within both the sulfide and selenide series, in accordance with the lanthanide contraction (**Figure 8–2**).
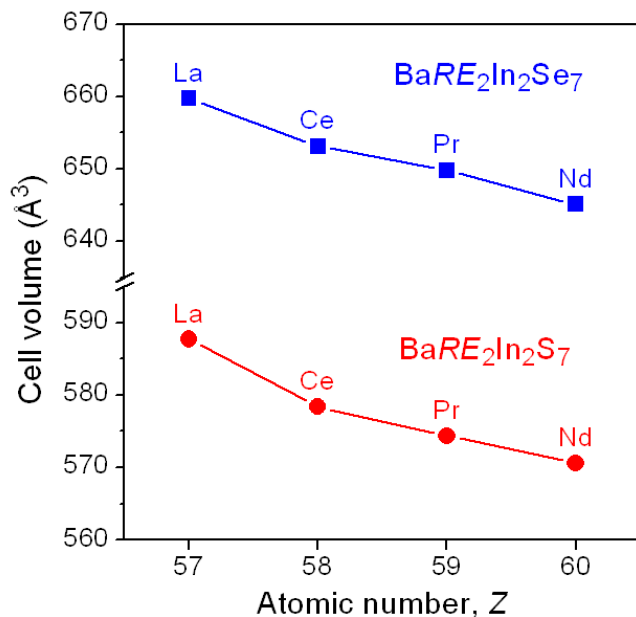
Figure 8-2. Plot of unit cell volumes for BaRE_2In$_2$$Ch_7$ (*RE* = La–Nd; *Ch* = S, Se).

For concreteness, we choose BaLa$_2$In$_2$S$_7$ to describe the structure and arbitrarily designate this member as the name of the structure type. The structure consists of one-dimensional arrangements of anionic [In$_2$S$_7$] ribbons which extend down the *c*-direction and are separated by Ba and La cations (**Figure 8–3**).

Figure 8-3. (a) Structure of BaRE_2In$_2$$Ch_7$ (RE = La–Nd; Ch = S, Se) viewed down the c-direction with one of the [In$_2$$Ch_7$] ribbons highlighted in polyhedral representation. (b) [In$_2$$Ch_7$] ribbon consisting of a double chain of corner-sharing InCh_5 trigonal bipyramids.
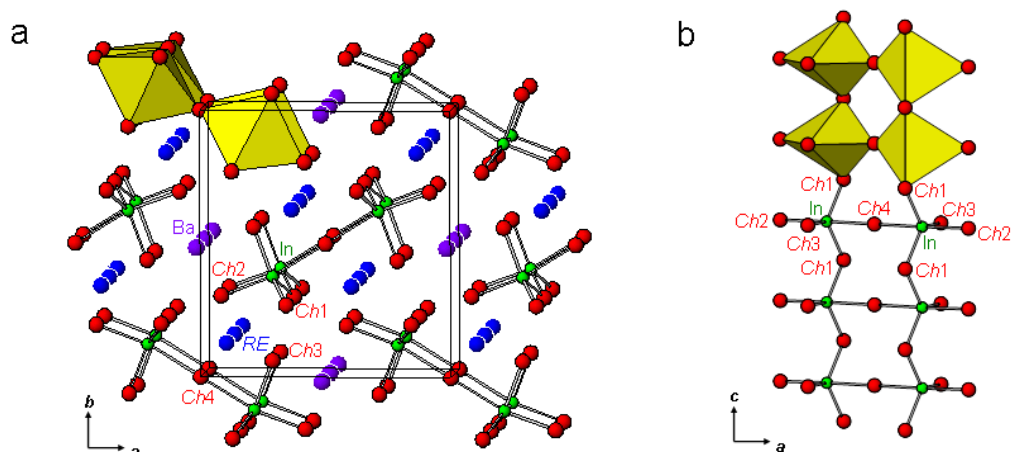
The local coordination geometries formed by the S atoms around the metal atoms are highly regular (**Figure 8–4**). The Ba atoms are centred within a slightly distorted cube (properly, a rectangular prism), with nearly equal Ba–S distances (3.2986(11)–3.2997(11) Å). Although eight-coordination is common for Ba atoms in many complex chalcogenides, cubic geometry is not typical.
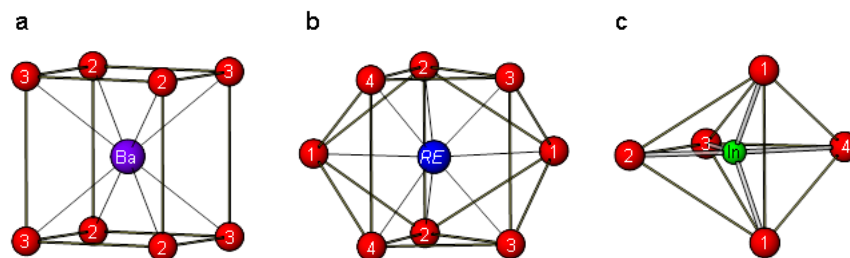
Figure 8-4. Coordination polyhedra in BaRE_2In$_2$$Ch_7$: (a) Ba in cubes (CN8), (b) RE in bicapped trigonal prisms (CN8), and (c) In in trigonal bipyramids (CN5).

177

A high-pressure form of BaS (with CsCl-type structure) exhibits Ba in cubic geometry;[35] BaS_3 contains Ba in cuboctahedral coordination (CN12) but if the four longer distances are neglected, then a cubic geometry is obtained.[36] The La atoms are also eight-coordinate but are centred within a bicapped trigonal prism, which is frequently observed, having shorter distances to the S atoms (2.8933(10)–3.2956(16) Å). The In atoms are five-coordinate and centred within a trigonal bipyramid, which is unusual. The distances from In to the three equatorial and one of the apical S atoms are short (2.4576(15)–2.5449(15) Å); the fifth distance to the remaining apical S atom is considerably longer (2.8979(5) Å). Thus it will be of interest to determine whether the fifth In–S distance is truly bonding and whether the coordination is more properly described as CN4+1. The same observation of a fifth longer distance applies to the In atoms within the corresponding quaternary selenides. In other In-containing chalcogenides, tetrahedral (CN4) and octahedral (CN6) coordination geometries are normally found around In atoms;[23–26] in contrast, examples of trigonal bipyramidal (CN5) geometry are few, being found in γ-In_2Se_3,[37,38] $AlInS_3$,[39] and $GaInS_3$.[40]

The In-centred trigonal bipyramids are connected in an interesting way. Pairs of InS_5 polyhedra are bridged by a common S4 atom to form In_2S_9 dimers, which then share corners, through the S1 atoms above and below along the c-direction, to form infinite double chains or ribbons with the formulation $[In_2S_5S_{4/2}]$, or $[In_2S_7]$. These one-dimensional ribbons are linked along the a-direction by the Ba atoms and along the b-direction by the La atoms to give the three-dimensional framework. This connectivity is quite different than found in the structures of other quaternary chalcogenides in the Ba–RE–M–Ch (M = Ga, In; Ch = S, Se) systems. More generally, the M-centred polyhedra are isolated, in the form of GaS_4 tetrahedra in Ba_2REGaS_5 (Cs_3CoCl_5-type),[22] $GaSe_4$ tetrahedra in $Ba_2REGaSe_5$ (Ba_2YGaSe_5-type),[23] and InS_6 octahedra in Ba_3REInS_6

($K_3NaFeCl_6$-type).[22] An exception is $Ba_2RE InSe_5$ (Ba_2BiInS_5-type), where $InSe_4$ tetrahedra share corners to form infinite chains.[23] As the RE component is changed in $BaRE_2In_2S_7$, the In_2S_9 dimers remain quite rigid, the bond lengths and angles varying little. Because the angle around the briding S4 atom is constrained by symmetry to be exactly 180°, the In_2S_9 dimer cannot distort by bending at this atom. Rather, the main effect is that the S1–In–S1 angle around the equatorial waist of each of the InS_5 trigonal bipyramids becomes slightly narrower (from 110.98(6)° in $BaLa_2In_2S_7$ to 109.28(6)° in $BaNd_2In_2S_7$), causing an overall compression of the $[In_2S_7]$ ribbons along c (which is the cell parameter that experiences the greatest contraction, by about 1.6%, upon substitution of the RE component). A less pronounced compression (with the Se1–In–Se1 angles decreasing from 108.41(3)° in $BaLa_2In_2Se_7$ to 106.97(5)° in $BaNd_2In_2Se_7$) is seen for the selenides $BaRE_2In_2Se_7$.

The quaternary chalcogenide $BaLa_2In_2S_7$ is easily derived from the ternary chalcogenide $Eu_3Sn_2S_7$ by comparing their charge-balanced formulations, $(Ba^{2+})(La^{3+})_2(In^{3+})_2(S^{2-})_7$ and $(Eu^{2+})_3(Sn^{4+})_2(S^{2-})_7$. To maintain charge neutrality, the aliovalent substitution of two Sn^{4+} cations in $Eu_3Sn_2S_7$ with two In^{3+} cations requires charge compensation as manifested by replacement of the electropositive divalent components with trivalent ones, to result in $BaLa_2In_2S_7$. Of the two Eu sites (both CN8) in $Eu_3Sn_2S_7$, the one in $2d$ having cubic coordination is slightly larger (with average Eu–S distance of 3.178 Å) than the one in $4h$ having bicapped trigonal prismatic coordination (with average Eu–S distance of 3.076 Å).[31] Correspondingly, in $BaLa_2In_2S_7$, the larger Ba atoms prefer the $2d$ site (with average Ba–S distance of 3.299 Å) while the smaller La atoms prefer the $4h$ site (with average La–S distance of 3.038 Å). The charge-balanced assignment is supported by calculations of bond valence sums[41] for all members of $BaRE_2In_2Ch_7$ (**Table 8–4**). These bond valence sums are 1.8–1.9 for the Ba atoms, 2.7–2.9 for the RE atoms, 3.0–3.2 for the In atoms, and 1.8–2.1 for the Ch atoms.

Table 8-4. Bond valence sums for BaRE$_2$In$_2$Ch$_7$ (RE = La–Nd; Ch = S, Se)

	BaLa$_2$In$_2$S$_7$	BaCe$_2$In$_2$S$_7$	BaPr$_2$In$_2$S$_7$	BaNd$_2$In$_2$S$_7$
Ba	1.91	1.93	1.92	1.92
RE	2.87	2.91	2.86	2.87
In	3.10	3.16	3.18	3.19
S1	1.91	2.02	1.94	1.94
S2	2.09	2.13	2.12	2.13
S3	2.01	2.04	2.02	2.02
S4	1.83	1.86	1.84	1.85
	BaLa$_2$In$_2$Se$_7$	BaCe$_2$In$_2$Se$_7$	BaPr$_2$In$_2$Se$_7$	BaNd$_2$In$_2$Se$_7$
Ba	1.88	1.87	1.85	1.85
RE	2.72	2.86	2.80	2.83
In	3.00	3.04	3.05	3.07
Se1	1.83	1.86	1.86	1.87
Se2	2.01	2.07	2.05	2.07
Se3	1.94	1.98	1.96	1.96
Se4	1.77	1.85	1.83	1.84

The electronic band structures were calculated for BaLa$_2$In$_2$S$_7$ and BaLa$_2$In$_2$Se$_7$; as the results are similar, only the former is discussed in detail here. The density of states (DOS) curve shows a gap of 1.55 eV between valence and conduction bands in BaLa$_2$In$_2$S$_7$ (**Figure 8–5a**). Band dispersion curves (not shown here) indicate that BaLa$_2$In$_2$S$_7$ is a direct band gap semiconductor at the Brillouin zone centre (Γ). As confirmed by the atomic projections of the DOS curve, the more electropositive Ba and La atoms contribute mostly to empty states above the Fermi level while the more electronegative In and S atoms contribute mostly to filled states below. However, there is some interaction of Ba and La s-orbitals with S p-orbitals, giving rise to covalent contributions to Ba–S and La–S bonding, as seen in the crystal orbital Hamilton population (COHP) curves (**Figure 8–5b**).
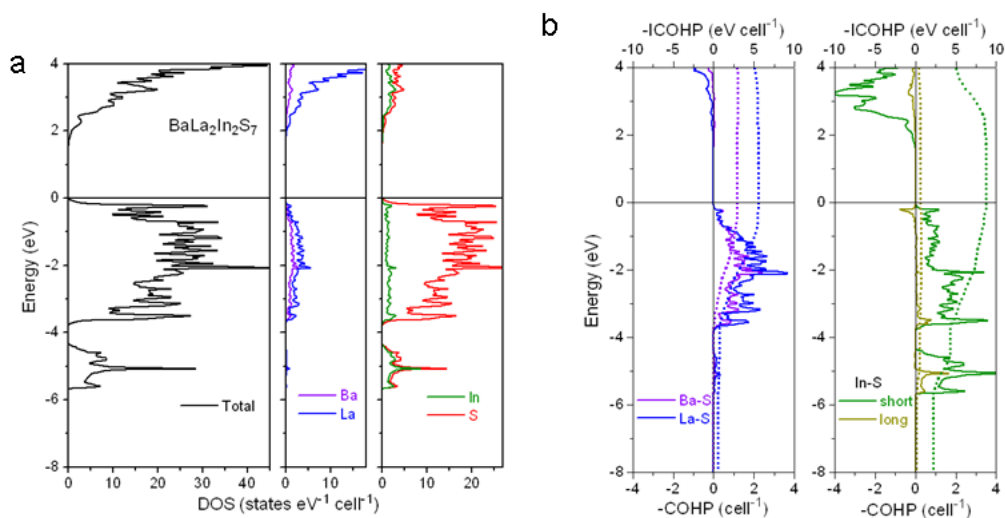
Figure 8-5. (a) Density of states (DOS) and (b) crystal orbital Hamilton population (–COHP) curves for BaLa$_2$In$_2$S$_7$.

These are non-negligible interactions, as gauged by the integrated COHP (–ICOHP) values of 0.37 eV/bond (or 2.9 eV/cell) for Ba–S and 0.69 eV/bond (or 5.5 eV/cell) for La–S contacts. The S p-orbitals are also mixed with In s-orbitals (at –5.7 to –4.2 eV) and In p-orbitals (at –3.8 to 0 eV), resulting in strong bonding interactions within the InS$_5$ trigonal bipyramid. Close inspection of the COHP curves reveals a clear distinction between the four short In–S contacts, for which bonding is optimized with filling of all bonding and no antibonding levels, and the fifth longer one, for which antibonding levels involving overlap of In p and S p orbitals are found just below the Fermi level. Nevertheless, this long In–S bond cannot be dismissed, as its strength is about 28% (–ICOHP of 0.62 eV/bond) that of the other four In–S bonds (–ICOHP of 2.18 eV/bond). Analogous conclusions can be drawn for the selenide BaLa$_2$In$_2$Se$_7$, for which the calculated band gap is smaller (0.92 eV) and the fifth long In–Se bond is about 25% (–ICOHP of 0.51 eV/bond) as strong as the other four In–Se bonds (–ICOHP of 2.06 eV/bond) (**Figure. A3–2**). A correct description of the coordination around the In atoms in Ba*RE*$_2$In$_2$*Ch*$_7$ is thus CN4+1, as proposed

181

above, and similarly for the Sn atoms in $Eu_3Sn_2S_7$ and $Sr_3Sn_2S_7$. In contrast, $Tl_3Cd_2I_7$ presents an interesting case where the fifth Cd–I bond is much longer (3.659 Å) than the other four (2.747–2.882 Å);[34] band structure calculations on this compound (not show) indicate that this long bond is much weaker (–ICOHP of 0.18 eV/bond) than the other four bonds (–ICOHP of 1.80 eV/bond), so that CN4 is more appropriate here.

UV-vis-NIR diffuse reflectance spectra were obtained for $BaLa_2In_2S_7$ and $BaLa_2In_2Se_7$ (**Figure 8–6**), which are predicted to be direct band gap semiconductors from the band structure calculations. The experimental optical band gaps, as deduced from plots of $(h\nu{\cdot}F(R))^2$ versus $h\nu$ through the straightforward extrapolation method,[42] were 1.87(2) eV for $BaLa_2In_2S_7$ and 1.66(2) eV for $BaLa_2In_2Se_7$, consistent with the black colour of these compounds.
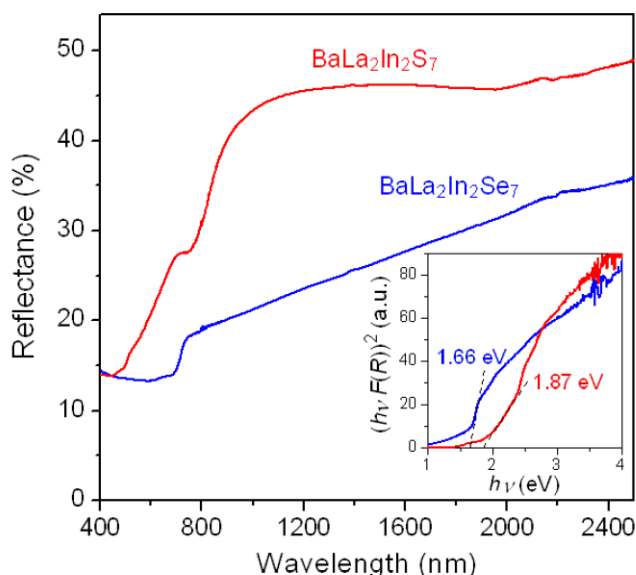
Figure 8-6. Optical spectra for $BaLa_2In_2S_7$ and $BaLa_2In_2Se_7$.

8.4 Conclusions

The new chalcogenides $BaRE_2In_2Ch_7$ further exemplify the potential richness of the quaternary Ba–RE–M–Ch (M = Ga, In; Ch = S, Se) systems and offered a new surprise in the form

of an unusual motif of InCh_5 trigonal bipyramids, different from the more typical occurrence of tetrahedra (and less commonly, octahedra) in the previously known series. The relationship between the BaLa$_2$In$_2$S$_7$ and Eu$_3$Sn$_2$S$_7$ structure types illustrated here may serve as inspiration to target other substitutions that maintain the same electron count. Substitution of the electropositive components with combinations of alkali, alkaline-earth, or other rare-earth metals would seem likely.

8.5   References

[1]   Wu, P.; Ibers, J. A. *J. Alloys Compd.* **1995**, *229*, 206–215.

[2]   Mitchell, K.; Ibers, J. A. *Chem. Rev.* **2002**, *102*, 1929–1952.

[3]   Gulay L. D.; Daszkiewicz, M. in *Handbook on the Physics and Chemistry of Rare Earths*, eds. Gschneidner, , Jr., K. A.; Bünzli, J.-C. G.; Pecharsky, V. K. Elsevier, Amsterdam, **2011**, 157–273.

[4]   Chung, I.; Kanatzidis, M. G. *Chem. Mater.* **2014**, *26*, 849–869.

[5]   Zhou, J. *Coord. Chem. Rev.* **2016**, *315*, 112–134.

[6]   Meng, C. -Y.; Chen, H.; Wang, P.; Chen, L. *Chem. Mater.* **2011**, *23*, 4910–4919.

[7]   Mitchell, K.; Haynes, C. L.; McFarland, A. D.; Van Duyne, R. P.; Ibers, J. A. *Inorg. Chem.* **2002**, *41*, 1199–1204.

[8]   Mitchell, K.; Huang, F. Q.; McFarland, A. D.; Haynes, C. L.; Somers, R. C.; Van Duyne, R. P.; Ibers, J. A. *Inorg. Chem.* **2003**, *42*, 4109–4116.

[9]   Mitchell, K.; Huang, F. Q.; Caspi, E. N.; McFarland, A. D.; Haynes, C. L.; Somers, R. C.; Jorgensen, J. D.; Van Duyne, R. P.; Ibers, J. A. *Inorg. Chem.* **2004**, *43*, 1082–1089.

[10]   Yao, J.; Deng, B.; Sherry, L. J.; McFarland, A. D.; Ellis, D. E.; Van Duyne, R. P.; Ibers, J. A. *Inorg. Chem.* **2004**, *43*, 7735–7740.

[11]   Chan, G. H.; Sherry, L. J.; Van Duyne, R. P.; Ibers, J. A. *Z. Anorg. Allg. Chem.* **2007**, *633*, 1343–1348.

[12]   Masuda, H.; Fujino, T.; Sato, N.; Yamada, K. *J. Solid State Chem.* **1999**, *146*, 336–343.

[13]   Wakeshima, M.; Hinatsu, Y. *J. Solid State Chem.* **2000**, *153*, 330–335.

[14]   Wakeshima, M.; Hinatsu, Y.; Oikawa, K.; Shimojo, Y.; Morii, Y. *J. Mater. Chem.* **2000**, *10*, 2183–2185.

[15]   Wakeshima, M.; Hinatsu, Y. *J. Solid State Chem.* **2001**, *159*, 163–169.

[16]   Ino, K.; Wakeshima, M.; Hinatsu, Y. *Mater. Res. Bull.* **2001**, *36*, 2207–2213.

[17]   Lozac'h, A.-M.; Guittard, M.; Flahaut, J. *Mater. Res. Bull.* **1973**, *8*, 75–86.

[18]   Agaev, A. B.; Aliev, V. O.; Aliev, O. M. *Zh. Neorg. Khim.* **1996**, *41*, 319–325.

[19]   Hidaka, C.; Takizawa, T. *J. Phys. Chem. Solids* **2008**, *69*, 358–361.

[20]   Yoo, H. S.; Im, W. B.; Vaidyanathan, S.; Park, B. J.; Jeon, D. Y. *J. Electrochem. Soc.*, **2008**, *155*, J66–J70.

[21]   Carpenter, J. D.; Hwu, S.-J. *Chem. Mater.* **1992**, *4*, 1368–1372.

[22]   Feng, K.; Shi, Y.; Yin, W.; Wang, W.; Yao, J.; Wu, Y. *Inorg. Chem.* **2012**, *51*, 11144–11149.

[23]   Yin, W.; Feng, K.; Wang, W.; Shi, Y.; Hao, W.; Yao, J.; Wu, Y. *Inorg. Chem.* **2012**, *51*, 6860–6867.

[24] Yin, W.; Wang, W.; Bai, L.; Feng, K.; Shi, Y.; Hao, W.; Yao, J.; Wu, Y. *Inorg. Chem.* **2012**, *51*, 11736–11744.

[25] Feng, K.; Yin, W.; Wang, W.; Kang, L.; Hao, W.; Yao, J.; Shi, Y.; Lin, Z.; Wu, Y. *Z. Anorg. Allg. Chem.*, **2013**, *639*, 1021–1025.

[26] Khan, W.; Borek, S.; Minar, J. *RSC Adv.* **2015**, *5*, 51461–51469.

[27] Sheldrick, G. M. *SHELXTL, version 6.12*, Bruker AXS Inc., Madison, WI, **2001**.

[28] Gelato, L. M.; Parthé, E. *J. Appl. Crystallogr.* **1987**, *20*, 139–143

[29] Kortüm, G. *Reflectance Spectroscopy*, Springer, New York, **1969**.

[30] Tank, R.; Jepsen, O.; Burkhardt, A.; Andersen, O. K. *TB-LMTO-ASA Program*, version 4.7; Max Planck Institut für Festkörperforschung: Stuttgart, Germany, **1998**.

[31] Jaulmes, S.; Julien-Pouzol, M. *Acta Crystallogr. Sect. B* **1977**, *33*, 3898–3901.

[32] Flahaut, J.; Laruelle, P.; Guittard, M.; Jaulmes, S.; Julien-Pouzol, M.; Lavenant, C. *J. Solid State Chem.*, **1979**, *29*, 125–136.

[33] Guittard, M.; Lavenant, C.; Palazzi, M. *C. R. Seances Acad. Sci., Ser. C* **1978**, *287*, 239–242.

[34] Petrov, V. V.; Bogdanova, A. V.; Mashkarinets, E. K.; Bel'skii, V. K.; Gladyshevskii, E. I.; Mokraya, I. R.; Pecharskii, V. K. *Izv. Akad. Nauk SSSR, Neorg. Mater.* **1987**, *23*, 1395–1396.

[35] Yamaoka, S.; Shimomura, O.; Nakazawa, H.; Fukunaga, O. *Solid State Commun.* **1980**, *33*, 87–89.

[36] Yamaoka, S.; Lemley, J. T.; Jenks; J. M.; Steinfink, H. *Inorg. Chem.* **1975**, *14*, 129–131.

[37] Likforman, A.; Carré, D.; Hillel, R. *Acta Crystallogr. Sect. B* **1978**, *34*, 1–5.

[38] Pfitzner, A.; Lutz, H. D. *J. Solid State Chem.* **1996**, *124*, 305–308.

[39] Schulte-Kellinghaus, M.; Krämer, V. *Acta Crystallogr. Sect. B* **1979**, *35*, 3016–3017.

[40] Guseinov, G. G.; Amiraslanov, I. R.; Kuliev, A. S.; Mamedov, Kh. S. *Izv. Akad. Nauk SSSR, Neorg. Mater.*, **1987**, *23*, 854–856.

[41] Brese, N. E.; O'Keeffe, M. *Acta. Crystallogr., Sect. B* **1991**, *47*, 192–197.

[42] Schevciw, O.; White, W. B. *Mater. Res. Bull.* **1983**, *18*, 1059–1068.

Chapter 9

Ba$_4$Ga$_2$Se$_8$: A ternary selenide containing chains and discrete Se$_2^{2-}$ units

A version of this chapter has been published Yin, W.; Iyer, A. K; Lin, X.; Mar, A. J. Solid State Chem. **2016**, *237,* 144–149. *Copyright (2016) b*y *Elsevier.*

9.1   Introduction

Exploratory synthesis of multinary metal chalcogenides over the last few decades has revealed a remarkable diversity of structures and properties. Some notable examples among numerous compounds that have received attention for their potential applications include: BaFe$_2$S$_3$ which undergoes pressure-induced superconductivity,[1] CsBi$_4$Te$_6$ which shows excellent thermoelectric properties at low temperatures ,[2] and Cs$_2$Hg$_6$S$_7$ which is a promising material for X-ray and γ-ray detection.[3]   Given the semiconducting behaviour found in many of these chalcogenides, a particular focus is to examine their potential as nonlinear optical (NLO) materials in the infrared range. Dozens of candidates have now been identified, including Rb$_3$Ta$_2$AsS$_{11}$,[4] La$_4$InSbS$_9$,[5] γ-NaAsSe$_2$,[6]   BaGa$_2$GeSe$_6$,[7,8]   Ba$_{23}$Ga$_8$Sb$_2$S$_{38}$,[9]   Ba$_4$CuGa$_5$Se$_{12}$,[10]   BaGa$_4$S$_7$,[11] BaGa$_2$SnSe$_6$,[12] and Ba$_2$Ga$_8$GeS$_{16}$,[13] all of which exhibit strong second harmonic generation (SHG) responses. Among these, the Ga-containing compounds take advantage of asymmetric GaS$_4$ or GaSe$_4$ tetrahedral units that are arranged to give noncentrosymmetric structures. Because the ternary Ba–Ga–S and Ba–Ga–Se systems have still not been thoroughly examined, it is important to investigate what other compounds occur in these systems.

Within the Ba–Ga–Se system, four compounds have been reported so far and all are semiconductors. Ba$_5$Ga$_2$Se$_8$ (with a 2.5 eV band gap) contains isolated GaSe$_4$ tetrahedra.[14] BaGa$_2$Se$_4$ (with a 3.2 eV band gap) contains chains of edge-sharing GaSe$_4$ tetrahedra and has been

tested as a host for luminescent materials.[15–17] $Ba_5Ga_4Se_{10}$ (with a 2.2 eV band gap) contains unusual discrete anionic $[Ga_4Se_{10}]^{10-}$ clusters with a Ga–Ga bond.[18] $BaGa_4Se_7$ (with a 2.6 eV band gap) contains a three-dimensional framework of corner-sharing $GaSe_4$ tetrahedra and is a newly developed infrared NLO material.[19–24] Here, we report the preparation of $Ba_4Ga_2Se_8$, which is a new member in this family, and describe its crystal structure, optical properties, and electronic structure.

9.2 Experimental

9.2.1 Synthesis

The following reagents were used as obtained: Ba shot (99%, Sigma-Aldrich), Ag powder (99.99%, Sigma-Aldrich), Ga shot (99.99%, Cerac), and Se powder (99.99%, Sigma-Aldrich). The binary starting materials, BaSe and Ga_2Se_3, were prepared by stoichiometric reaction of the elements at high temperatures (1173 K for BaSe and 1223 K for Ga_2Se_3) in sealed fused-silica tubes.

Crystals of $Ba_4Ga_2Se_8$ were initially obtained from a reaction of BaSe, Ga_2Se_3, Ag, and Se in the molar ratio of 6:1:2:1 in an attempt to prepare a quaternary selenide "$Ba_3AgGaSe_5$" to expand on the previously known representatives $Ba_4AgGa_5Se_{12}$, $Ba_7AgGa_5Se_{15}$, and $Ba_4AgGaSe_6$ in the Ba–Ag–Ga–Se system.[25–27] The mixture of starting materials (BaSe, 195 mg, 0.90 mmol; Ga_2Se_3, 57 mg, 0.15 mmol; Ag, 33 mg, 0.30 mmol; Se, 12 mg, 0.15 mmol) was finely ground and loaded into a fused-silica tube. The tube was evacuated and flame-sealed, and then placed in a computer-controlled furnace. The reaction mixture was heated to 1223 K over 20 h, kept at that temperature for 48 h, cooled to 923 K over 4 d, cooled to 723 K over 2 d, and then cooled to room temperature by shutting off the furnace. Black needle-shaped crystals, subsequently identified as $Ba_4Ga_2Se_8$, were found in the tube. Selected crystals were examined on a JEOL JSM-6010LA

InTouchScope scanning electron microscope (**Figure 9–1a**) and energy-dispersive X-ray (EDX) analysis revealed the presence of Ba, Ga, and Se in the approximate ratio of 4:2:8. The crystals are stable in air for months.
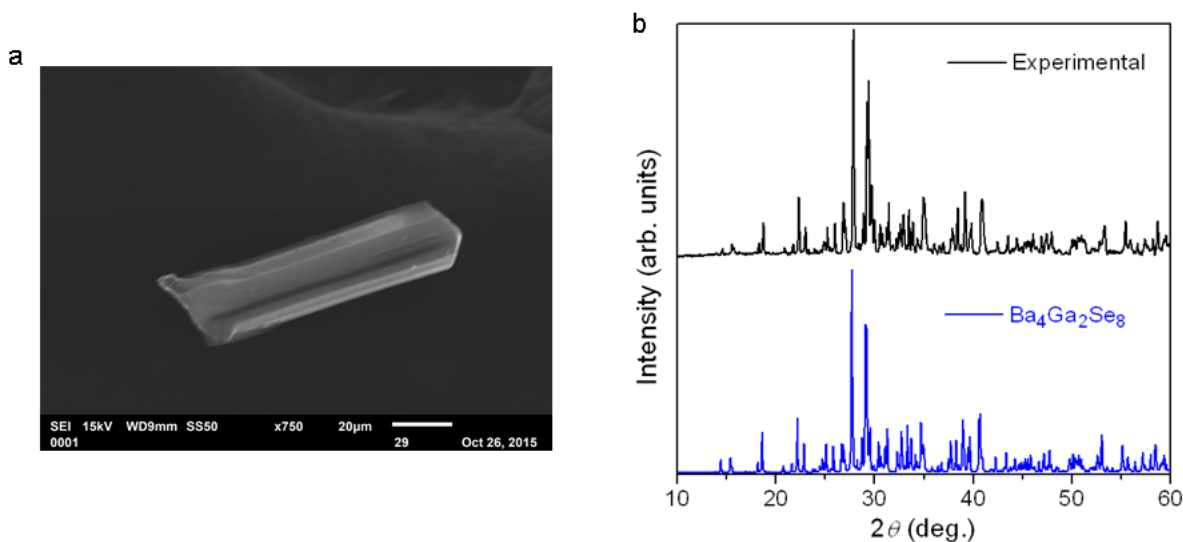
Figure 9-1.(a) SEM image of $Ba_4Ga_2Se_8$ crystal. (b) Powder XRD pattern of $Ba_4Ga_2Se_8$.

After the composition was established from the structure determination, $Ba_4Ga_2Se_8$ was prepared rationally through stoichiometric reaction of BaSe (0.216 g), Ga_2Se_3 (0.094 g), and Se (0.020 g) in the molar ratio of 4:1:1. As before, the mixture was finely ground and loaded into a fused-silica tube, which was evacuated and sealed. The tube was heated to 1023 K over 15 h, kept at that temperature for 96 h, and then cooled to room temperature by shutting off the furnace. The sample was analyzed by powder X-ray diffraction (XRD), performed on an Inel powder diffractometer equipped with a curved position-sensitive detector (CPS 120) and a Cu $K\alpha_1$ radiation source operated at 40 kV and 20 mA. The experimental XRD pattern is in excellent agreement with the simulated pattern based on the single-crystal structure (**Figure. 9–1b**). Crystal growth experiments were performed by subjecting the pure polycrystalline sample of $Ba_4Ga_2Se_8$

to the same heat treatment and slow-cooling profile described above. Black needle-shaped crystals (typically 0.1–0.2 mm in their longest dimension) obtained in the tube after the reaction were selected and verified by EDX analysis (observed: 34(4)% Ba, 11(2)% Ga, 55(6)% Se averaged over 4 crystals; expected: 29% Ba, 14% Ga, 57% Se) and unit cell measurements to be the desired compound.

9.2.2 Structure determination

Single-crystal X-ray diffraction data were collected at room temperature on a Bruker PLATFORM diffractometer equipped with a SMART APEX II CCD area detector and a graphite-monochromated Mo $K\alpha$ radiation source, using ω scans at six different ϕ angles with a frame width of 0.3º and an exposure time of 20 s per frame. Face-indexed numerical absorption corrections were applied. Structure solution and refinement were carried out with use of the SHELXTL (version 6.12) program package.[28] Initial atomic positions were located by direct methods and refinements proceeded in a straightforward fashion. All atomic sites were confirmed to be fully occupied and exhibited reasonable displacement parameters. Atomic coordinates were standardized with the program STRUCTURE TIDY.[29] The final refinement included anisotropic displacement parameters and a secondary extinction correction. Crystal data and further details are listed in **Table 9–1**, positional and equivalent isotropic displacement parameters in **Table 9–2**, and interatomic distances in **Table 9–3**.

Table 9-1. Crystallographic data for $Ba_4Ga_2Se_8$.

Formula	$Ba_4Ga_2Se_8$
Formula mass (amu)	1320.48
Space group	$P2_1/c$ (No. 14)
a (Å)	13.2393(5)
b (Å)	6.4305(2)
c (Å)	20.6432(8)
β (°)	104.3148(6)
V (Å^3)	1702.90(11)
Z	4
ρ_{calcd} (g cm^{-3})	5.151
T (K)	296(2)
Crystal dimensions (mm)	$0.10 \times 0.03 \times 0.03$
Radiation	Graphite monochromated Mo $K\alpha$, $\lambda = 0.71073$ Å
μ(Mo $K\alpha$) (mm^{-1})	29.29
Transmission factors	0.177–0.545
2θ limits	3.17–66.39°
Data collected	$-20 \leq h \leq 20, -9 \leq k \leq 9, -31 \leq l \leq 31$
No. of data collected	23800
No. of unique data, including $F_o^2 < 0$	6462 ($R_{int} = 0.058$)
No. of unique data, with $F_o^2 > 2\sigma(F_o^2)$	4568
No. of variables	128
$R(F)$ for $F_o^2 > 2\sigma(F_o^2)$ [a]	0.036
$R_w(F_o^2)$ [b]	0.086
Goodness of fit	1.052
$(\Delta\rho)_{max}, (\Delta\rho)_{min}$ (e Å^{-3})	3.22, −1.85

[a] $R(F) = \sum ||F_o| - |F_c|| / \sum |F_o|$. [b] $R_w(F_o^2) = [\sum[w(F_o^2 - F_c^2)^2] / \sum wF_o^4]^{1/2}$; $w^{-1} = [\sigma^2(F_o^2) + (Ap)^2 + Bp]$, where $p = [\max(F_o^2,0) + 2F_c^2] / 3$.

Table 9-2. Atomic coordinates and equivalent isotropic displacement parameters for $Ba_4Ga_2Se_8$.

Atom	Wyckoff position	x	y	z	U_{eq} (Å²) [a]
Ba1	4e	0.10703(3)	0.23543(6)	0.21588(2)	0.01792(9)
Ba2	4e	0.14642(3)	0.74287(5)	0.04884(2)	0.01620(8)
Ba3	4e	0.38150(3)	0.23679(5)	0.03748(2)	0.01630(8)
Ba4	4e	0.47370(3)	0.23184(5)	0.31263(2)	0.01592(8)
Ga1	4e	0.11465(6)	0.32190(11)	0.40173(4)	0.01611(15)
Ga2	4e	0.69640(6)	0.31602(11)	0.10019(4)	0.01523(14)
Se1	4e	0.04226(5)	0.73538(9)	0.17843(3)	0.01609(13)
Se2	4e	0.11592(5)	0.24527(9)	0.01461(3)	0.01631(13)
Se3	4e	0.12759(5)	0.69471(10)	0.38379(4)	0.01900(14)
Se4	4e	0.27135(5)	0.18871(10)	0.37405(3)	0.01670(13)
Se5	4e	0.31194(5)	0.42055(10)	0.17469(4)	0.01835(14)
Se6	4e	0.31287(5)	0.04928(10)	0.17398(3)	0.01811(14)
Se7	4e	0.57993(5)	0.22635(9)	0.16481(3)	0.01722(13)
Se8	4e	0.60976(5)	0.23526(9)	0.48230(3)	0.01657(13)

[a] U_{eq} is defined as one-third of the trace of the orthogonalized U_{ij} tensor.

Table 9-3. Interatomic distances (Å) for $Ba_4Ga_2Se_8$.

Ba1–Se5	3.2620(8)	Ba3–Se2	3.4304(8)
Ba1–Se6	3.2822(8)	Ba3–Se8	3.4878(8)
Ba1–Se3	3.2850(8)	Ba4–Se4	3.2466(8)
Ba1–Se1	3.2862(8)	Ba4–Se7	3.3160(7)
Ba1–Se1	3.3676(7)	Ba4–Se6	3.3302(8)
Ba1–Se1	3.3682(7)	Ba4–Se5	3.3394(8)
Ba1–Se4	3.4599(8)	Ba4–Se7	3.3839(7)
Ba2–Se2	3.2803(7)	Ba4–Se5	3.4297(8)
Ba2–Se1	3.2993(8)	Ba4–Se6	3.4412(8)
Ba2–Se2	3.3104(7)	Ba4–Se8	3.5204(8)
Ba2–Se3	3.3780(9)	Ba4–Se7	3.6624(8)
Ba2–Se2	3.3964(8)	Ga1–Se2	2.3658(10)
Ba2–Se8	3.4441(8)	Ga1–Se1	2.3800(10)
Ba2–Se6	3.5492(8)	Ga1–Se3	2.4383(10)
Ba2–Se5	3.6101(8)	Ga1–Se4	2.4393(10)
Ba3–Se7	3.2250(8)	Ga2–Se7	2.3467(10)
Ba3–Se8	3.2370(7)	Ga2–Se3	2.4013(10)
Ba3–Se8	3.2565(7)	Ga2–Se8	2.4428(10)
Ba3–Se4	3.3624(8)	Ga2–Se4	2.4691(10)
Ba3–Se6	3.3891(8)	Se5–Se6	2.3876(9)
Ba3–Se5	3.9996(8)		

9.2.3 Diffuse reflectance spectroscopy

A Cary 5000 UV-VIS-NIR spectrophotometer equipped with a diffuse reflectance accessory was used to collect the spectrum of $Ba_4Ga_2Se_8$ over the range of 350 nm (3.54 eV) to 2500 nm (0.50 eV). The powder sample was spread on a compacted base of $BaSO_4$, used as a 100% reflectance standard. The optical absorption spectrum was converted from the diffuse reflectance spectrum using the Kubelka-Munk function, $\alpha/S = (1-R)^2/2R$, where α is the Kubelka-Munk absorption coefficient and S is the scattering coefficient.[30]

9.2.4 Band structure calculation

Tight-binding linear muffin tin orbital band structure calculations were performed on $Ba_4Ga_2Se_8$ within the local density and atomic spheres approximation with use of the Stuttgart TB-LMTO-ASA program (version 4.7).[31] The basis set consisted of Ba 6s/6p/5d, Ga 4s/4p/4d, and Se 4s/4p/4d orbitals, with the Ba 6p, Ga 4d, and Se 4d orbitals being downfolded. Integrations in reciprocal space were carried out with an improved tetrahedron method over 50 irreducible k points within the first Brillouin zone.

9.3 Results and discussion

The ternary selenide $Ba_4Ga_2Se_8$ is a new member in the Ba–Ga–Se system; it is isotypic to the sulfide analogue $Ba_4Ga_2S_8$, which was recently reported.[32] $Ba_4Ga_2Se_8$ can be obtained in pure form by stoichiometric reaction of BaSe, Ga_2Se_3, and Se at 1023 K. Attempts to prepare other substitutional derivatives, such as In for Ga or Te for Se, were unsuccessful under similar conditions.

The monoclinic structure of $Ba_4Ga_2Se_8$ (space group $P2_1/c$) consists of 14 crystallograpically independent sites – four Ba, two Ga, and eight Se – all in Wyckoff position 4e.

The structure contains Ba^{2+} cations, one-dimensional anionic chains $[GaSe_3]^{3-}$, and discrete Se_2^{2-} units (**Figure 9–2**). (Although Ba_2GaSe_4 would be the simplest empirical formula, it is more informative to express the formula as $Ba_4Ga_2Se_6(Se_2)$ or $Ba_4Ga_2Se_8$ to highlight the presence of these units.) The chains are built from corner-sharing $GaSe_4$ tetrahedra, alternately centred by Ga1 and Ga2 atoms, that extend in a zigzag fashion along the *b*-direction.
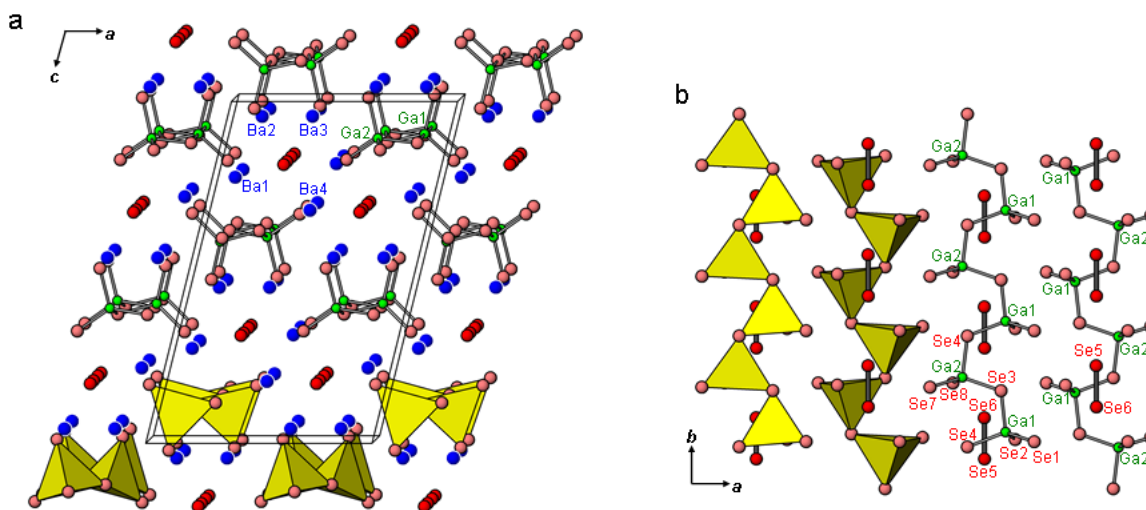
Figure 9-2. (a) Structure of $Ba_4Ga_2Se_8$ viewed down the *b*-direction. (b) A slice perpendicular to (001) showing chains of up- and down-pointing $GaSe_4$ tetrahedra, as well as Se_2^{2-} units; Ba atoms are omitted for clarity.

Within individual chains, the tetrahedra all point in the same direction, but the overall structure is nonpolar because the dipole moments of chains containing up-pointing tetrahedra cancel with those containing down-pointing tetrahedra. The tetrahedra are slightly distorted, with angles of 101.90(3)–115.76(4)° around Ga1 and 100.10(3)–126.42(4)° around Ga2. The Ga–Se distances in $Ba_4Ga_2Se_8$ (2.3658(10)–2.4393(10) Å around Ga1 and 2.3467(10)–2.4691(10) Å around Ga2) are similar to those found in $Ba_4Ga_4SnSe_{12}$ (2.387(2)–2.451(2) Å) [33] and $Ba_4AgGa_5Se_{12}$ (2.362(1)–2.427(1) Å),[25] where zigzag $[GaSe_3]^{3-}$ chains form fragments of three-dimensional networks. In

Ba$_4$Ga$_4$SnSe$_{12}$, the Sn atoms serve as linkages between the [GaSe$_3$]$^{3-}$ chains so that they all point in the same direction, giving rise to a noncentrosymmetric structure; however, in Ba$_4$AgGa$_5$Se$_{12}$, the connecting Ag atoms fail to bring about an overall polarity and the chains point in both directions. The Se$_2^{2-}$ units are also aligned along the *b*-direction, parallel to the [GaSe$_3$]$^{3-}$ chains. They are formed from Se5 and Se6 atoms bonded at a distance of 2.3876(9) Å. This short distance is typical of a Se–Se single bond, comparable to the 2.392(1)–2.407(1) distances found in the recent example of Ba$_8$PdU$_2$Se$_{12}$(Se$_2$)$_2$.[34] Three Ba sites share the Se$_2^{2-}$ unit (η^2) around their coordination environments, whereas the fourth Ba site is coordinated exclusively through single Se atoms (η^1) (**Figure 9–3**).
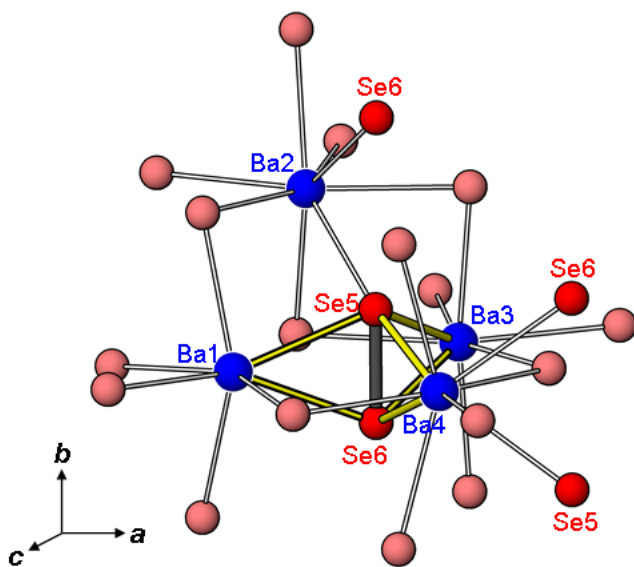
Figure 9-3. Coordination environments around Ba atoms in Ba$_4$Ga$_2$Se$_8$. The η^2 coordination of the Se$_2^{2-}$ dimer around Ba1, Ba3, and Ba4 atoms is highlighted by the yellow bonds.

The geometries around these Ba sites are rather irregular (with local site symmetry of 1), roughly monocapped trigonal prismatic (CN7) around Ba1, bicapped trigonal prismatic (CN8) around Ba2 and Ba3, and tricapped trigonal prismatic (CN9) around Ba4. The Ba–Se distances of

3.2466(8)–3.6624(8) Å agree well with those found in $Ba_8PdU_2Se_{12}(Se_2)_2$ (3.1625(10)–3.7114(10) Å)[34] and $Ba_6Sn_6Se_{13}$ (3.228(1)–3.770(1) Å).[35]

The charge-balanced formulation $(Ba^{2+})_4(Ga^{3+})_2(Se^{2-})_6(Se_2^{2-})$ is supported by calculations of bond valence sums,[36] which are 2.0–2.3 for the Ba atoms, 3.0 for the Ga atoms, and 2.0–2.2 for the isolated Se atoms; the Se5 and Se6 atoms would have bond valence sums of 1.3 if the Se–Se bond is neglected but they are restored to a more reasonable value of 2.2 if included. The interesting point of comparison is between $Ba_4Ga_2Se_8$ and the isostructural sulfide, $Ba_4Ga_2S_8$, which has been reported to be a semiconductor of a yellow colour with a band gap of 2.55 eV (experimental) or 1.79 eV (calculated).[32] The black colour of $Ba_4Ga_2Se_8$ implies that it has a smaller band gap than $Ba_4Ga_2S_8$. This is confirmed by the measured optical band gap of 1.63(2) eV, deduced by the extrapolation method[37] from the absorption spectrum of $Ba_4Ga_2Se_8$, which was converted from the diffuse reflectance spectrum using the Kubelka-Munk function (**Figure 9–4**). The band gap in $Ba_4Ga_2Se_8$ is considerably less than those in other Ba–Ga–Se phases (ranging from 2.2 eV in $Ba_5Ga_4Se_{10}$[18] to 3.2 eV in $BaGa_2Se_4$[15]), as described earlier, suggesting that the presence of the Se_2^{2-} units has a profound effect on the electronic structure. It would be desirable to measure the electrical band gap but unfortunately the crystals of $Ba_4Ga_2Se_8$ were too small (typically 0.1–0.2 mm in longest dimension) to permit single-crystal resistivity measurements.
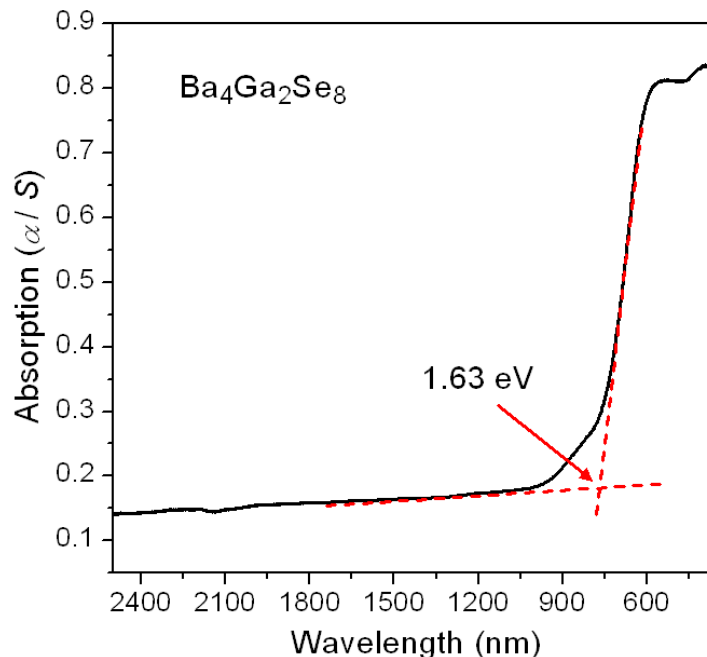
Figure 9-4. Optical absorption spectrum of $Ba_4Ga_2Se_8$.

A band structure calculation performed on $Ba_4Ga_2Se_8$ corroborates this point (**Figure 9–5**). The density of states (DOS) curve shows valence and conduction bands separated by a gap of 1.51 eV, in good agreement with the measured gap of 1.63 eV. Empty Ba-based levels are mostly found above the Fermi level, while filled Ga- and Se-based levels are mostly found below, consistent with the notion of electron transfer from electropositive Ba atoms to an anionic Ga–Se framework. Strong covalent Ga–Se interactions are indicated by the mixing of Se 4p states with Ga 4s (from –6.2 to –4.9 eV) and 4p states (from –3.6 to 0 eV). As seen in the crystal orbital Hamilton population (COHP) curves, these Ga–Se interactions are optimized, with all bonding and no antibonding levels occupied, resulting in an integrated COHP (–ICOHP) value of 2.75 eV/bond. However, there is also considerable mixing of Ba and Se states in the valence (from –3.6 to 0 eV) and conduction bands (from +1.5 eV upwards). Covalent character provides a small but non-negligible contribution to Ba–Se bonding, giving an –ICOHP value of 0.48 eV/bond. The

Se–Se COHP curve clearly shows the occupation of bonding and antibonding levels that are derived from the Se_2^{2-} dimers present in the structure: low-lying σ_{4s} and $\sigma*_{4s}$ levels (at –13 and –11 eV, not shown), σ_{4p} and π_{4p} levels (–3.6 to –1.6 eV), and $\pi*_{4p}$ levels (–1.6 to 0 eV). With the $\sigma*_{4p}$ levels (+1.5 eV upwards) remaining unoccupied, the electronic structure corresponds to the molecular orbital diagram for Se_2^{2-}, isoelectronic to Br_2. This Se–Se bond has an –ICOHP value of 2.82 eV/bond. Close inspection reveals that the top of the valence band and the bottom of the conduction bands are dominated by Se states involved in Se–Se bonding, and secondarily by Ba states involved in Ba–Se bonding. In the absence of Se_2^{2-} dimers, as occurs in other Ba–Ga–Se phases, the band gap would be greater than 2 eV, which corresponds to the energy in the conduction band above which Ga–Se antibonding levels only start to become prominent.
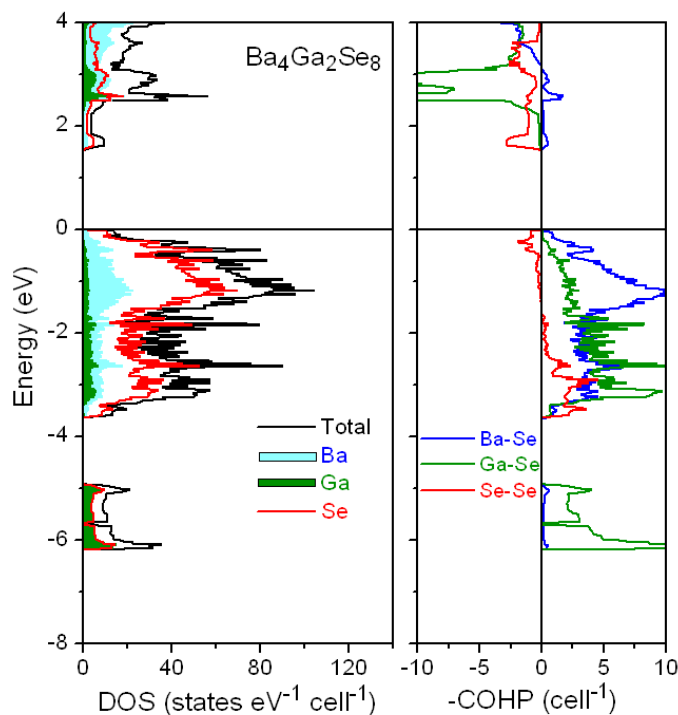
Figure 9-5. Density of states (DOS) and crystal orbital Hamilton population (–COHP) curves for $Ba_4Ga_2Se_8$.

9.4 Conclusions

The ternary selenide $Ba_4Ga_2Se_8$ is a new member in the Ba–Ga–Se system in which chains of corner-sharing $GaSe_4$ tetrahedra are formed but point in opposing directions so that an overall polar structure could not be attained. The anionic Se_2^{2-} units play an important role in decreasing the band gap to 1.6 eV, about 1 eV lower than in other Ba–Ga–Se phases that do not contain these units. Given that the corresponding sulfide $Ba_4Ga_2S_8$ has a measured band gap of 2.6 eV, the band gap is also narrowed by a similar magnitude upon substitution of S by Se, as a result of weaker π-bonding interactions in the Se_2^{2-} units.

9.5 References

[1]   Takahashi, H.; Sugimoto, A.; Nambu, Y.; Yamauchi, T.; Hirata, Y.; Kawakami, T.; Avdeev, M.; Matsubayashi, K.; Du, F.; Kawashima, C.; Soeda, H.; Nakano, S.; Uwatoko, Y.; Ueda, Y.; Sato, T. J.; Ohgushi, K. *Nat. Mater.* **2015**, *14*, 1008–1012.

[2]   Chung, D. -Y.; Hogan, T.; Brazis, P.; Rocci-Lane, M.; Kannewurf, C.; Bastea, P.; Uher, C.; Kanatzidis, M. G. *Science* **2000**, *287*, 1024–1027.

[3]   Li, H.; Peters, J. A.; Liu, Z.; Sebastian, M.; Malliakas, C. D.; Androulakis, J.; Zhao, L.; Chung, I.; Nguyen, S. L.; Johnsen, S.; Wessels, B. W.; Kanatzidis, M. G. *Cryst. Growth Des.* **2012**, *12*, 3250–3256.

[4]   Bera, T. K.; Jang, J. I.; Ketterson, J. B.; Kanatzidis, M. G. *J. Am. Chem. Soc.* **2009**, *131*, 75–77.

[5]   Zhao, H. -J.; Zhang, Y. -F.; Chen, L. *J. Am. Chem. Soc.* **2012**, *134*, 1993–1995.

[6]   Bera, T. K.; Jang, J. I.; Song, J. -H.; Malliakas, C. D.; Freeman, A. J.; Ketterson, J. B.; Kanatzidis, M. G. *J. Am. Chem. Soc.* **2010**, *132*, 3484–3495.

[7]   Yin, W.; Feng, K.; He, R.; Mei, D.; Lin, Z.; Yao, J. L.; Wu, Y. *Dalton Trans.* **2012**, *41*, 5653–5661.

[8]   Lin, X.; Guo, Y.; Ye, N. *J. Solid State Chem.* **2012**, *195*, 172–177.

[9]   Chen, M. C.; Wu, L. M.; Lin, H.; Zhou, L. J.; Chen, L. *J. Am.Chem. Soc.* **2012**, *134*, 6058−6060

[10] Kuo, S. -M.; Chang, Y. -M.; Chung, I.; Jang, J. -I.; Her, B. -H.; Yang, S. -H.; Ketterson, J. B.; Kanatzidis, M. G.; Hsu, K. -F. *Chem. Mater.* **2013**, *25*, 2427–2433.

[11] Lin, X.; Zhang, G.; Ye, N. *Cryst. Growth Des.* **2009**, *9*, 1186–1189.

[12] Li, X.; Li, C.; Gong, P.; Lin, Z.; Yao, Wu, J. Y. *J. Mater. Chem. C* **2015**, *3*, 10998–11004.

[13] Liu, B. -W.; Zeng, H. -Y.; Zhang, M. -J.; Fan, Y. -H.; Guo, G. -C.; Huang, J. -S.; Dong, Z. -C. *Inorg. Chem.* **2015**, *54*, 976–981.

[14] Mei, D.; Yin, W.; Lin, Z.; Yao, J. L.; Fu, P.; Y. Wu *J. Alloys Compd.* **2011**, *509*, 2981–2985

[15] Klee, W.; Schäfer, H. *Z. Anorg. Allg. Chem.* **1981**, *479*, 125–133.

[16] Kim, M. -Y.; Kim, W. -T.; Jin, M. -S.; Park, S. -A.; Choe, S. -H.; Lee, C. -I.; Hyun, S. -C.; Kim, C. -D. *J. Phys. Chem. Solids* **2003**, *64*, 625–629.

[17] Tagiev, B. G.; Abushov, S. A.; Tagiev, O. B. *J. Appl. Spectrosc.* **2010**, *77*, 115–119.

[18] Yin, W.; Mei, D.; Feng, K.; Yao, J.; Fu, P.; Wu, Y. *Dalton Trans.* **2011**, *40*, 9159–9162.

[19] Yao, J. L.; Mei, D.; Bai, L.; Lin, Z.; Yin, W.; Fu, P.; Wu, Y. *Inorg. Chem.* **2010**, *49*, 9212–9216.

[20] Badikov, V.; Badikov, D.; Shevyrdyaeva, G.; Tyazhev, A.; Marchev, G.; Panyutin, V.; Petrov, V.; Kwasniewski, A. *Phys. Status Solidi RRL* **2011**, *5*, 31–33.

[21]   Yao, J.; Yin, W.; Feng, K.; Li, X.; Mei, D.; Lu, Q.; Ni, Y.; Zhang, Z.; Hu, Z.; Wu, Y. *J. Cryst. Growth* **2012**, *346*, 1–4.

[22]   Yang, F.; Yao, J.; Xu, H.; Feng, K.; Yin, W.; Li, F.; Yang, J.; Du, S.; Peng, Q.; Zhang, J.; Cui, D.; Wu, Y.; Chen, C.; Xu, Z. *Opt. Lett.* **2013**, *38*, 3903–3905.

[23]   Zhang, X.; Yao, J.; Yin, W.; Zhu, Y.; Wu, Y.; Chen, C. *Opt. Express* **2015**, *23*, 552–558.

[24]   Yang, F.; Yao, J.; Xu, H.; Zhang, F.; Zhai, N.; Lin, Z.; Zong, N.; Peng, Q.; Zhang, J.; Cui, D.; Wu, Y.; Chen, C.; Xu, Z. *IEEE Photonics Technol. Lett.* **2015**, *27*, 1100–1103.

[25]   Yin, W.; Feng, K.; Mei, D.; Yao, J.; Fu, P.; Wu, Y. *Dalton Trans.* **2012**, *41*, 2272–2276.

[26]   Yin, W.; He, R.; Feng, K.; Hao, W.; Yao, J. L.; Wu, Y. *J. Alloys Compd.* **2013**, 565, 115–119.

[27]   Lei, X. W.; Yang, M.; Xia, S. Q.; Liu, X.-C.; Pan, M. Y.; Li, X.; Tao, X. T. *Chem. Asian J.* **2014**, *9*, 1123–1131.

[28]   Sheldrick, G. M. SHELXTL, version 6.12, Bruker AXS Inc., Madison, WI, 2001.

[29]   Gelato, L. M.; Parthé, E. *J. Appl. Crystallogr.* **1987**, *20*, 139–143.

[30]   Kortüm, G. *Reflectance Spectroscopy*, Springer, New York, **1969**.

[31]   Tank, R.; Jepsen, O.; Burkhardt, A.; Andersen, O. K. *TB-LMTO-ASA Program*, version 4.7; Max Planck Institut für Festkörperforschung: Stuttgart, Germany, **1998**.

[32]   Liu, J. -W.; Wang, P.; Chen, L. *Inorg. Chem.* **2011**, *50*, 5706–5713.

[33]   Yin, W.; Lin, Z.; Kang, L.; Kang, B.; Deng, J.; Lin, Z.; Yao, J.; Wu, Y. *Dalton Trans.* **2015**, *44*, 2259–2266.

[34]   Prakash, J.; Mesbah, A.; Lebègue, S.; Malliakas, C. D.; Ibers, J.A. *J. Solid State Chem.* **2015**, *230*, 70–74.

[35]   Feng, K.; Jiang, X.; Kang, L.; Yin, W.; Hao, W.; Lin, Z.; Yao, J.; Wu, Y.; Chen, C. *Dalton Trans.* **2013**, *42*, 13635–13641.

[36]   Brese, N. E.; O'Keeffe, M. *Acta. Crystallogr., Sect. B* **1991**, *47*, 192–197.

[37]   Schevciw, O.; White, W. B. *Mater. Res. Bull.* **1983**, *18*, 1059–1068.

Chapter 10

When one becomes two: $Ba_{12}In_4Se_{20}$, not quite isostructural to $Ba_{12}In_4S_{19}$

10.1 Introduction

The chalcogenide systems Ba–Ga–*Ch* (*Ch* = S, Se) are replete with many ternary phases: $Ba_5Ga_2S_8$,[1] $Ba_4Ga_2S_7$,[2] $Ba_4Ga_2S_8$,[3] $Ba_4Ga_4S_{10}$,[4] $Ba_3Ga_2S_6$,[2] $BaGa_2S_4$,[5] $BaGa_4S_7$;[6,7] $Ba_5Ga_2Se_8$,[8] $Ba_5Ga_4Se_{10}$,[9] $Ba_4Ga_2Se_8$,[10] $BaGa_2Se_4$,[11] $BaGa_4Se_7$.[12] Renewed efforts to investigate them systematically have been driven by the recent discovery that $BaGa_4S_7$ and $BaGa_4Se_7$ are promising infrared nonlinear optical (NLO) materials.[7,12] Among chalcogenides, there is an expectation that isostructural compounds are often formed for sulfides and selenides. However, this generalization can be suspect; more typically, as illustrated in the Ba–Ga–S vs Ba–Ga–Se systems, exceptions frequently occur and subtle differences exist. Among the ternary Ba–Ga–*Ch* phases listed above with identical compositions, $Ba_5Ga_2S_8$/$Ba_5Ga_2Se_8$ and $Ba_4Ga_2S_8$/$Ba_4Ga_2Se_8$ form isostructural pairs, but $BaGa_2S_4$/$BaGa_2Se_4$ and $BaGa_4S_7$/$BaGa_4Se_7$ do not.

Because substitution of In for Ga has been proposed to be beneficial in improving NLO properties (through enhancement of the second order susceptibility),[13] it seems worthwhile to examine the corresponding Ba–In–*Ch* systems. To date, fewer ternary phases are known here: $Ba_{12}In_4S_{19}$,[3] $Ba_4In_2S_8$,[3] $Ba_2In_2S_5$,[14,15] $BaIn_2S_4$;[16–18] $Ba_2In_2Se_5$,[14,15] $BaIn_2Se_4$.[19] In the course of investigating the Ba–In–Se system, we report here the identification of the new compound $Ba_{12}In_4Se_{20}$, which has nearly the same composition as the corresponding sulfide $Ba_{12}In_4S_{19}$ but differs in an interesting way in their structures.

10.2 Experimental

10.2.1 Synthesis

Ba shot (99%), In powder (99.99%), and Se powder (99.99%), all from Sigma-Aldrich, were used as obtained. BaSe and In_2Se_3, used as starting materials, were prepared by stoichiometric reaction of the elements at 1173 K and 873 K, respectively, in sealed fused-silica tubes. In the preparation of BaSe, the fused-silica tubes were carbon-coated to avoid deleterious reactions with elemental Ba. Crystals of $Ba_{12}In_4Se_{20}$ were initially obtained serendipitously in attempts to prepare the target compound "$Ba_4In_2Se_8$" as an In-containing analogue to $Ba_4Ga_2Se_8$.[10] A mixture of BaSe (260 mg, 1.2 mmol), In_2Se_3 (140 mg, 0.3 mmol) and Se (24 mg, 0.3 mmol) was finely ground and loaded into a fused-silica tube which was then evacuated and sealed. The tube was heated to 1223 K over 24 h, kept at that temperature for 48 h, cooled to 673 K over 2 d, and then cooled to room temperature by shutting off the furnace. Dark red (almost black), air-stable crystals were found in the product and examined on a JEOL JSM-6010LA scanning electron microscope (**inset of Figure 10–1**). Energy-dispersive X-ray (EDX) analysis on these crystals, averaged over multiple points, revealed a composition of 36(3)% Ba, 12(1)% In, and 52(3)% Se, in reasonable agreement with the expected composition of 33% Ba, 11% In, and 56% Se for $Ba_{12}In_4Se_{20}$. These crystals verified by EDX analysis were used for the structure determination.

Polycrystalline $Ba_{12}In_4Se_{20}$ can be prepared rationally through stoichiometric reaction of BaSe (324 mg, 1.5 mmol), In_2Se_3 (117 mg, 0.25 mmol), and Se (20 mg, 0.25 mmol). The mixture was placed in an evacuated and sealed fused-silica tube as before. In an optimized procedure, the tube was heated to 1023 K over 24 h, kept there for 72 h, and then cooled to room temperature by shutting off the furnace. The sample was reground, loaded into a new tube, and reheated at 1023 K for 96 h. The powder X-ray diffraction (XRD) pattern, collected on an Inel diffractometer

equipped with a curved position-sensitive detector (CPS 120) and a Cu $K\alpha_1$ radiation source operated at 40 kV and 20 mA, confirmed that the sample was single-phase (**Figure 10–1**). Unit cell parameters (a = 10.0562(2) Å, c = 78.3216(9) Å) refined from the powder XRD pattern agree well with those from the single crystal diffraction data (see below).
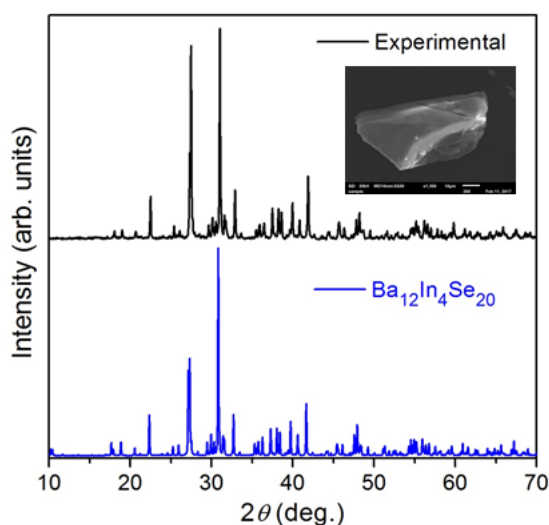
Figure 10-1. Powder XRD pattern of $Ba_{12}In_4Se_{20}$. The inset shows an SEM image of a typical crystal.

10.2.2 Structure determination

Single-crystal X-ray diffraction data were obtained for three samples of $Ba_{12}In_4Se_{20}$. The two data sets at room temperature (296 K) gave essentially identical results and we report only the results for one of them here. The third data set was obtained at low temperature (193 K) to ascertain whether the features of site splitting observed in the room-temperature data are retained. Intensity data were collected on a Bruker PLATFORM diffractometer equipped with a SMART APEX II CCD detector and a graphite-monochromated Mo $K\alpha$ radiation source, using ω scans at 4–8 different ϕ angles with a frame width of 0.3° and an exposure time of 20–25 s per frame. Face-indexed numerical absorption corrections were applied. Structure solution and refinement were

carried out with use of the SHELXTL (version 6.12) program package.[20] From examination of the room-temperature data sets, the centrosymmetric space group $R\bar{3}$ was chosen on the basis of the Laue symmetry, intensity statistics, and systematic absences. An initial model was considered consisting of four Ba, four In, and thirteen Se sites, whose positions were located by direct methods. The atomic coordinates were standardized with the program STRUCTURE TIDY.[21] Refinement of this model revealed somewhat larger displacement parameters around two of the In sites (0.029–0.035 Å^2 compared to 0.017–0.018 Å^2 for the two other In sites) and one of the Se sites (0.031 Å^2 compared to 0.015–0.023 Å^2 for the twelve other Se sites), as well as prominent residual peaks in the difference electron density map close to these sites. Thus, these sites were split and labeled as follows: In2A/In2B, In3A/In3B, and Se13/Se14. Each of these sites is in Wyckoff position $6c$ $(0,\ 0,\ z)$, except for Se13, which is in Wyckoff position $3a$ $(0,\ 0,\ 0)$. Constraints were applied such that the occupancies within each of these sets of split sites must sum to unity and that their displacement parameters are equal. Refinement of this split-site model then led to occupancies of $0.895(3)$ In2A / $0.105(3)$ In2B, $0.814(3)$ In3A / $0.186(3)$ In 3B, and $0.872(6)$ Se13 / $0.064(3)$ Se14, with more reasonable displacement parameters for each site. The difference map was now featureless and the agreement factors were acceptable. The split-site model was also refined using the low-temperature data set, leading to similar results except that the displacement parameters are generally smaller, as expected. The split sites remained, but the occupancies are slightly higher within the primary In sites ($0.957(2)$ In2A, $0.848(2)$ In3A) and about the same within the primary Se site ($0.862(5)$ Se13) compared to the room-temperature data.

Crystal data and further details are listed in **Table 10–1**, positional and equivalent isotropic displacement parameters in **Table 10–2**, and selected interatomic distances in **Table 10–3**.

Table 10-1. Crystallographic data for $Ba_{12}In_4Se_{20}$ at room and low temperatures.

T (K)	**296(2)**	**193(2)**
Formula mass (amu)	3686.56	3686.56
Space group	$R\bar{3}$ (No. 148)	$R\bar{3}$ (No. 148)
a (Å)	10.0360(6)	10.0108(8)
c (Å)	78.286(4)	78.184(7)
V (Å^3)	6828.7(9)	6785.5(12)
Z	6	6
ρ_{calcd} (g cm^{-3})	5.379	5.413
Crystal dimensions (mm)	$0.08 \times 0.03 \times 0.03$	$0.07 \times 0.05 \times 0.04$
μ(Mo $K\alpha$) (mm^{-1})	28.16	28.34
Transmission factors	0.219–0.619	0.288–0.458
2θ limits	3.12–66.42°	3.13–66.41°
Data collected	$-15 \le h \le 15$, $-15 \le k \le 15$, $-117 \le l \le 117$	$-15 \le h \le 15$, $-15 \le k \le 15$, $-119 \le l \le 119$
No. of data collected	32502	33626
No. of unique data, including $F_o^2 < 0$	5800 (R_{int} = 0.094)	5805 (R_{int} = 0.061)
No. of unique data, with $F_o^2 > 2\sigma(F_o^2)$	3582	4157
No. of variables	116	116
$R(F)$ for $F_o^2 > 2\sigma(F_o^2)$ [a]	0.048	0.040
$R_w(F_o^2)$ [b]	0.125	0.097
Goodness of fit	1.054	1.075
$(\Delta\rho)_{max}$, $(\Delta\rho)_{min}$ (e Å^{-3})	4.08, –2.84	5.69, –2.45

[a] $R(F) = \sum ||F_o| - |F_c|| / \sum |F_o|$ for $F_o^2 > 2\sigma(F_o^2)$. [b] $R_w(F_o^2) = [\sum[w(F_o^2 - F_c^2)^2] / \sum wF_o^4]^{1/2}$; $w^{-1} = [\sigma^2(F_o^2) + (Ap)^2 + Bp]$, where $p = [\max(F_o^2, 0) + 2F_c^2] / 3$.

Table 10-2. Atomic coordinates and equivalent isotropic displacement parameters for $Ba_{12}In_4Se_{20}$ at room and low temperatures.

Atom	Wyckoff position	Occupancy	x	y	z	U_{eq} (Å²) [a]
			296 K			
Ba1	18f	1	0.04858(6)	0.33001(6)	0.10442(2)	0.01782(12)
Ba2	18f	1	0.05561(7)	0.32716(7)	0.02047(2)	0.02545(14)
Ba3	18f	1	0.06051(6)	0.33868(6)	0.27000(2)	0.02022(13)
Ba4	18f	1	0.06890(6)	0.34892(6)	0.18731(2)	0.01816(12)
In1	6c	1	0	0	0.07208(2)	0.0181(2)
In2A	6c	0.895(3)	0	0	0.15301(2)	0.0231(3)
In2B	6c	0.105(3)	0	0	0.14083(18)	0.0231(3)
In3A	6c	0.814(3)	0	0	0.22125(2)	0.0226(3)
In3B	6c	0.186(3)	0	0	0.23421(10)	0.0226(3)
In4	6c	1	0	0	0.30187(2)	0.0199(2)
Se1	18f	1	0.00026(11)	0.24820(11)	0.31113(2)	0.02065(19)
Se2	18f	1	0.00568(10)	0.25186(10)	0.14610(2)	0.01728(18)
Se3	18f	1	0.00781(10)	0.25252(10)	0.22835(2)	0.01658(17)
Se4	18f	1	0.01021(10)	0.25137(10)	0.06267(2)	0.01893(19)
Se5	6c	1	0	0	0.10491(2)	0.0177(3)
Se6	6c	1	0	0	0.18714(2)	0.0184(3)
Se7	6c	1	0	0	0.26893(2)	0.0180(3)
Se8	6c	1	0	0	0.34743(2)	0.0262(4)
Se9	6c	1	0	0	0.37767(2)	0.0239(3)
Se10	6c	1	0	0	0.42259(2)	0.0181(3)
Se11	6c	1	0	0	0.45381(2)	0.0182(3)
Se12	3b	1	0	0	½	0.0186(4)
Se13	3a	0.872(6)	0	0	0	0.0230(7)
Se14	6c	0.064(3)	0	0	0.0255(4)	0.0230(7)
			193 K			
Ba1	18f	1	0.04829(5)	0.32993(4)	0.10438(2)	0.01257(8)
Ba2	18f	1	0.05546(5)	0.32708(5)	0.02046(2)	0.01835(10)
Ba3	18f	1	0.06032(5)	0.33877(5)	0.27003(2)	0.01430(9)
Ba4	18f	1	0.06890(5)	0.34969(5)	0.18735(2)	0.01273(8)
In1	6c	1	0	0	0.07219(2)	0.01297(15)
In2A	6c	0.957(2)	0	0	0.15287(2)	0.0170(2)
In2B	6c	0.043(2)	0	0	0.1404(3)	0.0170(2)
In3A	6c	0.848(2)	0	0	0.22147(2)	0.0159(2)
In3B	6c	0.152(2)	0	0	0.23444(8)	0.0159(2)
In4	6c	1	0	0	0.30178(2)	0.01457(16)
Se1	18f	1	0.00061(8)	0.24889(8)	0.31112(2)	0.01483(14)
Se2	18f	1	0.00449(8)	0.25178(8)	0.14614(2)	0.01204(13)
Se3	18f	1	0.00747(7)	0.25294(7)	0.22832(2)	0.01175(12)

Se4	18f	1	0.00942(8)	0.25124(8)	0.06267(2)	0.01328(13)
Se5	6c	1	0	0	0.10500(2)	0.0129(2)
Se6	6c	1	0	0	0.18718(2)	0.0134(2)
Se7	6c	1	0	0	0.26884(2)	0.0130(2)
Se8	6c	1	0	0	0.34733(2)	0.0193(3)
Se9	6c	1	0	0	0.37763(2)	0.0172(2)
Se10	6c	1	0	0	0.42258(2)	0.0129(2)
Se11	6c	1	0	0	0.45382(2)	0.0127(2)
Se12	3b	1	0	0	½	0.0126(3)
Se13	3a	0.862(5)	0	0	0	0.0161(5)
Se14	6c	0.069(3)	0	0	0.0259(3)	0.0161(5)

Table 10-3. Selected interatomic distances (Å) in $Ba_{12}In_4Se_{20}$ at room and low temperatures.

	296 K	193 K
Ba1–Se5	3.0973(5)	3.0901(5)
Ba1–Se2	3.3333(10)	3.3346(8)
Ba1–Se3	3.3343(10)	3.3285(8)
Ba1–Se4	3.3391(10)	3.3318(8)
Ba1–Se10	3.3669(8)	3.3596(6)
Ba1–Se11	3.3922(8)	3.3869(6)
Ba1–Se3	3.4312(10)	3.4183(8)
Ba1–Se3	3.6929(10)	3.6802(8)
Ba2–Se8	3.1828(7)	3.1771(5)
Ba2–Se4	3.3696(11)	3.3658(8)
Ba2–Se1	3.4187(11)	3.4127(9)
Ba2–Se1	3.4385(11)	3.4336(9)
Ba2–Se13/Se14	3.4392(6)/3.069(4)	3.4309(5)/3.065(3)
Ba2–Se1	3.4813(12)	3.4702(9)
Ba2–Se1	3.6151(11)	3.6019(9)
Ba2–Se9	3.6568(11)	3.6480(8)
Ba3–Se7	3.1408(6)	3.1348(5)
Ba3–Se1	3.3176(11)	3.3090(8)
Ba3–Se4	3.3215(11)	3.3179(8)
Ba3–Se3	3.3472(10)	3.3468(8)
Ba3–Se9	3.3956(9)	3.3885(7)
Ba3–Se4	3.5549(11)	3.5382(9)
Ba3–Se4	3.6392(11)	3.6297(8)
Ba3–Se10	3.6660(10)	3.6593(8)
Ba4–Se6	3.2124(6)	3.2119(5)
Ba4–Se3	3.3224(10)	3.3138(8)
Ba4–Se2	3.3356(10)	3.3309(8)
Ba4–Se2	3.3381(10)	3.3352(8)
Ba4–Se12	3.3708(5)	3.3603(4)
Ba4–Se11	3.5703(11)	3.5568(8)
Ba4–Se2	3.5792(10)	3.5694(8)
Ba4–Se2	3.6021(11)	3.5853(8)
In1–Se5	2.5701(19)	2.5652(15)
In1–Se4 (×3)	2.5805(10)	2.5790(7)
In2A–Se2 (×3)	2.5575(10)	2.5532(7)
In2A–Se6	2.672(2)	2.6825(16)
In2B–Se2 (×3)	2.534(3)	2.538(4)
In2B–Se5	2.812(14)	2.77(2)
In3A–Se3 (×3)	2.5571(10)	2.5523(7)
In3A–Se6	2.670(2)	2.6809(17)
In3B–Se3 (×3)	2.5379(16)	2.5410(14)
In3B–Se7	2.718(8)	2.689(7)
In4–Se7	2.579(2)	2.5752(15)
In4–Se1 (×3)	2.5929(10)	2.5935(8)
Se8–Se9	2.367(2)	2.3691(19)

| Se10–Se11 | 2.444(2) | 2.4424(17) |

10.2.3 Diffuse reflectance spectroscopy

A Cary 5000 UV-vis-NIR spectrophotometer equipped with a diffuse reflectance accessory was used to collect the spectrum of $Ba_{12}In_4Se_{20}$ over the range of 300 nm (4.13 eV) to 2500 nm (0.50 eV). A compacted pellet of $BaSO_4$ was used as a 100% reflectance standard. The optical absorption spectrum was converted from the diffuse reflectance spectrum using the Kubelka-Munk function, $\alpha/S = (1-R)^2/2R$, where α is the Kubelka–Munk absorption coefficient, S is the scattering coefficient, and R is the reflectance.[22]

10.3 Results and discussion

$Ba_{12}In_4Se_{20}$ is a new ternary selenide in the Ba–In–Se system, in which $Ba_2In_2Se_5$[14,15] and $BaIn_2Se_4$[19] were the only other previously known ternary phases. Its composition is very close, but not identical to that of the sulfide $Ba_{12}In_4S_{19}$[3]. The selenide $Ba_{12}In_4Se_{20}$ was easily obtained as single-phase product by stoichiometric reaction of BaSe, In_2Se_3, and Se at 1023 K. In contrast, the sulfide $Ba_{12}In_4S_{19}$ has been reported to be difficult to prepare, requiring an excess of sulfur to obtain a product in which it occurs as a major phase (85%) along with a byproduct of $Ba_2In_2S_5$.[3] We did not observe formation of "$Ba_{12}In_4Se_{19}$" in our syntheses; conversely, attempts to prepare "$Ba_{12}In_4S_{20}$" were unsuccessful. The Ga-substituted analogue "$Ba_{12}Ga_4Se_{19}$" also did not form under similar conditions.

The trigonal structure of $Ba_{12}In_4Se_{20}$ (in space group $R\bar{3}$) is based on a unit cell with an extremely long c-parameter of over 78 Å. Aligned along the c-direction are one-dimensional stacks of $InSe_4$ tetrahedra, In_2Se_7 double tetrahedra, selenide Se^{2-} anions, and diselenide Se_2^{2-} anions, with Ba^{2+} cations located between these stacks (**Figure 10–2**). The stacks along ⅓, ⅔, z

and $\frac{2}{3}, \frac{1}{3}, z$ are displaced by $\frac{1}{3}c$ and $\frac{2}{3}c$, respectively, relative to those along $0, 0, z$. The Ba cations are each coordinated by eight Se atoms, in an irregular geometry probably best described as rather distorted square antiprismatic (**Figure A10–1**).
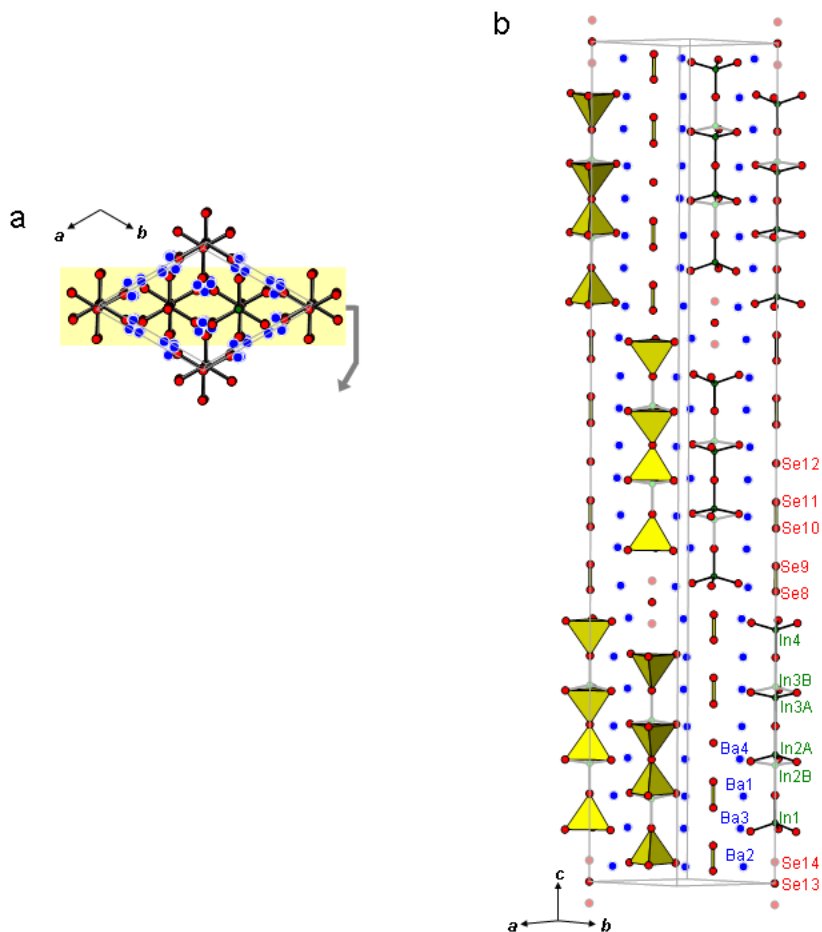
Figure 10-2. Structure of $Ba_{12}In_4Se_{20}$ viewed (a) down the c-direction and (b) normal to a slice parallel to (110) showing 1D stacks of $InSe_4$, In_2Se_7, Se^{2-}, and Se_2^{2-} units.

Although In-centred tetrahedra serve as a typical building block within In-containing chalcogenides, isolated $InSe_4$ units and, even more so, In_2Se_7 double tetrahedra (formed through linking of a common vertex, analogous to sorosilicate units Si_2O_7) are unusual. The first examples of isolated $InSe_4$ anions, in $K_{12}In_2Se_9$ and K_9InSe_7, were reported only recently.[23] In $Ba_{12}In_4Se_{20}$,

two InSe$_4$ tetrahedra surround opposite ends of a central In$_2$Se$_7$ unit. The isolated tetrahedra are quite regular, with In–Se bonds that are nearly equidistant (2.570(2)–2.593(1) Å) and Se–In–Se angles that do not deviate greatly from ideal values (106.23(3)–112.51(3)°). The double tetrahedra are more distorted, with In–Se bonds that are longer to the bridging Se atom (2.670(2)–2.672(2) Å) than those to the terminal Se atoms (2.557(1)–2.558(1) Å). A complicating feature is the occurrence of split sites close to each of the In atoms of the double tetrahedra. The occupancies of the primary sites within the In$_2$Se$_7$ units are 0.895(3) in In2A and 0.814(3) in In3A, whereas the occupancies of the secondary sites are 0.105(3) in In2B and 0.186(3) in In3B. The same occupancies, within error, were obtained in structure refinements of a second crystal: 0.898(3) in In2A, 0.812(2) in In3A, 0.102(3) in In2B, and 0.188(2) in In3B. If the grouping of InSe$_4$–In$_2$Se$_7$–InSe$_4$ units is viewed in terms of In atoms aligned collinearly along the axis of a stack of Se$_3$ triangles and Se atoms, then the occupation of these secondary sites can be interpreted as a displacement of In atoms along the central axis to undergo an umbrella-flip distortion. In the process, a terminal InSe$_4$ unit is converted into an In$_2$Se$_7$ double tetrahedron. This umbrella flip is facilitated by the close proximity of the In atoms to the plane of the Se$_3$ triangles. The primary In sites are favoured because they permit closer contacts to bridging Se atoms along the umbrella handles (2.670(2)–2.672(2) Å) than from the secondary In sites (2.718(8)–2.812(14) Å). Depending on which of the In sites is occupied, the local coordination could be InSe$_4$–In$_2$Se$_7$–InSe$_4$, In$_2$Se$_7$–InSe$_4$–InSe$_4$, InSe$_4$–InSe$_4$–In$_2$Se$_7$, or even In$_2$Se$_7$–Se–In$_2$Se$_7$ (**Figure A4–1** in Appendix). Related phenomena are seen in the structures of some other In-containing chalcogenides: K$_2$In$_{12}$Se$_{19}$ exhibits an average structure containing In sites that remain split and become half-occupied at high temperatures within a pair of face-sharing tetrahedra,[24] whereas Ba*RE*$_2$In$_2$*Ch*$_7$ contains five-coordinate In occurring strictly within a single site having trigonal

bipyramidal geometry.[25] Thus, the umbrella flip observed in $Ba_{12}In_4Se_{20}$ may become manifested at higher temperatures as two equally occupied In sites or perhaps as one In site having an elongated displacement ellipsoid, or at lower temperatures as enhanced occupations of the preferred sites. Corroborating the latter prediction, a low-temperature structure determination (at 193 K) of $Ba_{12}In_4Se_{20}$ reveals that the occupancies of the primary In sites are increased to 0.957(2) in In2A and 0.848(2) in In3A.

The remaining Se atoms occur in two different sets, lying between the $InSe_4$–In_2Se_7–$InSe_4$ groupings. First is a sequence of Se_2^{2-}–Se_2^{2-}–Se^{2-}–Se_2^{2-}–Se_2^{2-} units. The distances within the Se_2^{2-} units (2.367(2)–2.444(2) Å) are typical of Se–Se single bonds (e.g., 2.3876(9) Å in $Ba_4Ga_2Se_8$).[10] Second is what appears at first glance to be an isolated Se^{2-} anion, labeled Se13, located at the origin of the unit cell. Unlike all the other Se sites, Se13 is not bonded to In or Se atoms, and is centred within a rather large cavity delimited by six Ba2 atoms at long distances of 3.4392(6) Å in trigonal antiprismatic geometry (**Figure A4–2** in the Appendix), resulting in an anomalously low bond valence sum of 1.32 (**Table A4–1** in the Appendix).[26] To counteract this severe underbonding, this site is split so that there are two symmetry-equivalent secondary sites, labeled Se14, straddling it. Occupation of the Se14 sites, which are surrounded by three Ba2 atoms at closer distances of 3.069(4) Å in nearly trigonal planar geometry, allows a more reasonable bond valence sum of 1.80 to be recovered, but at the expense of creating larger empty voids in the structure. The occurrence of both primary Se13 (occupied at 0.872(6)) and secondary Se14 sites (occupied each at 0.064(3)) thus suggests a compromise between satisfying both space-filling and bonding requirements.

Perhaps the most remarkable point is that the selenide $Ba_{12}In_4Se_{20}$ is not quite isostructural to the sulfide $Ba_{12}In_4S_{19}$,[3] despite crystallizing in the same trigonal space group and having similar

unit cell parameters. Comparison of the one-dimensional stacks reveals the key differences (**Figure 10–3**). The most important is that the sulfide contains a sequence of S^{2-}–S_2^{2-}–S^{2-}–S_2^{2-}–S^{2-} units, corresponding to a total charge of 10– distributed over seven S atoms, whereas the selenide contains a sequence of Se_2^{2-}–Se_2^{2-}–Se^{2-}–Se_2^{2-}–Se_2^{2-} units, corresponding to the same total charge of 10– but distributed over nine Se atoms. Both compounds attain charge-balanced formulations, $(Ba^{2+})_{12}(In^{3+})_4(S^{2-})_{17}(S_2^{2-})$ vs $(Ba^{2+})_{12}(In^{3+})_4(Se^{2-})_{16}(Se_2^{2-})_2$, in which the same total positive charge of 36+ is balanced by different combinations of monoatomic Ch^{2-} and diatomic Ch_2^{2-} anions! A simple rationalization can be offered by invoking size factors. Substitution of S with Se atoms expands the structure isotropically, with both the *a* and *c* parameters becoming about 4% longer. Greater space is created to accommodate the longer distances from the Ba atoms which surround a sequence of Se atoms; to fill this expanded space, one of the smaller S^{2-} anions in the sulfide is effectively replaced by a larger Se_2^{2-} anion in the selenide. This explanation also applies to the occurrence of the split Se13/Se14 sites in the selenide. However, we note that the bond valence sum around the analogous S site in the sulfide has an equally low value of 1.40, implying that it may also be prone to splitting. Finally, we find no compelling reason why the In_2S_7 double tetrahedra in the sulfide only shows splitting of one of the In sites, and we suggest that splitting of both In sites, as occurs in the selenide, may be possible.
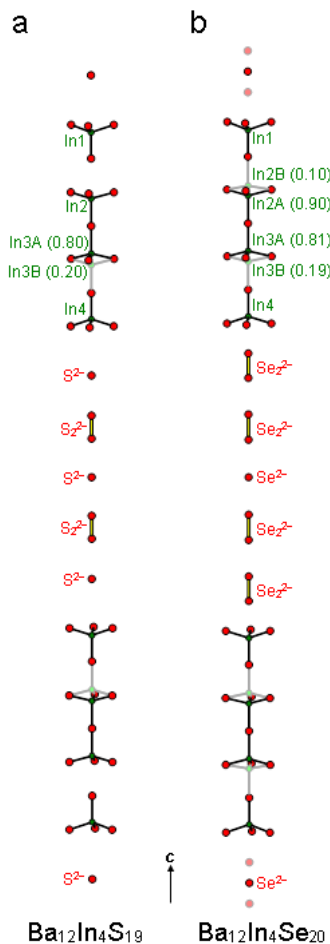
Figure 10-3. Comparison of 1D stacks in (a) $Ba_{12}In_4S_{19}$ and (b) $Ba_{12}In_4Se_{20}$, with occupancies of the split In sites shown.

The dark red colour, appearing almost black, of the selenide $Ba_{12}In_4Se_{20}$ suggests a smaller band gap than in the sulfide $Ba_{12}In_4S_{19}$, which is yellow.[3] An optical band gap of 1.70(2) eV for $Ba_{12}In_4Se_{20}$ was deduced by the straightforward extrapolation method from the optical absorption spectrum,[27] which was converted from the diffuse reflectance spectrum using the Kubelka-Munk function (**Figure 10–4**). In comparison, $Ba_{12}In_4S_{19}$ has a measured optical band gap of 2.56 eV. In both cases, the band gaps are considerably reduced (by as much as 1 eV) relative to the typical values found in related chalcogenides that do not contain Ch_2^{2-} units. For example, the band gaps

in other Ba–In–Se phases, which lack Se_2^{2-} units, are 2.12 eV in $Ba_2In_2Se_5$[15] and 2.62 eV in $BaIn_2Se_4$.[28] The band gap narrowing can be largely traced to the lowered energy of the bottom of the conduction band, as a result of contributions from $Ch–Ch$ π-antibonding levels. Interestingly, the band gaps in the Ga-containing chalcogenides $Ba_4Ga_2S_8$ (2.55 eV)[3] and $Ba_4Ga_2Se_8$ (1.63 eV),[10] which also contain Ch_2^{2-} units, are almost the same as in the In-containing chalcogenides $Ba_{12}In_4S_{19}$ and $Ba_{12}In_4Se_{20}$, respectively, despite their completely different structures. This suggests that the mere presence of Ch_2^{2-} units already has a dominant effect on the electronic structure of these chalcogenides.
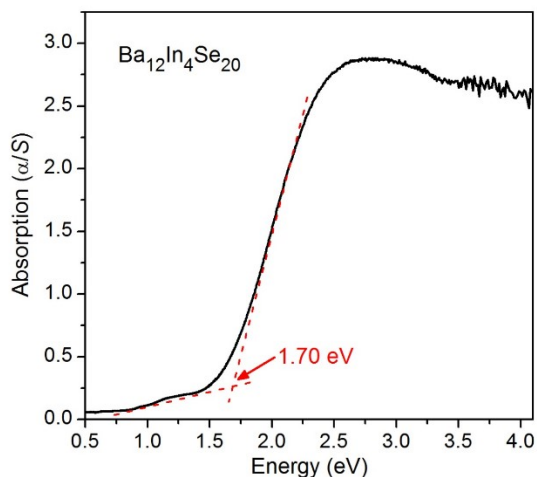
Figure 10-4. Diffuse reflectance spectrum for $Ba_{12}In_4Se_{20}$.

10.4 Conclusions

The selenide $Ba_{12}In_4Se_{20}$ is nearly, but not quite isostructural to the sulfide $Ba_{12}In_4S_{19}$, the key point of departure being the replacement of a diatomic Se_2^{2-} anion for a monoatomic S^{2-} anion. The occurrence of identical charges but different structures of these two compounds illustrates what could perhaps be described as "charge isomers." The band gap in $Ba_{12}In_4Se_{20}$ is significantly

lower than in other related ternary chalcogenides by virtue of being a selenide as well as through

the presence of these Se_2^{2-} units.

10.5 References

[1] Eisenmann, B.; Jakowski, M.; Schäfer, H. *Z. Naturforsch. B* **1984**, *39*, 27–30.
[2] Eisenmann, B.; Jakowski, M.; Schäfer, H. *Rev. Chim. Miner.* **1984**, *21*, 12–20
[3] Liu, J. -W.; Wang, P.; Chen, L. *Inorg. Chem.* **2011**, *50*, 5706–5713.
[4] Eisenmann, B.; Jakowski, M.; Schäfer, H. *Z. Naturforsch. B* **1983**, *38*, 1581–1584.
[5] Eisenmann, B.; Jakowski, M.; Schäfer, H. *Mater. Res. Bull.* **1982**, *17*, 1169–1175
[6] Eisenmann, B.; Jakowski, M.; Schäfer, H. *Rev. Chim. Miner.* **1984**, *20*, 329–337.
[7] Lin, X.; Zhang, G.; Ye, N. *Cryst. Growth Des.* **2009**, *9*, 1186–1189.
[8] Mei, D.; Yin, W.; Lin, Z.; Yao, J. L.; Fu, P.; Y. Wu *J. Alloys Compd.* **2011**, *509*, 2981–2985.
[9] Yin, W.; Mei, D.; Feng, K.; Yao, J.; Fu, P.; Wu, Y. *Dalton Trans.* **2011**, *40*, 9159–9162.
[10] Yin, W.; Iyer, A. K.; Lin, X.; Mar, A. *J. Solid State Chem.* **2016**, *237*, 144–149.
[11] Klee, W.; Schäfer, H. *Z. Anorg. Allg. Chem.* **1981**, *479*, 125–133.
[12] Yao, J. L.; Mei, D.; Bai, L.; Lin, Z.; Yin, W.; Fu, P.; Wu, Y. *Inorg. Chem.* **2010**, *49*, 9212–9216.
[13] Li, Y. -Y.; Liu, P. -F.; Lin, H.; Wang, M. -T.; Chen, L. *Inorg. Chem. Front.* **2016**, *3*, 952–958.
[14] Eisenmann, B.; Hofmann, A. *Z. Anorg. Allg. Chem.* **1990**, *580*, 151–159.
[15] Gao, W.; Wu, K.; Lai, K.; Yang, Z.; Pan, S. *Z. Anorg. Allg. Chem.* **2015**, *641*, 1329–1333.
[16] Eisenmann, B.; Jakowski, M.; Klee, W.; Schäfer, H. *Rev. Chim. Miner.* **1983**, *20*, 255–263.
[17] Ivanov-Emin, B. N.; Ivlieva, V. I.; Filatenko, L. A.; Zaitsev, B. E.; Kaziev, G. Z.; Sarabiya, M.G. *Zh. Neorg. Khim.* **1984**, *29*, 1960–1963.
[18] Kipp, D. O.; Lowe-Ma, C. K.; Vanderah, T. A. *Chem. Mater.* **1990**, *2*, 506–511.
[19] Klee, W.; Schäfer, H. *Chim. Miner.* **1979**, *16*,465–472.
[20] Sheldrick, G. M. *SHELXTL, version 6.12*, Bruker AXS Inc., Madison, WI, 2001.
[21] Gelato, L. M.; Parthé, E. *J. Appl. Crystallogr.* **1987**, *20*, 139–143
[22] Kortüm, G. *Reflectance Spectroscopy*, Springer, New York, **1969**.
[23] Heine, J.; Dehnen, S. *Z. Anorg. Allg. Chem.* **2008**, *634*, 2303–2308.
[24] Schlosser, M.; Reiner, C.; Deiseroth, H. -J.; Kienle, L. *Eur. J. Inorg. Chem.***2001**, 2241–2247.
[25] Yin, W.; Iyer, A. K.; Lin, X.; Li, C.; Yao, J.; Mar, A. *Dalton Trans.* **2016**, *45*, 12329–12337.
[26] Brese, N. E.; O'Keeffe, M. *Acta. Crystallogr., Sect. B* **1991**, *47*, 192–197.
[27] Schevciw, O.; White, W. B. *Mater. Res. Bull.* **1983**, *18*, 1059–1068.
[28] Park, S. -A.; Kim, M. -Y.; Kim, W. -T.; Jin, M. -S.; Chee, S. -H.; Park, T. -Y.; Park, K. -H.; Kim, D. -T. *J. Mater. Res.* **2002**, *17*, 2147–2152.

Chapter 11

Noncentrosymmetric selenide $Ba_4Ga_4GeSe_{12}$: Synthesis, structure, and optical properties

11.1 Introduction

Metal chalcogenides are the most promising candidates in the search for new nonlinear optical (NLO) materials in the infrared range.[1,2] They are usually ternary and quaternary compounds, typically containing triels (group 13 elements), as found in the benchmark compounds $AgGaS_2$ and $AgGaSe_2$ themselves. In the Ba–Ga–Q (Q = S, Se) systems, the compounds $BaGa_4S_7$[3] and $BaGa_4Se_7$ have been recently identified as new infrared NLO materials with excellent properties; interestingly, even though they have the same composition, the sulfide and the selenide adopt different three-dimensional crystal structures.[4] These systems, which are still incompletely explored, appear to be particularly rich and contain, besides $BaGa_4Q_7$, many other ternary phases ($BaGa_2S_4$, $Ba_2Ga_2S_5$, $Ba_3Ga_2S_6$, $Ba_4Ga_2S_7$, $Ba_4Ga_2S_8$, $Ba_5Ga_2S_8$, $BaGa_2Se_4$, $Ba_5Ga_4Se_{10}$, $Ba_5Ga_2Se_8$, $Ba_4Ga_2Se_8$).[5–13] A strategy to increase flexibility is to introduce another metal component M to the Ba–Ga–Q systems so that the combination of cations of different size, charge, bonding, and coordination preferences may generate new noncentrosymmetric quaternary chalcogenides Ba–Ga–M–Q with more complex structures. This approach has led to exciting developments in the discovery of compounds $Ba_{23}Ga_8Sb_2S_{38}$, $BaGa_2SnSe_6$, $Ba_4CuGa_5Se_{12}$, $Ba_2Ga_8GeS_{16}$, and $BaGa_2GeQ_6$ exhibiting good NLO properties.[14–19]

In the course of investigations of the Ba–Ga–Ge–Q (Q = S, Se) systems, the new compound $Ba_4Ga_4GeSe_{12}$ was prepared. We report here its crystal structure, electronic structure, and optical properties.

11.2 Experimental

11.2.1 Synthesis

Ba shot (99%, Sigma-Aldrich), Ga shot (99.99%, Cerac), Ge ingot (99.9999%, Alfa-Aesar), and Se powder (99.99%, Sigma-Aldrich) were used as obtained. Binary starting materials BaSe, Ga_2Se_3, and $GeSe_2$ were prepared by stoichiometric reaction of the elements at high temperatures (1173 K for BaSe, 1223 K for Ga_2Se_3, and 973 K for $GeSe_2$) in sealed fused-silica tubes. A mixture of BaSe (130 mg, 0.60 mmol), Ga_2Se_3 (113 mg, 0.30 mmol), and $GeSe_2$ (35 mg, 0.15 mmol) in a molar ratio of 4:2:1 was finely ground and loaded into a fused-silica tube, which was evacuated and flame-sealed. The tube was heated to 1173 K over 30 h, kept at that temperature for 72 h, cooled to 473 K over 48 h, and then slowly cooled to room temperature by shutting off the furnace. Orange-yellow block-shaped air-stable crystals were obtained, which were examined by energy-dispersive X-ray (EDX) analysis on a JEOL JSM-6010LA InTouchScope scanning electron microscope and found to contain 23(2)% Ba, 21(2)% Ga, 4(1)% Ge, and 52(4)% Se, in reasonable agreement with the expected composition (19% Ba, 19% Ga, 5% Ge, 57% Se). These crystals were selected for the single-crystal structure determination. In anticipation of optical measurements, a powder sample was prepared as before by stoichiometric reaction of BaSe, Ga_2Se_3, and $GeSe_2$ in a 4:2:1 ratio except that the dwell temperature was 1073 K and no slow cooling step was included; the sample was reground and the heat treatment was repeated. Powder X-ray diffraction (XRD), performed on an Inel powder diffractometer equipped with a curved position-sensitive detector (CPS 120) and a Cu $K\alpha_1$ radiation source operated at 40 kV and 20 mA, revealed that the powder sample is quantitatively phase-pure, with no traces of other phases (**Figure 11–1**).
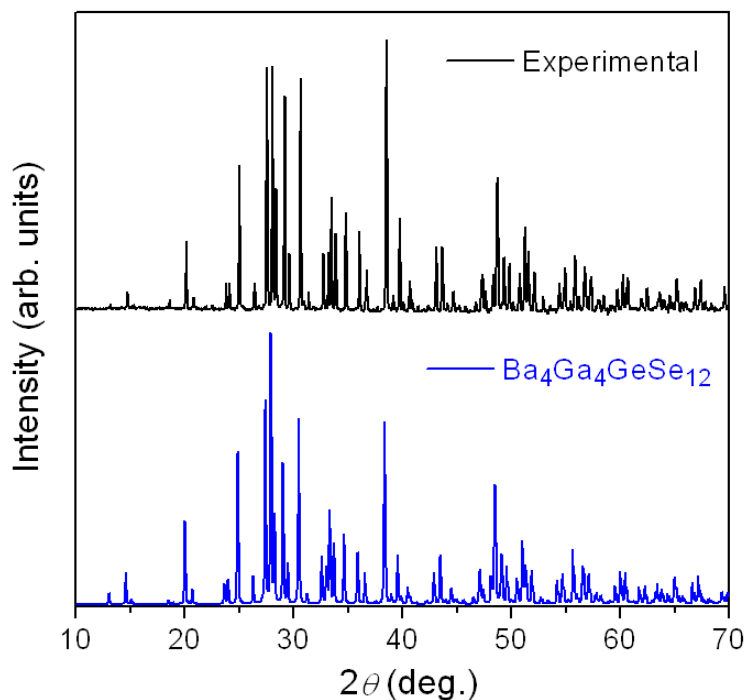
Figure 11-1. Powder XRD pattern of $Ba_4Ga_4GeSe_{12}$.

11.2.2 Structure determination

Intensity data were collected at room temperature on a Bruker PLATFORM diffractometer equipped with a SMART APEX II CCD area detector and a graphite-monochromated Mo $K\alpha$ radiation source, using ω scans at six different ϕ angles with a frame width of 0.3° and an exposure time of 25 s per frame. Face-indexed numerical absorption corrections were applied. Structure solution and refinement were carried out with use of the SHELXTL (version 6.12) program package.[20] Intensity statistics, Laue symmetry, and systematic absences led to the noncentrosymmetric tetragonal space group $P\bar{4}2_1c$ as the only possible choice. Initial positions for all atoms were located by direct methods. Two metal sites, $M1$ at $8e$ and $M2$ at $2b$, were found to be coordinated tetrahedrally by Se atoms and were thus appropriate for either Ga or Ge atoms. Given the formula $Ba_4Ga_4GeSe_{12}$, it was tempting to assume an ordered structure in which Ga

atoms are placed at 8*e* and Ge atoms at 2*b*. Other models were considered in which the site distributions were reversed or in which both sites were allowed to contain a mixture of the two atoms. Although the similar X-ray scattering factors of Ga and Ge may be anticipated to pose problems in occupancy refinements, surprisingly convergence could be achieved through judicious choice of weighting scheme. **Table 11–4** compares the results of these refinements of models with different site distributions, all other things being equal. Not surprisingly, these models cannot be easily distinguished on the basis of the agreement factors, which do not differ significantly; chemical features must also be examined to evaluate these models. The reversed model can be ruled out because the formula "$Ba_4GaGe_4Se_{12}$" is completely inconsistent with the synthetic stoichiometry and EDX analysis, and moreover would not be charge-balanced. In the variable occupancy model, where no constraints were placed on the overall composition, $M1$ contains approximately 0.75 Ga and 0.25 Ge, while $M2$ is close to 1.00 Ga; this partially disordered model gave slightly better agreement factors and corresponds to the expected formula $Ba_4Ga_4GeSe_{12}$, in agreement with the stoichiometry of the synthesis and the results of the EDX analysis. In subsequent refinements, the occupancies were fixed to exactly 0.75 Ga and 0.25 Ge in $M1$, and 1.00 Ga in $M2$. As discussed in more detail later, this model is also the most chemically sensible.

Atomic coordinates were standardized with the program STRUCTURE TIDY.[21] Crystal data and further details are listed in **Table 11–1**, positional and equivalent isotropic displacement parameters in **Table** 11–2, and interatomic distances in **Table** 11–3.

Table 11-1. Crystallographic data for $Ba_4Ga_4GeSe_{12}$.

Formula	$Ba_4Ga_4GeSe_{12}$
Formula mass (amu)	1848.35
Space group	$P\bar{4}2_1c$ (No. 114)
a (Å)	13.5468(4)
c (Å)	6.4915(2)
V (Å^3)	1191.29(8)
Z	2
ρ_{calcd} (g cm^{-3})	5.153
T (K)	296(2)
Crystal dimensions (mm)	$0.08 \times 0.07 \times 0.06$
Radiation	Graphite monochromated Mo $K\alpha$, $\lambda = 0.71073$ Å
μ(Mo $K\alpha$) (mm^{-1})	30.50
Transmission factors	0.170–0.297
2θ limits	4.25–66.50°
Data collected	$-20 \le h \le 20, -20 \le k \le 20, -9 \le l \le 9$
No. of data collected	16885
No. of unique data, including $F_o^2 < 0$	2273 ($R_{int} = 0.046$)
No. of unique data, with $F_o^2 > 2\sigma(F_o^2)$	2102
No. of variables	49
Flack parameter	0.02(2)
$R(F)$ for $F_o^2 > 2\sigma(F_o^2)$ [a]	0.023
$R_w(F_o^2)$ [b]	0.049
Goodness of fit	1.077
$(\Delta\rho)_{max}, (\Delta\rho)_{min}$ (e Å^{-3})	1.02, –0.78

[a] $R(F) = \sum||F_o| - |F_c|| / \sum|F_o|$.   [b] $R_w(F_o^2) = [\sum[w(F_o^2 - F_c^2)^2] / \sum wF_o^4]^{1/2}$; $w^{-1} = [\sigma^2(F_o^2) + (Ap)^2 + Bp]$, where $p = [\max(F_o^2,0) + 2F_c^2] / 3$.

Table 11-2. Atomic coordinates and equivalent isotropic displacement parameters for $Ba_4Ga_4GeSe_{12}$.

Atom	Wyckoff position	Occupancy	X	y	Z	U_{eq} (Å^2) [a]
Ba	8e	1	0.30043(3)	0.02173(3)	0.04834(6)	0.02167(9)
Ga1/Ge1	8e	0.75/0.25	0.14011(5)	0.24076(5)	0.44366(11)	0.01553(12)
Ga2	2b	1	0	0	0.5	0.0167(2)
Se1	8e	1	0.08689(5)	0.10007(4)	0.25419(10)	0.01780(12)
Se2	8e	1	0.29215(4)	0.30036(5)	0.28621(9)	0.01916(12)
Se3	8e	1	0.51483(4)	0.13992(4)	0.04535(10)	0.01822(11)

[a] U_{eq} is defined as one-third of the trace of the orthogonalized U_{ij} tensor.

Table 11-3. Interatomic distances (Å) for $Ba_4Ga_4GeSe_{12}$.

Ba–Se3	3.3166(7)
Ba–Se3	3.3255(7)
Ba–Se2	3.3342(7)
Ba–Se1	3.3587(7)
Ba–Se3	3.3626(8)
Ba–Se3	3.3999(8)
Ba–Se2	3.4234(7)
Ba–Se1	3.6591(7)
Ga1/Ge1–Se3	2.3447(8)
Ga1/Ge1–Se1	2.3801(9)
Ga1/Ge1–Se2	2.4070(9)
Ga1/Ge1–Se2	2.4370(9)
Ga2–Se1 (×4)	2.4019(6)

11.2.3 Diffuse reflectance spectroscopy

The spectrum of $Ba_4Ga_4GeSe_{12}$ was measured from 300 nm (4.13 eV) to 2500 nm (0.50 eV) on a Cary 5000 UV-VIS-NIR spectrophotometer equipped with a diffuse reflectance accessory. The powder sample was spread on a compacted base of $BaSO_4$, used as a 100% reflectance standard. The optical absorption spectrum was converted from the diffuse reflectance spectrum using the Kubelka-Munk function, $\alpha/S = (1–R)^2/2R$, where α is the Kubelka–Munk absorption coefficient, S is the scattering coefficient, and R is the reflectance.[22]

11.2.4 Second-harmonic generation measurements

An optical second-harmonic generation (SHG) test of $Ba_4Ga_4GeSe_{12}$ was performed by means of the Kurtz-Perry method.[23] Fundamental light of 2.09 μm wavelength was generated with a Q-switched Ho:Tm:Cr:YAG laser. The particle sizes of the sieved samples were 80–100 μm. Microcrystalline $AgGaS_2$ of similar particle sizes served as the reference.

11.2.5 Band structure calculation

Tight-binding linear muffin tin orbital band structure calculations were performed on $Ba_4Ga_4GeSe_{12}$ within the local density and atomic spheres approximation with use of the Stuttgart TB-LMTO-ASA program (version 4.7).[24] To treat the mixing of Ga and Ge atoms observed within one of the tetrahedral sites (in $8e$), an ordered model in monoclinic space group $P2$ was considered in which Ge atoms were distributed in 2 out of the 8 equivalent positions within the unit cell, so that half of the zigzag chains (described in further detail below) consist of alternating Ga- and Ge-centred corner-sharing tetrahedra. The basis set consisted of Ba 6s/6p/5d/4f, Ga 4s/4p/4d, Ge 4s/4p/4d, and Se 4s/4p/4d orbitals, with the Ba 6p/4f, Ga 4d, Ge 4d, and Se 4d orbitals being downfolded. Integrations in reciprocal space were carried out with an improved tetrahedron method over 80 irreducible k points within the first Brillouin zone.

11.3 Results and discussion

The selenide $Ba_4Ga_4GeSe_{12}$ was obtained by reaction of BaSe, Ga_2Se_3, and $GeSe_2$ and is the second quaternary compound found in the Ba–Ga–Ge–Se system, in which the only other previously known representative was $BaGa_2GeSe_6$.[18,19] This system is related to the pseudoternary ones AQ–Ga_2Q_3–GeQ_2 (A = alkaline-earth metal; Q = S, Se) which are of interest because of their propensity to form glasses. [25–28] In general, compositions closer to the GeQ_2 corner of these pseuedoternary systems tend to lead to noncrystalline phases because GeQ_2 is a better glass network former than Ga_2Q_3, whereas compositions farther away from this corner tend to lead to crystalline phases, as exemplified by the Ge-poorer compounds $Ba_4Ga_4GeSe_{12}$ and $BaGa_2GeSe_6$. Attempts to prepare substitutional derivatives of $Ba_4Ga_4GeSe_{12}$ (e.g., by replacing In for Ga, Sn for Ge, or S and Te for Se) were unsuccessful.

$Ba_4Ga_4GeSe_{12}$ crystallizes in the noncentrosymmetric space group $P\overline{4}2_1c$ and contains one Ba, two M, and three Se sites, all in Wyckoff position $8e$ (site symmetry 1) except for one of the M sites, which is in $2b$ (site symmetry $\overline{4}$). The basic building blocks are MSe_4 tetrahedra which are connected through corner-sharing to form a three-dimensional network whose voids are filled by Ba cations (**Figure 11–2**). The $M1$-centred tetrahedra are connected in a head-to-tail fashion to form one-dimensional chains extending in a zigzag fashion; all these tetrahedra are oriented so that the $M1$–Se2 bonds point roughly in the same direction, nearly parallel to the polar c-axis. Four zigzag chains, like the arms of a pinwheel, are connected by single $M2$-centred tetrahedra, which are oriented with their fourfold inversion axes along the c-direction. Thus, the dipoles of the $M1$-centred tetrahedra pointing in the same orientation along c are responsible for the overall polarity of the structure, whereas those of the $M2$-centred tetrahedra provide no contribution.
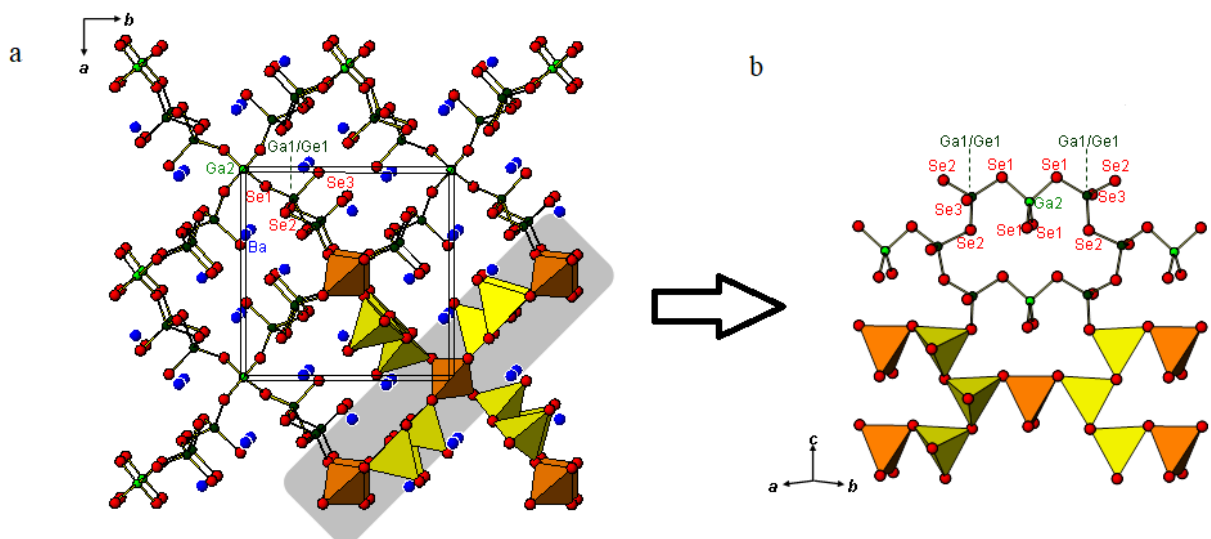
Figure 11-2. (a) Structure of $Ba_4Ga_4GeSe_{12}$ viewed down the c-direction, highlighting pinwheel motifs with zigzag chains of tetrahedra centred by $M1$ (yellow, occupied by 0.75 Ga and 0.25 Ge)

forming the spokes and single tetrahedra centred by $M2$ (orange, occupied by Ga) at the hubs. (b) View perpendicular to (110) showing corner-shared $M1$- and $M2$-centred tetrahedra.

Although $Ba_4Ga_4GeSe_{12}$ is isostructural to $Pb_4Ga_4GeQ_{12}$ ($Q = S$, Se)[29] and $Ba_4Ga_4SnSe_{12}$,[30] there are subtle differences in site ordering and coordination geometries. The previous compounds were assumed to have ordered structures, with $M1$ (in $8e$) containing Ga atoms and $M2$ (in $2b$) containing Ge or Sn atoms. Evaluation of models with different site distributions in $Ba_4Ga_4GeSe_{12}$ (**Table 11–4**) suggests that this assumption should be revisited, especially with careful attention being paid to bond lengths and bond valence sums. In $Ba_4Ga_4GeSe_{12}$, the distances of tetrahedrally coordinating Se atoms around $M1$ fall in the range of 2.3447(8)–2.4370(9) Å, for which the average distance of 2.39(4) Å is nearly the same as the four equivalent distances of 2.4019(6) Å around $M2$. A survey of about 3000–4000 entries in Pearson's Crystal Data indicates that Ga–Se distances are generally slightly longer (median of 2.43 Å) than Ge–Se distances (median of 2.35 Å).[31] On the basis of these distances, disorder of Ga and Ge is certainly possible and the $M2$ site should be preferred by the Ga atoms. Bond valence analysis[32,33] indicates that Ga atoms are suitable to occupy either $M1$ (giving a bond valence sum of $V = 3.16$) or $M2$ sites ($V = 3.04$). However, Ge atoms are underbonded if they occupy $M1$ ($V = 3.61$) and severely so in $M2$ ($V = 3.48$). A partially disordered model, confirmed by refinements on the diffraction data, is the most reasonable, in which $M1$ contains a mixture of 0.75 Ga and 0.25 Ge (giving a weighted bond valence sum of $V = 3.27$) and $M2$ contains exclusively Ga. All other sites in $Ba_4Ga_4GeSe_{12}$ are well behaved and exhibit the expected bond valence sums (Ba, 2.04; Se1, 1.99; Se2, 2.02; Se3, 2.07). It is interesting that in $Pb_4Ga_4GeSe_{12}$, there is greater differentiation between the bond lengths around $M1$ (2.338(4)–2.394(4) Å, or average of 2.37(3) Å) and around $M2$ (2.321(3) Å), so that an ordered model containing Ga atoms in $M1$ and Ge atoms in $M2$ is invoked.[29]

Table 11-4. Evaluation of models with different Ga/Ge site distributions.

Model	A	B	C	D
Formula	$Ba_4Ga_4GeSe_{12}$	$Ba_4GaGe_4Se_{12}$	$Ba_4Ga_{4.0(5)}Ge_{1.0(5)}Se_{12}$	$Ba_4Ga_4GeSe_{12}$
$M1$ at $8e$ (0.14, 0.24, 0.44)	1.00 Ga	1.00 Ge	0.75(13) Ga / 0.25(13) Ge	0.75 Ga / 0.25 Ge
$M2$ at $2b$ (0, 0, 0.5)	1.00 Ge	1.00 Ga	0.97(24) Ga / 0.03(24) Ge	1.00 Ga
Bond valence sum for $M1$	3.16	3.61	3.27	3.27
Bond valence sum for $M2$	3.48	3.04	3.05	3.04
$R(F)$ for $F_o^2 > 2\sigma(F_o^2)$	0.0235	0.0235	0.0232	0.0232
$R_w(F_o^2)$	0.0525	0.0527	0.0520	0.0520
A, B [a]	0.0261, 0.4522	0.0261, 0.4522	0.0261, 0.4522	0.0261, 0.4522
$(\Delta\rho)_{max}, (\Delta\rho)_{min}$ (e Å^{-3})	1.01, –0.92	1.05, –0.77	1.02, –0.78	1.02, –0.78

[a] Weighting parameters appearing in the expression $w^{-1} = [\sigma^2(F_o^2) + (Ap)^2 + Bp]$, where $p = [\max(F_o^2, 0) + 2F_c^2] / 3$.

The contrasting site distributions in $Ba_4Ga_4GeSe_{12}$ and $Pb_4Ga_4GeSe_{12}$ may be related to the different coordination environments around Ba vs. Pb atoms, which are surrounded by eight Se atoms in roughly square antiprismatic or bicapped trigonal prismatic geometries. However, the environment is much more symmetrical around the Ba atoms (3.3166(7)–3.6591(7) Å) in $Ba_4Ga_4GeSe_{12}$ than around the Pb atoms (2.902(4)–3.843(4) Å) in $Pb_4Ga_4GeSe_{12}$.[29] Notwithstanding the more distorted coordination geometry of the Pb atoms, the presence of stereochemically active lone pairs does not appear to be supported by an analysis of the electron localization function in $Pb_4Ga_4GeSe_{12}$.[29] In $Ba_4Ga_4SnSe_{12}$, it may be anticipated that the ordered model would be favoured by the greater size difference between Ga and Sn atoms; however, the Sn–Se bonds appear to be anomalously short (2.438(1) Å) and close inspection of the displacement parameters for the $M1$ and $M2$ sites suggests that perhaps some disorder may be present.[30]

With all atoms adopting their normal oxidation states, a charge-balanced formulation $(Ba^{2+})_4(Ga^{3+})_4(Ge^{4+})(Se^{2-})_{12}$ is obtained. The aliovalent substitution of Ge^{4+} with two cations summing to the same charge, such as Ga^{3+} and M^{1+}, leads to the previously reported compounds $Ba_4MGa_5Se_{12}$ (M = Li, Ag)[34] and $Ba_4CuGa_5Q_{12}$ (Q = S, Se),[16] whose structures can be derived by stuffing Li, Ag, or Cu atoms within two possible types of interstitial sites with tetrahedral geometry, as has been described in detail elsewhere.[29]

The absorption spectrum of $Ba_4Ga_4GeSe_{12}$, which was converted from the UV-visible-NIR diffuse reflectance spectrum using the Kubelka-Munk function, reveals a band gap of 2.18(2) eV, (**Figure 11–3**) as deduced through an extrapolation method.[35] This large band gap, which is consistent with the orange-yellow colour of the material, can be compared with those in the related compounds $Ba_4Ga_4SnSe_{12}$ (2.16 eV),[30] $Pb_4Ga_4GeSe_{12}$ (1.91 eV),[29] and $BaGa_2GeSe_6$ (2.81 eV[18] or 2.22 eV [19]).
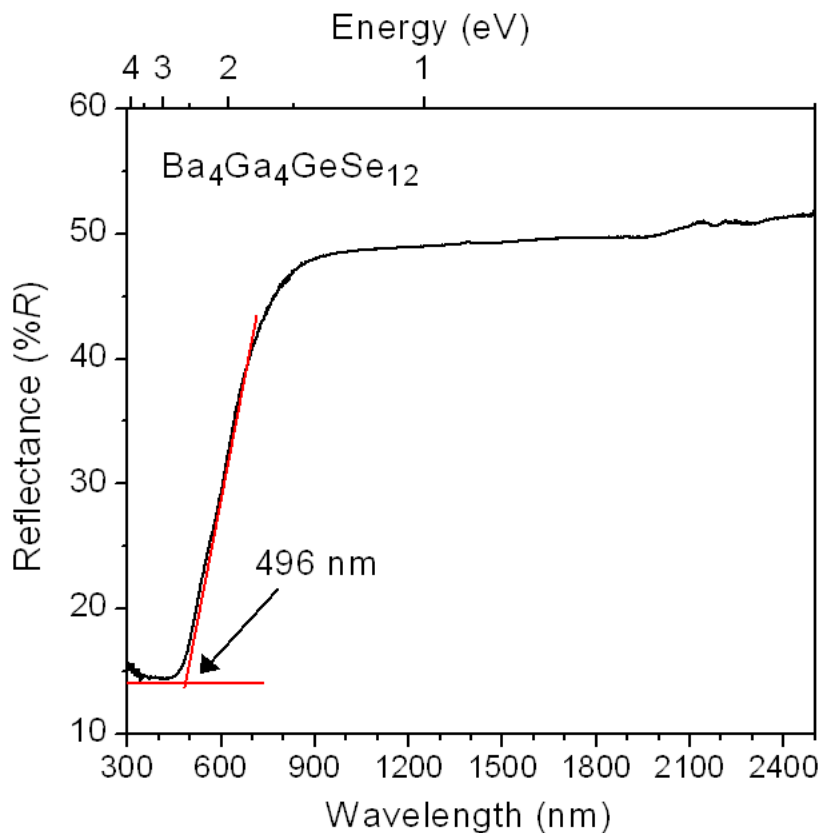
Figure 11-3. Optical absorption spectrum of $Ba_4Ga_4GeSe_{12}$.

An optical test performed on $Ba_4Ga_4GeSe_{12}$ using fundamental light with a wavelength of 2.09 μm showed only a very weak SHG signal, about one-tenth of the intensity of $AgGaS_2$ with similar particle size. For comparison, $Ba_4Ga_4SnSe_{12}$ does not show any SHG response with identical wavelength and similar particle sizes.[30] Optical measurements on the Pb-containing compounds conducted using fundamental light with a wavelength of 2.05 μm and $AgGaS_2$ having similar particle sizes as a reference indicated that $Pb_4Ga_4GeS_{12}$ shows no SHG response, whereas $Pb_4Ga_4GeSe_{12}$ exhibits a strong SHG response which as about twice that of $AgGaS_2$.[29] The tentative conclusion that can be drawn from these observations is that the good performance of $Pb_4Ga_4GeSe_{12}$ probably originates not from the $[Ga_4GeSe_{12}]^{8-}$ framework which is also common

to $Ba_4Ga_4GeSe_{12}$, but rather from the presence of the more asymmetric coordination of Se atoms around the Pb atoms.

Band structure calculations were performed on a hypothetically ordered model of $Ba_4Ga_4GeSe_{12}$ in which Ga and Ge atoms in an alternating sequence occupy half of the zigzag chains of corner-sharing tetrahedra centred by $M1$. Consistent with the charge-balanced formulation, the density of states (DOS) curve has a band gap at the Fermi level (**Figure 11–4a**). There is strong mixing of Se 4p states with Ga 4s (from –6.5 to –5.0 eV) and 4p states (from –3.5 to 0 eV), and similarly with Ge 4s (from –8.6 to –8.2 eV) and 4p states (from –4.3 to –3.8 eV), corresponding to Ga–Se and Ge–Se bonding levels that are completely filled up to the Fermi level, as confirmed by the crystal orbital Hamilton population (COHP) curves (**Figure 11–4b**). Empty bands above the Fermi level are primarily Ga–Se and Ge–Se antibonding in character. The small manifold of Ga–Se antibonding states lying 1.20 eV above the valence band results from the ordered superstructure model considered here, which tends to induce band-gap narrowing relative to a disordered model.[36] The bottom of the conduction band in a disordered model would correspond more closely to where the Ga–Se antibonding states appear, at 2.35 eV above the valence band, in good agreement with the measured optical band gap of 2.18 eV. The integrated COHP (–ICOHP) values are 2.9 eV/bond for Ga–Se and 3.4 eV/bond for Ge–Se contacts. Most Ba-based states are found well above the Fermi level, but some are found below, leading to a partial covalent contribution to Ba–Se bonding, corresponding to an –ICOHP value of 0.5 eV/bond. The total covalent bonding energy in the structure originates largely from Ga–Se interactions (67%), and the remainder is provided by Ge–Se (15%) and Ba–Se (18%) interactions.
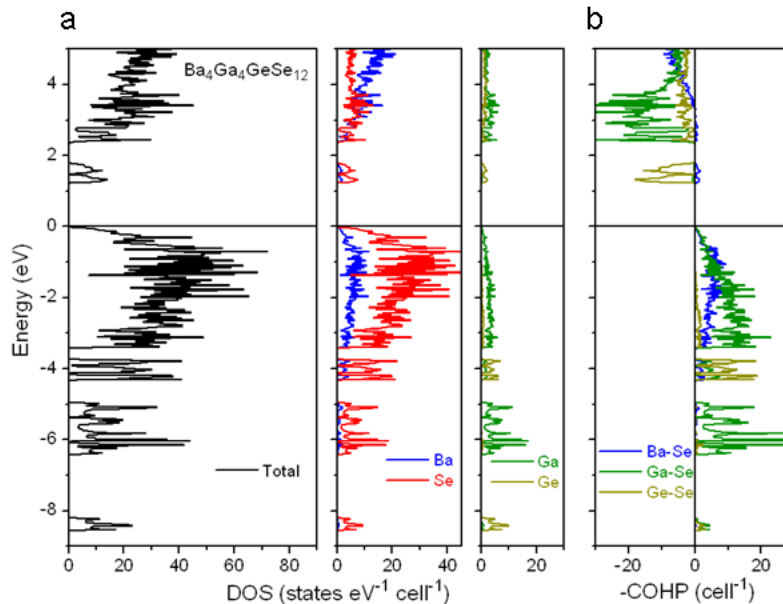
Figure 11-4. (a) Density of states (DOS) curve and its atomic projections, and (b) crystal orbital Hamilton population (–COHP) curves for an ordered superstructure model of $Ba_4Ga_4GeSe_{12}$.

11.4 Conclusions

Although $Ba_4Ga_4GeSe_{12}$ has a noncentrosymmetric structure, its NLO performance was not as good as $Pb_4Ga_4GeSe_{12}$, in which greater polarity is imparted by the more asymmetric coordination of Pb atoms, or $BaGa_2GeSe_6$, in which better alignment of tetrahedra is attained. The partial disorder of Ga and Ge atoms evidenced in $Ba_4Ga_4GeSe_{12}$ suggests that assumptions about site distributions should be carefully considered, and possibly re-evaluated in related compounds.

11.5 References

[1]   Chung, I.; Kanatzidis, M. G. *Chem. Mater.* **2014**, *26*, 849–869.
[2]   Zhao, H. -J.; Wu, X. -T.; Wu, L. -M. *Struct. Bond.* **2012**, *145*, 121–134.
[3]   Lin, X.; Zhang, G.; Ye, N. *Cryst. Growth Des.* **2009**, *2*, 1186–1189.
[4]   Yao, J. L.; Mei, D.; Bai, L.; Lin, Z.; Yin, W.; Fu, P.; Wu, Y. *Inorg. Chem.* **2010**, *49*, 9212–9216.
[5]   Eisenmann, B.; Jakowski, M.; Schäfer, H. *Mater. Res. Bull.* **1982**, *17*, 1169–1175.
[6]   Eisenmann, B.; Jakowski, M.; Schäfer, H. *Z. Naturforsch. B* **1983**, *38*, 1581–1584.
[7]   Eisenmann, B.; Jakowski, M.; Schäfer, H. *Rev. Chim. Miner.* **1984**, *21*, 12–20.
[8]   Liu, J. -W.; Wang, P.; Chen, L. *Inorg. Chem.* **2011**, *50*, 5706–5713.
[9]   Eisenmann, B.; Jakowski, M.; Schäfer, H. *Z. Naturforsch. B* **1984**, *39*, 27–30.
[10]   Klee, W.; Schäfer, H. *Z. Anorg. Allg. Chem.* **1981**, *479*, 125–133.
[11]   Yin, W.; Mei, D.; Feng, K.; Yao, J.; Fu, P.; Wu, Y. *Dalton Trans.* **2011**, *40*, 9159–9162.

[12] Mei, D.; Yin, W.; Lin, Z.; Yao, J. L.; Fu, P.; Y. Wu *J. Alloys Compd.* **2011**, *509*, 2981–2985.

[13] Yin, W.; Iyer, A. K.; Lin, X.; Mar, A. *J. Solid State Chem.* **2016**, *237*, 144–149.

[14] Chen, M. C.; Wu, L. M.; Lin, H.; Zhou, L. J.; Chen, L. *J. Am.Chem. Soc.* **2012**, *134*, 6058−6060.

[15] Li, X.; Li, C.; Gong, P.; Lin, Z.; Yao, Wu, J. Y. *J. Mater. Chem. C* **2015**, *3*, 10998–11004.

[16] Kuo, S. -M.; Chang, Y. -M.; Chung, I.; Jang, J. -I.; Her, B. -H.; Yang, S. -H.; Ketterson, J. B.; Kanatzidis, M. G.; Hsu, K. -F. *Chem. Mater.* **2013**, *25*, 2427–2433.

[17] Liu, B. -W.; Zeng, H. -Y.; Zhang, M. -J.; Fan, Y. -H.; Guo, G. -C.; Huang, J. -S.; Dong, Z. -C. *Inorg. Chem.* **2015**, *54*, 976–981.

[18] Lin, X.; Guo, Y.; Ye, N. *J. Solid State Chem.* **2012**, *195*, 172–177.

[19] Yin, W.; Feng, K.; Mei, D.; Yao, J.; Fu, P.; Wu, Y. *Dalton Trans.* **2012**, *41*, 2272–2276.

[20] Sheldrick, G. M. SHELXTL, version 6.12, Bruker AXS Inc., Madison, WI, **2001**.

[21] Gelato, L. M.; Parthé, E. *J. Appl. Crystallogr.* **1987**, *20*, 139–143.

[22] Kortüm, G. *Reflectance Spectroscopy*, Springer, New York, **1969.**

[23] Kurtz, S. K.; Perry, T. T. *J. Appl. Phys.* **1968**, *39*, 3798–3813.

[24] Tank, R.; Jepsen, O.; Burkhardt, A.; Andersen, O. K. *TB-LMTO-ASA Program*, version 4.7; Max Planck Institut für Festkörperforschung: Stuttgart, Germany, **1998**.

[25] Haeuseler, H.; Schmidt, C. *J. Alloys Compd.* **1994**, *204*, 209–213.

[26] Mao, A. W.; Aitken, B. G.; Sen, S. *J. Non-Cryst. Solids* **2013**, *369*, 38–43.

[27] Mao, A. W.; Kaseman, D. C.; Youngman, R. E.; Aitken, B. G.; Sen, S. *J. Non-Cryst. Solids* **2013**, *375*, 40–46.

[28] Mao, A. W.; Kaseman, D. C.; Aitken, B. G.; Sen, S. *J. Non-Cryst. Solids* **2015**, *427*, 62–68.

[29] Chen, Y. -K.; Chen, M. -C.; Zhou, L. -J.; Chen, L.; Wu, L. -M. *Inorg. Chem.* **2013**, *52*, 8334–8341.

[30] Yin, W.; Lin, Z.; Kang, L.; Kang, B.; Deng, J.; Lin, Z.; Yao, J.; Wu, Y. *Dalton Trans.* **2015**, *44*, 2259–2266.

[31] Villars, P.; Cenzual, K. Pearson's Crystal Data – Crystal Structure Database for Inorganic Compounds (on DVD), Release 2015/16, ASM International, Materials Park, OH, USA.

[32] Brese, N. E.; O'Keeffe, M. *Acta. Crystallogr., Sect. B* **1991**, *47*, 192–197.

[33] Brown, I. D. Bond Valence Parameters, www.iucr.org/resources/data/datasets/bond-valence-parameters.

[34] Yin, W.; Feng, K.; Mei, D.; Yao, J.; Fu, P.; Wu, Y. *Dalton Trans.* **2012**, *41*, 2272–2276.

[35] Schevciw, O.; White, W. B. *Mater. Res. Bull.* **1983**, *18*, 1059–1068.

[36] Wei, S. -H.; Zunger, A. *Appl. Phys. Lett.* **1990**, *56*, 662–664.

Chapter 12

Ba₅CdGa₆Se₁₅, a congruently-melting infrared nonlinear optical material with strong SHG response

A version of this chapter has been published. Yin, W.; Iyer, A. K; Li, C.; Yao, J.; Mar, A. J. Mater Chem. C **2017**, *5,* 1057–1063. *Copyright (2017) by Royal Society of Chemistry.*

12.1 Introduction

Nonlinear optical (NLO) materials have diverse applications resulting from their ability to generate coherent light at desired frequencies. Although NLO materials operating in the UV and visible regions are now plentiful, those operating in the IR region are still limited to a few benchmark materials such as $AgGaS_2$, $AgGaSe_2$, and $ZnGeP_2$.[1] The desired features of a viable IR NLO material include large NLO coefficients, high transmittance, wide transparency in the IR region, high laser damage thresholds, minimal two-photon absorption, and phase matchability. These criteria are fulfilled by metal chalcogenides, many of which have been evaluated as potential candidates for IR NLO materials.[2] However, the major challenge is that these candidates should exhibit noncentrosymmetric structures, in order for NLO properties to be manifested in the first place. To date, there is no guaranteed way of predicting whether a given compound will adopt such structures, although there are many strategies available to increase the likelihood that this will happen. Generally, these involve the incorporation of many anionic groups that lack inversion centres, such as triangles, trigonal pyramids, and tetrahedra; or, these groups are susceptible to distortion because they contain metal centres with d^0 or d^{10} configuration, or they exhibit stereochemically active lone pairs.[3]

As part of a broader investigation of complex metal chalcogenides, we have been interested in quaternary systems *A–TM–Tr–Ch* (*A* = alkaline-earth metal; *TM* = Zn, Cd, Hg; *Tr* (triel or Group 13 element) = Al, Ga, In; *Ch* = S, Se, Te) because the chemical components satisfy many of the

criteria required for IR NLO materials. Although no quaternary phases have been reported in these systems to date, ternary phases in the bounding A–TM–Ch and A–Tr–Ch systems are plentiful. The structures of these ternary chalcogenides typically contain $TMCh_4$ tetrahedra (e.g., Ba_2ZnS_3, Ba_2CdCh_3 (Ch = S, Se, Te))[4–6] or $TMCh_3$ trigonal pyramids (e.g., $BaCdS_2$, $BaHgSe_2$)[5,7] in the A–TM–Ch systems and $TrCh_4$ tetrahedra (e.g., $SrGa_2Se_4$, $Sr_2Ga_2S_5$, $Ba_2In_2S_5$, $Ba_2In_2Se_5$, $Ba_5Al_2Se_8$, $Ba_5Ga_2Se_8$, $Ba_5Ga_4Se_{10}$)[8–11] in the A–Tr–Ch systems. The structure of any new quaternary chalcogenides in the target system may thus be anticipated to contain a combination of these types of building units, in a more complicated arrangement that may be more amenable for exhibiting noncentrosymmetry. These efforts have led to the discovery of the quaternary selenide $Ba_5CdGa_6Se_{15}$, which is a new IR NLO material with attractive properties.

12.2 Experimental

12.2.1 Synthesis

Ba shot (99%, Sigma-Aldrich), CdSe powder (99.99%, Sinopharm), Ga shot (99.99%, Cerac), and Se powder (99.99%, Sigma-Aldrich) were used as obtained. Binary starting materials BaSe and Ga_2Se_3 were prepared by stoichiometric reactions of the elements at high temperatures (1173 K for BaSe and 1223 K for Ga_2Se_3) in sealed fused-silica tubes. The ternary starting material $CdGa_2Se_4$ was prepared by reaction of CdSe and Ga_2Se_3 in a molar ratio of 1:1 at 973 K in a sealed fused-silica tube. Mixtures of BaSe (130 mg, 0.60 mmol) and $CdGa_2Se_4$ (114 mg, 0.20) mmol in a molar ratio of 3:1 were finely ground and loaded into fused-silica tubes which were evacuated and sealed. The tubes were heated to 1273 K over 24 h, kept at that temperature for 48 h, cooled to 773 K over 144 h, and then cooled to room temperature by shutting off the furnace. Light yellow, air-stable crystals were obtained. Energy-dispersive X-ray (EDX) analysis of these crystals, examined on a JEOL JSM-6010LA InTouchScope scanning electron microscope,

revealed a composition of 21(3)% Ba, 4(1)% Cd, 17(3)% Ga, and 58(3)% Se, in good agreement with the expected composition of 18% Ba, 4% Cd, 22% Ga, and 56% Se. These crystals were used for the single-crystal structure determination.

An optimized synthesis resulting in pure-phase powder sample proceeded by reaction of BaSe, CdSe, and Ga_2Se_3 in a molar ratio of 5:1:3. The mixture was heated to 1073 K over 24 h, kept at that temperature for 96 h, and then cooled to room temperature by shutting off the furnace. The obtained sample, which was yellow, was reground, and the heat treatment was repeated. The powder X-ray diffraction (XRD) pattern, collected on an Inel diffractometer equipped with a curved position-sensitive detector (CPS 120) and a Cu $K\alpha_1$ radiation source operated at 40 kV and 20 mA, revealed that the sample is quantitatively pure (**Figure 12–1**).
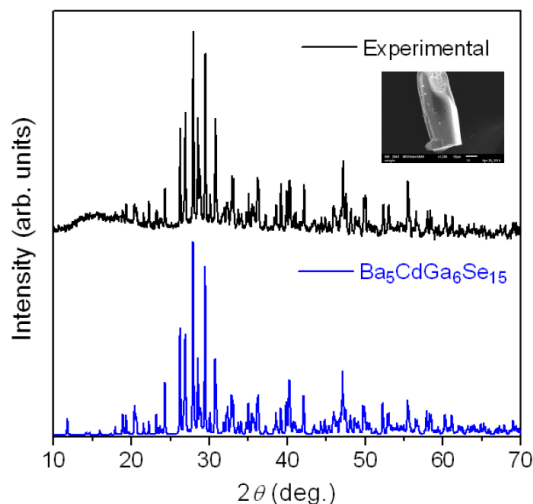
Figure 12-1. Powder XRD pattern of $Ba_5CdGa_6Se_{15}$. The inset shows an SEM image of a typical crystal in the compound.

12.2.2 Structure determination

Intensity data were collected at –80 °C on a Bruker PLATFORM diffractometer equipped with a SMART APEX II CCD area detector and a graphite-monochromated Mo $K\alpha$ radiation source,

using ω scans at 8 different ϕ angles with a frame width of 0.3º and an exposure time of 20 s per frame. Face-indexed numerical absorption corrections were applied. Structure solution and refinement were carried out with use of the SHELXTL (version 6.12) program package.[12]

Laue symmetry and systematic absences led to the orthorhombic space groups $Ama2$, $A2_1am$ (nonstandard setting of $Cmc2_1$), and $Amam$ (nonstandard setting of $Cmcm$) as possible choices. Intensity statistics (mean $|E^2 - 1| = 0.773$) favoured the noncentrosymmetric space groups $Ama2$ and $A2_1am$ (with CFOM values of 6.27 and 2.70, respectively). Despite its lower CFOM, space group $A2_1am$ led to no sensible solution. However, a reasonable model was possible in space group $Ama2$ and initial positions for all atoms were easily located by direct methods. Five metal sites, labeled $M1$ to $M5$, were found to be tetrahedrally coordinated by Se atoms and could be occupied by either Cd or Ga atoms. Instead of attempting to arbitrarily assign site distributions on the basis of interatomic distances, which are expected to be slightly longer for Cd–Se than for Ga–Se contacts, refinements were performed in which each site was allowed to be occupied by a mixture of Cd or Ga atoms. Without any constraints placed on the overall composition, these occupancies converged to 0.01(1) Cd / 0.99(1) Ga in $M1$, 0.40(1) Cd / 0.60(1) Ga in $M2$, 0.03(2) Cd / 0.97(2) Ga in $M3$, 0.21(2) Cd / 0.79(2) Ga in $M4$, and 0.09(2) Cd / 0.91(2) Ga in $M5$, corresponding to a formula of $Ba_5Cd_{1.1(1)}Ga_{5.8(1)}Se_{15}$. These results imply that $M1$ and $M3$ are occupied exclusively by Ga atoms, and that $M2$ and $M4$ contain a disordered mixture of Cd and Ga atoms. For simplicity, we will also assume the $M5$ site to contain Ga atoms exclusively. When the refinements were repeated with disorder invoked on only the $M2$ and $M4$ sites, the occupancies converged to 0.41(1) Cd / 0.59(1) Ga in $M2$ and 0.20(1) Cd / 0.80(1) Ga in $M4$, corresponding to a formula of $Ba_5Cd_{1.0(1)}Ga_{6.0(1)}Se_{15}$, in perfect agreement with the experimentally observed composition and a charge-balanced formulation. This partially ordered model is also readily

rationalized by arguments involving bond distances and bond valence sums, presented later. The displacement parameters were reasonable in all sites, the difference electron density map is featureless, and the agreement factors were excellent.

Analysis of the refined structures with use of the ADDSYM routine in the PLATON suite of programs revealed no additional symmetry.[13] Atomic coordinates were standardized with the program STRUCTURE TIDY.[14] Crystal data and further details are listed in **Table 12–1**, **12–2** and **12–3**. Full listings of positional and equivalent isotropic displacement parameters, and interatomic distances are provided elsewhere (**Tables A6–1 and A6–2** in the Appendix).

Table 12-1. Crystallographic data for $Ba_5CdGa_6Se_{15}$.

Formula	$Ba_5CdGa_6Se_{15}$
Formula mass (amu)	2401.82
Space group	*Ama*2 (No. 40)
a (Å)	24.2458(8)
b (Å)	19.1582(7)
c (Å)	6.6208(2)
V (Å^3)	3075.40(18)
Z	4
ρ_{calcd} (g cm^{-3})	5.187
T (K)	193(2)
Crystal dimensions (mm)	$0.09 \times 0.05 \times 0.04$
μ(Mo $K\alpha$) (mm^{-1})	29.87
Transmission factors	0.181–0.400
2θ limits	3.36–66.59°
Data collected	$-37 \le h \le 37, -29 \le k \le 29, -10 \le l \le 10$
No. of data collected	22577
No. of unique data, including $F_o^2 < 0$	6014 (R_{int} = 0.049)
No. of unique data, with $F_o^2 > 2\sigma(F_o^2)$	5213
No. of variables	136
Flack parameter	0.02(2)
$R(F)$ for $F_o^2 > 2\sigma(F_o^2)$ [a]	0.032
$R_w(F_o^2)$ [b]	0.066
Goodness of fit	1.043
$(\Delta\rho)_{max}, (\Delta\rho)_{min}$ (e Å^{-3})	1.91, –1.78

[a] $R(F) = \sum||F_o| - |F_c|| / \sum|F_o|$ for $F_o^2 > 2\sigma(F_o^2)$. [b] $R_w(F_o^2) = [\sum[w(F_o^2 - F_c^2)^2] / \sum wF_o^4]^{1/2}$; $w^{-1} = [\sigma^2(F_o^2) + (Ap)^2 + Bp]$, where $p = [\max(F_o^2,0) + 2F_c^2] / 3$.

Table 12-2. Atomic coordinates and equivalent isotropic displacement parameters (Å^2) for $Ba_5CdGa_6Se_{15}$.

Atom	Wyck.	Occupancy	x	y	Z	U_{eq} (Å^2) [a]
Ba1	8c	1	0.11158(2)	0.16313(3)	0.53149(8)	0.02311(13)
Ba2	8c	1	0.61573(2)	0.13084(3)	0.49176(8)	0.01937(11)
Ba3	4b	1	¼	0.15388(4)	0.08079(11)	0.01982(15)
M1	8c	1 Ga	0.02912(4)	0.19363(5)	0.06038(14)	0.01622(19)
M2	8c	0.408(9) Cd, 0.592(9) Ga	0.15858(4)	0.47028(4)	0.47523(14)	0.0230(3)
M3	4b	1 Ga	¼	0.30720(7)	0.6096(2)	0.0174(3)
M4	4b	0.195(12) Cd, 0.805(12) Ga	¼	0.47167(7)	0.95279(19)	0.0181(4)
M5	4a	1 Ga	0	0	0.0000(2)	0.0172(3)
Se1	8c	1	0.00009(4)	0.09428(4)	0.24606(15)	0.01900(18)
Se2	8c	1	0.01066(4)	0.30348(5)	0.22983(15)	0.02121(19)
Se3	8c	1	0.07855(5)	0.50724(5)	0.27451(16)	0.0296(2)
Se4	8c	1	0.12625(3)	0.19928(4)	0.01776(14)	0.01841(18)
Se5	8c	1	0.15950(4)	0.34053(5)	0.48910(15)	0.02062(18)
Se6	8c	1	0.16694(4)	0.02270(5)	0.31479(15)	0.0231(2)
Se7	4b	1	¼	0.18387(6)	0.57922(19)	0.0178(2)
Se8	4b	1	¼	0.50882(7)	0.3097(2)	0.0257(3)
Se9	4b	1	¼	0.84371(7)	0.46676(19)	0.0184(2)

[a] U_{eq} is defined as one-third of the trace of the orthogonalized U_{ij} tensor.

Table 12-3. Interatomic distances (Å) for $Ba_5CdGa_6Se_{15}$.

Ba1–Se2	3.3042(12)	Ba3–Se7	3.3701(15)
Ba1–Se4	3.3123(11)	Ba3–Se6 (×2)	3.5737(12)
Ba1–Se6	3.3314(11)	Ba3–Se9	3.7143(15)
Ba1–Se7	3.3942(6)	Ga1–Se1	2.3728(13)
Ba1–Se3	3.4856(11)	Ga1–Se4	2.3742(13)
Ba1–Se4	3.4893(11)	Ga1–Se2	2.3923(13)
Ba1–Se1	3.5523(11)	Ga1–Se2	2.4265(13)
Ba1–Se5	3.6027(11)	Cd/Ga2–Se3	2.4561(15)
Ba2–Se2	3.2492(11)	Cd/Ga2–Se6	2.4706(14)
Ba2–Se4	3.2691(10)	Cd/Ga2–Se5	2.4876(12)
Ba2–Se9	3.2959(5)	Cd/Ga2–Se8	2.5805(11)
Ba2–Se1	3.3200(11)	Ga3–Se7	2.3713(18)
Ba2–Se3	3.3638(11)	Ga3–Se5 (×2)	2.4205(11)
Ba2–Se6	3.4011(11)	Ga3–Se9	2.4660(19)
Ba2–Se5	3.5028(11)	Cd/Ga4–Se6 (×2)	2.4177(12)
Ba2–Se5	3.5359(11)	Cd/Ga4–Se9	2.4532(18)
Ba3–Se4 (×2)	3.1517(9)	Cd/Ga4–Se8	2.4679(19)
Ba3–Se8	3.3083(16)	Ga5–Se3 (×2)	2.4239(13)
Ba3–Se7	3.3496(15)	Ga5–Se1 (×2)	2.4323(13)

12.2.3 Diffuse reflectance spectroscopy

The spectrum of $Ba_5CdGa_6Se_{15}$ was measured from 300 nm (4.13 eV) to 2500 nm (0.50 eV) on a Cary 5000 UV-vis-NIR spectrophotometer equipped with a diffuse reflectance accessory. A compacted pellet of $BaSO_4$ was used as a 100% reflectance standard. The optical absorption spectrum was converted from the diffuse reflectance spectrum using the Kubelka-Munk function, $\alpha/S = (1-R)^2/2R$, where α is the Kubelka–Munk absorption coefficient, S is the scattering coefficient, and R is the reflectance.[15]

12.2.4 Second-harmonic generation measurements

Optical second-harmonic generation (SHG) tests of $Ba_5CdGa_6Se_{15}$ were performed on sieved polycrystalline samples using the Kurtz-Perry method.[16] Fundamental light of 2090 nm wavelength was generated with a Q-switched Ho:Tm:Cr:YAG laser. The samples were ground and sieved with particle sizes of 20–41, 41–74, 74–105, 105–150, and 150–200 μm. Microcrystalline $AgGaS_2$ of similar particle sizes served as the reference.

12.2.5 Thermal analysis

Differential scanning calorimetry (DSC) was carried out on a Labsys TG-DTA16 (SETARAM) thermal analyzer, calibrated with Al_2O_3. About 15 mg of $Ba_5CdGa_6Se_{15}$ powder was sealed within a fused-silica tube evacuated to 10^{-3} Pa. The heating and cooling rates were 20 K min^{-1} for the DSC measurement.

12.2.6 Band structure calculations

Tight-binding linear muffin tin orbital band structure calculations were performed within the local density and atomic spheres approximation with use of the Stuttgart TB-LMTO-ASA program (version 4.7).[17] A model "$Ba_5Ga_7Se_{15}$" was first considered in which all five M sites contain

exclusively Ga atoms, with cell parameters and atomic positions taken from the crystal structure of $Ba_5CdGa_6Se_{15}$ in space group $Ama2$. The calculation was then repeated on a model of $Ba_5CdGa_6Se_{15}$ in which only the $M2$ site (in $8c$) contains an ordered distribution of Cd and Ga atoms to mimic the nearly 50:50 occupancies, within the lower symmetry space group $A2$ and the same cell parameters as before. The unit cell is already very big (>3000 $Å^3$ and >100 atoms) and attempts to invoke larger superstructure models were prohibitive given the computing resources available to us. The basis sets consisted of Ba $6s/(6p)/5d/4f$, Cd $5s/5p/4d/(4f)$, Ga $4s/4p/(4d)$, and Se $4s/4p/(4d)$ orbitals, with the orbitals shown in parentheses being downfolded. Integrations in reciprocal space were carried out with an improved tetrahedron method over 108 irreducible k points within the first Brillouin zone.

12.3 Results and discussion

The selenide $Ba_5CdGa_6Se_{15}$ is the first quaternary phase found within the A–TM–Tr–Ch (A = alkaline-earth metal; TM = Zn, Cd, Hg; Tr = Al, Ga, In; Ch = S, Se, Te) systems. It was prepared by reaction of BaSe and $CdGa_2Se_4$, or by reaction of BaSe, CdSe, and Ga_2Se_3. Attempts to substitute other chemical components in $A_5TMTr_6Ch_{15}$ under similar synthetic conditions were unsuccessful.

$Ba_5CdGa_6Se_{15}$ adopts the $Pb_5ZnGa_6S_{15}$-type structure, a unique one which was just reported recently,[18] but with some important differences as explained later. Within the noncentrosymmetric othorhombic space group $Ama2$, there are three Ba, five M (occupied by Cd and Ga), and nine Se sites. A complex three-dimensional anionic framework is formed by sharing corners of M-centred tetrahedra; viewed down the short c-axis, this framework defines irregular voids that are filled by Ba cations (**Figure 12–2a**). Two kinds of motifs are apparent, highlighted by the fragments labeled A and B, which are linked by a common $M5$-centred tetrahedron located

at the origin (and its symmetry-related positions) of the unit cell (**Figure 12–2b**). First, zigzag chains of $M1$-centred tetrahedra extend along the c-direction, and these chains are connected by the $M5$-centred tetrahedra along the b-direction to form slabs parallel to the bc-plane. Second, four tetrahedra centred by $M2$, $M2$, $M3$, and $M4$ atoms link to form larger tetrahedra (called a "T2-supertetrahedron" as popularized in the open-framework structure literature),[19] which in turn are connected by the Se8 atoms to form chains extending along the c-direction. The Ba atoms are each coordinated by eight Se atoms, roughly in a bicapped trigonal prismatic geometry, at distances of 3.2–3.7 Å.
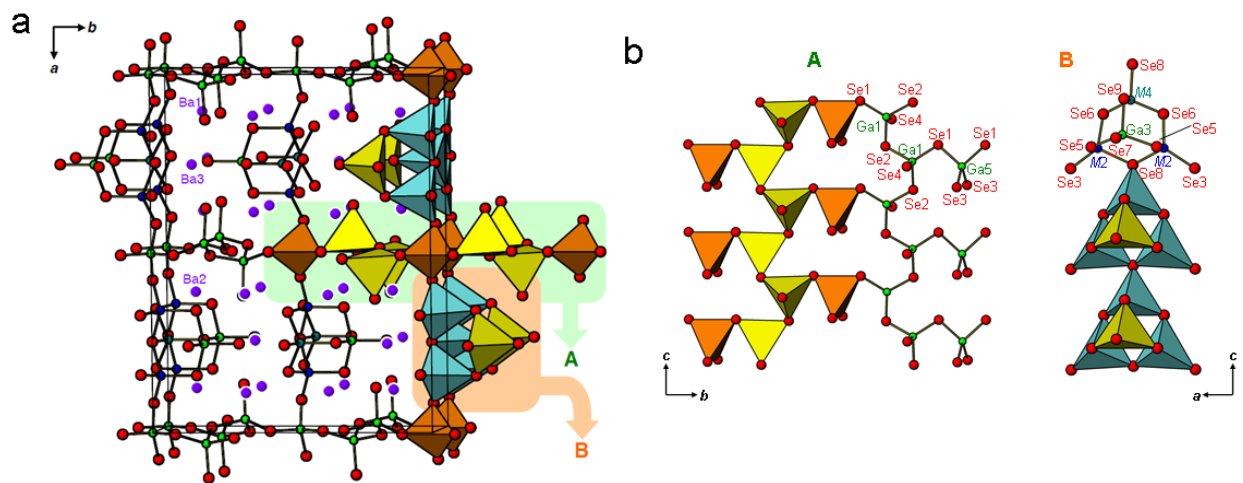
Figure 12-2. (a) Structure of $Ba_5CdGa_6Se_{15}$ viewed down the c-direction. (b) Fragments of corner-sharing tetrahedra centred by Cd and Ga atoms, with the $M2$ and $M4$ sites containing a mixture of both atoms.

The site distribution of the Cd and Ga atoms is an interesting feature of this compound, which exhibits partial disorder within the five M sites. The $M1$, $M3$, and $M5$ sites are occupied exclusively (or nearly so) by Ga atoms, whereas the $M2$ and $M4$ sites contain a mixture of Cd and Ga atoms. The Cd atoms prefer the $M2$ site (0.41(1) Cd / 0.59(1) Ga) over the $M4$ site (0.20(1) Cd / 0.80(1) Ga). This site preference correlates well with distances between the M sites and the

surrounding Se atoms, with an increasing proportion of Cd atoms occupying the larger sites (**Figure 12–3**). There is no sharp separation among these sets of interatomic distances, which explains why complete ordering does not take place. Although the sum of tetrahedral covalent radii (Ga–Se, 2.40 Å; Cd–Se, 2.62 Å)[20] suggests a marked size difference, in fact, the range of typical Ga–Se distances (2.30–2.60 Å) overlaps with the range of typical Cd–Se distances (2.45–2.80 Å) found in the literature.[21]

The average M–Se distances are quite similar around $M5$ (2.428 Å) and $M4$ (2.439 Å), and are at the limit of the shortest Cd–Se distances observed in other compounds. However, the $M4$ site is more amenable to accommodate a small proportion of Cd atoms because the distances are more irregular than around the $M5$ site. Bond valence sums offer further insight into the site preference (**Table 12–4**).[22] If these sites are occupied solely by Ga atoms, the bond valence sums around $M1$, $M3$, and $M5$ (3.13 to 2.83) conform closely to the expected value of 3, but they decrease around $M4$ (2.75) and especially $M2$ (2.36), implying significant underbonding that can be rectified by partial occupation with larger Cd atoms. Nevertheless, complete occupation of the $M2$ site with Cd atoms is not favoured because this would then lead to the opposite problem of significant overbonding (bond valence sum of 3.09 instead of 2 for Cd atoms).

The partial ordering in $Ba_5CdGa_6Se_{15}$ could be established confidently because Cd and Ga atoms are distinguishable by the X-ray scattering factors. However, the same cannot be said about $Pb_5ZnGa_6S_{15}$, for which a completely ordered model was proposed,[18] with Zn atoms occupying the unique site at $4a$ (0, 0, 0.00), labeled as $M5$ in our present work, and Ga atoms occupying the other four sites. Bond valence sums can be evaluated for these five sites in $Pb_5ZnGa_5S_{15}$. In particular, the $M5$ site has a bond valence sum of 2.30 if occupied by Zn atoms or 2.86 if occupied by Ga atoms. The other sites have bond valence sums lying in the range of 2.34–2.47 if occupied

by Zn atoms, or 2.94–3.06 if occupied by Ga atoms. To be sure, the $M5$ site is likely most preferred

by the Zn atoms, but we aver that Zn/Ga disorder cannot be ruled out and probably occurs in all

five sites. Another contrasting feature is that the coordination environments around the Ba atoms

in $Ba_5CdGa_6Se_{15}$ are quite regular (CN8), whereas those around the Pb atoms in $Pb_5ZnGa_6S_{15}$ are

much more irregular (CN7, CN6+1, or CN6+2), a manifestation of the stereochemical activity of

lone pair electrons.

Table 12-4. Bond valence sums (BVS) in $Ba_5CdGa_6Se_{15}$.

Site	BVS	Site	BVS
Ba1	1.86	Se1	2.20
Ba2	2.22	Se2	2.18
Ba3	2.23	Se3	1.92
$M1$ (Cd or Ga)	4.10 or 3.13	Se4	2.15
$M2$ (Cd or Ga)	3.09 or 2.36	Se5	1.90
$M3$ (Cd or Ga)	3.81 or 2.91	Se6	2.18
$M4$ (Cd or Ga)	3.60 or 2.75	Se7	1.87
$M5$ (Cd or Ga)	3.71 or 2.83	Se8	2.04
		Se9	2.09
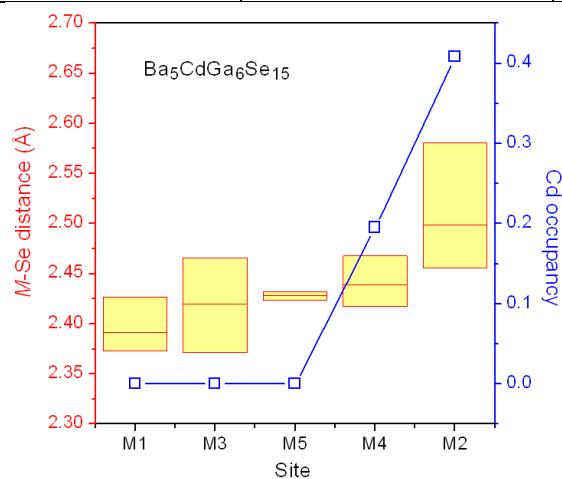
Figure 12-3. Ranges of M–Se distances (and average distance, marked by the middle horizontal line) and Cd occupancies within the five M sites in $Ba_5CdGa_6Se_{15}$.

The charge-balanced formulation $(Ba^{2+})_5(Cd^{2+})(Ga^{3+})_6(Se^{2-})_{15}$ is entirely consistent with

the structure, which exhibits only heteroatomic bonding, and suggests that this compound should

be a semiconductor. As a first approximation to the electronic structure, the model $Ba_5Ga_7Se_{15}$

containing only Ga atoms within the five M sites would lead to an electron excess. Accordingly,

the Fermi level is located at the bottom of the conduction band, separated by 1.24 eV from the

valence band in the density of states (DOS) curve (**Figure 12–4a**). The gap arises from strong

mixing of Ga 4s/4p and Se 4p states, leading to bonding states below the Fermi level and

antibonding states above. Substituting one of the Ga atoms with Cd atoms decreases the electron

count by 1 e⁻ per formula unit and lowers the Fermi level so that it falls within the gap. This

expectation is confirmed when the calculation was repeated on a hypothetically ordered model of

$Ba_5CdGa_6Se_{15}$ in which Cd and Ga atoms are each present in 50% occupancy within the $M2$ site

(**Figure 12–3b**). The Cd 5s/5p states contribute little to the DOS near the Fermi level, and the Cd

4d states are found well below in the Fermi level, appearing as the sharp spike near –9 eV. Thus,

the primary effect of the Cd substitution is to reduce the electron count and the band gap remains

essentially unchanged at 1.25 eV.
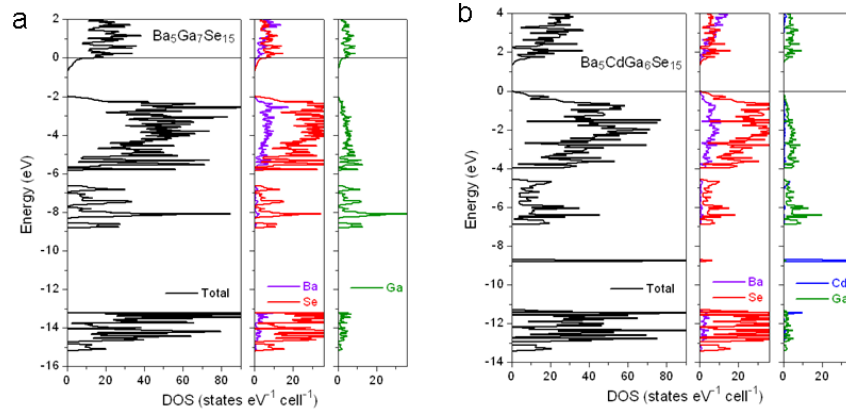
Figure 12-4. Density of states (DOS) and atomic projections for (a) $Ba_5Ga_7Se_{15}$ and (b) $Ba_5CdGa_6Se_{15}$.

In agreement with predictions, experimental measurements reveal that $Ba_5CdGa_6Se_{15}$ exhibits a band gap. The UV-vis-NIR diffuse reflectance spectrum was converted using the Kubelka-Munk function to an optical absorption spectrum, from which an optical band gap of 2.60(2) eV was deduced by applying a straightforward extrapolation method (**Figure 12–5**).[23] This large band gap is consistent with the light yellow colour of the material. (The calculated value of 1.25 eV should be considered as a lower bound because band gaps can be underestimated by as much as 1.5 eV as a result of the LDA.) It is greater than or comparable to the band gaps found in the benchmark IR NLO materials $AgGaSe_2$ (1.8 eV), $AgGaS_2$ (2.7 eV), and $ZnGeP_2$ (2.0 eV), or in the newly developed material $BaGa_4Se_7$ (2.6 eV).[1,24] Thus, $Ba_5CdGa_6Se_{15}$ offers the promise of exhibiting high laser damage thresholds and avoiding the two-photon absorption problem when conventional 1 μm (Nd:YAG) or 1.55 μm (Yb:YAG) laser wavelengths are pumped.
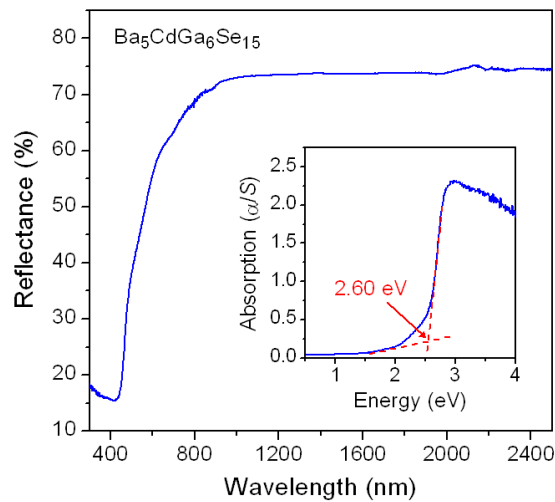
Figure 12-5. Optical diffuse reflectance spectrum for $Ba_5CdGa_6Se_{15}$, converted to absorption spectrum (inset).

Optical measurements performed using fundamental light with a wavelength of 2090 nm revealed that $Ba_5CdGa_6Se_{15}$ generated a strong SHG response, with signal intensities that are about

half that of the benchmark material AgGaS$_2$ over similar particle sizes (Figure 12–6). The increase in SHG intensity with particle size indicates that type-I phase matching is achieved in the infrared region.
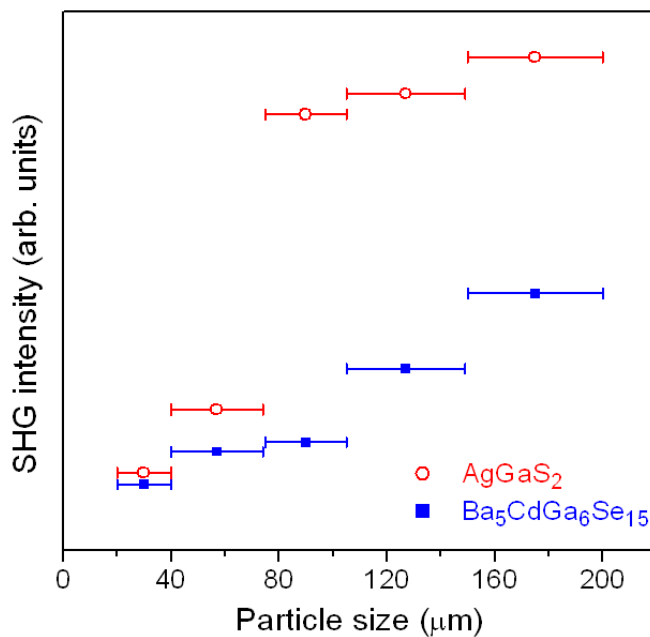
Figure 12-6. Dependence of SHG intensities on particle sizes for Ba$_5$CdGa$_6$Se$_{15}$ and AgGaS$_2$.

    Ba$_5$CdGa$_6$Se$_{15}$ melts congruently at a temperature of 866 °C, as revealed in the DSC curve (**Figure 12–7**). This melting temperature is much lower than in other commercially available or newly developed IR NLO materials (AgGaS$_2$, 998 °C; ZnGeP$_2$, 1025 °C; BaGa$_4$Se$_7$, 968 °C) or is comparable (AgGaSe$_2$, 860 °C; BaGa$_2$GeSe$_6$, 880 °C).[1,24,25] Practical applications involving IR NLO materials demand the availability of large single crystals, for which considerable effort must be expended to optimize the conditions for growth, such as through the Bridgman-Stockbarger technique. Ba$_5$CdGa$_6$Se$_{15}$ may be an attractive candidate for such an undertaking because of its congruent melting behaviour and low melting temperature.
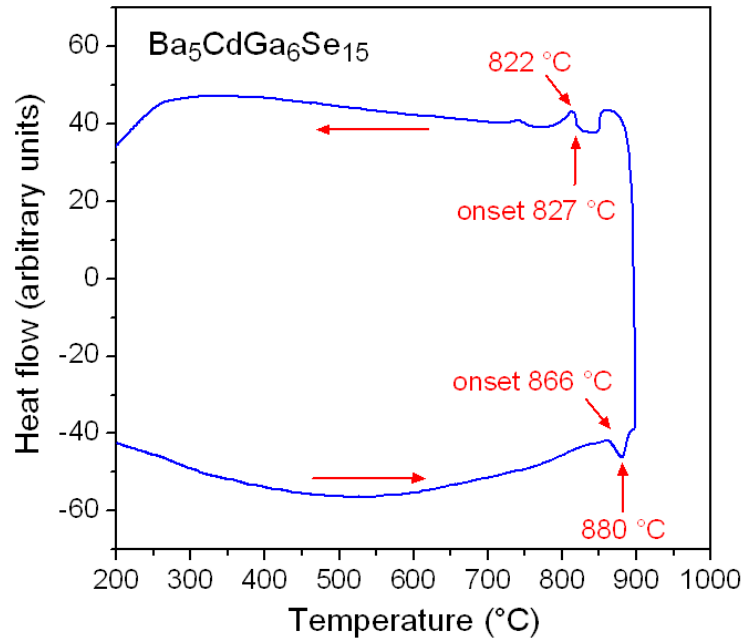
Figure 12-7. DSC curve for $Ba_5CdGa_6Se_{15}$.

12.4 Conclusions

$Ba_5CdGa_6Se_{15}$ is a new chalcogenide adopting a noncentrosymmetric structure in which partial disorder of Cd and Ga atoms takes place. This investigation led to improvements over the related compound $Pb_5ZnGa_6S_{15}$, which could not be obtained in pure phase and gave only a very weak SHG signal, notwithstanding calculated SHG coefficients that should be very high.[18] Measurements on $Ba_5CdGa_6Se_{15}$, which were obtained as quantitatively pure samples, revealed favourable features as a potential IR NLO material: easy preparation, large band gap, strong SHG signals, type-I phase matching, and low congruent melting temperature.

References

[1]   Nikogosyan, D. N. *Nonlinear Optical Crystals: A Complete Survey*, Springer, New York, **2005**.

[2]   Chung I.; Kanatzidis, M. G. *Chem. Mater.* **2014**, *26*, 849–869.

[3]   Ok, K. M. *Acc. Chem. Res.*, doi:10.1021/acs.accounts.6b00452.

[4]   Schnering, H. G.; Hoppe, R. *Z. Anorg. Allg. Chem.*, **1961**, *312*, 99–109.

[5]   Iglesias, J. E.; Pachali K. E.; Steinfink, H. *J. Solid State Chem.* **1974**, *9*, 6–14.

[6]   Wang Y. C.; DiSalvo, F. J. *J. Solid State Chem.* **1999**, *148*, 464–467.

[7]   Li, C.; Yin, W.; Gong, P.; Li, X.; Zhou, M.; Mar, A.; Lin, Z.; Yao, J.; Wu Y.; Chen, C. *J. Am. Chem. Soc.* **2016**, *138*, 6135–6138.

[8]   Klee, W.; Schäfer, H. *Z. Anorg. Allg. Chem.* **1983**, *499*, 145–152.

[9]   B. Eisenmann and A. Hofmann, *Z. Anorg. Allg. Chem.* **1990**, *580*, 151–159.

[10] Mei, D.; Yin, W.; Lin, Z.; He, R.; Yao, J.; Fu, P.; Wu, Y. *J. Alloys Compd.* **2011**, *509*, 2981–2985.

[11] Yin, W.; Mei, D.; Feng, K.; Yao, J.; Fu; P.; Wu, Y. *Dalton Trans.* **2011**, *40*, 9159–9163.

[12] Sheldrick, G. M. *SHELXTL, version 6.12*, Bruker AXS Inc., Madison, WI, 2001.

[13] Spek, A. L. *Acta Crystallogr., Sect. D* **2009**, *65*, 148–155.

[14] Gelato, L. M.; Parthé, E. *J. Appl. Crystallogr.* **1987**, *20*, 139–143.

[15] Kortüm, G. *Reflectance Spectroscopy*, Springer, New York, **1969**.

[16] Kurtz S. K.; Perry, T. T. *J. Appl. Phys.* **1968**, *39*, 3798–3813.

[17] Tank, R.; Jepsen, O.; Burkhardt A.; Andersen, O. K. *TB–LMTO–ASA Program, version 4.7*, Max Planck Institut für Festkörperforschung, Stuttgart, **1998**.

[18] Duan, R. -H.; Yu, J. -S.; Lin, H.; Zheng, Y. -J.; Zhao, H. -J.; Huang-Fu, S.- X.; Khan, M. A.; Chen, L.; Wu, L. -M. *Dalton Trans.* **2016**, *45*, 12288–12291.

[19] Li, H.; Eddaoudi, M.; Laine, A.; O'Keeffe; M.; Yaghi, O. M. *J. Am. Chem. Soc.* **1999**, *121*, 6096–6097.

[20] Pauling, L. *The Nature of the Chemical Bond*, 3rd ed., Cornell University Press, Ithaca, NY, **1960**.

[21] Villars P.; Cenzual, K. *Pearson's Crystal Data – Crystal Structure Database for Inorganic Compounds (on DVD), release 2015/16*, ASM International, Materials Park, OH, 2016.

[22] Brese, N. E.; O'Keeffe, M. *Acta. Crystallogr., Sect. B* **1991**, *47*, 192–197.

[23] Schevciv, O.; White, W. B. *Mater. Res. Bull.* **1983**, *18*, 1059–1068.

[24] Yao, J.; Mei, D.; Bai, L.; Lin, Z.; Yin, W.; Fu, P.; Wu, Y. *Inorg. Chem.* **2010**, *49*, 9212–9216.

[25] Yin, W.; Feng, K.; He, R.; Mei, D.; Lin, Z.; Yao; J.; Wu, Y. *Dalton Trans.* **2012**, *41*, 5653–5661.

Chapter 13

Noncentrosymmetric chalcogenides BaZnSiSe$_4$ and BaZnGeSe$_4$ featuring one-dimensional structures

A version of this chapter has been published. Yin, W; Iyer, A. K; Li, C.; Yao, J.; Mar, A. J. Alloys Compd. **2017***, 708,* 424–430. *Copyright (2017) by Elsevier.*

13.1 Introduction

Infrared nonlinear optical (NLO) crystals are the key components in mid- and far-IR lasers used in diverse applications such as atmospheric monitoring and laser communication. Despite decades of development, commercially viable IR NLO materials are still limited (AgGaS$_2$, AgGaSe$_2$, ZnGeP$_2$) and the search continues for improved properties (increasing laser damage threshold, minimizing two-photon absorption, and ensuring phase matching).[1] Among new candidates, chalcogenides remain the most promising because they generally exhibit large NLO coefficients, high transmittance, and wide transparency range in the IR region.[2] Recent examples of chalcogenides showing strong second harmonic generation (SHG) responses include: BaHgSe$_2$, Rb$_3$Ta$_2$AsS$_{11}$, La$_4$InSbS$_9$, γ-NaAsSe$_2$, BaGa$_2$GeSe$_6$, Ba$_{23}$Ga$_8$Sb$_2$S$_{38}$, BaGa$_4$S$_7$, and Ba$_2$Ga$_8$GeS$_{16}$.[3–11] In these compounds, the common feature is the occurrence of anionic groups (such as metal-centred triangles and tetrahedra) that are connected or aligned to generate a dipole moment. However, whether the overall crystal structure turns out to be noncentrosymmetric depends on a complex and unpredictable interplay involving the combination of cations with different sizes, charges, and coordination preferences.

Many potential quaternary phases may be expected to be found within the systems *A–M–Tr–Ch* (*A* = alkaline-earth metal; *M* = Cu, Ag, Au; *Tr* (triel or Group 13 element) = Al, Ga, In; *Ch* = S, Se, Te), but thus far all the ones reported are Ba-containing. Some of these are

centrosymmetric (Ba$_4$$MTrCh_6$ (M = Cu, Ag; Tr = Ga, In; Ch = S, Se), Ba$_2$AgInS$_4$), but others are noncentrosymmetric (Ba$_4$$MGaCh_{12}$ (M = Cu, Ag; Ch = S, Se), Ba$_7$AgGa$_5$Se$_{12}$). Strong IR NLO responses have been reported for Ba$_4$CuGa$_5$S$_{12}$ and Ba$_4$CuGa$_5$Se$_{12}$.[12–15] Substitution of the M or Tr component with other metals with similar coordination preferences may be anticipated to yield a rich variety of quaternary compounds. For example, on proceeding to the right of the Cu triad or to the right of the triels, the systems A–M–Tt–Ch (A = alkaline-earth metal; M = Zn, Cd, Hg; Tt (tetrel or Group 14 element) = Si, Ge, Sn; Ch = S, Se, Te) consist of quaternary phases, again all Ba-containing, that adopt centrosymmetric (Ba$_3$CdSn$_2$S$_8$) but mostly noncentrosymmetric structures (BaCdGeS$_4$, BaMSnS$_4$ (M = Zn, Cd, Hg), BaCdSnSe$_4$).[17–23] The compound BaCdSnSe$_4$ has also been implicated as a potential IR NLO material.[23]

As part of an ongoing effort to synthesize and characterize multinary chalcogenides, we report here two new noncentrosymmetric quaternary selenides, BaZnSiSe$_4$ and BaZnGeSe$_4$, which are different from the other chalcogenides described above with the composition $AMTtCh_4$. We examine structural relationships, investigate optical properties, and evaluate the bonding in these compounds.

13.2 Experimental

13.2.1 Synthesis

Ba shot (99%, Sigma-Aldrich), ZnSe powder (99.99%, Sinopharm), Si powder (99.999%, Alfa-Aesar), Ge ingot (99.9999%, Alfa-Aesar), and Se powder (99.99%, Sigma-Aldrich) were used as obtained. The binary starting material BaSe was prepared by stoichiometric reaction of the elements at 1173 K in a sealed fused-silica tube. Mixtures of BaSe (87 mg, 0.40 mmol), ZnSe (58 mg, 0.40 mmol), Tt (Si or Ge, 0.40 mmol), and Se (63 mg, 0.80 mmol) were combined in a molar ratio of 1:1:1:2, finely ground, and loaded into fused-silica tubes which were evacuated and

sealed. The tubes were heated to 1173 K over 15 h, kept at that temperature for 60 h, slowly cooled

to 673 K over 144 h, and then cooled to room temperature by shutting off the furnace. The products

contained light yellow crystals of $BaZnSiSe_4$ or orange-yellow crystals of $BaZnGeSe_4$, which were

air-stable (**Figure A7–1** in the appendix). These crystals were examined on a JEOL JSM-6010LA

InTouchScope scanning electron microscope and found by energy-dispersive X-ray (EDX)

analysis to contain 14(2)–18(3)% Ba, 12(2)–15(2)% Zn, 10(2)–12(2)% *Tt*, and 58(4)–60(4)% Se,

in reasonable agreement with the expected composition (14% Ba, 14% Zn, 14% *Tt*, 57% Se).
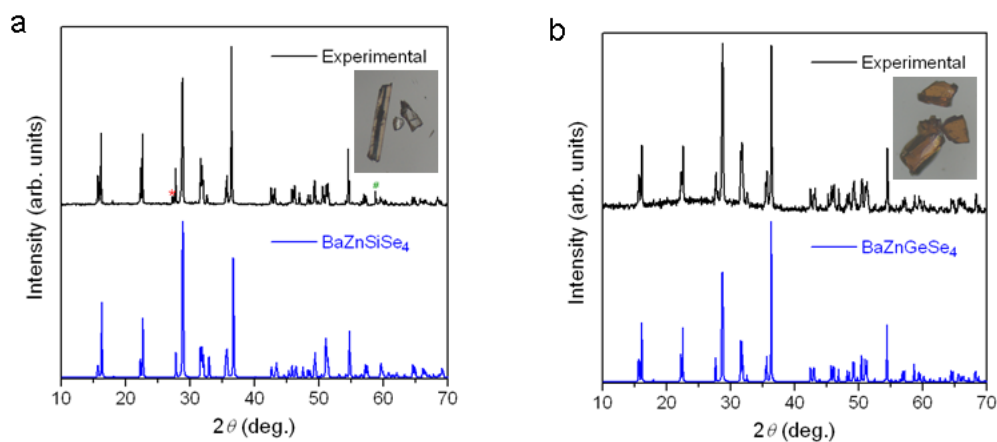
Figure 13-1. Powder XRD patterns of (a) $BaZnSiSe_4$ (with small impurity peaks assigned to ZnSe (*) and Si (#)) and (b) $BaZnGeSe_4$. The insets show typical single crystals.

In anticipation of optical measurements, powder samples were prepared by reaction of

BaSe, ZnSe, *Tt*, and Se in a molar ratio of 1:1:1:2 as before, except that two heat treatments were

applied. The mixtures were heated to 1023 K over 24 h, kept at that temperature for 24 h, and then

cooled by shutting off the furnace. The obtained samples were reground and the heat treatment

was repeated. Powder X-ray diffraction (XRD) patterns of the samples were collected on an Inel

diffractometer equipped with a curved position-sensitive detector (CPS 120) and a Cu $K\alpha_1$

radiation source operated at 40 kV and 20 mA (**Figure 13–1**). The $BaZnSiSe_4$ sample still

contained small amounts of ZnSe and Si as byproducts, whereas the $BaZnGeSe_4$ sample appeared to be quantitatively pure.

13.2.2 Structure determination

Intensity data were collected at room temperature on a Bruker PLATFORM diffractometer equipped with a SMART APEX II CCD area detector and a graphite-monochromated Mo $K\alpha$ radiation source, using ω scans at 7–8 different ϕ angles with a frame width of 0.3º and an exposure time of 15 s per frame. Face-indexed numerical absorption corrections were applied. Structure solution and refinement were carried out with use of the SHELXTL (version 6.12) program package.[24]

For $BaZnSiSe_4$ and $BaZnGeSe_4$, Laue symmetry and systematic absences led to the orthorhombic space groups *Ama*2, *A*2$_1$*am* (nonstandard setting of *Cmc*2$_1$), and *Amam* (nonstandard setting of *Cmcm*) as possible choices. Intensity statistics favoured the noncentrosymmetric space groups *Ama*2 and *A*2$_1$*am*. However, a chemically sensible model could only be found in space group *Ama*2 by direct methods, through which initial positions for all atoms were located. The chief ambiguity concerned the assignment of Zn and *Tt* atoms within two possible sites, *M*1 at 4*b* (¼, ~0.25, ~0.52) and *M*2 at 4*b* (¼, ~0.26, ~0.01), both of which are tetrahedrally coordinated by Se atoms. The range of *M*1–Se distances is the same in both compounds (2.44–2.53 Å), suggesting that *M*1 is occupied by Zn atoms, common to these compounds. The range of *M*2–Se distances is 2.27–2.30 Å in $BaZnSiSe_4$ and 2.34–2.39 Å in $BaZnGeSe_4$, which would be consistent with the relative sizes of Si and Ge if *M*2 is occupied by these atoms. From these bond length considerations alone, the assignment of these sites seemed straightforward. However, it was more convincing to attempt refinements of three models with the following site distributions: (A) Zn in *M*1 and *Tt* in *M*2 (current model), (B) *Tt* in *M*1 and Zn in *M*2 (reversed model), and (C) disordered

mixture of Zn and *Tt* in both sites (**Table A7–1** in the Appendix). For BaZnSiSe$_4$, discrimination between Zn and Si atoms should be possible because of their quite different X-ray scattering factors. Model A was clearly favoured, with refinements resulting in excellent agreement factors (conventional $R(F)$ of 0.019) and featureless difference electron density maps ($\Delta\rho_{min}$, $\Delta\rho_{max}$ = 1.4, –0.9 e$^-$ Å^{-3}). Model B led to unreasonable displacement parameters (non-positive definite for M1 and anomalously large values for M2), poor agreement factors ($R(F)$ of 0.072), and noisy difference electron density maps ($\Delta\rho_{min}$, $\Delta\rho_{max}$ = 8.0, –5.7 e$^-$ Å^{-3}). Model C confirmed that the site distribution is ordered, with M1 containing 1.00(1) Zn / 0.00(1) Si and M2 containing –0.03(1) Zn / 1.03(1) Si. For BaZnGeSe$_4$, in contrast, discrimination of Zn and Ge atoms was expected to be problematic because of their similar X-ray scattering factors. Nevertheless, Model A was still found to be slightly favoured ($R(F)$ = 0.024; $\Delta\rho_{min}$, $\Delta\rho_{max}$ = 2.3, –1.6 e$^-$ Å^{-3}) over model B ($R(F)$ = 0.027; $\Delta\rho_{min}$, $\Delta\rho_{max}$ = 2.5, –1.7 e$^-$ Å^{-3}). Without any restraints, refinement of model C was unstable. However, when a SUMP restraint was applied so that the sum of the occupancies must correspond to the overall formula BaZnGeSe$_4$, then convergence could be achieved and an ordered site distribution consistent with Model A was attained, with M1 containing 1.2(1) Zn / –0.2(1) Ge and M2 containing –0.2(1) Zn / 1.2(1) Ge. These ordered models for BaZnSiSe$_4$ and BaZnGeSe$_4$ were also supported by bond valence sum arguments, as presented later.

Analysis of the refined structures with use of the ADDSYM routine in the PLATON suite of programs[25] revealed no additional symmetry. Atomic coordinates were standardized with the program STRUCTURE TIDY.[26] Crystal data and further details are listed in **Table 13–1**, positional and equivalent isotropic displacement parameters in **Table 13–2**, and interatomic distances in **Table 13–3**.

Table 13-1. Crystallographic data for BaZnTtSe$_4$ (Tt = Si, Ge).

	BaZnSiSe$_4$	**BaZnGeSe$_4$**
Formula mass (amu)	546.64	591.14
Space group	*Ama*2 (No. 40)	*Ama*2 (No. 40)
a (Å)	11.3055(8)	11.3255(6)
b (Å)	11.2344(7)	11.2527(6)
c (Å)	6.1994(4)	6.2917(3)
V (Å^3)	787.39(9)	801.83(7)
Z	4	4
ρ_{calcd} (g cm^{-3})	4.611	4.897
T (K)	296(2)	296(2)
Crystal dimensions (mm)	0.11 × 0.07 × 0.04	0.11 × 0.06 × 0.03
μ(Mo $K\alpha$) (mm^{-1})	26.55	29.60
Transmission factors	0.160–0.378	0.173–0.491
2θ limits	7.21–66.59°	7.20–66.47°
Data collected	$-17 \leq h \leq 17, -17 \leq k \leq 17, -9 \leq l \leq 9$	$-17 \leq h \leq 17, -17 \leq k \leq 17, -9 \leq l \leq 9$
No. of data collected	5738	5749
No. of unique data, including $F_o^2 < 0$	1580 (R_{int} = 0.023)	1588 (R_{int} = 0.028)
No. of unique data, with $F_o^2 > 2\sigma(F_o^2)$	1500	1431
No. of variables	41	40
Flack parameter	0.02(3)	0.04(5)
$R(F)$ for $F_o^2 > 2\sigma(F_o^2)$ ^{a}	0.019	0.024
$R_w(F_o^2)$ ^{b}	0.040	0.052
Goodness of fit	1.074	1.115
$(\Delta\rho)_{max}$, $(\Delta\rho)_{min}$ (e Å^{-3})	1.42, –0.86	2.10, –1.64

^{a} $R(F) = \sum||F_o| - |F_c|| / \sum|F_o|$ for $F_o^2 > 2\sigma(F_o^2)$. ^{b} $R_w(F_o^2) = [\sum[w(F_o^2 - F_c^2)^2] / \sum wF_o^4]^{1/2}$; $w^{-1} = [\sigma^2(F_o^2) + (Ap)^2 + Bp]$, where $p = [\max(F_o^2, 0) + 2F_c^2] / 3$.

Table 13-2. Atomic coordinates and equivalent isotropic displacement parameters (Å^2) for BaZn*Tt*Se$_4$ (*Tt* = Si, Ge).

Atom	Wyckoff position	*x*	*Y*	*z*	U_{eq} (Å^2) [a]
			BaZnSiSe$_4$		
Ba	4*a*	0	0	0.0000(1)	0.0176(1)
Zn	4*b*	¼	0.24559(7)	0.5144(2)	0.0193(2)
Si	4*b*	¼	0.26196(14)	0.0118(3)	0.0122(3)
Se1	8*c*	0.59014(4)	0.24081(4)	0.2871(1)	0.0160(1)
Se2	4*b*	¼	0.09594(6)	0.2287(1)	0.0145(2)
Se3	4*b*	¼	0.41620(6)	0.2480(1)	0.0162(2)
			BaZnGeSe$_4$		
Ba	4*a*	0	0	0.0000(2)	0.0183(1)
Zn	4*b*	¼	0.24292(8)	0.5090(2)	0.0198(2)
Ge	4*b*	¼	0.26125(7)	0.0068(2)	0.0139(2)
Se1	8*c*	0.58685(5)	0.24464(6)	0.2726(1)	0.0172(1)
Se2	4*b*	¼	0.09055(8)	0.2316(1)	0.0158(2)
Se3	4*b*	¼	0.41751(8)	0.2534(1)	0.0174(2)

[a] U_{eq} is defined as one-third of the trace of the orthogonalized U_{ij} tensor.

Table 13-3. Interatomic distances (Å) for BaZn*Tt*Se$_4$ (*Tt* = Si, Ge).

	BaZnSiSe$_4$	**BaZnGeSe$_4$**
Ba–Se2 (×2)	3.3408(5)	3.3435(7)
Ba–Se1 (×2)	3.3555(6)	3.3574(8)
Ba–Se3 (×2)	3.3639(5)	3.3595(7)
Ba–Se1 (×2)	3.3949(6)	3.3892(9)
Zn–Se2	2.4420(11)	2.4465(15)
Zn–Se1 (×2)	2.4794(8)	2.4865(11)
Zn–Se3	2.5303(11)	2.5391(14)
Tt–Se3	2.268(2)	2.3449(13)
Tt–Se1 (×2)	2.2820(14)	2.3644(9)
Tt–Se2	2.2995(19)	2.3855(13)

13.2.3 Diffuse reflectance spectroscopy

Spectra for powder samples of BaZnSiSe$_4$ and BaZnGeSe$_4$ were collected from 350 nm (3.54 eV) to 2500 nm (0.50 eV) on a Cary 5000 UV-vis-NIR spectrophotometer equipped with a

diffuse reflectance accessory. A compacted pellet of $BaSO_4$ was used as a 100% reflectance standard.

13.2.4 Second-harmonic generation measurements

Optical second-harmonic generation (SHG) tests of $BaZnSiSe_4$ and $BaZnGeSe_4$ were performed on sieved polycrystalline samples using the Kurtz-Perry method.[27] Fundamental light of 2090 nm wavelength was generated with a Q-switched Ho:Tm:Cr:YAG laser with a pulse duration of 100 ns. The test repetition rate was 1 Hz and the pulse energy was 10 mJ. For $BaZnSiSe_4$, the measurement was conducted only on particles with sizes of 41–74 μm because the powder was rather fine and sticky. For $BaZnGeSe_4$, the samples were ground and sieved with particle sizes of 20–41, 41–74, 74–105, 105–150, and 150–200 μm. Microcrystalline $AgGaS_2$ (prepared by stoichiometric reaction of high-purity elements (99.99%) at 1273 K in a fused-silica tube) of similar particle sizes served as the reference.

13.2.5 Band structure calculations

Tight-binding linear muffin tin orbital band structure calculations on $BaZnSiSe_4$ and $BaZnGeSe_4$ were performed within the local density and atomic spheres approximation with use of the Stuttgart TB-LMTO-ASA program (version 4.7).[28] The basis set consisted of Ba 6s/(6p)/5d/(4f), Zn 4s/4p/4d, Si 3s/3p/(3d), Ge 4s/4p/(4d), and Se 4s/4p/(4d) orbitals, with the orbitals shown in parentheses being downfolded. Integrations in reciprocal space were carried out with an improved tetrahedron method over 108 irreducible k points within the first Brillouin zone.

13.3 Results and discussion

The selenides $BaZnSiSe_4$ and $BaZnGeSe_4$ were obtained by reactions of BaSe, ZnSe, Tt, and Se at 1023 K. They are the first quaternary phases to be identified in the Ba–Zn–Tt–Se (Tt =

Si, Ge) systems. Attempts to prepare the sulfide analogues were unsuccessful under similar conditions. Substitution of Zn with Cd appears to be possible but crystals of BaCdSiSe$_4$ and BaCdGeSe$_4$ were of poor quality and further synthetic optimization is ongoing.

Other quaternary chalcogenides with similar composition crystallize with noncentrosymmetric structures in space group $Fdd2$ (BaZnSnS$_4$, BaCdSnS$_4$, BaCdSnSe$_4$, BaCdGeS$_4$) or $Pnn2$ (BaHgSnS$_4$), in which pairs of edge-sharing tetrahedra are connected to form two-dimensional nets in both cases. [18–23] BaZnSiSe$_4$ and BaZnGeSe$_4$ also adopt noncentrosymmetric orthorhombic structures, but in a different space group, $Ama2$. There are one Ba, one Zn, one Tt, and three Se sites, all fully occupied. One-dimensional anionic chains of edge-sharing tetrahedra, alternately centred by Zn and Tt atoms, lie parallel to the polar c-direction and are separated by Ba cations (**Figure 13–2a**). Because of the lack of inversion symmetry, all the Zn-centred tetrahedra have the same orientation within a given chain, and likewise for all the Tt-centred tetrahedra; adjacent chains are displaced by half the c-parameter (**Figure. 13–2b**).
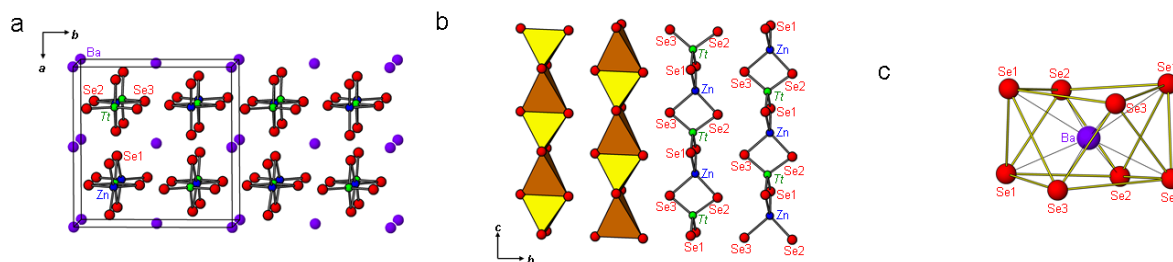
Figure 13-2. (a) Structure of BaZnTtSe$_4$ (Tt = Si, Ge) viewed down the c-direction. (b) Ordered arrangement of Zn and Tt atoms within chains of edge-sharing tetrahedra. (c) Coordination polyhedron around Ba atom.

The ordered arrangement of Zn and Tt atoms within these chains is supported by the Zn–Se distances (2.4420(11)–2.5303(11) Å in BaZnSiSe$_4$; 2.4465(15)–2.5391(14) Å in BaZnGeSe$_4$) being consistently greater than the Tt–Se distances (2.268(2)–2.2995(19) Å in BaZnSiSe$_4$;

2.3449(13)–2.3855(13) Å in BaZnGeSe$_4$). These distances agree well with typical Zn–Se (2.38–

2.62 Å), Si–Se (2.15–2.32 Å), and Ge–Se distances (2.25–2.55 Å) found in the literature.[29]

Moreover, the bond valence sums for all atoms conform to expectations (**Table 13–5**).[30]

Table 13-4. Bond valence sums for BaZn*Tt*Se$_4$ (*Tt* = Si, Ge).

	BaZnSiSe$_4$	**BaZnGeSe$_4$**
Ba	2.17	2.17
Zn	1.97	1.94
Tt	3.76	3.85
Se1	1.96	1.98
Se2	2.02	2.02
Se3	1.95	1.98

In particular, these sums are 1.9–2.0 for the divalent Zn atoms and 3.8–3.9 for the

tetravalent *Tt* atoms, but if the assignments are reversed, they attain unreasonable values (2.7–3.4

for Zn; 2.2–2.8 for *Tt*) (**Table 13–1**). All the tetrahedra are slightly stretched along the *c*-direction.

For example, in BaZnSiSe$_4$, the angles subtending the shared edges (92.75(4)–93.60(4)° around

Zn; 104.01(9)–104.75(9)° around Si) are always smaller than the other angles (113.48(2)–

122.47(2)° around Zn; 110.24(5)–113.85(5)° around Si). The Ba atoms are surrounded by Se

atoms in eight-coordination within quite a narrow range of distances (3.3408(5)–3.3949(6) Å in

BaZnSiSe$_4$; 3.3435(7)–3.3892(9) Å in BaZnGeSe$_4$), with a geometry that could be described as

either distorted tetragonal antiprismatic or bicapped trigonal prismatic (**Figure 13–2c**).

Structural relationships can be sought with other chemically related chalcogenides. It may

appear that BaCu$_2$SnSe$_4$, which crystallizes in space group *Ama*2 (with the SrCu$_2$GeSe$_4$-type

structure) and has similar cell parameters as in BaZn*Tt*Se$_4$ (*Tt* = Si, Ge), should show a close

relationship, but it does not because the polyhedral connectivity is completely different.[31,32] In

BaCu$_2$SnSe$_4$, pairs of Cu-centred tetrahedra are linked by Sn-centred tetrahedra to form a three-

dimensional network, in contrast to the one-dimensional chains found in BaZn*Tt*Se$_4$. As a more

suitable comparison, the only other compounds having crystal structures in space group $Ama2$ with exactly the same Wyckoff sequence (cb^4a) and similar cell parameters as BaZnTtSe$_4$ (Tt = Si, Ge) are Sr$_2$SnS$_4$, Sr$_2$GeSe$_4$, and NaEuAsS$_4$.[33–34] Although they appear to be isotypic, there are significant deviations in the positional coordinates of several sites such that an appropriate description of the relationship is that they belong to different structure type branches. If the three related structure types are arbitrarily designated as BaZnSiSe$_4$, Sr$_2$SnS$_4$, and NaEuAsS$_4$, the key difference lies in the position of the Zn site (¼, 0.25, 0.51), one of the Sr sites (¼, 0.19, 0.54), or the Na site (¼, 0.18, 0.56), respectively. BaZnSiSe$_4$ forms one branch in which Zn atoms are found in a fairly regular tetrahedral coordination environment of Se atoms and are collinear with the Si atoms parallel to the c-direction (**Figure 13–3a**). Sr$_2$SnS$_4$ forms another branch in which Sr atoms are substantially displaced so that they are no longer collinear with the Sn atoms and now become coordinated to seven S atoms, which are also shifted, in a distorted pentagonal bipyramidal environment (**Figure 13–3b**). NaEuAsS$_4$ can be regarded as a quaternary variant in which the two Sr sites in Sr$_2$SnS$_4$ are occupied in an ordered fashion, the first (at the origin of the unit cell) by Eu atoms and the second (not quite collinear with the As atoms) by Na atoms. As before, the Na atoms are displaced but the environment is much more asymmetric, with four shorter distances to the surrounding S atoms and three longer ones that are essentially nonbonding, so that the coordination number is effectively four and the geometry is a trigonal pyramid with the Na atoms nearly coplanar with the triangular base (**Figure 13–3c**). Of course, from the point of view of bonding character, BaZnSiSe$_4$ is also quite different in that it contains one-dimensional chains with covalent bonds formed within the Zn- and Si-centred tetrahedra, whereas the other compounds contain only isolated tetrahedra interrupted by the placement of highly electropositive atoms involved in ionic bonding. Lastly, BaCu$_2$SnSe$_4$ can be seen to exhibit a completely different

connectivity as a result of the occupation of Cu atoms in a site of higher multiplicity ($8c$ instead of $4b$), so that the Wyckoff sequence is c^2b^3a (**Figure 13–3d**). Another closely related structure is that of LiEuPSe$_4$,[35] which has similar cell parameters in space group *Ama*2 but a slightly different Wyckoff sequence (cb^3a^2). Here, Li atoms are located at the origin of the unit cell (after the structure is standardized), Eu atoms are found at 0, 0, ~0.51, and vacancies occur in place of the Zn atoms in BaZnSiSe$_4$.
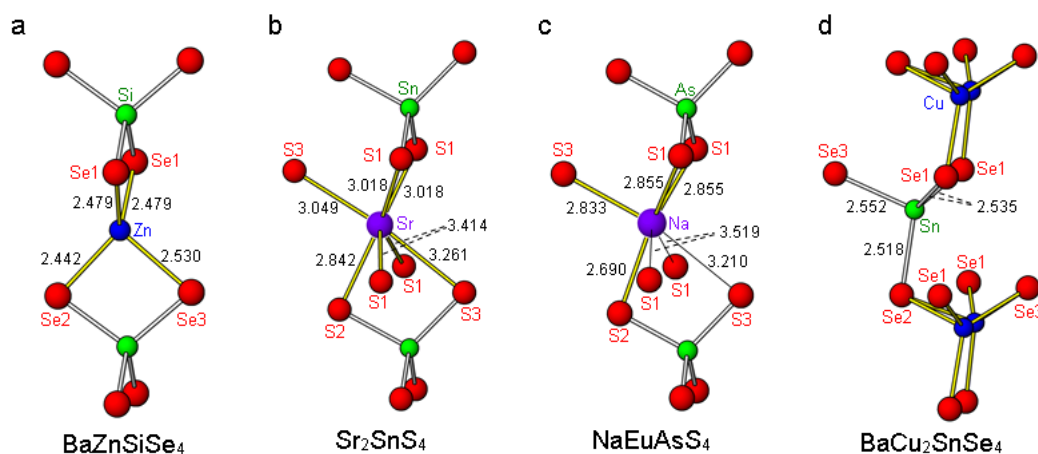
Figure 13-3.   Comparison of one-dimensional chains in (a) BaZnSiSe$_4$, (b) Sr$_2$SnS$_4$, (c) NaEuAsS$_4$, and (d) BaCu$_2$SnSe$_4$. Distances (in Å) are shown around the Zn, Sr, Na, and Sn atoms, respectively, in these structures.

The simple charge-balanced formulation (Ba^{2+})(Zn^{2+})(Tt^{4+})(Se^{2-})$_4$, which also agrees with the bond valence sum calculations (**Table 13–5**), implies the absence of homoatomic Tt–Tt or Se–Se bonds. The electronic band structures were evaluated for BaZnSiSe$_4$ (**Figure 13–4**) and BaZnGeSe$_4$ (**Figure 13–5**), but because they are quite similar, only the former is discussed here in detail.
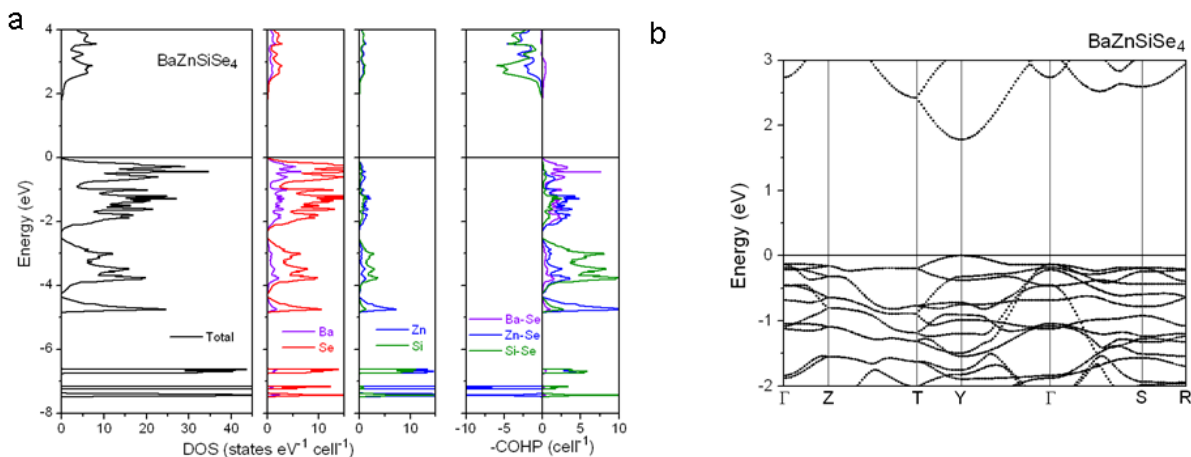
Figure 13-4. (a) Density of states (DOS) (left panel), atomic projections (middle panels), and crystal orbital Hamilton population (–COHP) curves (right panel) for BaZnSiSe$_4$. (b) Band dispersion diagram for BaZnSiSe$_4$.

The density of states (DOS) curve reveals valence and conduction bands separated by a gap of 1.80 eV in BaZnSiSe$_4$; the band dispersion curve shows that the gap is a direct one (at the special symmetry point Y). Empty Ba-based states mostly contribute to the broad conduction bands, well above 2.0 eV. The valence bands are derived by considerable mixing of Se p with Zn s/p and Si p states from –4.9 to 0 eV, giving rise to strong covalent bonding interactions, as seen in the crystal orbital Hamilton population (COHP) curves. The sharp spikes in the DOS curve lower in energy between –7.5 and –6.5 eV originate largely from Zn d states. Much further down in energy (below –11 eV, not shown in the figure) are bands involving bonding interactions between Se s and Si s states. The Ba states are not entirely innocent of covalent bonding; they mix with Se states below the Fermi level to give non-negligible contributions of Ba–Se bonding. The integrated COHP values (–ICOHP) indicate that Si–Se interactions are the most important in terms of inherent strength and contribution to the total bonding (3.90 eV/bond; 15.6 eV/cell), followed by Zn–Se interactions (1.74 eV/bond; 7.0 eV/cell) and Ba–Se interactions (0.47 eV/bond; 3.8

eV/cell). On proceeding to BaZnGeSe$_4$, the major effect is a narrowing of the band gap to 1.23

eV; interestingly, this gap is now an indirect one (from Γ to Y). The relative order of bonding

strengths is retained, as indicated by –ICOHP values of 3.28 eV/bond for Ge–Se, 1.77 eV/bond

for Zn–Se, and 0.47 eV/bond for Ba–Se interactions.
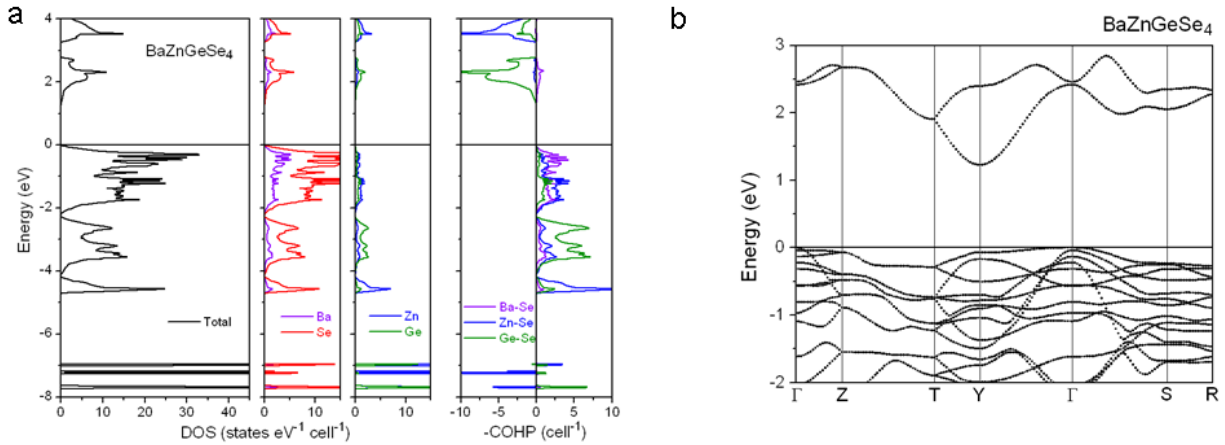
Figure 13-5. (a) Density of states (DOS) (left panel), atomic projections (middle panels), and crystal orbital Hamilton population (–COHP) curves (right panel) for BaZnGeSe$_4$. (b) Band dispersion diagram for BaZnGeSe$_4$.

From the UV-vis-NIR diffuse reflectance spectra, optical band gaps of 2.71(2) eV for

BaZnSiSe$_4$ and 2.46(2) eV for BaZnGeSe$_4$ were deduced from the absorption edges of 457 nm and

504 nm, respectively, by applying an extrapolation method (**Figure 13–6**).[36] These experimental

band gaps are larger than predicted by the band structure calculations, but the relative order is

preserved and the magnitudes are consistent with the yellow or orange colour of these materials.

For comparison, the band gaps of some benchmark infrared NLO materials are 1.8 eV in AgGaSe$_2$,

2.7 eV in AgGaS$_2$, 2.0 eV in ZnGeP$_2$;[37] for a newly developed material such as BaGa$_4$Se$_7$, the band

gap is 2.6 eV.[38] Large band gaps are desirable because they provide high laser damage thresholds

and avoid problems of two-photon absorption when conventional 1 μm (Nd:YAG) or 1.55 μm

(Yb:YAG) laser wavelengths are pumped. BaZnSiSe$_4$ and BaZnGeSe$_4$ may thus be promising in this regard.
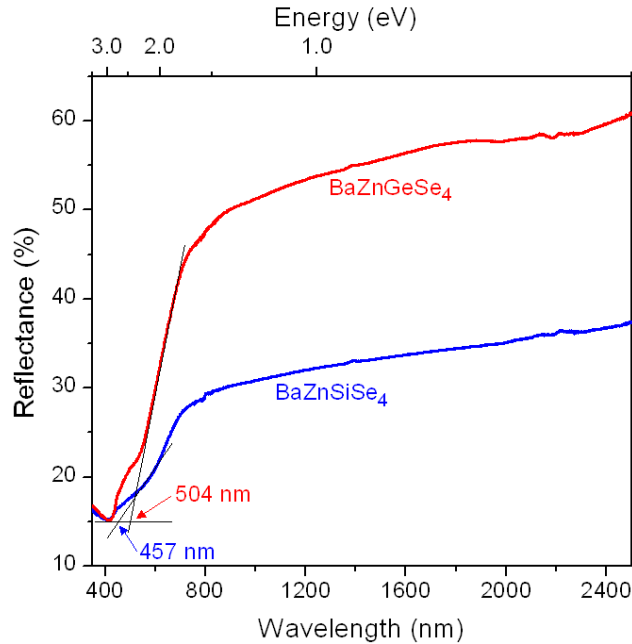
Figure 13-6. Diffuse reflectance spectra for BaZnSiSe$_4$ and BaZnGeSe$_4$.

Optical measurements were performed on BaZnSiSe$_4$ and BaZnGeSe$_4$ using fundamental light with a wavelength of 2090 nm. BaZnSiSe$_4$ gave a SHG signal with an intensity of about one-third that of AgGaS$_2$ over a range of 41–74 μm particle sizes (not shown). However, BaZnGeSe$_4$ gave a good SHG response, equally as strong as that of AgGaS$_2$ over similar particle sizes (**Figure 13–7**). The SHG intensity increases with particle size, indicating that BaZnGeSe$_4$ achieves type-I phase matching in the infrared region.
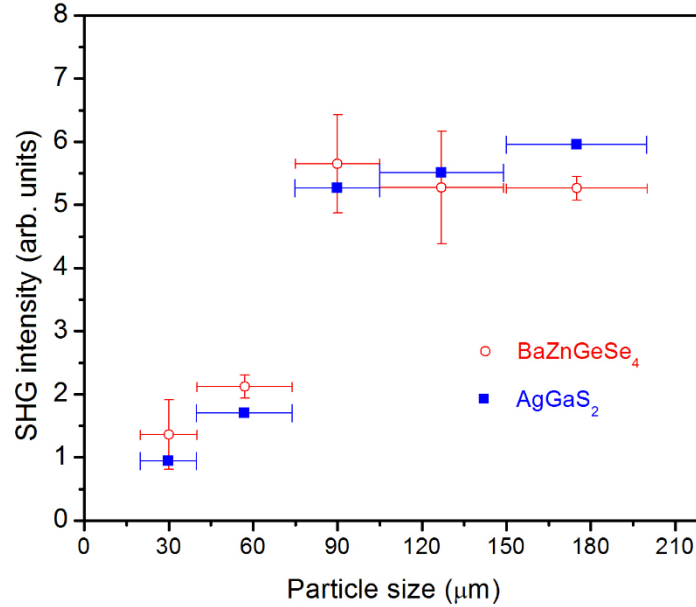
Figure 13-7. SHG intensities of BaZnGeSe$_4$ and AgGaS$_2$ using fundamental light with 2090 nm wavelength.

It is interesting to speculate on the reasons for the NLO behaviour of BaZnSiSe$_4$ and BaZnGeSe$_4$. The structural origin can be traced to the arrangement of dipole moments of the ZnSe$_4$ and TtSe$_4$ tetrahedra within the one-dimensional chains along the polar c-direction. The net dipole moments within each of these units can be evaluated through a simple approach in which bond valences are used to estimate the charge distribution of coordinating ligands around a central atom.[39,40] Because these tetrahedra are slightly distorted, nonzero dipole moments arise which point roughly towards the longer bonds to the surrounding Se atoms. In both compounds, the dipole moments within the ZnSe$_4$ and TtSe$_4$ tetrahedra are oriented not quite perpendicular to the chain direction and are aligned in an antiparallel fashion to each other (**Figure 13–8**). The dipole moments do not cancel out because they are inequivalent in magnitude and are slightly canted, so that there is an overall polarization within these chains. The net polarization points in the same direction along c within all chains. The stronger SHG signal observed in BaZnGeSe$_4$ may be

attributed in part to the greater polarization of these chains originating mainly from the contribution of the $ZnSe_4$ dipole moments.
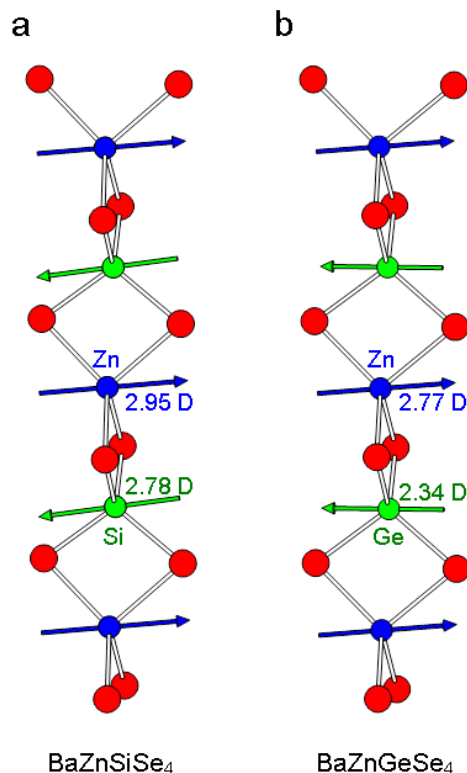
Figure 13-8. Dipole moments (in Debye) evaluated from bond valences for the tetrahedral units within chains for (a) $BaZnSiSe_4$ and (b) $BaZnGeSe_4$.

13.4 Conclusions

$BaZnSiSe_4$ and $BaZnGeSe_4$ represent a new class of noncentrosymmetric chalcogenides whose structure contains an ordered arrangement of Zn and *Tt* atoms within one-dimensional chains. They are promising candidates for developing new IR NLO materials because they exhibit large band gaps and moderate SHG signals; more importantly, $BaZnGeSe_4$ exhibits type-I phase matching, which is an essential criterion for practical NLO materials. They are likely amenable to other chemical substitutions, which may lead to improvement of these properties. Although large

band gaps are desirable for improving laser damage thresholds and could be achieved by preparing the corresponding sulfides, these selenides offer the advantage of greater bond polarizability to enhance the SHG response. Substitution of Cd for Zn appears to be possible and it would be worthwhile investigating the optical properties of these compounds.

13.5 References

[1]   Jiang, X. -M.; Guo, S. -P.; Zeng, H. -Y.; Zhang, M. -J.; Guo, G. -C. *Struct. Bonding* **2012**, *145*, 1–44.
[2]   Chung, I.; Kanatzidis, M. G. *Chem. Mater.* **2014**, *26*, 849–869.
[3]   Li, C.; Yin, W.; Gong, P.; Li, X.; Zhou, M.; A. Mar, A.; Lin, Z.; Yao, J.; Wu, Y.; Chen, C. *J. Am. Chem. Soc.* **2016**, *138*, 6135–6138.
[4]   Bera, T. K.; Jang, J. I.; Ketterson, J. B.; Kanatzidis, M. G. *J. Am. Chem. Soc.* **2009**, *131*, 75–77.
[5]   Zhao, H. -J.; Zhang, Y. -F.; Chen, L. *J. Am. Chem. Soc.* **2012**, *134* 1993–1995.
[6]   Bera, T. K.; Jang, J. I.; Song, J. -H.; Malliakas, C. D.; Freeman, A. J.; Ketterson, J. B.; Kanatzidis, M. G. *J. Am. Chem. Soc.* **2010**, *132*, 3484–3495.
[7]   Yin, W.; Feng, K.; He, R.; Mei, D.; Lin, Z.; Yao, J.; Wu, Y. *Dalton Trans.* **2012**, *41*, 5653–5661.
[8]   Lin, X.; Guo, Y.; Ye, N.; *J. Solid State Chem.* **2012**, *195*, 172–177.
[9]   Chen, M. C.; Wu, L. M.; Lin, H.; Zhou, L. J.; Chen, L. *J. Am.Chem. Soc.* **2012**, *134*, 6058−6060.
[10]   Lin, X.; Zhang, G.; Ye, N. *Cryst. Growth Des.* **2009**, *9*, 1186–1189.
[11]   Liu, B. -W.; Zeng, H. -Y.; Zhang, M. -J.; Fan, Y. -H.; Guo, G. -C.; Huang, J. -S.; Dong, Z. -C. *Inorg. Chem.* **2015**, *54*, 976–981.
[12]   Yin, W.; Feng, K.; Hao, W.; Yao, J.; Wu, Y. *J. Solid State Chem.* **2012**, *192*, 168–171.
[13]   Lei, X. -W.; Yang, M.; Xia, S. -Q.; Liu, X. -C.; Pan, M. -Y.; Li, X.; Tao, X. -T. *Chem. Asian J.* **2014**, *9*, 1123–1131.
[14]   Yin, W.; Feng, K.; Mei, D.; Yao, J.; Fu, P.; Wu, Y. *Dalton Trans.* **2012**, *41*, 2272–2276.
[15]   Kuo, S. -M.; Chang, Y. -M.; Chung, I.; Jang, J. -I.; Her, B. -H.; Yang, S. -H.; Ketterson, J. B.; Kanatzidis, M. G.; Hsu, K. -F. *Chem. Mater.* **2013**, *25*, 2427–2433.
[16]   Yin, W.; He, R.; Feng, K.; Hao, W.; Yao, J. L.; Wu, Y. *J. Alloys Compd.* **2013**, *565*, 115–119.
[17]   Teske, C. L. *Z. Anorg. Allg. Chem.* **1985**, *522*, 122–130.
[18]   Zhen, K.; Wu, N.; Wang, Y.; Li, Q.; Gao, W.; Hou, D.; Yang, Z.; Jang, H.; Dong, Y.; Pan, S. *Dalton Trans.* **2016**, *45*, 10681–10688.
[19]   Teske, C.L. *Z. Anorg. Allg. Chem.* **1980**, *468*, 27–34.
[20]   Teske, C. L. *Z. Naturforsch. B* **1980**, *35,* 509–510.
[21]   Teske, C. L. *Z. Anorg. Allg. Chem.* **1980**, *460*, 163–168.
[22]   Teske, C. L. *Z. Naturforsch. B* **1980**, *35*, 7–11.
[23]   Wu, K.; Su, X.; Yang, Z.; Pan, S. *Dalton Trans.* **2015**, *44*, 19856–19864.
[24]   Sheldrick, G. M. *SHELXTL, version 6.12*, Bruker AXS Inc., Madison, WI, **2001**.
[25]   Spek, A. L. *Acta Crystallogr., Sect. D* **2009**, *65*, 148–155.
[26]   Gelato, L. M.; Parthé, E. *J. Appl. Crystallogr.* **1987**, *20*, 139–143.
[27]   Kurtz, S. K.; Perry, T. T. *J. Appl. Phys.* **1968**, *39*, 3798–3813.
[28]   Tank, R.; Jepsen, O.; Burkhardt, A.; Andersen, O. K. *TB-LMTO-ASA Program*, version 4.7; Max Planck Institut für Festkörperforschung: Stuttgart, Germany, **1998**.
[29]   Villars, P.; Cenzual, K. Pearson's Crystal Data – Crystal Structure Database for Inorganic Compounds, ASM International, Materials Park, OH, 2010.
[30]   Brese, N. E.; O'Keeffe, M. *Acta. Crystallogr., Sect. B* **1991**, *47*, 192–197.

[31]   Assoud, A.; Soheilnia, N.; Kleinke, H. *Chem. Mater.* **2005**, *17*, 2255–2261.

[32]   Tampier, M.; Johrendt, D. *Z. Anorg. Allg. Chem.* **2001**, *627*, 312-320.

[33]   Pocha, R.; Tampier, M.; Hoffmann, R. -D.; Mosel, B. D.; Pöttgen, R.; Johrendt, D. *Z. Anorg. Allg. Chem.* **2003**, *629*, 1379–1384.

[34]   Bera, T. K.; Kanatzidis, M. G. *Inorg. Chem.* **2012**, *51*, 4293–4299.

[35]   Aitken, J. A.; Chondroudis, K.; Young Jr., V. G.; Kanatzidis, M. G. *Inorg. Chem.* **2000**, *39*, 1525–1533.

[36]   Schevciw, O.; White, W. B. *Mater. Res. Bull.* **1983**, *18*, 1059–1068.

[37]   Nikogosyan, D. N. Nonlinear Optical Crystals: A Complete Survey, Springer, New York, **2005**.

[38]   Yao, J.; Mei, D.; Bai, L.; Lin, Z.; Yin, W.; Fu, P.; Wu, Y. *Inorg. Chem.* **2010**, *49*, 9212–9216.

[39]   Maggard, P. A.; Nault, T. S.; Stern, C. L.; Poeppelmeier, K. R. *J. Solid State Chem.* **2003**, *175*, 27–33.

[40]   Izumi, H. K.; Kirsch, J. E.; Stern, C. L.; Poeppelmeier, K. R. *Inorg. Chem.* **2005**, *44*, 884–895.

Chapter 14

14.1 Conclusions

In pursuit of the general goal of discovering new multinary chalcogenides and the more specific goal of identifying such chalcogenides that adopt noncentrosymmetric structures, this thesis has succeeded in characterizing about 40 new noncentrosymmetric chalcogenides which may be potentially interesting for their magnetic properties, ionic conductivity, and nonlinear optical behaviour. Many of these compounds belong to the quaternary $RE_3M_{1-x}M'Ch_7$ family, which exhibits considerably flexibility. Although most previously known compounds in this family are restricted by the condition that the valences of the M and M' atoms must sum to 5, several new examples that violate this condition were found, thus testing the limits of this rule. Several new ternary and quaternary Ba-containing chalcogenides were discovered, guided by the principle that tetrahedral building units may increase the chances of forming noncentrosymmetric structures. Five selenides were examined for their nonlinear optical behaviour; among these, $Ba_5CdGa_6Se_{15}$ and $BaZnMSe_4$ (M = Si, Ge) were found to have SHG intensities comparable to benchmark materials. The $BaRE_2In_2Ch_7$ compounds are unusual in exhibiting a rarely observed coordination geometry of edge-sharing $InCh_5$. Ternary compounds $Ba_4Ga_2Se_8$ and $Ba_{12}In_4Se_{19}$ feature diselenide units Se_2^{2-} which are not as common as the corresponding disulfide units S_2^{2-}. $Ba_{12}In_4Se_{19}$ was interesting because it is not quite isostructural to a closely related ternary sulfide. Throughout this work, bond valence sums have been helpful in rationalizing the of these compounds. Diverse experimental techniques include XRD, XPS, and NMR spectroscopy were applied to characterize these compounds.

14.1.1 Quaternary rare-earth chalcogenides

Prior to the work in this thesis, most compounds in the $RE_3M_{1-x}M'Ch_7$ family were limited to those satisfying the valence sum restriction ($M + M' = +5$) with the metal components being mostly transition metals. A major contribution is to identify a new subset of compounds which violate this condition (**Table 14–1**). Many of these compounds are electron-deficient with respect to the ideal charge-balanced formulation; for example, $(La^{3+})_3(Cu^{1+})(Ga^{3+})(Ch^{2-})_7$ is deficient by 1 e⁻ and $La_3Ag_{0.6}GaCh_7$ is deficient by 1.4 e⁻.

Table 14-1. New additions (red colour) to the $RE_3M_{1-x}M'Ch_7$ family.

Rare-Earth	**M**	**M** *occupancy*	**M′**	*Formula*
	I	100 %	**IV**	$RE_3MM'Ch_7$
	Cu, Ag		Tt = Si, Ge, Sn	e.g. La_3CuSiS_7
	II	100 %	**III**	$RE_3MM'Ch_7$
RE^{3+}	transition metals (Mn-Zn, Cd)		Tr = Al, Ga	e.g. La_3MnGaS_7
	III	100 %	**II**	$RE_3MM'Ch_7$
	Sc-Cr, Sb, Bi, In, Yb, Lu		Be	e.g. La_3CrBeS_7
	II	50 %	**IV**	$RE_3M_{0.50}M'Ch_7$
	transition metals Mn-Ni		Tt = Si, Ge, Sn	e.g. $La_3Mn_{0.5}SiS_7$
	I	100%	**III**	$RE_3M_{1-x}M'Ch_7$
	Cu and Ag		Ga	e.g. $La_3Ag_{0.6}GaS_7$
	IV	50%	**III**	$RE_3M_{0.50}M'Ch_7$
	Sn		In	e.g. $La_3Sn_{0.5}InCh_7$

Many $RE_3M_{1-x}M'Ch_7$ compounds were previously characterized in the literature solely through powder XRD methods, which has limitations on accurately identifying disordered models and site occupancies. Frequently, assumptions were made about the site distributions without firm evidence. For example, it can be hard to establish the level of partial occupancies (e.g., $La_3Ga_{1.67}Ch_7$) or to differentiate between isostructural ternary and quaternary compounds (e.g., $La_3Sn_{1.25}Ch_7$, $La_3In_{1.67}Ch_7$, $La_3Sn_{0.5}InCh_7$). New single-crystal structure determinations have revealed that the actual site distributions are more complicated than previously believed, and that

some of these site preferences can be understood in terms of optimizing bond valence sums not just for the metal atoms but also for the Ch atoms.

To support the assignments of oxidation states, experimental XPS and NMR spectroscopy measurements have been applied. Expanding on previous XPS studies on related compounds, we have confirmed that Cu and Ag atoms are universally monovalent in these chalcogenides. The compound $La_3Sn_{0.5}InCh_7$ presents an interesting case that violates the principle that the higher-valent metal prefers the tetrahedral site and the lower-valent metal prefers the octahedral site. This site distribution was confirmed by solid-state ^{119}Sn NMR spectroscopy, which remains relatively undeveloped. There is the possibility that such violations may be observed in other cases; for example, representatives containing Cr(II) on the tetrahedral site and Be(III) on the octahedral site have been proposed but have only been characterized so far by powder XRD.

The compound $Y_3Pd_{0.5}SiS_7$ marks the first time that a second-row transition metal has been substituted into the $RE_3M_{1-x}M'Ch_7$ family, and opens up the possibility that other substitutions with heavier metals may be likely. Substitutions of the other components were also attempted. In particular, all attempts to prepare tellurides were unsuccessful, suggesting that there may be size factors that prevent such structures from being stable. In general, while sulfides and selenides are often isostructural, tellurides tend to adopt different structures. Moreover, binary tellurides tended to form in the products suggesting that they are thermodynamic sinks.

By extending the RE_3MGaS_7 series to include a larger range of transition metals, and the RE_3MInS_7 series to include a Sn-containing representative, trends in the electronic structure have become clearer (**Figure 14–1**). The band gap in the RE_3MGaS_7 series narrows as the M substituent progresses from Fe to Zn, mainly as a result of the lowering in energy of the valence band. The ternary compound $La_3Ga_{1.67}Ch_7$ is an unusual case that requires further study.
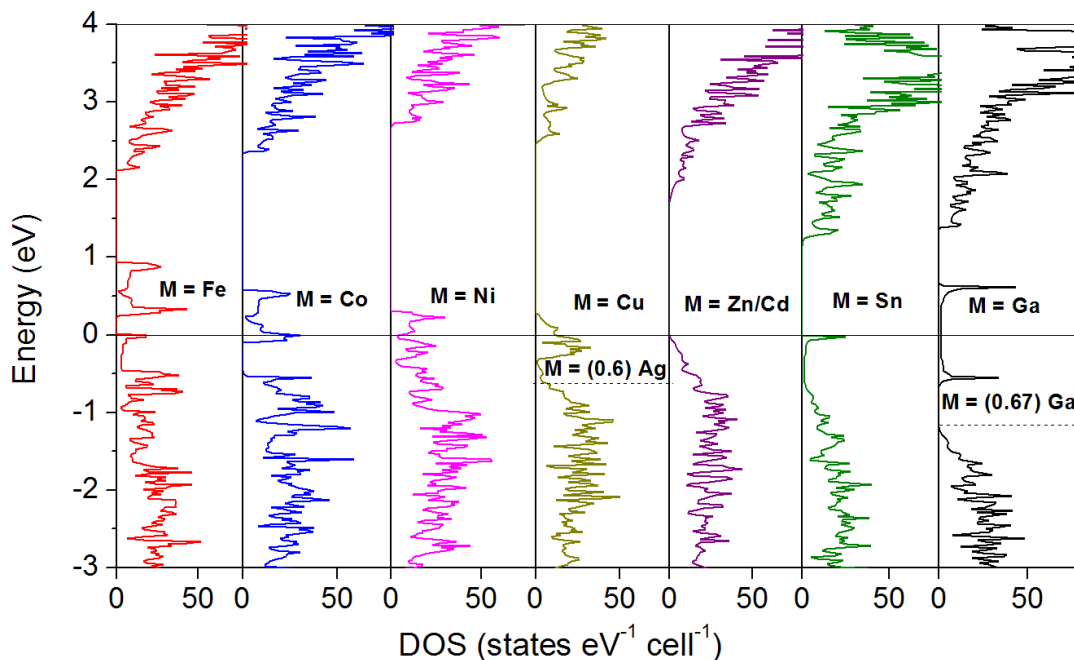
Figure 14-1. Schematic representation of density of states curve of the La$_3$$MM'Ch_7$.

In addition to the $RE_3M_{1-x}M'Ch_7$ family, other quaternary rare-earth chalcogenides were investigated. Although many quaternary chalcogenides have been reported, most of these are sulfides, and the range of combinations has been far from fully explored. Some of these compounds exhibit good SHG behaviour (e.g., La$_4$InSbS$_9$ and Sm$_4$GaSbS$_9$ with SHG intensities that are 1.5 and 3.8 times greater, respectively, than the benchmark material AgGaS$_2$). Attempts were made to extend these compounds to selenides and tellurides, and to examine their optical properties. The selenides RE_4InSbSe$_9$ were prepared but unfortunately their SHG signals were very weak. Nd$_7$FeInS$_{13}$ is a quaternary chalcogenide exhibiting a new structure type.

14.1.2 Ba containing chalcogenides

Given that Ba-containing chalcogenides, mostly sulfides, have been found to be promising NLO materials, it is interesting to examine the properties of the selenide analogues. These chalcogenides are typically coloured semiconductors. The selenides Ba$_4$Ga$_2$Se$_8$ and Ba$_{12}$In$_4$Se$_{20}$

exhibit the common feature of diselenide units $(Se_2)^{2-}$ whose presence tends to narrow the band gap by about 1 eV compared to the isostructural sulfides. The corresponding tellurides are unknown but it would be expected that they would exhibit even smaller band gaps. Many of these ternary chalcogenides remain centrosymmetric, which might be attributed to the occurrence of edge-sharing tetrahedra. By extending to quaternary chalcogenides, a greater number of components could introduce complexity that might favour the formation of noncentrosymmetric structures. BaZn*M*Se$_4$ is an example in which the presence of two different elements within tetrahedra results in a noncentrosymmetric structure. There is no guarantee, of course, that such compounds will be good NLO materials notwithstanding high SHG intensities (**Table 14–2**). In particular, type-I phase matching is a requirement that is satisfied for $Ba_5CdGa_6Se_{15}$ but not for BaZnSiSe$_4$. Indeed, a major challenge is to be able to design and predict materials that simultaneously show high SHG intensities and are phase-matchable. Even though the SHG intensity for $Ba_5CdGa_6Se_{15}$ is half as large as that of benchmark materials, this compound satisfies all of essential requirements of a good NLO material, including the ease of growing large single crystals.

Table 14-2. New noncentrosymmetric compounds (red) showing SHG behavior.

Compounds	Space group	Phase matchable (PM)/ Nonphase matchable (NPM)	SHG intensity	Reference
$Ba_{23}Ga_8Sb_2S_{38}$	$Cmc2_1$	NPM	$22 \times AgGaS_2$	125
Sm_4GaSbS_9	$Aba2$	NPM	$3.8 \times AgGaS_2$	52
La_4InSbS_9	$P4_12_12$	NPM	$1.5 \times AgGaS_2$	54
Ba_2BiInS_5	$Cmc2_1$	NPM	$0.8 \times KTiOPO_4$	114
$BaGa_2GeS_6$	$R3$	PM	$2.1 \times AgGaS_2$	115
$BaGa_2GeSe_6$	$R3$	PM	$3.5 \times AgGaS_2$	115
BaZnSiSe$_4$	$Ama2$	NPM	$1 \times AgGaS_2$	This work
$Ba_5CdGa6Se_{15}$	$Ama2$	PM	$0.5 \times AgGaS_2$	This work

14.2 Future Work

The major outcomes of this work were to prepare new chalcogenides, many of which are nonstoichiometric and defy the expectation that charge balance must always be satisfied, to apply bond valence sums to rationalize site distributions, to identify uncommon structural units such as diselenides $(Se_2)^{2-}$, and to propose viable new candidates for NLO materials.
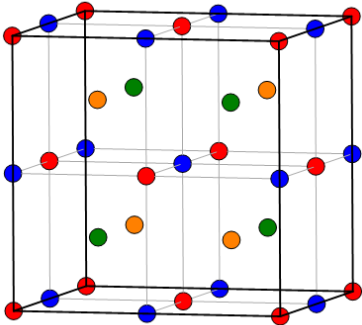
The formation of noncentrosymmetric structures remains an unsolved problem because there are no easy principles or obvious patterns that can be identified. It would be of great interest to find other structural commonalities to improve predictive ability. One approach might be to explore mixed-anion compounds. For example, introducing halogen or oxygen atoms, which are highly electronegative, into chalcogenides will create larger dipole moments. Oxychalcogenides, which are popular for other applications, could be a rewarding system to investigate. Attempts to prepare chalcogenides containing different combinations of M and M' atoms (involving only main-group elements) yielded only one new compound, $La_3Sb_{0.5}GaS_7$. Further combinations can be attempted in future projects. Substitution of Ba with other alkaline-earth metals would also be worthwhile. Some proposed compounds are listed in **Table 14–3**, with their motivations and applications being indicated.

Table 14-3. New compounds for expansion in chalcogenides.

Proposed compound	Probable Structure	Advantage	Application
$PbRE_2In_2Se_7$	*Pbam*	Replacing with heavier element with similar atomic radius	Low thermal conductivity
Ba_3MSe_4Br (M = Ga, In) RE_3MSe_8I	*Pnma* *C2/m*	Introduction of halides to tune the band gap	New optical materials
$RE_3M_{0.5}GeCh_7$ (M = Zn, Cd and Ti)	*P6$_3$*	Partial occupancy	Nonlinear optics
RE_3MCh_5O	*P2/m*	Introduction of oxygen by substitution	Magnetism
$RE_3Sb_{0.5}GaS_7$	*P6$_3$*	Further expansion in this family where M and M' being III but different elements	Nonlinear optics

Given that many of these chalcogenides are coloured, a related project that was initiated later in the Ph.D. program was to prepare intermetallic compounds that are also coloured. Although semiconductors are frequently coloured, intermetallic compounds are not because they normally do not exhibit a gap in their electronic density of states. The rare occurrence of colour in intermetallics arises when there is a small gap or pseudogap, as seen in elemental Cu or Au. Only about 100 examples, out of tens of thousands of known intermetallics, exhibit colour (e.g., red PdIn, dark blue $CoSi_2$, gold CuZn, violet $AuAl_2$). Most of these coloured intermetallics consist of precious metals (Au, Pt, Pd), and their structures are based on filling of octahedral or tetrahedral sites within an fcc arrangement (**Table 14–4**).

Table 14-4. Different structure types adopted by coloured interemetallic compounds.

Structure type	Space Group	Example
CsCl	$Pm\bar{3}m$	PdIn
CaF$_2$	$Fm\bar{3}m$	CoSi$_2$
Cu$_2$MnAl (Heusler)	$Fm\bar{3}m$	PtLiAl$_2$
Li$_2$AgSb (inverse-Heusler)	$F\bar{4}3m$	AgLi$_2$Sn
Ordered Li$_2$AgSb	$F\bar{4}3m$	PtLiMgSb

The synthesis of intermetallic compounds involves various techniques that may be quite different from the preparation of chalcogenides. Two new coloured intermetallics that were prepared were pink Cu$_2$LiAl and yellow Cu$_2$LiGa. The elements were handled within an Ar-filled glove box and placed within a Nb or Ta tube, which was sealed with an arc welder. The metal ampoules were then placed within a water-cooled quartz chamber of an induction furnace (Easy Heat, Model 7590). The samples were heated in the induction furnace at 350–450 °C for 5 minutes and then at 700–800 °C for 20 minutes, after which the furnace was shut off. The tubes were opened in a glove box to minimize exposure to air.

Powder XRD patterns revealed that Cu$_2$LiAl adopts the CsCl-type structure while Cu$_2$LiGa adopts the Heusler (Cu$_2$MnAl-type) structure (**Figure 14–2a** and **Figure 14–2b**). The solid-state ^{7}Li NMR spectrum of Cu$_2$LiAl shows two peaks, which may be attributed to disorder of Li atoms over two sites, or perhaps the presence of an impurity phase. Actually, it is very difficult to differentiate between CsCl-type, Heusler, and inverse Heusler structures, and further structural

characterization, including synchrotron studies, must be performed to establish the correct structure.
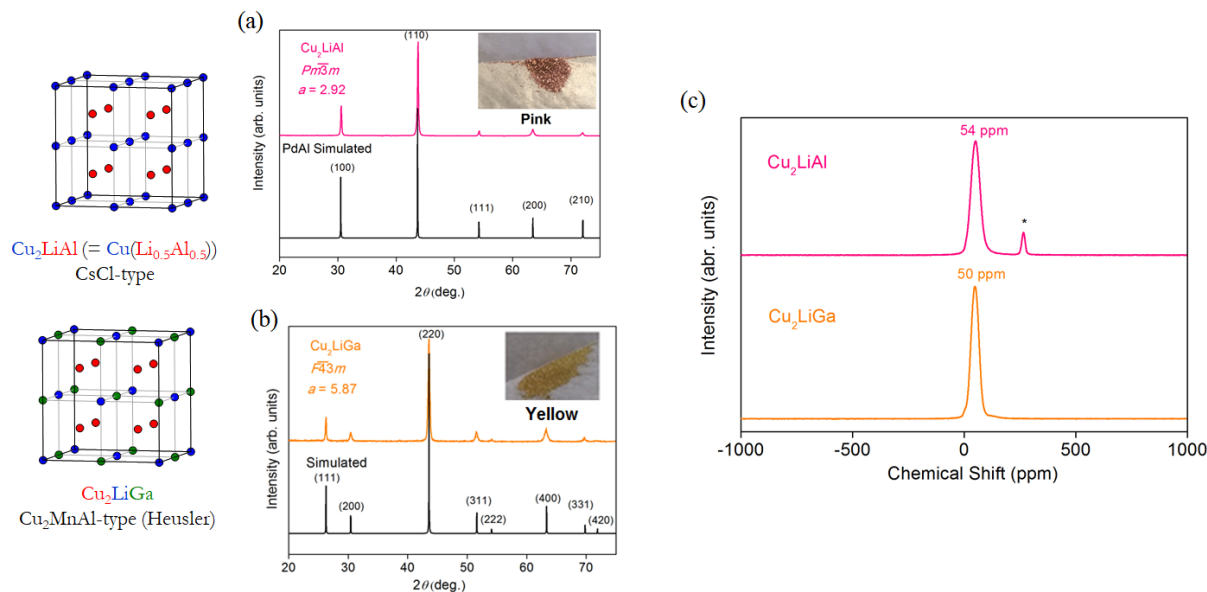
Figure 14-2. (a) pXRD for Cu₂LiAl with pink colour (inset), CsCl structure type; (b) pXRD for Cu₂LiGa yellow colour (inset), Cu₂MnAl; (c) ^{7}Li NMR for both the compounds.

Reference

[1]   Steinemann, S. G.; Wolf, W.; Poudloucky, R. in J. H. Westbrook R. L. Flescher (Eds.), *Intermetallic Compounds – Principles and Practice*, **2002**, *3*, 231-246.

Bibliography

[1] Makovicky, E. *Rev. Mineral Geochem.* **2006**, *61*, 7–125.

[2] Sunshine, S. A.; Keszler, D. A.; Ibers, J. A. *Acc. Chem. Res.* **1987**, *20*, 395–400.

[3] Kadam, R. M.; Rajeswari, B.; Sengupta, A.; Achary, S. N.; Kshirsagar, R. J.; Natarajan, V. *Spectrochim. Acta, Part A* **2015**, *137*, 363–370.

[4] McKelvy, M. J.; Glaunsinger, W. S. *Mat. Res. Bull.*, **1986**, *21*, 835–842.

[5] Late, D. J.; Rout, C. S.; Chakravarty, D.; Ratha, S. *Can. Chem. Trans.* **2015**, *3*, 118–157.

[6] Pachmayr, U.; Johrendt, D. *Chem. Commun.,* **2015**, *51*, 4689–4692.

[7] Cotter, D.; Manning, R. J.; Blow, K. J.; Ellis, A. D.; Kelly, A. E.; Nesset, D.; Phillips, I. D.; Poustie, A. J.; Rogers, D. C. *Science* **1999**, *286*, 1523−1528.

[8] Chung, I.; Kanatzidis, M. G. *Chem. Mater.* **2014**, *26*, 849–869.

[9] Pushkarsky, M. B.; Webber, M. E.; Macdonald, T.; Patel, C. K. N. *Appl. Phys. Lett.* **2006**, *88*, 1–3.

[10] Pestov, D.; Wang, X.; Ariunbold, G. O.; Murawski, R. K.; Sautenkov, V. A.; Dogariu, A.; Sokolov, A. V.; Scully, M. O. *Proc. Natl. Acad. Sci.* U.S.A. **2008**, *105*, 422−427.

[11] Pushkarsky, M. B.; Dunayevskiy, I. G.; Prasanna, M.; Tsekoun, A. G.; Go, R.; Patel, C. K. N. *Proc. Natl. Acad. Sci.* U.S.A. **2006**, *103*, 19630−19634.

[12] Nikogosyan, D. N. *Nonlinear optical crystals: a complete survey*,1st ed.; Springer: New York, **2005**.

[13] Guang, S. H.; Song, H. L., *Physics of Nonlinear Optics*, 1st ed., World Scientific Publishing, Singapore, **1999**.

[14] Dougherty, J. P.; Kurtz, S. K. *J. Appl. Crystallogr.*, **1976**, *9*, 145.

[15] Boyd, R. Nonlinear Optics, 3rd ed.; Elsevier, New York, **2008**.

[16] Zhang, W.; Yu, H.; Wu, H.; Halasyamani, P. S. *Chem. Mater.* **2017**, *29*, 2655−2668.

[17] Halasyamani, P. S.; Poeppelmeier, K. R. *Chem. Mater.* **1998,** *10,* 2753–2769.

[18] Liang, F.; Kang, L.; Lin, Z.; Wu, Yicheng. *Cryst. Growth des.* **2017**, *17*, 2254–2289.

[19] Collin, G.; Étienne, J.; Flahaut, J.; Guittard, M.; Laruelle, P. *Rev. Chim. Miner.* **1973**, *10*, 225–238.

[20] Palazzi, M.; Carcaly, J.; Flahaut, J. *J. Solid State Chem.* **1980**, *35*, 150–155.

[21] Daszkiewicz, M; Gulay, L. D.; Lychmanyuk, O. S. *Acta Crystallogr. B* **2009**, *65*, 126–133.

[22] Nanjundaswamy, K. S.; Gopalakrishnan, J. J. Solid State Chem., *49*, **1983**, 51–58.

[23] Gitzendanner R. L.; Spencer C. M.; DiSalvo F. J.; Pell M. A.; Ibers J. A. *J. Solid State Chem.* **1997**, *131*, 399–404.

[24] Abrahams, S. C. *Acta Crystallogr. B*, **1990**, *46*, 311–324.

[25] Guo S. P.; Guo G. C.; Wang M. S.; Zou J. P.; Xu G.; Wang G. J.; Long X. F.; Huang J. S. *Inorg. Chem.* **2009**, *48*, 7059–7065.

[26] Shi, Y. -F.; Chen, Y. -K.; Chen, M. -K.; Wu, L. -M.; Lin, H.; Zhou, L. -J; Chen, L. *Chem. Mater.* **2015**, *27*, 1876–1884.

[27] Hartenbach, I.; Nilges, T.; Schleid T. *Z. Anorg. Allg. Chem.* **2007**, *633*, 2445–2452.

[28] Gulay, L. D.; Lychmanyuk, O. S; Olekseyuk; I. D.; Daszkiewicz; M.; Stępień-Damm, J.; Pietraszko, A. *J. Alloys Compd.* **2007**, *431*, 185–190.

[29] Hartenbach, I.; Müller, C.; Schleid T. *Z. Anorg. Allg. Chem.* **2006**, *632*, 2147.

[30] Gulay, L. D.; Lychmanyuk, O. S.; Wolcyrz, M.; Pietraszko, A.; Olekseyuk I. D. *J Alloys Compd.* **2006**, *425*, 159–163.

[31] Strok, O. M.; Daszkiewicz, M.; Gulay, L. D.; Kaczorowski D. *J. Alloys Compd.* **2010**, *493*, 47–49.

[32] Gulay, L. D.; Olekseyuk, I. D.; Wolcyrz, M.; Stępień-Damm, J. *Z. Anorg. Allg. Chem*. **2005**, *631*, 1919–1923.

[33] Daszkiewicz, M; Gulay, L. D.; Lychmanyuk, O. S; Pietraszko, A. *J. Alloys Compd*. **2008**, *460*, 201–205.

[34] Daszkiewicz, M; Gulay, L. D.; Lychmanyuk, O. S; Pietraszko, A. *J. Alloys Compd.* **2009**, *467*, 168–172.

[35] Daszkiewicz, M; Gulay, L. D.; Lychmanyuk, O. S. *Acta Crystallogr. B* **2009**, *65*, 126–133.

[36] Daszkiewicz, M; Gulay, L. D.; Lychmanyuk, O. S; Pietraszko, A. *J. Alloys Compd.* **2009**, *467*, 168–172.

[37] Daszkiewicz, M; Gulay, L. D.; M.; Pietraszko, A.; Shemet, V. Y. *J. Solid State Chem.* **2007**, *180*, 2053–2060.

[38] Choudhury, A.; Dorhout, P. K. *Inorg. Chem.* **2015**, *54*, 1055–1065.

[39] He, J.; Wang, Z.; Zhang, X.; Cheng, Y.; Gong, Y.; Lai, X.; Zheng C.; Lin J.; Huang F. *RSC Adv.* **2015**, *5*, 52629–52635.

[40] Rudyk, B. W.; Stoyko, S. S.; Oliynyk, A. O.; Mar, A. *J. Solid State Chem.* **2014**, *210*, 79–88.

[41] Yin, W.; Wang, W.; Kang, L.; Lin, Z.; Feng, K.; Shi, Y.; Hao, W.; Yao, J. L.; Wu, Y. *J. Solid State Chem.* **2013**, *202*, 269–275.

[42] Rudyk, B. W.; Stoyko, S. S.; Mar, A *J. Solid State Chem.* **2013**, *208*, 78–85.

[43] Huch, M. R.; Gulay, L. D.; Olekseyuk, I. D. *J. Alloys Compd.* **2006**, *424*, 114–118.

[44] Strok, O. M.; Daszkiewicz, M.; Gulay, L. D *Chem. Met. Alloys* **2015**, *8*, 16–21.

[45] Daszkiewicz, M.; Marchuk, O. V.; Gulay, L. D.; Kaczorowski, D. *J. Alloys Compd.* **2014**, *610*, 258–263.

[46] Daszkiewicz, M.; Pashynska, Y. O.; Marchuk, O. V.; Gulay, L. D.; Kaczorowski, D. *J. Alloys Compd.* **2014**, *616*, 243–249.

[47] Assoud A.; Sankar C. R.; Kleinke H. *Solid State Sci.* **2014**, *38*, 124–128.

[48] Zhao, H. J *J. Solid State Chem*. **2015**, *227*, 5–9.

[49] Zhao, H. J *Z. Anorg. Allg. Chem*. **2015**, *641*, 917–921.

[50] Zeng H. Y.; Zheng F. K.; Guo G. C.; Huang J. S. *J. Alloys Compd.* **2008**, *458*, 123–129

[51] Villars, P.; Cenzual, K. Pearson's Crystal Data - Crystal Structure Database for Inorganic Compounds, Release **2017/18**, ASM international, Materials Park, Ohio, USA.

[52] Chen, M. -C.; Li, L. -H.; Chen, Y. -B.; Chen, L. *J. Am. Chem. Soc.* **2011**, *133*, 4617–4624.

[53] Zhao, H. -J. *J. Solid State Chem.* **2016**, *237*, 99–104.

[54] Zhao, H. -J.; Zhang, Y. -F.; Chen, L. *J. Am. Chem. Soc.* **2012**, *134* 1993–1995.

[55] Zhao, H. -J. *Z. Anorg. Allg. Chem.* **2016**, *642*, 56–59.

[56] Huch, M. R.; Gulay, L. D.; Olekseyuk, I. D.; Pietraszko, A. *J. Alloys Compd.* **2006**, *425* 230–234.

[57] Huch, M. R.; Gulay, L. D.; Olekseyuk, I. D. *J. Alloys Compd.* **2007**, *439*, 156–161.

[58] Gulay, L. D.; Olekseyuk, I. D.; Wołcryz, M.; Stępień-Damm, J. *J. Alloys Compd.* **2005**, *399*, 189–195.

[59] Gulay, L. D.; Olekseyuk, I. D. *J. Alloys Compd.* **2005**, *387*, 160–164.

[60] Gulay, L. D.; Stępień-Damm, J.; Pietraszko, A.; Olekseyuk, I. D. *J. Alloys Compd.* **2006**, *413*, 90–95.

[61] Zhao, H. -J.; Li, L. -H.; Wu, L. -M.; Chen, L. *Inorg. Chem.* **2009**, *48*, 11518–11524.

[62] Daszkiewicz, M.; Marchuk, O. V.; Gulay, L. D.; Kaczorowski, D. *J. Alloys Compd.* **2012**, *519*, 85–91.

[63] Kanatzidis, M. G. *Inorg. Chem.* **2017**, *56*, 3158–3173.

[64] Donohue, P. C.; Hanlon, J. E. *J. Electrochem. Soc.* **1974**, *121*, 137–142.

[65] Lin, X.; Zhang, G.; Ye, N. *Cryst. Growth Des.* **2009**, *9*, 1186–1189.

[66] Yao, J. L.; Mei, D.; Bai, L.; Lin, Z.; Yin, W.; Fu, P.; Wu, Y. *Inorg. Chem.* **2010**, *49*, 9212–9216.

[67] Eisenmann, B.; Jakowski, M.; Klee, W.; Schäfer, H. *Rev. Chim. Miner.* **1983**, *20*, 255–263.

[68] Mei, D.; Yin, W.; Bai, L.; Lin, Z.; Yao, J. L.; Fu, P.; Y. Wu *Dalton Trans.* **2011**, *40*, 3610–3615.

[69] Mei, D.; Yin, W.; Lin, Z.; Yao, J. L.; Fu, P.; Y. Wu *J. Alloys Compd.* **2011**, *509*, 2981–2985.

[70] Eisenmann, B.; Jakowski, M.; Schäfer, H. *Z. Naturforsch. B* **1984**, *39*, 27–30.

[71] Eisenmann, B.; Jakowski, M.; Schäfer, H. *Rev. Chim. Miner.* **1984**, *21*, 12–20.

[72] Eisenmann, B.; Jakowski, M.; Schäfer, H. *Z. Naturforsch. B* **1983**, *38*, 1581–1584.

[73] Eisenmann, B.; Jakowski, M.; Schäfer, H. *Mater. Res. Bull.* **1982**, *17*, 1169–1175.

[74] Klee, W.; Schäfer, H. *Z. Anorg. Allg. Chem.* **1981**, *479*, 125–133.

[75] Liu, J. W.; Wang, P.; Chen, L. *Inorg. Chem.* **2011**, *50*, 5706–5713.

[76] Yin, W.; Mei, D.; Feng, K.; Yao, J.; Fu, P.; Wu, Y. *Dalton Trans.* **2011**, *40*, 9159–9162.

[77] Lemely, J. T. *Acta Crystallogr. B* **1974**, *30*, 549–550.

[78] Wu, K.; Pan, S.; Yang, Z. *RSC Adv.* **2015**, *5*, 33646–33652.

[79] Wu, K.; Su, X.; Yang, Z.; Pan, S. *Dalton Trans.* **2015,** *44*, 19856–19864.

[80] Assoud, A.; Soheilnia, N.; Kleinke, H. *Z. Naturforsch. B* **2004**, *59*, 975–979.

[81] Jumas, J. C.; Philippot E.; Vermot G. D. F.; Ribes M.; Maurin M. *J. Solid State Chem.* **1975**, *14*, 319–327.

[82] Luo, Z. Z.; Lin, C. S.; Cheng, W. D.; Zhang, H.; Zhang, W. L.; He, Z. Z *Inorg. Chem.* **2013**, *52*, 273–279.

[83] Ribes, M.; Olivier, F. J.; Philippot, E.; Maurin, M. *J. Solid State Chem.* **1973**, *8*, 195–205.

[84] Luo, Z. Z.; Lin, C. S.; Zhang, W. L.; Zhang, H.; He, Z. Z.; Cheng, W.D. *Chem. Mater.* **2014**, *26*, 1093–1099.

[85] Assoud, A.; Klienke, H. *Chem. Mater.* **2005**, *17*, 4509–4513.

[86] Feng, K.; Jiang, X.; Kang, L.; Yin, W.; Hao, W.; Lin, Z.; Yao, J. L.; Wu, Y.; Chen, C. *Dalton Trans.* **2013**, *42*, 13635–13641.

[87] Assoud, A.; Derakhshan S.; Soheilnia N.; Klienke, H. *Chem. Mater.*, **2004**, *16*, 4193–4198.

[88] Assoud, A.; Soheilnia, N.; Kleinke, H. *J. Solid State Chem.* **2005**, *178*, 1087–1093.

[89] Johrendt, D.; Tampier, M. *Chem. Eur. J.* **2000**, *6*, 994–998.

[90] Brinkmann, C.; Eisenmann, B.; Schäfer, H. *Anorg. Allg. Chem.* **1984**, *517*, 143–148.

[91] Pan, M. Y.; Xia, S. Q.; Liu X. C.; Tao X. T. *J. Solid State Chem.* **2014**, *219*, 74–79.

[92] Jörgens, S.; Mewis, A. *Z. Anorg. Allg. Chem.* **2007**, *633*, 570–574.

[93] Jörgens, S.; Mewis, A.; Hoffmann, R. D.; Pöttgen, R.; Mosel, B. D. *Z. Anorg. Allg. Chem.* **2003**, *629*, 429–433.

[94] Wang, J.; Lee, K.; Kovnir, K. *Z. Anorg. Allg. Chem.* **2015**, *641*, 1087–1092.

[95] Cordier, G.; Schwidetzky, C.; Schäfer, H. *J. Solid State Chem.* **1984**, *54*, 84–88.

[96] Iordanidis, L.; Ghelani, N. A.; Hogan, T. P.; Kanatzidis, M. G.; Brazis, P. W.; Kyratsi, T.; Ireland, J. R.; Lane, M.; Chen, W.; Dyck, J. S.; Uher, C. *Chem. Mater.* **2001**, *13*, 622–633.

[97] Cordier, G.; Schwidetzky, C.; Schäfer, H. *Rev. Chim. Miner.* **1983**, *20*, 877–883.

[98] Cordier, G.; Schwidetzky, C.; Schäfer, H. *Rev. Chim. Miner.* **1985**, *22*, 93–100.

[99] Wang, J.; Lee, K.; Kovnir, K. *J. Mater. Chem. C* **2015**, *3*, 9811–9818.

[100] Wang, Y. C.; DiSalvo, F. J. *Chem. Mater.* **2000**, *12*, 1011–1017.

[101] Chung, D. Y.; Jobic, S.; Hogan, T. P.; Kannewurf, C. R.; Brec, R.; Rouxel, J.; Kanatzidis, M. G. *J. Am. Chem. Soc.* **1997**, *119*, 2505–2515.

[102] Jörgens, S.; Johrendt, D.; Mewis, A. *Chem. Eur. J.* **2003**, *9*, 2405–2410.

[103] Dörrscheidt, W.; Schäfer, H. *Z. Naturforsch. B* **1981**, *36*, 410–414.

[104] Yin, W.; Feng, K.; He, R.; Mei, D.; Lin, Z.; Yao, J.; Wu, Y. *Dalton Trans.* **2012**, *41*, 5653–5661.

[105] Lei, X. W.; Yang, M.; Xia, S. Q.; Liu, X. C.; Pan, M. Y.; Li, X.; Tao, X. T. *Chem. Asian J.* **2014**, *9*, 1123-1131.

[106] Kuo, S.-M.; Chang, Y.-M.; Chung, I.; Jang, J.-I.; Her, B.-H.; Yang, S.-H.; Ketterson, J. B.; Kanatzidis, M. G.; Hsu, K.-F. *Chem. Mater.* **2013**, *25,* 2427–2433.

[107] Yin, W.; He, R.; Feng, K.; Hao, W.; Yao, J. L.; Wu, Y. *J. Alloys Compd.* **2013**, *565*, 115–119.

[108] Tampier, M.; Johrendt, D. *Z. Naturforsch. B* **1998**, *53*, 1483–1488.

[109] Teske, C. L. *Z. Naturforsch. B* **1979**, *34*, 386–389.

[110] Frazer, L.; Chang, Y. -M.; Liu, T. -K.; Lin, J.-F.; Liang, I. -C.; Sheu, H. -S.; Ketterson, J. B.; Kanatzidis, M. G.; Hsu, K. -F. *Chem. Mater.* **2015**, *27*, 1316–1326.

[111] Tampier, M.; Johrendt, D. *Z. Anorg. Allg. Chem.* **2001**, *627*, 312-320.

[112] Assoud, A.; Soheilnia, N.; Kleinke, H. *Chem. Mater.* **2005**, *17*, 2255–2261.

[113] Teske, C. L. *Z. Naturforsch. B* **1980**, *35*, 509–510.

[114] Geng, L.; Cheng, W. D.; Lin, C. S.; Zhang, W. L.; Zhang, H.; He, Z. Z. *Inorg. Chem.* **2011**, *50*, 5679–5686.

[115] Lin, X.; Guo, Y.; Ye, N.; *J. Solid State Chem.* **2012**, *195*, 172–177.

[116] Yin, W.; Feng, K.; He, R.; Mei, D.; Lin, Z.; Yao, J. L.; Wu, Y. *Dalton Trans.* **2012**, *41*, 5653–5661.

[117] Liu B. W.; Zeng H. Y.; Zhang M. J.; Fan Y. H.; Guo G. C.; Huang J. S.; Dong Z. C. *Inorg. Chem.* **2015**, *54*, 976–981.

[118] Geng, L.; Zhang, H.; Cheng, W. D. *J. Struct. Chem.* **2013**, *32*, 538–544.

[119] Li, C.; Li, X.; Huang, H., Yao, J.; Wu, Y. *Inorg. Chem.* **2015**, *54*, 9785–9789.

[120] Hao, W.; Mei, D.; Yin, W.; Feng, K.; Yao, J. L.; Wu, Y. *J. Solid State Chem.* **2013**, *198*, 81–86.

[121] Yin, W.; Lin, Z.; Kang, L.; Kang, B.; Deng, J.; Lin, Z.; Yao, J.; Wu, Y. *Dalton Trans.* **2015**, *44*, 2259–2266.

[122] Geng L. *Acta Crystallogr. E* **2013**, *69*, i24.

[123] Chung, M. Y.; Lee, C. S. *Inorg. Chem.* **2012**, *51*, 13328–13333.

[124] Choi, K. S.; Kanatzidis, M. G. *Inorg. Chem.* **2001**, *40*, 101–104.

[125] Chen, M. C.; Wu, L. M.; Lin, H.; Zhou, L. J.; Chen, L. *J. Am.Chem. Soc.* **2012**, *134*, 6058−6060.

[126] Massa, W. *Crystal Structure Determination*, 2nd ed., Springer–Verlag: Berlin, 2004.

[127] West, A. R. *Basic Solid State Chemistry*, 2nd ed., Wiley: New York, 1999.

[128] Bragg, W. H.; Bragg W. L. *Proc. R. Soc. Lond. A* **1913**, *88*, 428–438.

[129] Brese, N. E.; O'Keeffe, M. *Acta. Crystallogr., Sect. B* **1991**, *47*, 192–197.

[130] Russ, J. C. *Fundamentals of energy dispersive X-ray analysis*, Butterworth: London, **1984**.

[131] Dronskowski, R. *Computational Chemistry of Solid State Materials*, Wiley-VCH, Weinheim, **2005**.

[132] Hoffman, R. *Angew. Chem.*, *Int. Ed. Engl.* **1987**, *26*, 846–878.

[133] Tank, R.; Jepsen, O.; Burkhardt, A.; Andersen, O. K. *TB-LMTO-ASA Program*, version 4.7; Max Planck Institut für Festkörperforschung: Stuttgart, Germany, 1998.

[134] Kubelka, P.; Munk, F. *Z. Techn. Physik.* **1931***, 12*, 593.

[135] Abramowitz, M.; Sutter, R. T.; Davidson, M. W., accessed 5 May 2016 <http://www.olympusmicro.com/primer/java/reflection/specular/>.

[136] Mitchell, K.; Ibers, J. A. *Chem. Rev.* **2002**, *102*, 1929–1952.

[137] Chung, I.; Kanatzidis, M. G. *Chem. Mater.* **2014**, *26*, 849–869.

[138] Guittard, M.; Julien-Pouzol, M.; Laruelle, P.; Flahaut, J. *C. R. Acad. Sci., Ser. C* **1968**, *267*, 767–769.

[139] Villars, P.; Cenzual, K. Pearson's Crystal Data – Crystal Structure Database for Inorganic Compounds, ASM International, Materials Park, OH, 2010.

[140] Collin, G.; Étienne, J.; Flahaut, J.; Guittard, M.; Laruelle, P. *Rev. Chim. Miner.* **1973**, *10*, 225–238.

[141] Choudhury, A.; Dorhout, P. K. *Inorg. Chem.* **2015**, *54*, 1055–1065 and references therein.

[142] Collin, G.; Flahaut, J. *C. R. Acad. Sci., Ser. C* **1970**, *270*, 488–490.

[143] Collin, G.; Flahaut, J. *Bull. Soc. Chim. Fr.* **1972**, 2207–2209.

[144] Rodier, N.; Guittard, M.; Flahaut, J. *C. R. Acad. Sci., Ser. 2* **1983**, *296,* 65–70.

[145] Nanjundaswamy, K. S.; Gopalakrishnan, J. *J. Solid State Chem.* **1983**, *49*, 51–58.

[146] Van Calcar, P. M.; Dorhout, P. K. *Mater. Sci. Forum* **1999**, *315*, 322–330.

[147] Wu, L. -B.; Huang, F. -Q. *Z. Kristallogr. – New Cryst. Struct.* **2005**, *220*, 305–306.

[148] Yin, W.; Wang, W.; Kang, L.; Lin, Z.; Feng, K.; Shi, Y.; Hao, W.; Yao, J. L.; Wu, Y. *J. Solid State Chem.* **2013**, 202, 269–275.

[149] Rudyk, B. W.; Stoyko, S. S.; Mar, A *J. Solid State Chem.* **2013**, *208*, 78–85.

[150] Rudyk, B. W.; Stoyko, S. S.; Oliynyk, A. O.; Mar, A. *J. Solid State Chem.* **2014**, *210*, 79–88

[151] Patrie, M.; Guittard, M. *C. R. Acad. Sci., Ser. C* **1969**, *268,* 1136–1138.

[152] Collin, G.; Laruelle, P. *C. R. Acad. Sci., Ser. C* **1970***, 270,*410–412.

[153] Guo S. -P.; Guo G. -C.; Wang M. -S.; Zou J. -P.; Xu, G.; Wang, G. J.; Long, X. -F.; Huang, J. -S. *Inorg. Chem.* **2009**, *48*, 7059–7065.

[154] Abrahams, S. C. *Acta Crystallogr., Sect. B* **1990**, *46*, 311–324.

[155] Daszkiewicz, M.; Gulay, L. D. *Mater. Res. Bull.* **2012**, *47*, 497–499.

[156] Hartenbach, I.; Nilges, T.; Schleid T. *Z. Anorg. Allg. Chem.* **2007**, *633*, 2445–2452.

[157] Shi, Y. -F.; Chen, Y. -K.; Chen, M. -K.; Wu, L. -M.; Lin, H.; Zhou, L. -J; Chen, L. *Chem. Mater.* **2015**, *27*, 1876–1884.

[158] Zhang, X.; Chen, W.; Mei, D.; Zheng, C.; Liao, F.; Li, Y.; Lin, J.; Huang, F. *J. Alloys Compd.* **2014**, *610*, 671–675.

[159] Sheldrick, G. M. *SHELXTL*, version 6.12; Bruker AXS Inc.: Madison, WI, 2001.

[160] Gelato, L. M.; Parthé, E. *J. Appl. Crystallogr.* **1987**, *20*, 139–143.

[161] Hwu, S. -J.; Bucher, C. K.; Carpenter, J. D.; Taylor, S. P. *Inorg. Chem.* **1995**, *34*, 1979–1980.

[162] Lin, S. -H.; Mao, J. -G.; Guo, G. -C.; Huang, J. -S. *J. Alloys Compd.* **1997**, *252*, L8–L11.

[163] Wu, L. -B.; Huang, F. -Q. *Z. Kristallogr. – New Cryst. Struct.* **2005**, *220*, 307–308.

[164] Gulay, L. D.; Lychmanyuk, O. S.; Wołcyrz, M.; Pietraszko, A.; Olekseyuk, I. D. *J. Alloys Compd.* **2006**, *425*, 159–163.

[165] Gulay, L. D.; Lychmanyuk, O. S.; Olekseyuk, I. D.; Daszkiewicz, M.; Stępień-Damm, J.; Pietraszko, A. *J. Alloys Compd.* **2007** *431*, 185–190.

[166] Daszkiewicz, M; Gulay, L. D.; M.; Pietraszko, A.; Shemet, V. Y. *J. Solid State Chem.* **2007**, *180*, 2053–2060.

[167] Fairley, N. CasaXPS, version 2.3.9, Casa Software Ltd., Teighnmouth, Devon, UK, 2003, http://www.casaxps.com.

[168] Tank, R.; Jepsen, O.; Burkhardt, A.; Andersen, O. K. *TB-LMTO-ASA Program*, version 4.7; Max Planck Institut für Festkörperforschung: Stuttgart, Germany, **1998**.

[169] Brese, N. E.; O'Keeffe, M. *Acta. Crystallogr., Sect. B* **1991**, *47*, 192–197.

[170] Evans, Jr., H. T.; Konnert, J. A. *Am. Mineral.* **1976**, *61*, 996–1000.

[171] Ohmasa, M.; Suzuki, M.; Takeuchi, Y. *Mineral. J.* **1977**, *8*, 311–319.

[172] Fjellvåg, H.; Grønvold, F.; Stølen, S.; Andresen, A. F.; Müller-Käfer, R.; Simon, A. *Z. Kristallogr.* **1988**, *184*, 111–121.

[173] Gotsis, H. J.; Barnes, A. C.; Strange, P. *J. Phys.: Condens. Matter* **1992**, *4*, 10461–10468.

[174] Okamoto, K.; Kawai, S.; Kiriyama, R. *Jap. J. Appl. Phys.* **1969**, *8*, 718–724.

[175] Nozaki, H.; Shibata, K.; Ohhashi, N. *J. Solid State Chem.* **1991**, *91*, 306–311.

[176] Gaarenstroom, S. W.; Winograd, N. *J. Chem. Phys.* **1977**, *67*, 3500–3506.

[177] Folmer, J. C. W.; Jellinek, F. *J. Less-Common Met.* **1980**, *76*, 153–162.

[178] Folmer, J. C. W.; Jellinek, F.; Calis, G. H. M. *J. Solid State Chem.* **1988**, *72*, 137–144.

[179]   Chawla, S. K.; Sankarraman, N.; Payer, J. H. *J. Electron Spectrosc. Relat. Phenom.* **1992**, *61*, 1–18.

[180]   Patrick, R. A. D.; Mosselmans, J. F. W.; Charnock, J. M.; England, K. E. R.; Helz, G. R.; Gardner, C. D.; Vaughan, D. J. *Geochim. Cosmochim. Acta* **1997**, *61*, 2023–2036.

[181]   Goh, S. W.; Buckley, A. N.; Lamb, R. N. *Miner. Eng.* **2006**, *19*, 204–208.

[182]   Wagner, C. D.; Naumkin, A. V.; Kraut-Vass, A.; Allison, J. W.; Powell, C. J.; Rumble Jr., J. R. NIST X-ray Photoelectron Spectroscopy Database, version 3.5 (web version), National Institute of Standards and Technology, Gaithersburg, MD 2003, http://srdata.nist.gov/xps.

[183]   Burroughs, P.; Hamnett, A.; Orchard, A. F.; Thornton, G. *J. Chem. Soc., Dalton Trans.* **1976**, 1686–1698.

[184]   Kotani, A.; Jo, T.; Parlebas, J. C. *Adv. Phys.* **1988**, *37*, 37–85.

[185]   LeNormand, F.; El Fallah, J.; Hilaire, L.; Légaré, P.; Kotani, A.; Parlebas, J. C. *Solid State Commun.* **1989**, *71*, 885–889.

[186]   Bêche, E.; Charvin, P.; Perarnau, D.; Abanades, S.; Flamant, G. *Surf. Interface Anal.* **2008**, *40*, 264–267.

[187]   Villars, P.; Cenzual, K. Pearson's Crystal Data – Crystal Structure Database for Inorganic Compounds (on DVD), Release 2015/16, ASM International, Materials Park, OH, USA.

[188]   de Saint-Giniez, D.; Laruelle, P.; Flahaut, J. *C. R. Acad. Sci., Ser. C* **1968**, *267*, 1029–1032.

[189]   Collin, G.; Laruelle, P. *Bull. Soc. Fr. Mineral. Cristallogr.* **1971**, *94*, 175–176.

[190]   Collin, G.; Étienne, J.; Flahaut, J.; Guittard, M.; Laruelle, P. *Rev. Chim. Miner.* **1973**, *10*, 225–238.

[191]   Choudhury, A.; Dorhout, P. K. *Inorg. Chem.* **2015**, *54*, 1055–1065 and references therein.

[192]   Collin, G.; Flahaut, J. *C. R. Acad. Sci., Ser. C* **1970**, *270*, 488–490.

[193]   Collin, G.; Flahaut, J. *Bull. Soc. Chim. Fr.* **1972**, 2207–2209.

[194]   Rodier, N.; Guittard, M.; Flahaut, J. *C. R. Acad. Sci., Ser. 2* **1983**, *296,* 65–70.

[195]   Nanjundaswamy, K. S.; Gopalakrishnan, J. *J. Solid State Chem.* **1983**, *49*, 51–58.

[196]   Van Calcar, P. M.; Dorhout, P. K. *Mater. Sci. Forum* **1999**, *315*, 322–330.

[197]   Wu, L. -B.; Huang, F. -Q. *Z. Kristallogr. – New Cryst. Struct.* **2005**, *220*, 305–306.

[198]   Yin, W.; Wang, W.; Kang, L.; Lin, Z.; Feng, K.; Shi, Y.; Hao, W.; Yao, J. L.; Wu Y. *J. Solid State Chem.* **2013**, *202*, 269–275.

[199]   Rudyk, B. W.; Stoyko, S. S.; Mar, A *J. Solid State Chem.* **2013**, *208*, 78–85.

[200]   Rudyk, B. W.; Stoyko, S. S.; Oliynyk, A. O.; Mar, A. *J. Solid State Chem.* **2014**, *210*, 79–88

[201]   Patrie, M.; Guittard, M. *C. R. Acad. Sci., Ser. C* **1969**, *268,* 1136–1138.

[202]   Collin, G.; Laruelle, P. *C. R. Acad. Sci., Ser. C* **1970***, 270*,410–412.

[203]   Iyer, A. K.; Rudyk, B. W.; Lin, X.; Singh, H.; Sharma, A. Z.; Wiebe, C. R.; Mar, A. *J. Solid State Chem.* **2015**, *229*, 150–159.

[204]   Daszkiewicz, M; Gulay, L. D.; Pietraszko, A.; Shemet, V. Y. *J. Solid State Chem.* **2007**, *180*, 2053–2060

[205]   Daszkiewicz, M; Gulay, L. D.; Lychmanyuk; O. S; Pietraszko, A. *J. Alloys Compd.* **2008**, *460*, 201–205

[206]   Daszkiewicz, M; Gulay, L. D.; Lychmanyuk; O. S; Pietraszko, A. *J. Alloys Compd.* **2009**, *467*, 168–172

[207]   Daszkiewicz, M.; Gulay, L. D. *Mater. Res. Bull.* **2012**, *47*, 497–499.

[208]   Daszkiewicz, M; Gulay, L. D.; Lychmanyuk; O. S. *Acta Crystallogr. B* **2009**, *65*, 126–133.

[209]   Poduska, K. M.; DiSalvo, F. J.; Min, K.; Halasyamani, P. S. *J. Alloys Compd.* **2002**, *335*, L5–L9.

[210]   Guo S. -P.; Guo G. -C.; Wang M. -S.; Zou J. -P.; Xu, G.; Wang, G. J.; Long, X. -F.; Huang, J. -S. *Inorg. Chem.* **2009**, *48*, 7059–7065

[211] Shi, Y. -F.; Chen, Y. -K.; Chen, M. -K.; Wu, L. -M.; Lin, H.; Zhou, L. -J; Chen, L. *Chem. Mater.* **2015**, *27*, 1876–1884.

[212] Hartenbach, I.; Nilges, T.; Schleid T. *Z. Anorg. Allg. Chem.* **2007**, *633*, 2445–2452

[213] Sheldrick, G. M. *SHELXTL*, version 6.12; Bruker AXS Inc.: Madison, WI, **2001**.

[214] Bindi, L.; Evain, M. *Am. Mineral.* **2007**, *92*, 886–891.

[215] Petřiček, V.; Dušek, M.; Palatinus, L. *Z. Kristallogr.* **2014**, *229*, 345–352.

[216] Fairley, N. CasaXPS, version 2.3.9, Casa Software Ltd., Teighnmouth, Devon, UK, 2003, http://www.casaxps.com.

[217] Tank, R.; Jepsen, O.; Burkhardt, A.; Andersen, O. K. *TB-LMTO-ASA Program*, version 4.7; Max Planck Institut für Festkörperforschung: Stuttgart, Germany, **1998**.

[218] Brese, N. E.; O'Keeffe, M. *Acta Crystallogr., Sect. B* **1991**, *47*, 192–197.

[219] Hull, S. *Rep. Prog. Phys.* **2004**, *67*, 1233–1314.

[220] Kaushik, V. K. *J. Electron Spectrosc. Relat. Phenom.* **1991**, *56*, 273–277.

[221] Ferraria, A. M.; Carapeto, A. P.; Botelho do Rego, A. M. *Vacuum* **2012**, *86*, 1988–1991.

[222] Wagner, C. D.; Naumkin, A. V.; Kraut-Vass, A.; Allison, J. W.; Powell, C. J.; Rumble Jr., J. R. NIST X-ray Photoelectron Spectroscopy Database, version 3.5 (web version), National Institute of Standards and Technology, Gaithersburg, MD 2003, http://srdata.nist.gov/xps.

[223] Mitchell, K.; Ibers, J. A. *Chem. Rev.* **2002**, *102*, 1929–1952.

[224] Guittard, M.; Julien-Pouzol, M.; Laruelle, P.; Flahaut, J. *C. R. Acad. Sci., Ser. C* **1968**, *267*, 767–769.

[225] Michelet, A.; Flahaut, J. *C. R. Acad. Sci., Ser. C* **1969**, *269*, 1203–1205.

[226] Collin, G.; Flahaut, J. *C. R. Acad. Sci., Ser. C* **1970**, *270*, 410–412.

[227] Collin, G.; Flahaut, J. *C. R. Acad. Sci., Ser. C* **1970**, *270*, 488–490.

[228] Guittard, M.; Julien-Pouzol *Bull. Soc. Chim. Fr.* **1970**, 2467–2469.

[229] Collin, G.; Laruelle, P. *Bull. Soc. Fr. Mineral. Cristallogr.* **1971**, *94*, 175–176.

[230] Collin, G.; Flahaut, J. *Bull. Soc. Chim. Fr.* **1972**, 2207–2209.

[231] Collin, G.; Étienne, J.; Laruelle, P. *Bull. Soc. Fr. Mineral. Cristallogr.* **1973**, *96*, 12–17.

[232] Perez, G.; Darriet-Duale, M.; Hagenmuller, P. *J. Solid State Chem.* **1970**, *2*, 42–48.

[233] Collin, G.; Étienne, J.; Flahaut, J.; Guittard, M.; Laruelle, P. *Rev. Chim. Miner.* **1973**, *10*, 225–238.

[234] Villars, P.; Cenzual, K. Pearson's Crystal Data – Crystal Structure Database for Inorganic Compounds (on DVD), Release 2015/16, ASM International, Materials Park, OH, USA.

[235] Choudhury, A.; Dorhout, P. K. *Inorg. Chem.* **2015**, *54*, 1055–1065 and references therein.

[236] Rodier, N.; Guittard, M.; Flahaut, J. *C. R. Acad. Sci., Ser. 2* **1983**, *296*, 65–70.

[237] Nanjundaswamy, K. S.; Gopalakrishnan, J. *J. Solid State Chem.* **1983**, *49*, 51–58.

[238] Van Calcar, P. M.; Dorhout, P. K. *Mater. Sci. Forum* **1999**, *315*, 322–330.

[239] Yin, W.; Wang, W.; Kang, L.; Lin, Z.; Feng, K.; Shi, Y.; Hao, W.; Yao, J. L.; Wu Y. *J. Solid State Chem.* **2013**, 202, 269–275.

[240] Rudyk, B. W.; Stoyko, S. S.; Mar, A *J. Solid State Chem.* **2013**, 208, 78–85.

[241] Rudyk, B. W.; Stoyko, S. S.; Oliynyk, A. O.; Mar, A. *J. Solid State Chem.* **2014**, *210*, 79–88.

[242] Yin, W.; Shi, Y.; Kang, B.; Deng, J.; Yao, J.; Wu, Y. *J. Solid State Chem.* **2014**, *213*, 87–92.

[243] Jin, Z.; Li, Z.; Du, Y. *Yingyong Huaxue* **1985**, *2*, 42–46.

[244] Meng, Y.; Fan, Y.; Lu, R.; Cui, Q.; Zou, G. *Physica* **1986**, *139&140B,* 337–340.

[245] Gitzendanner, R. L.; Spencer, C. M.; DiSalvo, F. J.; Pell, M. A.; Ibers, J. A. *J. Solid State Chem.* **1996**, *131*, 399–404.

[246] Huch, M. R.; Gulay, L. D.; Olekseyuk, I. D. *J. Alloys Compd.* **2006**, *424*, 114–118.

[247] Gulay, L. D; Daszkiewicz, M.; Huch, M. R.; Pietraszko, A. *Acta Crystallogr., Sect. E*, **2007**, *63*, i187.

[248]   Guo, S. P.; Guo, G. C.; Wang, M. S.; Zou, J. P.; Xu G.; Wang G. J.; Long X. F.; Huang J.S. *Inorg. Chem.* **2009**, 48, 7059–7065.

[249]   Daszkiewicz, M.; Marchuk, O. V.; Gulay, L. D.; Kaczorowski, D. *J. Alloys Compd.* **2014**, 610, 258–263.

[250]   Daszkiewicz, M.; Pashynska, Y. O.; Marchuk, O. V.; Gulay, L. D.; Kaczorowski, D. *J. Alloys Compd.* **2014,** 616, 243–249

[251]   Assoud A.; Sankar C. R.; Kleinke H. *Solid State Sci.* **2014**, *38*, 124–128.

[252]   Strok, O. M.; Daszkiewicz, M.; Gulay, L. D. *Chem. Met. Alloys* **2015**, *8*, 16–21.

[253]   He, J.; Wang, Z.; Zhang, X.; Cheng, Y.; Gong, Y.; Lai, X.; Zheng C.; Lin J.; Huang F. *RSC Adv.* **2015**, *5*, 52629–52635

[254]   Sun, Y. -L.; Chi, Y.; Guo, S. -P. *Jiegou Huaxue* **2016**, *35*, 1369–1375.

[255]   Shi, Y. -F.; Chen, Y. -K.; Chen, M. -K.; Wu, L. -M.; Lin, H.; Zhou, L. -J; Chen, L. *Chem. Mater.* **2015**, *27*, 1876–1884.

[256]   de Saint-Giniez, D.; Laruelle, P.; Flahaut, J. *C. R. Acad. Sci., Ser. C* **1968**, *267*, 1029–1032.

[257]   Patrie, M.; Guittard, M. *C. R. Acad. Sci., Ser. C* **1969,** *268*, 1136–1138.

[258]   Jaulmes, S.; Palazzi, M.; Laruelle, P. *Mater. Res. Bull.* **1988**, *23*, 831–835.

[259]   Hartenbach, I.; Nilges, T.; Schleid T. *Z. Anorg. Allg. Chem.* **2007**, *633*, 2445–2452.

[260]   Daszkiewicz, M; Gulay, L. D.; M.; Pietraszko, A.; Shemet, V. Y. *J. Solid State Chem.* **2007**, *180*, 2053–2060.

[261]   Daszkiewicz, M; Gulay, L. D.; Lychmanyuk; O. S; Pietraszko, A. *J. Alloys Compd.* **2008**, *460*, 201–205.

[262]   Daszkiewicz, M; Gulay, L. D.; Lychmanyuk; O. S; Pietraszko, A. *J. Alloys Compd.* **2009**, *467*, 168–172

[263]   Daszkiewicz, M; Gulay, L. D. *Mater. Res. Bull.* **2012**, *47*, 497–499.

[264]   Daszkiewicz, M; Gulay, L. D.; Lychmanyuk; O. S. *Acta Crystallogr. B* **2009**, *65*, 126–133.

[265]   Iyer, A. K.; Rudyk, B. W.; Lin, X; Singh, H.; Sharma, A. Z.; Wiebe, C. R.; Mar, A. *J. Solid State Chem.* **2015**, *229*, 150–159.

[266]   Iyer, A. K.; Yin, W.; Rudyk, B. W.; Lin, X; Nilges, T.; Mar, A. *J. Solid State Chem.* **2016**, *243*, 221–231.

[267]   Zhao, H. -J. *J. Solid State Chem.* **2015**, *227*, 5–9.

[268]   Zhang, X.; Chen, W.; Mei, D.; Zheng, C.; Liao, F.; Li, Y.; Lin, J.; Huang, F. *J. Alloys Compd.* **2014**, *610*, 671–675.

[269]   Abrahams, S. C. *Acta Crystallogr. B*, **1990**, *46*, 311–324.

[270]   Sheldrick, G. M. *SHELXTL*, version 6.12; Bruker AXS Inc.: Madison, WI, 2001.

[271]   Gelato, L. M.; Parthé, E. *J. Appl. Crystallogr.* **1987**, *20*, 139–143.

[272]   Tank, R.; Jepsen, O.; Burkhardt, A.; Andersen, O. K. *TB-LMTO-ASA Program*, version 4.7; Max Planck Institut für Festkörperforschung: Stuttgart, Germany, **1998**.

[273]   Michelet, A.; Flahaut, J. *C. R. Acad. Sci., Ser. C* **1969**, *268*, 326–329.

[274]   Michelet, A.; Mazurier, A.; Collin, G.; Laruelle, P.; Flahaut, J. *J. Solid State Chem.* **1975**, *13*, 65–76.

[275]   Zeng H. Y.; Zheng F. K.; Guo G. C.; Huang J. S. *J. Alloys Compd.* **2008**, *458*, 123–129.

[276]   Daszkiewicz, M.; Strok, O. M.; Gulay, L. D.; Kaczorowski, D. *J. Alloys Compd.* **2010**, *508*, 258–261.

[277]   Brese, N. E.; O'Keeffe, M. *Acta Crystallogr., Sect. B* **1991**, *47*, 192–197.

[278]   Bronger, W.; Koelman, W.; Schmitz, D. *Z. Anorg. Allg. Chem.* **1995**, *621*, 405–408.

[279] Chareev, D. A.; Kurnosov, A. V.; Dubrovinsky, L. S.; Narygina, O. V.; Gavrilenko, P. G.; Zarechnaya, E. Yu.; Dubrovinskaya, N. A.; Litvin, Yu. A.; Osadchii, E. G. *Dokl. Earth Sci.* **2010**, *432*, 771–774.

[280] Zabel, M.; Wandinger, S.; Range, K. -J. *Z. Naturforsch. B* **1979**, *34*, 238–241.

[281] Guittard, M.; Julien-Pouzol, M.; Laruelle, P.; Flahaut, J. *C. R. Acad. Sci., Ser. C* 1968, *267*, 767–769.

[282] Michelet, A.; Flahaut, J. *C. R. Acad. Sci., Ser. C* **1969**, *269*, 1203–1205.

[283] Shi, Y. -F.; Chen, Y. -K.; Chen, M. -K.; Wu, L. -M.; Lin, H.; Zhou, L. -J; Chen, L. *Chem. Mater.* **2015**, *27*, 1876–1884.

[284] Collin, G.; Étienne, J.; Flahaut, J.; Guittard, M.; Laruelle, P. *Rev. Chim. Miner.* **1973**, *10*, 225–238.

[285] Daszkiewicz, M; Gulay, L. D.; Lychmanyuk; O. S. *Acta Crystallogr. B* **2009**, *65*, 126–13.

[286] Villars, P.; Cenzual, K. Pearson's Crystal Data – Crystal Structure Database for Inorganic Compounds (on DVD), Release 2015/16, ASM International, Materials Park, OH, USA.

[287] Collin, G.; Flahaut, J. *C. R. Acad. Sci., Ser. C* **1970**, *270*, 488–490.

[288] Perez, G.; Darriet-Duale, M.; Hagenmuller, P. *J. Solid State Chem.* **1970**, *2*, 42–48.

[289] Jin, Z.; Li, Z.; Du, Y. *Yingyong Huaxue* **1985**, *2*, 42–46.

[290] Meng, Y.; Fan, Y.; Lu, R.; Cui, Q.; Zou, G. *Physica* **1986**, *139&140B,* 337–340.

[291] Gitzendanner, R. L.; Spencer, C. M.; DiSalvo, F. J.; Pell, M. A.; Ibers, J. A. *J. Solid State Chem.* **1996**, *131*, 399–404.

[292] Huch, M. R.; Gulay, L. D.; Olekseyuk, I. D. *J. Alloys Compd.* **2006**, *424*, 114–118.

[293] Gulay, L. D; Daszkiewicz, M.; Huch, M. R.; Pietraszko, A. *Acta Crystallogr., Sect. E,* **2007**, *63*, i187.

[294] Guo S. P.; Guo G. C.; Wang M. S.; Zou J. P.; Xu G.; Wang G. J.; Long X. F.; Huang J.S. *Inorg. Chem.* **2009**, 48, 7059–7065.

[295] Daszkiewicz, M.; Marchuk, O. V.; Gulay, L. D.; Kaczorowski, D. *J. Alloys Compd.* **2014**, 610, 258–263.

[296] Daszkiewicz, M.; Pashynska, Y. O.; Marchuk, O. V.; Gulay, L. D.; Kaczorowski, D. *J. Alloys Compd.* **2014,** *616*, 243–249.

[297] Assoud A.; Sankar C. R.; Kleinke H. *Solid State Sci.* **2014**, *38*, 124–128.

[298] Strok, O. M.; Daszkiewicz, M.; Gulay, L. D. *Chem. Met. Alloys* **2015**, *8*, 16–21.

[299] Daszkiewicz, M.; Pashynska, Y. O.; Marchuk, O. V.; Gulay, L. D.; Kaczorowski, D. *J. Alloys Compd* **2015**, *647*, 445–455.

[300] He, J.; Wang, Z.; Zhang, X.; Cheng, Y.; Gong, Y.; Lai, X.; Zheng C.; Lin J.; Huang F. *RSC Adv.* **2015**, *5*, 52629–52635

[301] Sun, Y. -L.; Chi, Y.; Guo, S. -P. *Jiegou Huaxue* **2016**, *35*, 1369–1375.

[302] Iyer, A. K.; Yin, W.; Lee, E. J.; Lin, X; Mar, A. *J. Solid State Chem.* **2017**, *250*, 14–23.

[303] Collin, G.; Étienne, J.; Laruelle, P. *Bull. Soc. Fr. Mineral. Cristallogr.* **1973**, *96*, 12–17.

[304] Guo, S. P.; Zeng, H. Y.; Jiang, X. M.; Guo, G. C. *Jiegou Huaxue* **2009**, *28*, 1448–1452.

[305] Zhao, H.-J. *J. Solid State Chem.* **2015**, *227*, 5–9.

[306] de Saint-Giniez, D.; Laruelle, P.; Flahaut, J. *C. R. Acad. Sci., Ser. C* **1968**, *267*, 1029–1032.

[307] Patrie, M.; Guittard, M. *C. R. Acad. Sci., Ser. C* **1969**, *268,* 1136–1138

[308] Zeng, H. Y.; Zheng, F. K.; Guo, G. C.; Huang, J. S. *J. Alloys Compd.* **2008**, *458*, 123–129.

[309] Gulay, L. D.; Daszkiewicz, M; Huch, M. R. *J. Solid State Chem.* **2008**, *181*, 2626–2632

[310] Brese, N. E.; O'Keeffe, M. *Acta Crystallogr., Sect. B* **1991**, *47*, 192–197.

[311] Mundus, C.; Taillades, G.; Pradel, A.; Ribes, M. *Solid State Nucl. Magn. Reson.* **1996**, *7*, 141–146.

[312]   Pietrass, T.; Taulelle, F. *Magn. Reson. Chem.* **1997**, *35*, 363–366.

[313]   Jiang, T.; Ozin, G. A.; Bedard, R. L. *J. Mater. Chem.* **1998**, *8*, 1641–1648.

[314]   MacKenzie, K.; Smith, M. E. *Multinuclear Solid-State Nuclear Magnetic Resonance of Inorganic Materials*, Elsevier, Oxford, **2002**.

[315]   Schevciv, O.; White, W. B. *Mater. Res. Bull.* **1983**, *18*, 1059–1068.

[316]   Sheldrick, G. M. *SHELXTL*, version 6.12; Bruker AXS Inc.: Madison, WI, **2001**.

[317]   Gelato, L. M.; Parthé, E. *J. Appl. Crystallogr.* **1987**, *20*, 139–143

[318]   Harris, R. K.; Sebald, A. *Magn. Reson. Chem.* **1987**, *25*, 1058–1062.

[319]   Kortüm, G. *Reflectance Spectroscopy*, Springer, New York, **1969**.

[320]   Tank, R.; Jepsen, O.; Burkhardt, A.; Andersen, O. K. *TB-LMTO-ASA Program*, version 4.7; Max Planck Institut für Festkörperforschung: Stuttgart, Germany, **1998**.

[321]   Mitchell, K. A.; Ibers, J. A. *Chem. Rev.* **2002**, *102*, 1929–1952.

[322]   Koscielski, L. A.; Ibers, J. A. *Z. Anorg. Allg. Chem.* **2012**, *638*, 2585–2593.

[323]   Meng, C. -Y.; Chen, H.; Wang, P.; Chen, L. *Chem. Mater.* **2011**, *23*, 4910–4919.

[324]   Iyer, A. K.; Yin, W.; Rudyk, B. W.; Lin, X.; Nilges, T.; Mar, A. *J. Solid State Chem.* **2016**, *243*, 221–231 and references therein.

[325]   Chen, M. -C.; Li, L. -H.; Chen, Y.-B.; Chen, L. *J. Am. Chem. Soc.* **2011**, *133*, 4617–4624.

[326]   Zhao, H. -J. *J. Solid State Chem.* **2016**, *237*, 99–104.

[327]   Zhao, H. -J.; Zhang, Y. -F.; Chen, L. *J. Am. Chem. Soc.* **2012**, *134*, 1993–1995.

[328]   Zhao, H. -J. *Z. Anorg. Allg. Chem.* **2016**, *642*. 56–59.

[329]   Sheldrick, G. M. *SHELXTL*, version 6.12; Bruker AXS Inc.: Madison, WI, **2001**.

[330]   Gelato, L. M.; Parthé, E. *J. Appl. Crystallogr.* **1987**, *20*, 139–143.

[331]   Villars, P.; Cenzual, K. Pearson's Crystal Data – Crystal Structure Database for Inorganic Compounds (on DVD), release 2015/16, ASM International, Materials Park, OH, 2016.

[332]   Kortüm, G. Reflectance Spectroscopy, Springer, New York, **1969**.

[333]   Ward, M. D.; Pozzi, E. A.; Van Duyne, R. P.; Ibers, J. A. *J. Solid State Chem.* **2014**, *212*, 191–196.

[334]   Eisenmann, B.; Hofmann, A.; *Z. Anorg. Allg. Chem.* **1990**, 580, 151–159.

[335]   Tideswell, N. W.; Kruse, F. H.; McCullough, J. D. *Acta Crystallogr.* **1957**, *10*, 99–102.

[336]   Brese, N. E.; O'Keeffe, M. *Acta. Crystallogr., Sect. B* **1991**, *47*, 192–197.

[337]   Mitchell, K.; Ibers, J. A. *Chem. Rev.* **2002**, *102*, 1929–1952.

[338]   Villars, P.; Cenzual, K. Pearson's Crystal Data – Crystal Structure Database for Inorganic Compounds (on DVD), Release 2015/16, ASM International, Materials Park, OH, USA.

[339]   Kanatzidis, M. G.; Sutorik, A. C. *Prog. Inorg. Chem.* **1995**, *43*, 151–265.

[340]   Daszkiewicz, M; Gulay, L. D.; Lychmanyuk; O. S. *Acta Crystallogr. B* **2009**, *65*, 126–133.

[341]   Huch, M. R.; Gulay, L. D.; Olekseyuk, I. D.; Pietraszko, A. *J. Alloys Compd.* **2006**, *425* 230–234.

[342]   Huch, M. R.; Gulay, L. D.; Olekseyuk, I. D. *J. Alloys Compd.* **2007**, *439*, 156–161.

[343]   Gulay, L. D.; Olekseyuk, I. D.; Wołcryz, M.; Stępień-Damm, J. *J. Alloys Compd.* **2005**, *399*, 189–195.

[344]   Gulay, L. D.; Olekseyuk, I. D. *J. Alloys Compd.* **2005**, *387*, 160–164.

[345]   Gulay, L. D.; Stępień-Damm, J.; Pietraszko, A.; Olekseyuk, I. D. *J. Alloys Compd.* **2006**, *413*, 90–95.

[346]   Zhao, H. -J.; Li, L. -H.; Wu, L. -M.; Chen, L. *Inorg. Chem.* **2010**, *49*, 5811–5817.

[347]   Rudyk, B. W.; Stoyko, S. S.; Mar, A *J. Solid State Chem.* **2013**, *208*, 78–85.

[348]   Sheldrick, G. M. *SHELXTL*, version 6.12; Bruker AXS Inc.: Madison, WI, **2001**.

[349]   Gelato, L. M.; Parthé, E. *J. Appl. Crystallogr.* **1987**, *20*, 139–143.

[350]   Hong, H. Y.; Steinfink, H. J. Solid State Chem. **1972**, *5*, 93–104.

[351]   Reiff, W. M.; Grey, I. E.; Fan, A.; Eliezer, Z.; Steinfink, H. *J. Solid State Chem.* **1975**, 13, 32–40.

[352] Nakayama, N.; Kosuge, K.; Kachi, S.; Shinjo, T.; Takada, T. *J. Solid State Chem.* **1980**, *33*, 351–356.

[353] Baikie, T.; Maignan, A.; Francesconi, M. G. *Chem. Commun* **2004**, 836–837.

[354] Baikie, T.; Hardy, V.; Maignan, A.; Francesconi, M. G. *Chem. Commun* **2005**, 5077–5079.

[355] Barnes, A. D. J.; Baikie, T.; Hardy, V.; Lepetit, M. -B.; Maignan, A.; Young, N. A.; Francesconi, M. G. *J. Mater. Chem.* **2006**, *16*, 3489–3502.

[356] Headspith, D. A.; Battle, P. D.; Francesconi, M. G. *J. Solid State Chem.* **2007**, *180*, 2859-2863.

[357] Mezzadri, F.; Gilioli, E.; Calestani, G.; Migliori, A.; Harrison, M. R.; Headspith, D. A.; Francesconi, M. G. *Inorg. Chem.* **2012**, *51*, 397–404.

[358] Carré, D.; Guittard, M.; Adolphe, C. *Acta Cryst. Sect. B* **1978**, *34*, 3499–3501.

[359] Aliev, O. M. *Inorg. Mater.* **1980**,*16*, 1027–1031 (Transl. *Neorg. Mater.* **1980**, *16*, 1514–1518.

[360] Besrest, F.; Collin, G. *J. Solid State Chem.* **1977**, *21*, 161–170.

[361] Brese, N. E.; O'Keeffe, M. *Acta. Crystallogr., Sect. B* **1991**, *47*, 192–197.

[362] Donohue, P. C.; Jeitschko, W. *Mater. Res. Bull.* **1974**, *9*, 1333–1336.

[363] Jeitschko, W.; Donohue, P.C. *Acta Crystallogr. Sect. B* **1975**, *31*, 1890–1895.

[364] Gladyshevskii, R. E.; Cenzual, K.; Zhao, J. T.; Parthé, E. *Acta Cryst. Sect. C* **1992**, *48*, 221–225.

[365] Sleight, A. W.; Prewitt, C. T. *Inorg. Chem.* **1968**, *7*, 2282–2288.

[366] Wu, P.; Ibers, J. A. *J. Alloys Compd.* **1995**, *229*, 206–215.

[367] Mitchell, K.; Ibers, J. A. *Chem. Rev.* **2002**, *102*, 1929–1952.

[368] Gulay L. D.; Daszkiewicz, M. in *Handbook on the Physics and Chemistry of Rare Earths*, eds. Gschneidner, , Jr., K. A.; Bünzli, J.-C. G.; Pecharsky, V. K. Elsevier, Amsterdam, 2011, pp. 157–273.

[369] Chung, I.; Kanatzidis, M. G. *Chem. Mater.* **2014**, *26*, 849–869.

[370] Zhou, J. *Coord. Chem. Rev.* **2016**, *315*, 112–134.

[371] Meng, C. -Y.; Chen, H.; Wang, P.; Chen, L. *Chem. Mater.* **2011**, *23*, 4910–4919.

[372] Mitchell, K.; Haynes, C. L.; McFarland, A. D.; Van Duyne, R. P.; Ibers, J. A. *Inorg. Chem.* **2002**, *41*, 1199–1204.

[373] Mitchell, K.; Huang, F. Q.; McFarland, A. D.; Haynes, C. L.; Somers, R. C.; Van Duyne, R. P.; Ibers, J. A. *Inorg. Chem.* **2003**, *42*, 4109–4116.

[374] Mitchell, K.; Huang, F. Q.; Caspi, E. N.; McFarland, A. D.; Haynes, C. L.; Somers, R. C.; Jorgensen, J. D.; Van Duyne, R. P.; Ibers, J. A. *Inorg. Chem.* **2004**, *43*, 1082–1089.

[375] Yao, J.; Deng, B.; Sherry, L. J.; McFarland, A. D.; Ellis, D. E.; Van Duyne, R. P.; Ibers, J. A. *Inorg. Chem.* **2004**, *43*, 7735–7740.

[376] Chan, G. H.; Sherry, L. J.; Van Duyne, R. P.; Ibers, J. A. *Z. Anorg. Allg. Chem.* **2007**, *633*, 1343–1348.

[377] Masuda, H.; Fujino, T.; Sato, N.; Yamada, K. *J. Solid State Chem.* **1999**, *146*, 336–343.

[378] Wakeshima, M.; Hinatsu, Y. *J. Solid State Chem.* **2000**, *153*, 330–335.

[379] Wakeshima, M.; Hinatsu, Y.; Oikawa, K.; Shimojo, Y.; Morii, Y. *J. Mater. Chem.* **2000**, *10*, 2183–2185.

[380] Wakeshima, M.; Hinatsu, Y. *J. Solid State Chem.* **2001**, *159*, 163–169.

[381] Ino, K.; Wakeshima, M.; Hinatsu, Y. *Mater. Res. Bull.* **2001**, *36*, 2207–2213.

[382] Lozac'h, A.-M.; Guittard, M.; Flahaut, J. *Mater. Res. Bull.* **1973**, *8*, 75–86.

[383] Agaev, A. B.; Aliev, V. O.; Aliev, O. M. *Zh. Neorg. Khim.* **1996**, *41*, 319–325.

[384] Hidaka, C.; Takizawa, T. *J. Phys. Chem. Solids* **2008**, *69*, 358–361.

[385] Yoo, H. S.; Im, W. B.; Vaidyanathan, S.; Park, B. J.; Jeon, D. Y. *J. Electrochem. Soc.*, **2008**, *155*, J66–J70.

[386]   Carpenter, J. D.; Hwu, S.-J. *Chem. Mater.* **1992**, *4*, 1368–1372.

[387]   Feng, K.; Shi, Y.; Yin, W.; Wang, W.; Yao, J.; Wu, Y. *Inorg. Chem.* **2012**, *51*, 11144–11149.

[388]   Yin, W.; Feng, K.; Wang, W.; Shi, Y.; Hao, W.; Yao, J.; Wu, Y. *Inorg. Chem.* **2012**, *51*, 6860–6867.

[389]   Yin, W.; Wang, W.; Bai, L.; Feng, K.; Shi, Y.; Hao, W.; Yao, J.; Wu, Y. *Inorg. Chem.* **2012**, *51*, 11736–11744.

[390]   Feng, K.; Yin, W.; Wang, W.; Kang, L.; Hao, W.; Yao, J.; Shi, Y.; Lin, Z.; Wu, Y. *Z. Anorg. Allg. Chem.*, **2013**, *639*, 1021–1025.

[391]   Khan, W.; Borek, S.; Minar, J. *RSC Adv.* **2015**, *5*, 51461–51469.

[392]   Sheldrick, G. M. *SHELXTL, version 6.12*, Bruker AXS Inc., Madison, WI, **2001**.

[393]   Gelato, L. M.; Parthé, E. *J. Appl. Crystallogr.* **1987**, *20*, 139–143

[394]   Kortüm, G. *Reflectance Spectroscopy*, Springer, New York, **1969**.

[395]   Tank, R.; Jepsen, O.; Burkhardt, A.; Andersen, O. K. *TB-LMTO-ASA Program*, version 4.7; Max Planck Institut für Festkörperforschung: Stuttgart, Germany, **1998**.

[396]   Jaulmes, S.; Julien-Pouzol, M. *Acta Crystallogr. Sect. B* **1977**, *33*, 3898–3901.

[397]   Flahaut, J.; Laruelle, P.; Guittard, M.; Jaulmes, S.; Julien-Pouzol, M.; Lavenant, C. *J. Solid State Chem.*, **1979**, *29*, 125–136.

[398]   Guittard, M.; Lavenant, C.; Palazzi, M. *C. R. Seances Acad. Sci., Ser. C* **1978**, *287*, 239–242.

[399]   Petrov, V. V.; Bogdanova, A. V.; Mashkarinets, E. K.; Bel'skii, V. K.; Gladyshevskii, E. I.; Mokraya, I. R.; Pecharskii, V. K. *Izv. Akad. Nauk SSSR, Neorg. Mater.* **1987**, *23*, 1395–1396.

[400]   Yamaoka, S.; Shimomura, O.; Nakazawa, H.; Fukunaga, O. *Solid State Commun.* **1980**, *33*, 87–89.

[401]   Yamaoka, S.; Lemley, J. T.; Jenks; J. M.; Steinfink, H. *Inorg. Chem.* **1975**, *14*, 129–131.

[402]   Likforman, A.; Carré, D.; Hillel, R. *Acta Crystallogr. Sect. B* **1978**, *34*, 1–5.

[403]   Pfitzner, A.; Lutz, H. D. *J. Solid State Chem.* **1996**, *124*, 305–308.

[404]   Schulte-Kellinghaus, M.; Krämer, V. *Acta Crystallogr. Sect. B* **1979**, *35*, 3016–3017.

[405]   Guseinov, G. G.; Amiraslanov, I. R.; Kuliev, A. S.; Mamedov, Kh. S. *Izv. Akad. Nauk SSSR, Neorg. Mater.*, **1987**, *23*, 854–856.

[406]   Brese, N. E.; O'Keeffe, M. *Acta. Crystallogr., Sect. B* **1991**, *47*, 192–197.

[407]   Schevciw, O.; White, W. B. *Mater. Res. Bull.* **1983**, *18*, 1059–1068.

[408]   Takahashi, H.; Sugimoto, A.; Nambu, Y.; Yamauchi, T.; Hirata, Y.; Kawakami, T.; Avdeev, M.; Matsubayashi, K.; Du, F.; Kawashima, C.; Soeda, H.; Nakano, S.; Uwatoko, Y.; Ueda, Y.; Sato, T. J.; Ohgushi, K. *Nat. Mater.* **2015**, *14*, 1008–1012.

[409]   Chung, D. -Y.; Hogan, T.; Brazis, P.; Rocci-Lane, M.; Kannewurf, C.; Bastea, P.; Uher, C.; Kanatzidis, M. G. *Science* **2000**, *287*, 1024–1027.

[410]   Li, H.; Peters, J. A.; Liu, Z.; Sebastian, M.; Malliakas, C. D.; Androulakis, J.; Zhao, L.; Chung, I.; Nguyen, S. L.; Johnsen, S.; Wessels, B. W.; Kanatzidis, M. G. *Cryst. Growth Des.* **2012**, *12*, 3250–3256.

[411]   Bera, T. K.; Jang, J. I.; Ketterson, J. B.; Kanatzidis, M. G. *J. Am. Chem. Soc.* **2009**, *131*, 75–77.

[412]   Zhao, H. -J.; Zhang, Y. -F.; Chen, L. *J. Am. Chem. Soc.* **2012**, *134*, 1993–1995.

[413]   Bera, T. K.; Jang, J. I.; Song, J. -H.; Malliakas, C. D.; Freeman, A. J.; Ketterson, J. B.; Kanatzidis, M. G. *J. Am. Chem. Soc.* **2010**, *132*, 3484–3495.

[414]   Yin, W.; Feng, K.; He, R.; Mei, D.; Lin, Z.; Yao, J. L.; Wu, Y. *Dalton Trans.* **2012**, *41*, 5653–5661.

[415]   Lin, X.; Guo, Y.; Ye, N. *J. Solid State Chem.* **2012**, *195*, 172–177.

[416]   Chen, M. C.; Wu, L. M.; Lin, H.; Zhou, L. J.; Chen, L. *J. Am.Chem. Soc.* **2012**, *134*, 6058−6060

[417]   Kuo, S. -M.; Chang, Y. -M.; Chung, I.; Jang, J. -I.; Her, B. -H.; Yang, S. -H.; Ketterson, J. B.; Kanatzidis, M. G.; Hsu, K. -F. *Chem. Mater.* **2013**, *25*, 2427–2433.

[418]   Lin, X.; Zhang, G.; Ye, N. *Cryst. Growth Des.* **2009**, *9*, 1186–1189.

[419]   Li, X.; Li, C.; Gong, P.; Lin, Z.; Yao, Wu, J. Y. *J. Mater. Chem. C* **2015**, *3*, 10998–11004.

[420]   Liu, B. -W.; Zeng, H. -Y.; Zhang, M. -J.; Fan, Y. -H.; Guo, G. -C.; Huang, J. -S.; Dong, Z. -C. *Inorg. Chem.* **2015**, *54*, 976–981.

[421]   Mei, D.; Yin, W.; Lin, Z.; Yao, J. L.; Fu, P.; Y. Wu *J. Alloys Compd.* **2011**, *509*, 2981–2985

[422]   Klee, W.; Schäfer, H. *Z. Anorg. Allg. Chem.* **1981**, *479*, 125–133.

[423]   Kim, M. -Y.; Kim, W. -T.; Jin, M. -S.; Park, S. -A.; Choe, S. -H.; Lee, C. -I.; Hyun, S. -C.; Kim, C. -D. *J. Phys. Chem. Solids* **2003**, 64, 625–629.

[424]   Tagiev, B. G.; Abushov, S. A.; Tagiev, O. B. *J. Appl. Spectrosc.* **2010**, *77*, 115–119.

[425]   Yin, W.; Mei, D.; Feng, K.; Yao, J.; Fu, P.; Wu, Y. *Dalton Trans.* **2011**, *40*, 9159–9162.

[426]   Yao, J. L.; Mei, D.; Bai, L.; Lin, Z.; Yin, W.; Fu, P.; Wu, Y. *Inorg. Chem.* **2010**, *49*, 9212–9216.

[427]   Badikov, V.; Badikov, D.; Shevyrdyaeva, G.; Tyazhev, A.; Marchev, G.; Panyutin, V.; Petrov, V.; Kwasniewski, A. *Phys. Status Solidi RRL* **2011**, *5*, 31–33.

[428]   Yao, J.; Yin, W.; Feng, K.; Li, X.; Mei, D.; Lu, Q.; Ni, Y.; Zhang, Z.; Hu, Z.; Wu, Y. *J. Cryst. Growth* **2012**, *346*, 1–4.

[429]   Yang, F.; Yao, J.; Xu, H.; Feng, K.; Yin, W.; Li, F.; Yang, J.; Du, S.; Peng, Q.; Zhang, J.; Cui, D.; Wu, Y.; Chen, C.; Xu, Z. *Opt. Lett.* **2013**, *38*, 3903–3905.

[430]   Zhang, X.; Yao, J.; Yin, W.; Zhu, Y.; Wu, Y.; Chen, C. *Opt. Express* **2015**, *23*, 552–558.

[431]   Yang, F.; Yao, J.; Xu, H.; Zhang, F.; Zhai, N.; Lin, Z.; Zong, N.; Peng, Q.; Zhang, J.; Cui, D.; Wu, Y.; Chen, C.; Xu, Z. *IEEE Photonics Technol. Lett.* **2015**, *27*, 1100–1103.

[432]   Yin, W.; Feng, K.; Mei, D.; Yao, J.; Fu, P.; Wu, Y. *Dalton Trans.* **2012**, *41*, 2272–2276.

[433]   Yin, W.; He, R.; Feng, K.; Hao, W.; Yao, J. L.; Wu, Y. *J. Alloys Compd.* **2013**, 565, 115–119.

[434]   Lei, X. W.; Yang, M.; Xia, S. Q.; Liu, X.-C.; Pan, M. Y.; Li, X.; Tao, X. T. *Chem. Asian J.* **2014**, *9*, 1123–1131.

[435]   Sheldrick, G. M. SHELXTL, version 6.12, Bruker AXS Inc., Madison, WI, **2001**.

[436]   Gelato, L. M.; Parthé, E. *J. Appl. Crystallogr.* **1987**, *20*, 139–143.

[437]   Kortüm, G. *Reflectance Spectroscopy*, Springer, New York, **1969**.

[438]   Tank, R.; Jepsen, O.; Burkhardt, A.; Andersen, O. K. *TB-LMTO-ASA Program*, version 4.7; Max Planck Institut für Festkörperforschung: Stuttgart, Germany, **1998**.

[439]   Liu, J. -W.; Wang, P.; Chen, L. *Inorg. Chem.* **2011**, *50*, 5706–5713.

[440]   Yin, W.; Lin, Z.; Kang, L.; Kang, B.; Deng, J.; Lin, Z.; Yao, J.; Wu, Y. *Dalton Trans.* **2015**, *44*, 2259–2266.

[441]   Prakash, J.; Mesbah, A.; Lebègue, S.; Malliakas, C. D.; Ibers, J.A. *J. Solid State Chem.* **2015**, *230*, 70–74.

[442]   Feng, K.; Jiang, X.; Kang, L.; Yin, W.; Hao, W.; Lin, Z.; Yao, J.; Wu, Y.; Chen, C. *Dalton Trans.* **2013**, *42*, 13635–13641.

[443]   Brese, N. E.; O'Keeffe, M. *Acta. Crystallogr., Sect. B* **1991**, *47*, 192–197.

[444]   Schevciw, O.; White, W. B. *Mater. Res. Bull.* **1983**, *18*, 1059–1068.

[445]   Eisenmann, B.; Jakowski, M.; Schäfer, H. *Z. Naturforsch. B* **1984**, *39*, 27–30.

[446]   Eisenmann, B.; Jakowski, M.; Schäfer, H. *Rev. Chim. Miner.* **1984**, *21*, 12–20

[447]   Liu, J. -W.; Wang, P.; Chen, L. *Inorg. Chem.* **2011**, *50*, 5706–5713.

[448]   Eisenmann, B.; Jakowski, M.; Schäfer, H. *Z. Naturforsch. B* **1983**, *38*, 1581–1584.

[449]   Eisenmann, B.; Jakowski, M.; Schäfer, H. *Mater. Res. Bull.* **1982**, *17*, 1169–1175

[450]   Eisenmann, B.; Jakowski, M.; Schäfer, H. *Rev. Chim. Miner.* **1984**, *20*, 329–337.

[451]   Lin, X.; Zhang, G.; Ye, N. *Cryst. Growth Des.* **2009**, *9*, 1186–1189.

[452]   Mei, D.; Yin, W.; Lin, Z.; Yao, J. L.; Fu, P.; Y. Wu *J. Alloys Compd.* **2011**, *509*, 2981–2985.

[453]   Yin, W.; Mei, D.; Feng, K.; Yao, J.; Fu, P.; Wu, Y. *Dalton Trans.* **2011**, *40*, 9159–9162.

[454]   Yin, W.; Iyer, A. K.; Lin, X.; Mar, A. *J. Solid State Chem.* **2016**, *237*, 144–149.

[455]   Klee, W.; Schäfer, H. *Z. Anorg. Allg. Chem.* **1981**, *479*, 125–133.

[456]   Yao, J. L.; Mei, D.; Bai, L.; Lin, Z.; Yin, W.; Fu, P.; Wu, Y. *Inorg. Chem.* **2010**, *49*, 9212–9216.

[457]   Li, Y. -Y.; Liu, P. -F.; Lin, H.; Wang, M. -T.; Chen, L. *Inorg. Chem. Front.* **2016**, *3*, 952–958.

[458]   Eisenmann, B.; Hofmann, A. *Z. Anorg. Allg. Chem.* **1990**, *580*, 151–159.

[459]   Gao, W.; Wu, K.; Lai, K.; Yang, Z.; Pan, S. *Z. Anorg. Allg. Chem.* **2015**, *641*, 1329–1333.

[460]   Eisenmann, B.; Jakowski, M.; Klee, W.; Schäfer, H. *Rev. Chim. Miner.* **1983**, *20*, 255–263.

[461]   Ivanov-Emin, B. N.; Ivlieva, V. I.; Filatenko, L. A.; Zaitsev, B. E.; Kaziev, G. Z.; Sarabiya, M.G. *Zh. Neorg. Khim.* **1984**, *29*, 1960–1963.

[462]   Kipp, D. O.; Lowe-Ma, C. K.; Vanderah, T. A. *Chem. Mater.* **1990**, *2*, 506–511.

[463]   Klee, W.; Schäfer, H. *Chim. Miner.* **1979**, *16*,465–472.

[464]   Sheldrick, G. M. *SHELXTL, version 6.12*, Bruker AXS Inc., Madison, WI, 2001.

[465]   Gelato, L. M.; Parthé, E. *J. Appl. Crystallogr.* **1987**, *20*, 139–143

[466]   Kortüm, G. *Reflectance Spectroscopy*, Springer, New York, **1969**.

[467]   Heine, J.; Dehnen, S. *Z. Anorg. Allg. Chem.* **2008**, *634*, 2303–2308.

[468]   Schlosser, M.; Reiner, C.; Deiseroth, H. -J.; Kienle, L. *Eur. J. Inorg. Chem.***2001**, 2241–2247.

[469]   Yin, W.; Iyer, A. K.; Lin, X.; Li, C.; Yao, J.; Mar, A. *Dalton Trans.* **2016**, *45*, 12329–12337.

[470]   Brese, N. E.; O'Keeffe, M. *Acta. Crystallogr., Sect. B* **1991**, *47*, 192–197.

[471]   Schevciw, O.; White, W. B. *Mater. Res. Bull.* **1983**, *18*, 1059–1068.

[472]   Park, S. -A.; Kim, M. -Y.; Kim, W. -T.; Jin, M. -S.; Chee, S. -H.; Park, T. -Y.; Park, K. -H.; Kim, D. -T. *J. Mater. Res.* **2002**, *17*, 2147–2152.

[473]   Chung, I.; Kanatzidis, M. G. *Chem. Mater.* **2014**, *26*, 849–869.

[474]   Zhao, H. -J.; Wu, X. -T.; Wu, L. -M. *Struct. Bond.* **2012**, *145*, 121–134.

[475]   Lin, X.; Zhang, G.; Ye, N. *Cryst. Growth Des.* **2009**, *2*, 1186–1189.

[476]   Yao, J. L.; Mei, D.; Bai, L.; Lin, Z.; Yin, W.; Fu, P.; Wu, Y. *Inorg. Chem.* **2010**, *49*, 9212–9216.

[477]   Eisenmann, B.; Jakowski, M.; Schäfer, H. *Mater. Res. Bull.* **1982**, *17*, 1169–1175.

[478]   Eisenmann, B.; Jakowski, M.; Schäfer, H. *Z. Naturforsch. B* **1983**, *38*, 1581–1584.

[479]   Eisenmann, B.; Jakowski, M.; Schäfer, H. *Rev. Chim. Miner.* **1984**, *21*, 12–20.

[480]   Liu, J. -W.; Wang, P.; Chen, L. *Inorg. Chem.* **2011**, *50*, 5706–5713.

[481]   Eisenmann, B.; Jakowski, M.; Schäfer, H. *Z. Naturforsch. B* **1984**, *39*, 27–30.

[482]   Klee, W.; Schäfer, H. *Z. Anorg. Allg. Chem.* **1981**, *479*, 125–133.

[483]   Yin, W.; Mei, D.; Feng, K.; Yao, J.; Fu, P.; Wu, Y. *Dalton Trans.* **2011**, *40*, 9159–9162.

[484]   Mei, D.; Yin, W.; Lin, Z.; Yao, J. L.; Fu, P.; Y. Wu *J. Alloys Compd.* **2011**, *509*, 2981–2985.

[485]   Yin, W.; Iyer, A. K.; Lin, X.; Mar, A. *J. Solid State Chem.* **2016**, *237*, 144–149.

[486]   Chen, M. C.; Wu, L. M.; Lin, H.; Zhou, L. J.; Chen, L. *J. Am.Chem. Soc.* **2012**, *134*, 6058−6060.

[487]   Li, X.; Li, C.; Gong, P.; Lin, Z.; Yao, Wu, J. Y. *J. Mater. Chem. C* **2015**, *3*, 10998–11004.

[488]   Kuo, S. -M.; Chang, Y. -M.; Chung, I.; Jang, J. -I.; Her, B. -H.; Yang, S. -H.; Ketterson, J. B.; Kanatzidis, M. G.; Hsu, K. -F. *Chem. Mater.* **2013**, *25*, 2427–2433.

[489]   Liu, B. -W.; Zeng, H. -Y.; Zhang, M. -J.; Fan, Y. -H.; Guo, G. -C.; Huang, J. -S.; Dong, Z. -C. *Inorg. Chem.* **2015**, *54*, 976–981.

[490]   Lin, X.; Guo, Y.; Ye, N. *J. Solid State Chem.* **2012**, *195*, 172–177.

[491]   Yin, W.; Feng, K.; Mei, D.; Yao, J.; Fu, P.; Wu, Y. *Dalton Trans.* **2012**, *41*, 2272–2276.

[492]   Sheldrick, G. M. SHELXTL, version 6.12, Bruker AXS Inc., Madison, WI, 2001.

[493]   Gelato, L. M.; Parthé, E. *J. Appl. Crystallogr.* **1987**, *20*, 139–143.

[494]   Kortüm, G. *Reflectance Spectroscopy*, Springer, New York, **1969.**

[495]   Kurtz, S. K.; Perry, T. T. *J. Appl. Phys.* **1968**, *39*, 3798–3813.

[496]   Tank, R.; Jepsen, O.; Burkhardt, A.; Andersen, O. K. *TB-LMTO-ASA Program*, version 4.7; Max Planck Institut für Festkörperforschung: Stuttgart, Germany, **1998**.

[497]   Haeuseler, H.; Schmidt, C. *J. Alloys Compd.* **1994**, *204*, 209–213.

[498]   Mao, A. W.; Aitken, B. G.; Sen, S. *J. Non-Cryst. Solids* **2013**, *369*, 38–43.

[499]   Mao, A. W.; Kaseman, D. C.; Youngman, R. E.; Aitken, B. G.; Sen, S. *J. Non-Cryst. Solids* **2013**, *375*, 40–46.

[500]   Mao, A. W.; Kaseman, D. C.; Aitken, B. G.; Sen, S. *J. Non-Cryst. Solids* **2015**, *427*, 62–68.

[501]   Chen, Y. -K.; Chen, M. -C.; Zhou, L. -J.; Chen, L.; Wu, L. -M. *Inorg. Chem.* **2013**, *52*, 8334–8341.

[502]   Yin, W.; Lin, Z.; Kang, L.; Kang, B.; Deng, J.; Lin, Z.; Yao, J.; Wu, Y. *Dalton Trans.* **2015**, *44*, 2259–2266.

[503]   Villars, P.; Cenzual, K. Pearson's Crystal Data – Crystal Structure Database for Inorganic Compounds (on DVD), Release 2015/16, ASM International, Materials Park, OH, USA.

[504]   Brese, N. E.; O'Keeffe, M. *Acta. Crystallogr., Sect. B* **1991**, *47*, 192–197.

[505]   Brown, I. D. Bond Valence Parameters, www.iucr.org/resources/data/datasets/bond-valence-parameters.

[506]   Yin, W.; Feng, K.; Mei, D.; Yao, J.; Fu, P.; Wu, Y. *Dalton Trans.* **2012**, *41*, 2272–2276.

[507]   Schevciw, O.; White, W. B. *Mater. Res. Bull.* **1983**, *18*, 1059–1068.

[508]   Wei, S. -H.; Zunger, A. *Appl. Phys. Lett.* **1990**, *56*, 662–664.

[509]   Nikogosyan, D. N. *Nonlinear Optical Crystals: A Complete Survey*, Springer, New York, 2005.

[510]   Chung I.; Kanatzidis, M. G. *Chem. Mater.* **2014**, *26*, 849–869.

[511]   Ok, K. M. *Acc. Chem. Res.*, doi:10.1021/acs.accounts.6b00452.

[512]   Schnering, H. G.; Hoppe, R. *Z. Anorg. Allg. Chem.*, **1961**, *312*, 99–109.

[513]   Iglesias, J. E.; Pachali K. E.; Steinfink, H. *J. Solid State Chem.* **1974**, *9*, 6–14.

[514]   Wang Y. C.; DiSalvo, F. J. *J. Solid State Chem.* **1999**, *148*, 464–467.

[515]   Li, C.; Yin, W.; Gong, P.; Li, X.; Zhou, M.; Mar, A.; Lin, Z.; Yao, J.; Wu Y.; Chen, C. *J. Am. Chem. Soc.* **2016**, *138*, 6135–6138.

[516]   Klee, W.; Schäfer, H. *Z. Anorg. Allg. Chem.* **1983**, *499*, 145–152.

[517]   B. Eisenmann and A. Hofmann, *Z. Anorg. Allg. Chem.* **1990**, *580*, 151–159.

[518]   Mei, D.; Yin, W.; Lin, Z.; He, R.; Yao, J.; Fu, P.; Wu, Y. *J. Alloys Compd.* **2011**, *509*, 2981–2985.

[519]   Yin, W.; Mei, D.; Feng, K.; Yao, J.; Fu; P.; Wu, Y. *Dalton Trans.* **2011**, *40*, 9159–9163.

[520]   Sheldrick, G. M. *SHELXTL, version 6.12*, Bruker AXS Inc., Madison, WI, 2001.

[521]   Spek, A. L. *Acta Crystallogr., Sect. D* **2009**, *65*, 148–155.

[522]   Gelato, L. M.; Parthé, E. *J. Appl. Crystallogr.* **1987**, *20*, 139–143.

[523]   Kortüm, G. *Reflectance Spectroscopy*, Springer, New York, 1969.

[524]   Kurtz S. K.; Perry, T. T. *J. Appl. Phys.* **1968**, *39*, 3798–3813.

[525]   Tank, R.; Jepsen, O.; Burkhardt A.; Andersen, O. K. *TB–LMTO–ASA Program, version 4.7*, Max Planck Institut für Festkörperforschung, Stuttgart, 1998.

[526]   Duan, R. -H.; Yu, J. -S.; Lin, H.; Zheng, Y. -J.; Zhao, H. -J.; Huang-Fu, S.- X.; Khan, M. A.; Chen, L.; Wu, L. -M. *Dalton Trans.* **2016**, *45*, 12288–12291.

[527]   Li, H.; Eddaoudi, M.; Laine, A.; O'Keeffe; M.; Yaghi, O. M. *J. Am. Chem. Soc.* **1999**, *121*, 6096–6097.

[528]   Pauling, L. *The Nature of the Chemical Bond*, 3rd ed., Cornell University Press, Ithaca, NY, 1960.

[529]   Villars P.; Cenzual, K. *Pearson's Crystal Data – Crystal Structure Database for Inorganic Compounds (on DVD), release 2015/16*, ASM International, Materials Park, OH, 2016.

[530]   Brese, N. E.; O'Keeffe, M. *Acta. Crystallogr., Sect. B* **1991**, *47*, 192–197.

[531]   Schevciv, O.; White, W. B. *Mater. Res. Bull.* **1983**, *18*, 1059–1068.

[532]   Yao, J.; Mei, D.; Bai, L.; Lin, Z.; Yin, W.; Fu, P.; Wu, Y. *Inorg. Chem.* **2010**, *49*, 9212–9216.

[533]   Yin, W.; Feng, K.; He, R.; Mei, D.; Lin, Z.; Yao; J.; Wu, Y. *Dalton Trans.* **2012**, *41*, 5653–5661.

[534] Jiang, X. -M.; Guo, S. -P.; Zeng, H. -Y.; Zhang, M. -J.; Guo, G. -C. *Struct. Bonding* **2012**, *145*, 1–44.

[535] Chung, I.; Kanatzidis, M. G. *Chem. Mater.* **2014**, *26*, 849–869.

[536] Li, C.; Yin, W.; Gong, P.; Li, X.; Zhou, M.; A. Mar, A.; Lin, Z.; Yao, J.; Wu, Y.; Chen, C. *J. Am. Chem. Soc.* **2016**, *138*, 6135–6138.

[537] Bera, T. K.; Jang, J. I.; Ketterson, J. B.; Kanatzidis, M. G. *J. Am. Chem. Soc.* **2009**, *131*, 75–77.

[538] Zhao, H. -J.; Zhang, Y. -F.; Chen, L. *J. Am. Chem. Soc.* **2012**, *134* 1993–1995.

[539] Bera, T. K.; Jang, J. I.; Song, J. -H.; Malliakas, C. D.; Freeman, A. J.; Ketterson, J. B.; Kanatzidis, M. G. *J. Am. Chem. Soc.* **2010**, *132*, 3484–3495.

[540] Yin, W.; Feng, K.; He, R.; Mei, D.; Lin, Z.; Yao, J.; Wu, Y. *Dalton Trans.* **2012**, *41*, 5653–5661.

[541] Lin, X.; Guo, Y.; Ye, N.; *J. Solid State Chem.* **2012**, *195*, 172–177.

[542] Chen, M. C.; Wu, L. M.; Lin, H.; Zhou, L. J.; Chen, L. *J. Am.Chem. Soc.* **2012**, *134*, 6058−6060.

[543] Lin, X.; Zhang, G.; Ye, N. *Cryst. Growth Des.* **2009**, *9*, 1186–1189.

[544] Liu, B. -W.; Zeng, H. -Y.; Zhang, M. -J.; Fan, Y. -H.; Guo, G. -C.; Huang, J. -S.; Dong, Z. -C. *Inorg. Chem.* **2015**, *54*, 976–981.

[545] Yin, W.; Feng, K.; Hao, W.; Yao, J.; Wu, Y. *J. Solid State Chem.* **2012**, *192*, 168–171.

[546] Lei, X. -W.; Yang, M.; Xia, S. -Q.; Liu, X. -C.; Pan, M. -Y.; Li, X.; Tao, X. -T. *Chem. Asian J.* **2014**, *9*, 1123–1131.

[547] Yin, W.; Feng, K.; Mei, D.; Yao, J.; Fu, P.; Wu, Y. *Dalton Trans.* **2012**, *41*, 2272–2276.

[548] Kuo, S. -M.; Chang, Y. -M.; Chung, I.; Jang, J. -I.; Her, B. -H.; Yang, S. -H.; Ketterson, J. B.; Kanatzidis, M. G.; Hsu, K. -F. *Chem. Mater.* **2013**, *25*, 2427–2433.

[549] Yin, W.; He, R.; Feng, K.; Hao, W.; Yao, J. L.; Wu, Y. *J. Alloys Compd.* **2013**, *565*, 115–119.

[550] Teske, C. L. *Z. Anorg. Allg. Chem.* **1985**, *522*, 122–130.

[551] Zhen, K.; Wu, N.; Wang, Y.; Li, Q.; Gao, W.; Hou, D.; Yang, Z.; Jang, H.; Dong, Y.; Pan, S. *Dalton Trans.* **2016**, *45*, 10681–10688.

[552] Teske, C.L. *Z. Anorg. Allg. Chem.* **1980**, *468*, 27–34.

[553] Teske, C. L. *Z. Naturforsch. B* **1980**, *35,* 509–510.

[554] Teske, C. L. *Z. Anorg. Allg. Chem.* **1980**, *460*, 163–168.

[555] Teske, C. L. *Z. Naturforsch. B* **1980**, *35*, 7–11.

[556] Wu, K.; Su, X.; Yang, Z.; Pan, S. *Dalton Trans.* **2015**, *44*, 19856–19864.

[557] Sheldrick, G. M. *SHELXTL, version 6.12*, Bruker AXS Inc., Madison, WI, **2001**.

[558] Spek, A. L. *Acta Crystallogr., Sect. D* **2009**, *65*, 148–155.

[559] Gelato, L. M.; Parthé, E. *J. Appl. Crystallogr.* **1987**, *20*, 139–143.

[560] Kurtz, S. K.; Perry, T. T. *J. Appl. Phys.* **1968**, *39*, 3798–3813.

[561] Tank, R.; Jepsen, O.; Burkhardt, A.; Andersen, O. K. *TB-LMTO-ASA Program*, version 4.7; Max Planck Institut für Festkörperforschung: Stuttgart, Germany, 1998.

[562] Villars, P.; Cenzual, K. Pearson's Crystal Data – Crystal Structure Database for Inorganic Compounds, ASM International, Materials Park, OH, 2010.

[563] Brese, N. E.; O'Keeffe, M. *Acta. Crystallogr., Sect. B* **1991**, *47*, 192–197.

[564] Assoud, A.; Soheilnia, N.; Kleinke, H. *Chem. Mater.* **2005**, *17*, 2255–2261.

[565] Tampier, M.; Johrendt, D. *Z. Anorg. Allg. Chem.* **2001**, *627*, 312-320.

[566] Pocha, R.; Tampier, M.; Hoffmann, R. -D.; Mosel, B. D.; Pöttgen, R.; Johrendt, D. *Z. Anorg. Allg. Chem.* **2003**, *629*, 1379–1384.

[567] Bera, T. K.; Kanatzidis, M. G. *Inorg. Chem.* **2012**, *51*, 4293–4299.

[568] Aitken, J. A.; Chondroudis, K.; Young Jr., V. G.; Kanatzidis, M. G. *Inorg. Chem.* **2000**, *39*, 1525–1533.

[569] Schevciw, O.; White, W. B. *Mater. Res. Bull.* **1983**, *18*, 1059–1068.

[570]   Nikogosyan, D. N. *Nonlinear Optical Crystals: A Complete Survey, Springer*, New York, **2005**.

[571]   Yao, J.; Mei, D.; Bai, L.; Lin, Z.; Yin, W.; Fu, P.; Wu, Y. *Inorg. Chem.* **2010**, *49*, 9212–9216.

[572]   Maggard, P. A.; Nault, T. S.; Stern, C. L.; Poeppelmeier, K. R. *J. Solid State Chem.* **2003**, *175*, 27–33.

[573]   Izumi, H. K.; Kirsch, J. E.; Stern, C. L.; Poeppelmeier, K. R. *Inorg. Chem.* **2005**, *44*, 884–895.

[574]   Steinemann, S. G.; Wolf, W.; Poudloucky, R. in J. H. Westbrook R. L. Flescher (Eds.), *Intermetallic Compounds – Principles and Practice*, **2002**, *3*, 231-246.

Appendix 1
Supplementary Data for Chapter 3

Table A1–1. Harmonic (U_{ij}) and non-harmonic (C_{ijk}) displacement parameters ($\mathring{A}^2$) for Ag site in $La_3Ag_{0.6}GaS_7$.

U_{11}	0.0176(6)	C_{111}	0.0003(7)
U_{22}	0.0176(6)	C_{112}	0.0003(7)
U_{33}	0.676(16)	C_{113}	0.013(4)
U_{12}	0.0881(3)	C_{122}	0
U_{13}	0	C_{123}	0.006(2)
U_{23}	0	C_{133}	0
U_{eq}	0.237(5)	C_{222}	–0.0003(7)
		C_{223}	0.013(4)
		C_{233}	0
		C_{333}	–0.1(8)

Supplementary Data for Chapter 7

a

b

c

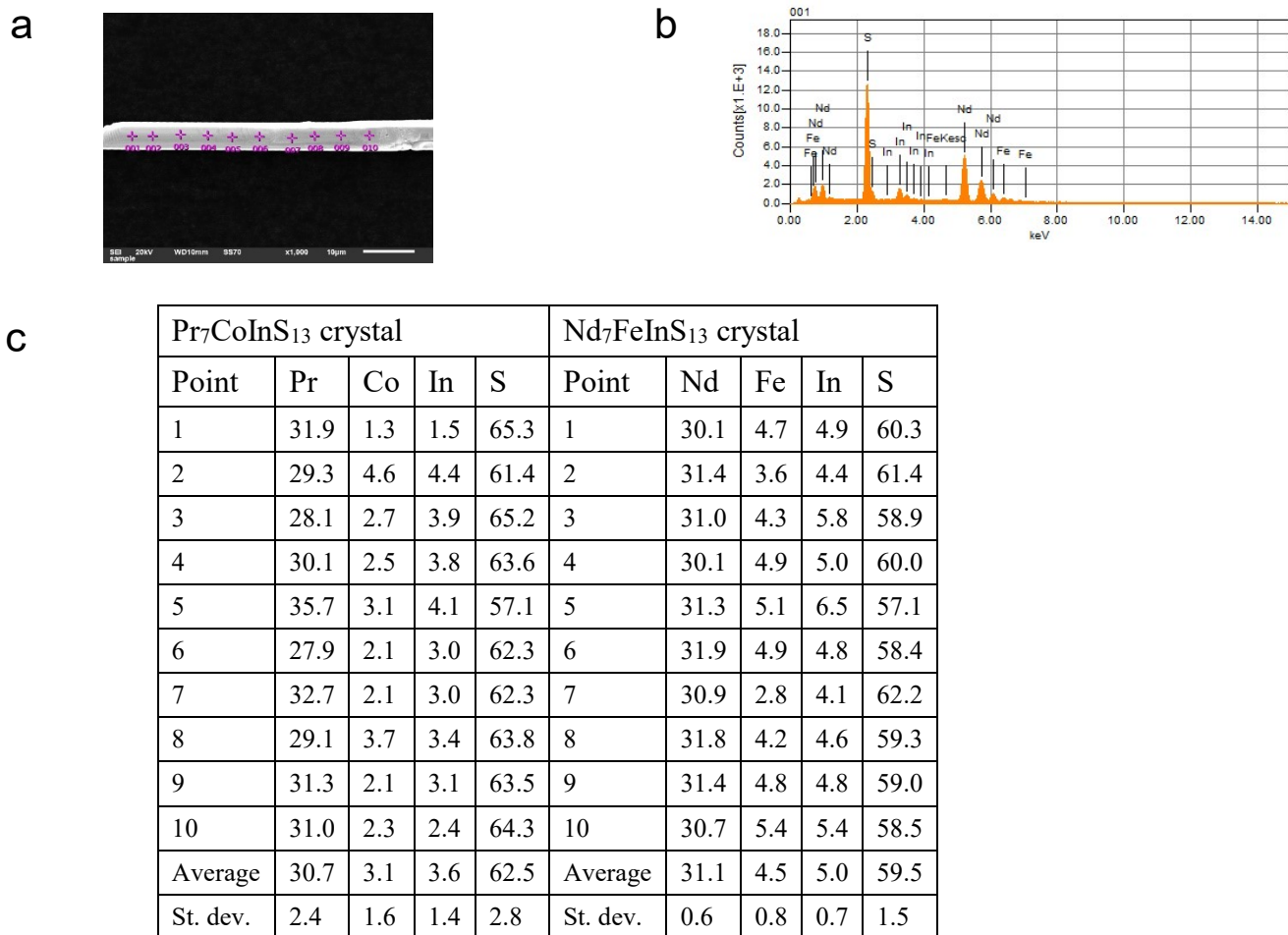| Pr$_7$CoInS$_{13}$ crystal					Nd$_7$FeInS$_{13}$ crystal				
Point	Pr	Co	In	S	Point	Nd	Fe	In	S
1	31.9	1.3	1.5	65.3	1	30.1	4.7	4.9	60.3
2	29.3	4.6	4.4	61.4	2	31.4	3.6	4.4	61.4
3	28.1	2.7	3.9	65.2	3	31.0	4.3	5.8	58.9
4	30.1	2.5	3.8	63.6	4	30.1	4.9	5.0	60.0
5	35.7	3.1	4.1	57.1	5	31.3	5.1	6.5	57.1
6	27.9	2.1	3.0	62.3	6	31.9	4.9	4.8	58.4
7	32.7	2.1	3.0	62.3	7	30.9	2.8	4.1	62.2
8	29.1	3.7	3.4	63.8	8	31.8	4.2	4.6	59.3
9	31.3	2.1	3.1	63.5	9	31.4	4.8	4.8	59.0
10	31.0	2.3	2.4	64.3	10	30.7	5.4	5.4	58.5
Average	30.7	3.1	3.6	62.5	Average	31.1	4.5	5.0	59.5
St. dev.	2.4	1.6	1.4	2.8	St. dev.	0.6	0.8	0.7	1.5

Fig. A2-1. (a) Representative SEM image and (b) EDX spectrum for Nd$_7$FeInS$_{13}$. (c) Representative EDX analyses (mol. %) for Pr$_7$CoInS$_{13}$ and Nd$_7$FeInS$_{13}$.

Appendix 3

Supplementary Data for Chapter 8

Table A3–1. EDX analyses of BaRE_2In$_2$Ch$_7$ (RE = La–Nd; Ch = S, Se). [a]

Compound	No. of analyses	at. % Ba	at. % RE	at. % In	at. % Ch
BaLa$_2$In$_2$S$_7$	6	7(1)	18(2)	17(2)	58(3)
BaCe$_2$In$_2$S$_7$	3	10(1)	17(2)	16(2)	58(3)
BaPr$_2$In$_2$S$_7$	6	8(1)	18(2)	17(2)	57(3)
BaNd$_2$In$_2$S$_7$	5	9(1)	17(2)	16(2)	58(3)
BaLa$_2$In$_2$Se$_7$	3	6(1)	18(2)	18(2)	58(3)
BaCe$_2$In$_2$Se$_7$	5	10(1)	18(2)	16(2)	56(3)
BaPr$_2$In$_2$Se$_7$	6	7(1)	15(2)	15(2)	62(3)
BaNd$_2$In$_2$Se$_7$	6	10(2)	20(3)	17(2)	53(5)

[a] Expected compositions are 8% Ba, 17% RE, 17% In, and 58% Ch
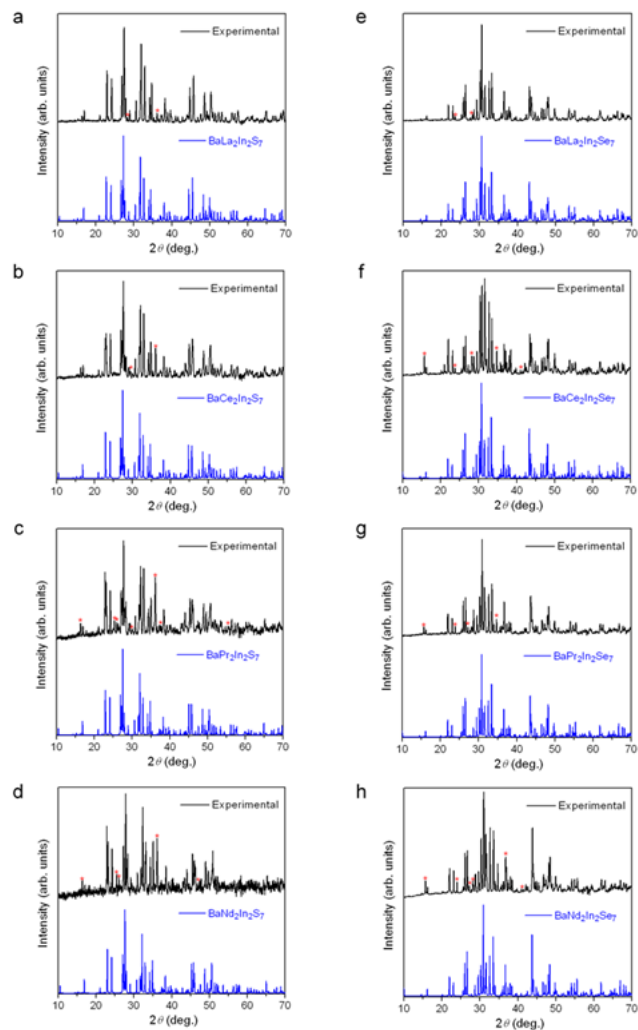
Figure A3–1. Powder XRD patterns for BaRE_2In$_2$$Ch_7$ (RE = La–Nd; Ch = S, Se).
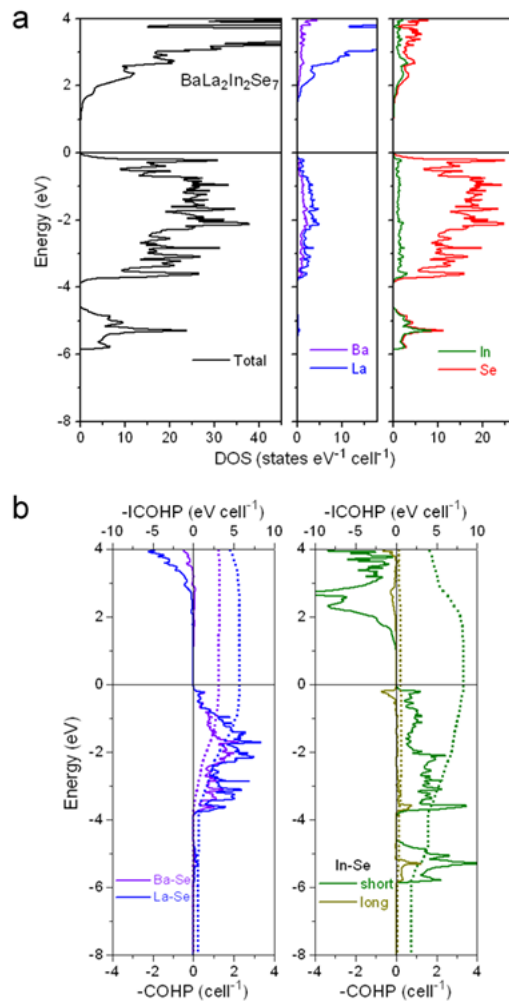
Figure A3–2. (a) Density of states (DOS) and (b) crystal orbital Hamilton population (–COHP) curves for $BaLa_2In_2Se_7$.

Appendix 4

Supplementary Data for Chapter 10

Table A4–1. Bond valence sums in $Ba_{12}In_4Se_{20}$

Ba1	2.29	Se3	2.01
Ba2	1.85	Se4	1.89
Ba3	2.04	Se5	2.47
Ba4	2.01	Se6	2.22
In1	2.99	Se7	2.32
In2A	2.95	Se8	2.30
In2B	2.92	Se9	2.09
In3A	2.95	Se10	1.96
In3B	3.01	Se11	2.01
In4	2.90	Se12	1.66
Se1	1.81	S13	1.32
Se2	1.96	Se14	1.80

Figure A4–1. Coordination polyhedra around Ba and Se13/Se14 atoms in $Ba_{12}In_4Se_{20}$.

Figure A4–2. Possible models for local coordination of In atoms within stacks of In-centred tetrahedra in $Ba_{12}In_4Se_{20}$.
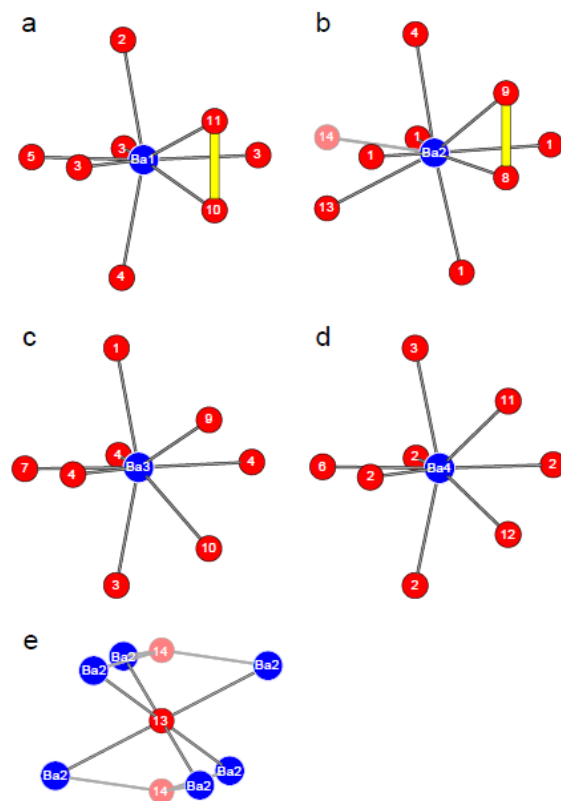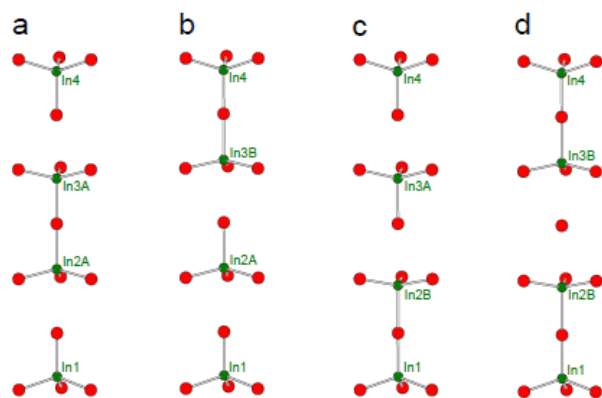
Appendix 5

Supplementary Data for Chapter 11

Table A5–1. Evaluation of models with different Ga/Ge site distributions.

Model	A	B	C	D
Formula	$Ba_4Ga_4GeSe_{12}$	$Ba_4GaGe_4Se_{12}$	$Ba_4Ga_{4.0(5)}Ge_{1.0(5)}Se_{12}$	$Ba_4Ga_4GeSe_{12}$
$M1$ at $8e$ (0.14, 0.24, 0.44)	1.00 Ga	1.00 Ge	0.75(13) Ga / 0.25(13) Ge	0.75 Ga / 0.25 Ge
$M2$ at $2b$ (0, 0, 0.5)	1.00 Ge	1.00 Ga	0.97(24) Ga / 0.03(24) Ge	1.00 Ga
Bond valence sum for $M1$	3.16	3.61	3.27	3.27
Bond valence sum for $M2$	3.48	3.04	3.05	3.04
$R(F)$ for $F_o^2 > 2\sigma(F_o^2)$	0.0235	0.0235	0.0232	0.0232
$R_w(F_o^2)$	0.0525	0.0527	0.0520	0.0520
A, B [a]	0.0261, 0.4522	0.0261, 0.4522	0.0261, 0.4522	0.0261, 0.4522
$(\Delta\rho)_{max}, (\Delta\rho)_{min}$ (e Å^{-3})	1.01, –0.92	1.05, –0.77	1.02, –0.78	1.02, –0.78

[a] Weighting parameters appearing in the expression $w^{-1} = [\sigma^2(F_o^2) + (Ap)^2 + Bp]$, where $p = [\max(F_o^2,0) + 2F_c^2] / 3$.

a

SEI 0001 20kV WD9mm SS70 x800 20μm 101 Jan 12, 2016

b

009

Counts[x1 E+3]

keV

c

Point	Ba	Ga	Ge	Se
1	23.27	22.39	4.24	50.10
2	22.97	22.46	4.88	49.69
3	23.80	22.39	3.96	49.84
4	23.69	21.73	4.68	49.90
5	23.22	22.65	4.30	49.82
6	22.26	19.89	3.82	54.03
7	20.70	16.37	3.66	59.27
8	23.64	22.27	4.61	49.49
Average	22.94	21.27	4.27	51.52

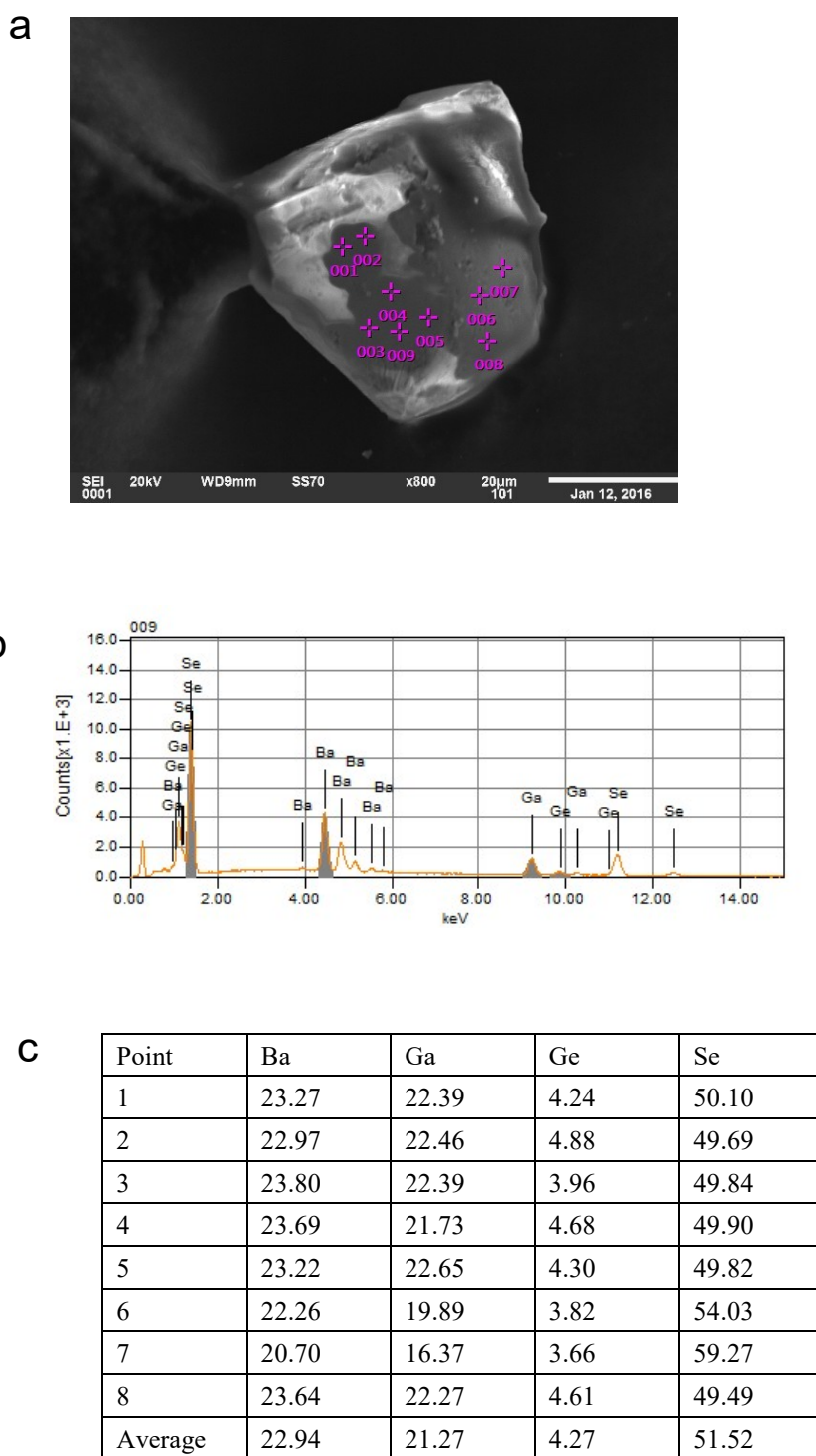**Figure A5–1**. (a) SEM image of $Ba_4Ga_4GeSe_{12}$ crystal, (b) representative EDX spectrum, and (c) analysis (mol. %) of numbered points on the crystal.

Appendix 6

Supplementary Data for Chapter 12

Table A6–1. Atomic coordinates and equivalent isotropic displacement parameters (Å^2) for $Ba_5CdGa_6Se_{15}$

Atom	Wyckoff position	Occupancy	x	y	z	U_{eq} (Å^2) [a]
Ba1	8c	1	0.11158(2)	0.16313(3)	0.53149(8)	0.02311(13)
Ba2	8c	1	0.61573(2)	0.13084(3)	0.49176(8)	0.01937(11)
Ba3	4b	1	¼	0.15388(4)	0.08079(11)	0.01982(15)
*M*1	8c	1 Ga	0.02912(4)	0.19363(5)	0.06038(14)	0.01622(19)
*M*2	8c	0.408(9) Cd, 0.592(9) Ga	0.15858(4)	0.47028(4)	0.47523(14)	0.0230(3)
*M*3	4b	1 Ga	¼	0.30720(7)	0.6096(2)	0.0174(3)
*M*4	4b	0.195(12) Cd, 0.805(12) Ga	¼	0.47167(7)	0.95279(19)	0.0181(4)
*M*5	4a	1 Ga	0	0	0.0000(2)	0.0172(3)
Se1	8c	1	0.00009(4)	0.09428(4)	0.24606(15)	0.01900(18)
Se2	8c	1	0.01066(4)	0.30348(5)	0.22983(15)	0.02121(19)
Se3	8c	1	0.07855(5)	0.50724(5)	0.27451(16)	0.0296(2)
Se4	8c	1	0.12625(3)	0.19928(4)	0.01776(14)	0.01841(18)
Se5	8c	1	0.15950(4)	0.34053(5)	0.48910(15)	0.02062(18)
Se6	8c	1	0.16694(4)	0.02270(5)	0.31479(15)	0.0231(2)
Se7	4b	1	¼	0.18387(6)	0.57922(19)	0.0178(2)
Se8	4b	1	¼	0.50882(7)	0.3097(2)	0.0257(3)
Se9	4b	1	¼	0.84371(7)	0.46676(19)	0.0184(2)

[a] U_{eq} is defined as one-third of the trace of the orthogonalized U_{ij} tensor.

Table A6–2. Interatomic distances (Å) for Ba$_5$CdGa$_6$Se$_{15}$

Ba1–Se2	3.3042(12)	Ba3–Se7	3.3701(15)
Ba1–Se4	3.3123(11)	Ba3–Se6 (×2)	3.5737(12)
Ba1–Se6	3.3314(11)	Ba3–Se9	3.7143(15)
Ba1–Se7	3.3942(6)	Ga1–Se1	2.3728(13)
Ba1–Se3	3.4856(11)	Ga1–Se4	2.3742(13)
Ba1–Se4	3.4893(11)	Ga1–Se2	2.3923(13)
Ba1–Se1	3.5523(11)	Ga1–Se2	2.4265(13)
Ba1–Se5	3.6027(11)	Cd/Ga2–Se3	2.4561(15)
Ba2–Se2	3.2492(11)	Cd/Ga2–Se6	2.4706(14)
Ba2–Se4	3.2691(10)	Cd/Ga2–Se5	2.4876(12)
Ba2–Se9	3.2959(5)	Cd/Ga2–Se8	2.5805(11)
Ba2–Se1	3.3200(11)	Ga3–Se7	2.3713(18)
Ba2–Se3	3.3638(11)	Ga3–Se5 (×2)	2.4205(11)
Ba2–Se6	3.4011(11)	Ga3–Se9	2.4660(19)
Ba2–Se5	3.5028(11)	Cd/Ga4–Se6 (×2)	2.4177(12)
Ba2–Se5	3.5359(11)	Cd/Ga4–Se9	2.4532(18)
Ba3–Se4 (×2)	3.1517(9)	Cd/Ga4–Se8	2.4679(19)
Ba3–Se8	3.3083(16)	Ga5–Se3 (×2)	2.4239(13)
Ba3–Se7	3.3496(15)	Ga5–Se1 (×2)	2.4323(13)

Appendix 7

Supplementary Data for Chapter 13

Table A7–1. Evaluation of models for BaZnTtSe$_4$ (Tt = Si, Ge) with different site distributions.

Model	A	B	C
BaZnSiSe$_4$			
M1 at 4b (¼, 0.25, 0.52)			
Occupancy	1.00 Zn	1.00 Si	1.00(1) Zn / 0.00(1) Si
U_{eq} (Å^2)	0.0193(2)	–0.0127(9) (NPD)	0.0193(2)
Bond valence sum	1.97	2.20	2.20
M2 at 4b (¼, 0.26, 0.01)			
Occupancy	1.00 Si	1.00 Zn	–0.03(1) Zn / 1.03(1) Si
U_{eq} (Å^2)	0.0122(3)	0.0656(25)	0.0111(5)
Bond valence sum	3.76	3.38	3.77
$R(F)$ for $F_o^2 > 2\sigma(F_o^2)$	0.0194	0.0717	0.0204
$R_w(F_o^2)$	0.0403	0.2484	0.0432
A, B [a]	0.0171, 1.0206	0.0171, 1.0206	0.0171, 1.0206
$(\Delta\rho)_{max}, (\Delta\rho)_{min}$ (e Å^{-3})	1.42, –0.86	8.03, –5.68	1.30, –2.24
BaZnGeSe$_4$			
M1 at 4b (¼, 0.25, 0.52)			
Occupancy	1.00 Zn	1.00 Ge	1.2(1) Zn / –0.2(1) Ge
U_{eq} (Å^2)	0.0198(2)	0.0249(3)	0.0288(8)
Bond valence sum	1.94	2.75	1.78
M2 at 4b (¼, 0.26, 0.01)			
Occupancy	1.00 Ge	1.00 Zn	–0.2(1) Zn / 1.2(1) Ge
U_{eq} (Å^2)	0.0140(2)	0.0096(2)	0.0217(6)
Bond valence sum	3.85	2.71	4.07
$R(F)$ for $F_o^2 > 2\sigma(F_o^2)$	0.0240	0.0270	0.0422
$R_w(F_o^2)$	0.0523	0.0675	0.1222
A, B [a]	0.0223, 0.7629	0.0223, 0.7629	0.0223, 0.7629
$(\Delta\rho)_{max}, (\Delta\rho)_{min}$ (e Å^{-3})	2.32, –1.59	2.45, –1.74	3.38, –3.75

[a] Weighting parameters appearing in the expression $w^{-1} = [\sigma^2(F_o^2) + (Ap)^2 + Bp]$, where $p = [\max(F_o^2,0) + 2F_c^2] / 3$.
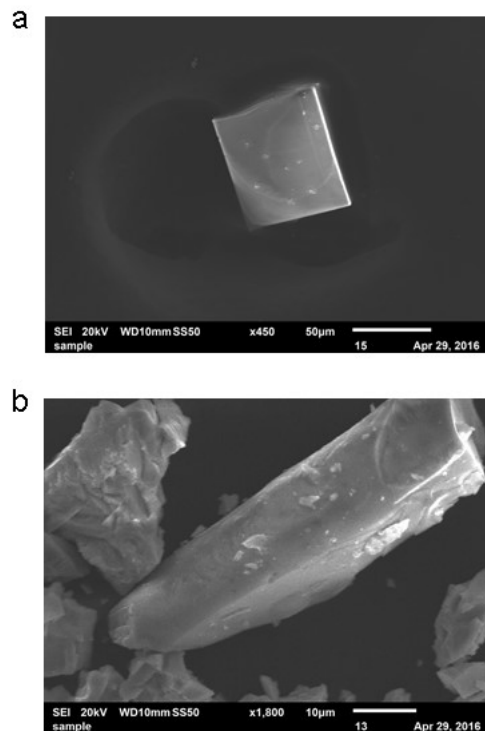
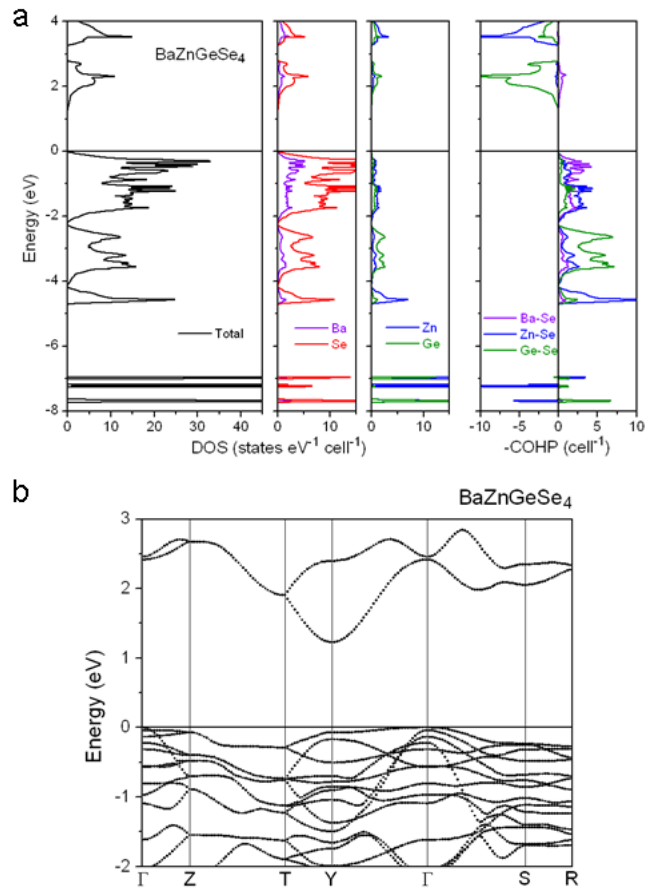**Figure A7–1.** SEM images of crystals of (a) $BaZnSiSe_4$ and (b) $BaZnGeSe_4$.

Figure A7–2. (a) Density of states (DOS) (left panel), atomic projections (middle panels), and crystal orbital Hamilton population (–COHP) curves (right panel) for BaZnGeSe₄. (b) Band dispersion diagram for BaZnGeSe₄.